# Vapor sensing behavior of sensor materials based on conductive polymer nanocomposites

DISSERTATION

Zur Erlangung des akademischen Grades

Doktor rerum naturalium

(Dr. rer. nat.)

Vorgelegt

dem Bereich für Chemie und Lebensmittelchemie

der Technischen Universität Dresden

von

**Yilong Li**

geboren am 31.12.1988 in Henan, V.R. China

Eingereicht am 09.09.2019

# Acknowledgements

This thesis would not be possible without the help of many people including supervisors, colleagues, technicians and friends.

I would like to express my gratitude to my supervisor, Prof. Brigitte Voit, for providing me an opportunity to work and study as a student at IPF and TU Dresden. I really appreciate her invaluable guidance and support through my research in the past four years. Besides, I would also like to thank my supervisors, Dr. Petra Pötschke and Dr. Jürgen Pionteck, for their great sources of ideas and knowledge about my projects. We had many insightful discussions for the research results and paper writing. Their enthusiasm and passion about research have influenced my research attitude profoundly. Moreover, their encouragement is a compact support to help me move forward during my tough period in research. All what I learned from them not only academic knowledge but also attitude to overcome difficulties that are priceless for me.

I also want to thank all the people who helped me by contributing their time and knowledge to my work during the past four years. I thank Dr. Petr Formanek, Dr. Minoj Gnanaseelan and Mrs. Manuela Heber for their SEM and TEM observation, Dr. Beate Krause and Mrs. Ulrike Jentzsch-Hutschenreuther for melt compounding training, microtome training and OM observation, Dr. Roland Vogel for rheology training and measurements, Mrs. Sabine Krause for DSC measurements, and Dr. Kai Ke and Mr. Andreas Scholze for hot compression molding training. Besides, thanks are given to my colleagues of NB department Dr. Lothar Jakisch, Dr. Ulrike Staudinger, Dr. Karina Kunz, and Mr. Piotr Rzeczkowski, who gave me many useful suggestions and advices on my work.

Special thanks are delivered to my Chinese friends in IPF. It is really an amazing life in Dresden with them. At the early time I arrived in Dresden, they helped me a lot in both academic and living regards. Moreover, they are always exchanging thoughts with me, which helps me to think comprehensively and profoundly. I will remember the life here forever, together with their excellent cooking skills and tasty cuisines.

I want to acknowledge the financial support from China Scholarship Council (CSC) to support my living and work in Dresden. Similarly, thanks are also delivered to IPF for the financial support for attending international conferences.

Most of all, I would especially thank my parents, for their love, care, support and encouragement to me. My parents' nurturing on my growth and personalities such as perseverance push me forward in my career. Last but not least, I want to thank my girlfriend, Yanjun Zheng, for her enormous support and encouragement during past several years.

# Symbols and Abbreviations

## Symbols

| | |
|---|---|
| $A_{agg}$ | Area ratio of remaining nanotube agglomerates |
| $\Omega$ | Ohm |
| $\sigma$ | Electrical conductivity |
| $\sigma_0$ | Scaling factor in power law of percolation theory |
| wt% | Weight percent |
| vol% | Volume percent |
| $\varphi_c$ | Percolation threshold |
| $R$ | Resistance |
| $R_0$ | Initial resistance |
| $R_{rel}$ | Relative resistance change |
| $\delta$ | Solubility parameter |
| $\delta_d$ | Dispersion part of solubility parameter |
| $\delta_p$ | Polar part of solubility parameter |
| $\delta_h$ | Hydrogen bonding part of solubility parameter |
| 2D | Two-dimensional |
| 3D | Three-dimensional |
| nm | Nanometer |
| μm | Micrometer |
| $T$ | Temperature |
| $\alpha$ | Thermal expansion coefficient |
| $\chi_{12}$ | Flory-Huggins interaction parameter |
| $\eta^*$ | Complex viscosity |
| $G'$ | Storage modulus |
| $G''$ | Loss modulus |

## Abbreviations

| | |
|---|---|
| **PC** | Polycarbonate |
| **PVDF** | Poly(vinylidene fluoride) |
| **PS** | Polystyrene |
| **PLA** | Poly(lactic acid) |
| **PCL** | Polycaprolactone |
| **PVA** | Poly(vinyl alcohol) |
| **TPU** | Thermoplastic polyurethane |
| **PP** | Polypropylene |
| **ABS** | Acrylonitrile-butadiene-styrene copolymer |
| **PMMA** | Poly(methyl methacrylate) |
| **PAA** | Poly(amic acid) |
| **PI** | Polyimide |
| **PA66** | Polyamide 6.6 |
| **PA12** | Polyamide 12 |
| **PA6** | Polyamide 6 |
| **PE** | Polyethylene |
| **EVA** | Poly(ethylene-co-vinyl acetate) |
| **UHMWPE** | Ultra-high molecular weight polyethylene |
| **HDPE** | High density polyethylene |
| **PEH** | Poly(ethylene-*co*-hexane) |
| **SBS** | Poly(styrene-*b*-butadiene-*b*-styrene) |
| **PB** | Polybutadiene |
| **PDMS** | Poly(dimethylsiloxane) |
| **PVA** | Polyvinyl alcohol |
| **PAA** | Polyacrylic acid |
| **ODA** | 4,4'-oxydianiline |

| | |
|---|---|
| **GO** | Graphene oxide |
| **CB** | Carbon black |
| **CF** | Carbon fiber |
| **CNT** | Carbon nanotube |
| **CNS** | Carbon nanostructure |
| **CNF** | Carbon nanofiber |
| **GNP** | Graphene nanoplate |
| **MWCNT** | Multi-walled carbon nanotubes |
| **SWCNT** | Single-walled carbon nanotubes |
| **CPCs** | Conductive polymer composites |
| **CVD** | Chemical vapor deposition |
| **TLM** | Transmission light microscopy |
| **SEM** | Scanning electron microscopy |
| **TEM** | Transmission electron microscopy |
| **EMI** | Electromagnetic interference shielding |
| **VOCs** | Volatile organic compounds |
| **HSP** | Hansen solubility parameter |
| **MO** | Metal oxide |
| **CP** | Conjugated polymer |
| **DMF** | N,N'-dimethylformamide |
| **DCM** | Dichloromethane |
| **PVC** | Positive vapor coefficient |
| **NVC** | Negative vapor coefficient |

# Contents

# 1. Introduction

## 1.1 Motivation

Nowadays, polymer products have been widely used all over the world. In order to meet the rapid development of technology, functional polymer composites are extensively prepared and investigated because of their versatility. According to their thermal properties and their behavior upon heating, polymers can be divided into thermosets and thermoplastics. Thermosetting polymers can be irreversibly hardened after being cured. The cross-linking process can maintain the product shape when heat is applied, which makes thermosets a kind of good candidate for heat resistance applications. Comparing to thermosetting polymers, thermoplastic polymers can be soft when being heated and become more fluid as additional heat is applied. However, such softening process is reversible as no chemical bonding happens among molecular chains. Therefore, thermoplastic polymers can be shaped using different processing methods such as extrusion molding, injection molding, hot-pressing, solution casting, melt-spinning, electrospinning and so on.

Due to the excellent processing properties and variable processing methods of thermoplastic polymers, there has been an increasing interest in fabricating thermoplastic polymer composites with enhanced properties or with additional features like enhanced mechanical strength, electrical conductivity and increased ductility, thermal insulation, etc. Most of the thermoplastic materials are electrically insulating polymers, lightweight and easy to process. However, polymer composites can be conductive when certain amount conductive fillers are incorporated into polymer matrix to make the composites electrically conductive. The combination of polymer and conductive fillers can not only retain their individual properties, but also endow the composites certain special characteristics, which cannot be achieved by single component alone [1]. Given these merits, conductive polymer composites (CPCs) are proposed and investigated extensively because of their electrical properties.

Widely used conductive fillers in CPCs are carbon black (CB) [2-4], carbon fiber (CF) [5, 6], carbon nanotube (CNT) [7, 8] and graphite nanoplate (GNP) [9, 10]. Low filler loading does not result in much conductivity increase because these conductive fillers are isolated dispersed and do not form the conductive path. With increasing conductive filler content, a sharp increase in conductivity can be observed when critical filler content is reached in polymer matrix. This phenomenon is termed as electrical percolation and its threshold as electrical percolation concentration ($\varphi_c$). From a microscopic perspective, the isolated conductive fillers in polymer matrix start contacting with each other gradually and form a

conductive network that leads to the electrical percolation. Therefore, the conductive network in polymer matrix is crucial to the electrical properties of CPCs.

Among those processing methods used for CPCs fabrication, melt processing approaches like injection molding or extrusion are most widely applied in consideration of their low cost and large-scale production. However, there should be a good balance between filler-filler and filler-polymer interactions in composites. If fillers have self-interaction force such as Van der Waals force, they would tend to form agglomerates in the viscous polymer matrix. Conversely, an exceedingly good interaction of filler and polymer leads to an insulating polymer layer around particles and prevent the formation of a conductive network [11]. Therefore, the selection of filler and polymer should be considered comprehensively. Apart from that, filler loading is another important issue, which should be as low as possible; otherwise the composite processing will be much more difficult, accompanied with impaired mechanical properties and increased cost. For instance, Zhao et al. reported that less CNTs are needed to construct a conductive network in polypropylene (PP) as compared to CB [12]. This is because CNTs with high aspect ratio can more easily connect with neighboring nanotubes as compared to spherical CB particles. Therefore, less amount of CNTs are required to achieve electrical percolation than in case of CB. Moreover, GNPs with larger surface area is also regarded as a promising candidate in reducing $\varphi_c$ of CPCs [9, 13, 14]. In addition to the large aspect ratio or surface area of CNTs or GNPs, their excellent electrical properties also make them good filler candidates for CPCs.

In addition to the selection of suitable conductive fillers, there are still many other methods that can be used for tailoring the conductive network and resulting electrical properties of CPCs. For instance, Sang et al. prepared carbon nanostructure/thermoplastic polyurethane (CNS/TPU) composites using a solution/melt mixing method. Inspired by the brick-wall structure, they firstly grinded CNS and TPU powder with the aid of ethanol and then these dried mixtures were hot compression molded. By virtue of constructing such segregated structure, the $\varphi_c$ of CPCs is only 0.06 wt%, which is currently the lowest values for CNS/TPU composites [15]. Gupta et al. fabricated segregated CB/acrylonitrile-butadiene-styrene copolymer(ABS) composites with an ultralow $\varphi_c$ of 0.0054 vol%, which was the lowest value for CB based CPC composites [16]. A systematic review on segregated CPCs was given by Pang et al. [17]. In segregated CPCs, the conductive fillers are primarily located at the interfaces among the polymer matrix particles instead of being randomly dispersed throughout the entire CPCs. Kovacs et al. [18] demonstrated that processing parameters can significantly influence the conductive network and the $\varphi_c$ of epoxy/CNTs composites. As

shown in **Fig. 1.1**, the conductivity of CPCs containing 0.1 wt% CNTs and prepared under slow stirring (50 rpm) and medium stirring (500 rpm) is higher than that prepared with fast stirring (2000 rpm), which indicates that shearing force can determine the conductive network state of CPCs. Moreover, the optical microscopy (OM) images of CPCs containing 0.1 wt% CNTs also proves that the conductive network can be maintained well under slow stirring as compared to medium or fast stirring.
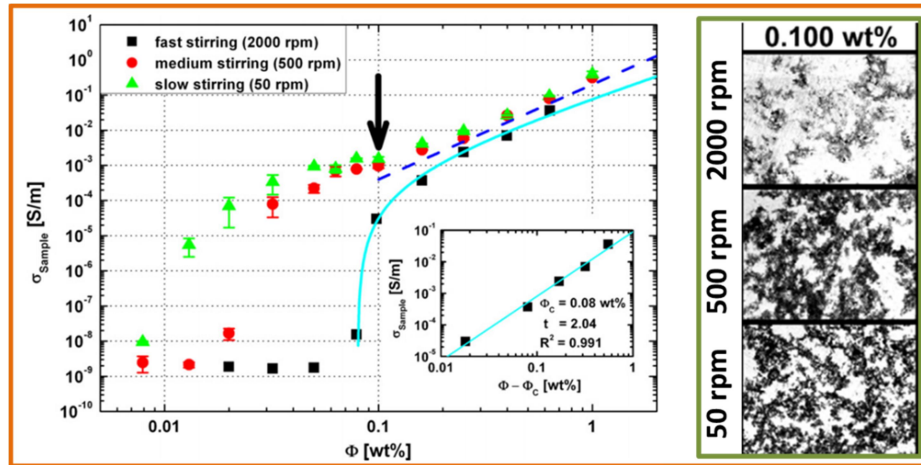


**Fig. 1.1** Electrical percolation curves of epoxy/CNTs composites and the OM images of different conductive network morphology of cured CPCs prepared under different stirring speeds. Reused with permission from Elsevier [18].

Incorporating hybrid fillers into polymer matrices is a facile technique to fabricate conductive polymer nanocomposites with a good combination of excellent electrical and mechanical properties as well as price. Researchers have done much work regarding hybrid carbon filler filled CPCs ranging from 0 dimensional CB (0D-CB), 1 dimensional CNTs (1D-CNTs) to 2 dimensional GNPs (2D-GNPs) [19-24]. For instance, Ma et al. investigated MWCNT and CB hybrid fillers filled epoxy based nanocomposites. The $\varphi_c$ of epoxy/MWCNT composites was around 0.3 wt%. In comparison, when adding 0.2 wt% CB into the nanocomposites containing 0.2 wt% MWCNT, a remarkable conductivity increase by 6 orders of magnitude was observed, even if at that MWCNT content the epoxy/MWCNT was not conductive. It was confirmed that CB nanoparticles could effectively fill the gaps between MWCNT and link them together which gave rise to the conductivity enhancement of CPCs [20]. Yu et al. explored the synergistic behavior on the thermal conductivity of SWCNT/GNPs/epoxy composites. The maximum thermal conductivity was achieved when GNP/SWCNT ratio was 3:1 by weight, which manifested a perfect conductive network at such condition. Meanwhile, they also presented the CNP-SWCNT network in epoxy, where 1D-SWCNT acted as thread to string the isolated 2D-GNPs together. The surface area of

conductive network was increased significantly by applying hybrid filler strategy, leading to a promoted electrical properties of CPCs [19]. Socher et al. studied melt mixed composites based on polyamide 12 (PA12) composites containing hybrid filler systems of CB and MWCNT in the weight ratios of 50/50 and 25/75. At loadings well above the percolation threshold, higher volume conductivities were obtained for samples containing MWCNT/CB, especially at the weight ratio of 50/50, as compared to samples filled with only MWCNT or CB. Furthermore, the addition of CB reduced the MWCNT agglomeration in the PA12 matrix [21].

Another effective method to tune conductive network of CPCs is introducing polymer blends. Due to their polarity differences the polymer components of blends are mostly immiscible or partially miscible [25]. Therefore, multiple-phase microstructures can be achieved based on different blend compositions, physical properties of the polymer component (*e.g.* melt viscosity and interfacial tensions), and even the processing conditions. The mostly studied morphologies of polymer blends can be categorized into four different types: matrix-dispersed particle structure, matrix-fiber structure, lamellar structure and co-continuous structure [26, 27]. The combination of two polymer components with preferred localization of conductive fillers makes polymer blends a good candidate for conductive polymer blends, whose conductive network can be tailored by changing the blend microstructure. Sumita et al. described the electrical conductivity of polypropylene (PP) based blends with either poly(methyl methacrylate) (PMMA) or high density polyethylene (HDPE) filled with CB [28]. They observed an uneven distribution of the CB, which is localized in HDPE component of PP/HDPE blends but at the interface in the PP/PMMA blends. Consequently, PP/PMMA/CB showed much lower $\varphi_c$ as compared to PMMA/CB composites, whereas not much difference was found between PP/HDPE/CB and HDPE/CB composites. Based on such findings, Sumita et al. proposed the double percolation concept, i.e. the conductive fillers are selectively distributed in one component or at the polymer-polymer interface of co-continuous polymer blends, and then this continuous conductive component allows the whole composite to be conductive. By this strategy, a lower filler amount is needed to construct the conductive pathways in the blend composites.

Because of the advantages like easy processing and tunable conductive networks, CPCs have many promising applications such as antistatic materials [29], electromagnetic interference shielding (EMI) materials [30-33], chemical sensors [34-38], temperature sensors [39-41], and strain sensors [14, 42-45]. More recently, there is an increasing interest to explore CPC based sensor materials due to their abundant responses towards external stimuli

such as mechanical stress and organic solvent/vapor. These responses are derived from the resistance changes induced by conductive network changes upon stimuli. Taking liquid sensor as an example, when CPC sensors are immersed into an organic solvent, depending on the solvent-polymer interaction the polymer swells because of solvent penetration. The conductive network in composites is disconnected under polymer swelling, leading to a resistance increase of the CPC sensor. Conversely, when CPC sensors are taken out from the organic solvent the neighboring filler particles start reconnecting under polymer de-swelling and forming new conductive pathways, accompanied with a resistance decrease of CPC sensors [37].

Volatile organic compounds (VOCs) are regarded as hazardous chemicals, which poses great threat on environment and health of human beings. Therefore, efficient detection of VOCs is of great necessity in environmental monitoring and human health [46-49]. Till now, many kinds of vapor sensors or e-noses have been intensively investigated, including metal oxide sensors [50, 51], conjugated polymer sensors [52], carbonaceous nanomaterial sensors [53], and CPC based sensors [54, 55]. In consideration of cost and processability, CPC based vapor sensor may be a promising candidate owing to some advantages such as low cost, easy processability and designable compositions. For instance, Mondal et al. investigated vapor sensing behavior of poly(dimethylsiloxane) (PDMS)/CB/MWCNT composites towards aromatic hydrocarbon vapors [46]. It was found that those CPC based chemiresistors exhibited different sensing responses when changing the hybrid filler compositions of CB and MWCNT. In addition, the relationship between relative resistance change ($R_{rel}$) and hydrocarbon vapor concentrations was discussed. Villmow et al. [56] illustrated CNT based CPC sensors used as leakage detectors for organic solvents. They also proposed some potential application fields of sensory CPC textiles as shown in **Fig. 1.2**. The CPC based sensory textiles can be used in building construction, where piping system and building parts have to be monitored in detecting chemical leakage. Furthermore, these sensory textiles can also be used in industrial parts such as mobile tanks in ships and trucks as well as barrels. Another interesting application is the monitoring of waste disposal sites, where the contamination of the ground water has to be avoided. Stoppa et al. [57] presented a review of CPC vapor sensor applications. Smart cloths were fabricated by assembling CPC sensors onto flexible woven clothes, which cannot only detect the vapor leakage in a factory but also indoor air pollutions. Health of human beings can be protected by giving a warning signal triggered upon pollution or hazardous chemicals.
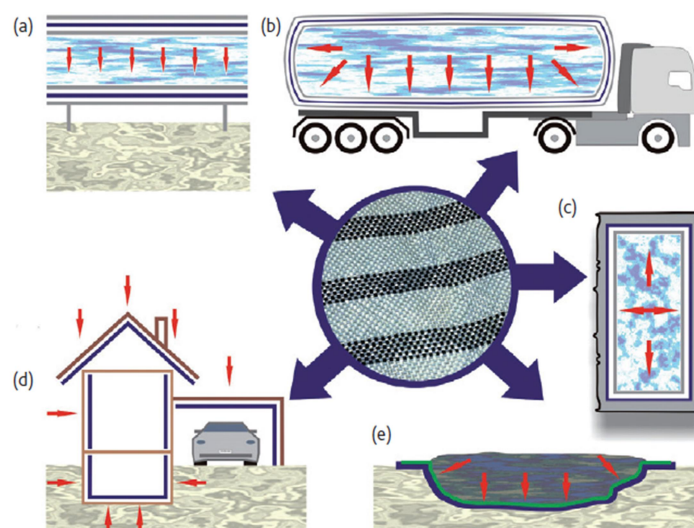
**Fig. 1.2** Possible applications of sensory CPC textiles in building construction and industrial plants: (a) a piping system, (b) a tank on a truck, (c) a barrel, (d) buildings with flat and slanted roofs, and (e) a waste disposal site. Reused with permission from Elsevier [56].

## 1.2 Aim of the work

So far, only some studies regarding CPC vapor sensors have been reported. In these reported cases, the vapor sensing behavior of CPCs was studied from the aspects of conductive filler content and polymer-vapor interaction. However, the influence of the conductive network structure and composite microstructure on the vapor sensing behavior of CPCs has not been studied yet in detail. When the work started, no publications were known on vapor sensing with immiscible polymer blends, selectively filled with CNTs. Thus, this new way of tuning the network structure was selected as a suitable route to improve the sensing performance. A systematic investigation on the processing-structure-property relationship of CPCs was performed. To be specific, it was the aim to improve the vapor sensing behavior of CPCs by tuning the conductive network structure and filler localization in single composites and polymer blend based composites. In addition to the electrical and vapor sensing discussion, other properties such as morphological, thermal and rheological properties were characterized in order to get deeper understanding of the CPCs.

In terms of vapor sensing behavior of CPC sensors, the interaction between the polymer and the organic vapor is a decisive factor in determining the sensing performance of CPCs. Ideally, the chosen polymer matrix should be able to swell without dissolving during vapor exposure so that the conductive network within the matrix can be disconnected, giving rise to the resistance change of CPCs. In some reported cases, polymers such as PLA and polycaprolactone (PCL) are degradable polymers, which are not durable when being exposed to environmental conditions for a long time [36, 58]. Therefore, it is necessary to make sure

14

whether the selected polymers are resistive to vapors or not. There are two options for the polymer selection. One is to select a polymer that is only swellable in a specific or few organic solvents; another one is to select a polymer that is swellable to a variety of solvents. Since CPC sensors are used for detecting as many as possible hazardous chemicals to human beings or environment, the second case is more desired because of its broader window of detection. The solubility parameter is effective to characterize the interaction of polymers and organic solvents/vapors, which was firstly proposed by Charles Hansen [59]. Initially, the Hansen solubility parameter (HSP) was used to predict the compatibility between polymer partners, chemical resistance, permeation rates, and even to characterize the surface of fillers. Liquids with similar solubility parameter ($\delta$) are miscible, and polymers will dissolve in solvents whose $\delta$ is similar to their own value. This behavior is recognized as "like dissolves like". Based on the description above, CPCs that can be used as liquid/vapor sensor materials should meet the following two requirements: 1) the chosen polymer should be swellable to vapors; 2) the CPCs as sensor materials have to be electrically conductive. Therefore, the relationship between conductive network and vapor sensing behavior of CPCs was investigated from the following aspects:

1) According to the previous studies, CB/polymer composites exhibit poor reversibility in cyclic vapor sensing tests because of the susceptible conductive network formed by CB particles. Thus, there is a need to improve the reversibility and increase the relative resistance change ($R_{rel}$) of CPCs. MWCNTs, as 1-dimensional carbon fillers with high aspect ratio, have excellent electrical and mechanical properties. Therefore, a hybrid filler system (MWCNT and CB) was utilized and incorporated in polycarbonate (PC) via melt compounding. PC was selected as the polymer matrix of CPCs because it showed high affinity with many commercial organic solvents/vapors as well as high and fast volume change upon organic solvents/vapors. In order to discuss the effect of conductive network formation on the vapor sensing behavior of PC/MWCNT/CB composites, two MWCNT contents were selected, which were lower and higher than the electrical percolation threshold of the PC/MWCNT composites. In the following, three CB contents were selected for the mixtures with MWCNT. The conductive networks composed of either MWCNT or hybrid CB/MWCNT are compared. The morphology of CPCs with different hybrid filler ratios was observed and investigated using SEM and OM. Moreover, to quantify the vapor sensing behavior of CPCs, some organic solvents were chosen and characterized by Flory-Huggins interaction parameter to demonstrate the polymer-vapor interaction. Afterwards, the cyclic vapor sensing was applied to illustrate the vapor sensing behavior of CPCs with different conductive network formations.

2) At moment, the filler dispersion is still a big challenge for MWCNT filled polymer composites due to the fact that the strong Van der Waals force among nanotubes makes them easily to entangle with each other resulting in the formation of agglomerates. A good filler dispersion state is desirable to achieve CPCs with low $\varphi_c$ and. In order to reduce the $\varphi_c$ of CPCs, immiscible polymer blend systems are introduced, which can have different blend microstructures by adjusting the polymer component ratios. In the second section, an immiscible polymer blend system based on two amorphous component, namely PC and polystyrene (PS), was chosen aiming to explain the influence of the blend morphology on the sensing performance of CPCs. PC/PS blends with different compositions filled with MWCNT were fabricated by melt mixing. The selective localization of MWCNTs in the blends was predicted using the Young's equation. Moreover, the composite morphology, filler dispersion, and distribution were characterized by SEM and TEM. In the following, three kinds of CPCs ranging from sea-island structure to co-continuous structure were selected for the cyclic sensing measurement. The relationship between composite microstructure and resulting vapor sensing behavior was evaluated and discussed.

3) The poor reversibility of CPCs towards good solvent vapors is still a problem that hinders the cyclic use of CPC sensor materials. As an important class of polymer, crystalline polymers are rigid and less affected by solvent penetration because of the well-arranged polymer chains. Therefore, the effect of polymer crystallinity on the vapor sensing behavior of CPCs is imperative to be studied. In the third section, poly(lactic acid) (PLA), a semi-crystalline polymer, was selected to melt-mixed with PS and MWCNTs with the aim to improve the sensing reversibility of CPCs towards organic vapors, especially good solvent vapors. Thermal annealing was utilized to tune the PLA crystallinity and the polymer blend microstructure of CPCs. The electrical, morphological, and thermal behavior of CPCs after different thermal annealing times is discussed. In the following, the effect of crystallinity on the vapor sensing behavior of the CPCs was studied in detail. Besides, the different sensing performances of the CPCs towards different vapors resulted from the selective localization of MWCNTs and increased polymer matrix crystallinity were investigated and compared.

4) As discussed for the amorphous polymer blends and crystalline polymer blends and their vapor sensing behavior. The comparison of compact and porous structure of CPCs is going to be studied. In the fourth section, studies to further improve the sensing performance and to find out the exact sensing mechanism of CPCs were performed. Therefore, poly(vinylidene fluoride) (PVDF), a solvent resistive polymer, was chosen to be melt-mixed with PC and MWCNTs. In order to compare the MWCNT dispersion and localization in the

blends, three kinds of PCs with different molecular weights were selected; hence, the viscosity ratio of immiscible blends was varied. Rheological, morphological, and electrical properties of CPCs were characterized. After that, the cyclic sensing and long-term immersion tests of CPCs towards different vapors were carried out to evaluate the vapor sensing behavior of compact CPCs with different blend viscosity ratios. Moreover, porous CPC sensors were prepared by extracting the PC component. The same sensing protocols were also applied to these porous sensor materials. The sensing mechanisms between compact CPC sensor and porous CPC sensor were compared and investigated.

## 2. Theoretical background of conductive polymer nanocomposites

### 2.1 Introduction

Polymer nanocomposites have widespread applications in many fields. They have demonstrated their potential as high-performance and multifunctional materials. Through the incorporation of nanofillers into the polymer matrix, the achieved composites possess the low density and flexibility of the polymer as well as excellent mechanical, electrical or other physical properties of the nanofiller. Therefore, polymer composites with such combined properties have many potential applications. In nature, many creatures can perceive the environment changes around them and adjust them to get used to the new environment. Inspired by this sensory phenomenon in living organisms, many biomimicry sensors have attracted much attention in both academic and industrial fields. Next to biomimicry sensors, there are many other composite sensor materials that are sensitive to external stimuli. As an important application of CPCs, CPC sensors have outstanding advantages such high efficiency, low cost and easy fabrication.

CPC sensors can perceive external changes or stimuli such as humidity, chemicals, temperature or mechanical forces. The sensing signals are typically electrical resistance changes of the composites which are caused by the external stimuli and result from changes of the electrically conductive filler network within the CPCs. Carbonaceous fillers such as CB, CNTs and GNPs are commonly used fillers for CPCs. However, the dispersion state of the conductive filler in the polymer matrix is still a key issue to be investigated, which has a direct influence on the formation of conductive networks in the polymer matrices. In addition to the dispersion state of fillers, filler loading and filler geometry are also influencing factors that determine the conductive network and overall properties of the CPCs. CNTs are the most favorable fillers for CPCs either in terms of cost or electrical property. However, CNTs are synthesized in an entangled structure and the strong Van der Waals forces between the individual tubes impede their dispersion so that agglomerates can remain in CPCs. In order to achieve a good filler dispersion in the polymer matrix, especially for CNTs, suitable processing methods such as solution mixing and melt mixing are used, whereby the processing parameters are varied depending on the composite system. In this chapter, some basic knowledge and principles including preparation and processing techniques of CPCs, characterization of conductive nanofillers, electrical percolation theory, and manipulating methods in reducing $\varphi_c$ will be introduced and described.

Compared to the semiconductor based sensors, no additional components such as integrated circuits are needed for CPC sensors. Furthermore, the sensing performance of CPC

sensors can be governed by tailoring the conductive network, which makes CPC a promising candidate for sensing applications. How this conductive network is affected by external stimuli, like pressure, strain, humidity or chemicals should be investigated roundly. Detailed description on the sensing mechanism and potential applications of CPC sensors are given in this chapter after the theoretical sections.

## 2.2 Preparation methods for CPCs

### 2.2.1 Overview

In general, CPCs are fabricated by adding conductive nanofillers into the insulating polymer matrix in such an amount that the composite gets electrically conductive. The filler dispersion and filler-polymer interaction have direct influence on the mechanical reinforcement and electrical conductivity of CPCs. It is therefore of great importance how the formation of filler agglomerate can be prevented and how good filler dispersion and homogeneous distribution can be achieved. Till now, various processing methods have been reported for CPC fabrication, which are *in-situ* polymerization, latex approach, solution mixing, and melt compounding. Among these processing methods, melt compounding and solution mixing are more favorable approaches as compared to *in-situ* polymerization and latex approaches from an overall perspective. For *in-situ* polymerization, good filler dispersion can be achieved if the used monomers or solvents are well infiltrated into filler agglomerates. Moreover, such technique is suitable for large-scale production of CPCs with high filler loading. The disadvantage of this method is the increase of viscosity along with the progress of the polymerization process that inhibits the manipulation and limits load fraction. The latex approach is only applicable for those polymers whose latex can be produced or those which can form stable dispersion in water. Solution mixing seems to be a promising method in CPC fabrication, however, the collection and processing of large amount solvent after mixing is still a big challenge. Therefore, this method is used rather for small-scale production than for industrial demands. Melt compounding is a low cost and effective method in preparing CPCs as the filler can be dispersed with the help of the shear forces of compounders. In addition, this method is deemed an environmentally friendly method as compared to those methods mentioned above, where large quantities of organic solvents might be used. In this part, these processing methods are briefly introduced in a view of explaining how CPCs are prepared. Advantages and disadvantages of these approaches are summarized.

## 2.2.2 Latex approach

Latex is a stable colloidal dispersion of submicron sized polymer particles in an aqueous medium, appearing as a milky liquid with approximately 50% water content. Latex particles are normally used to construct a segregated network of conductive filler particles. Francis et al. illustrated the electrical behavior of conductive CPC coatings fabricated by the latex approach [60]. The processing scheme is shown in **Fig. 2.1**. Firstly, an aqueous dispersion containing CB or single-walled carbon nanotubes (SWCNT) and polymer latex was prepared. Secondly, the latex and aqueous dispersion were mixed and casted onto a silicon plate. Subsequently, the casted coating was dried to remove water and further processed to get the segregated CPCs. Polymers like PS, PU, PVA etc. have been used to prepare CPCs with CB or CNTs using the latex approach [60-63]. This approach is very suitable to prepare CPC coatings and films. However, it should be mentioned that the limited polymers whose latex can be produced is still a restraining factor for practical applications.
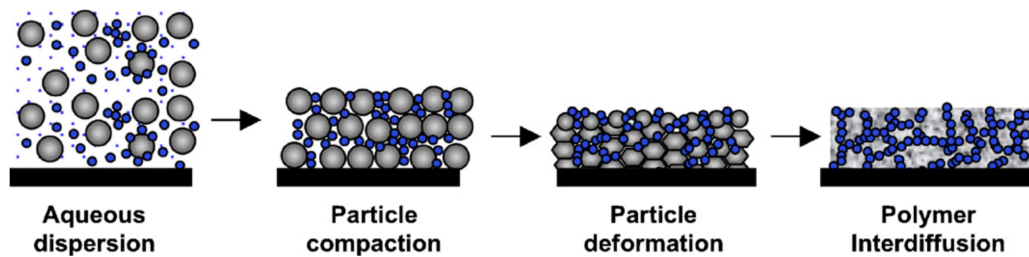


**Fig. 2.1** Schematic of microstructure development of a latex based CPCs. Reused with permission from Elsevier [60].

## 2.2.3 *In*-situ polymerization

*In-situ* polymerization is another method for dispersing conductive fillers in a polymer matrix. The advantage of this approach is that the polymer chains and the fillers can be dispersed and grafted on the molecular scale resulting in good filler dispersion and bonding strength between the filler and the polymer matrix. For the *in-situ* polymerization method, there are three frequently employed approaches. One is to pre-disperse the filler either in the liquid monomer or in the solvent media, followed by the polymerization process. The other two approaches are abbreviated as 'grafting from' and 'grafting to', the former one refers to the reaction of monomers with functionalized fillers and the latter one refers to the reaction between polymer functional groups and pristine or functionalized fillers. Luong et al. synthesized polyimide/functionalized graphene composites (PI/FGS) by the *in-situ* polymerization method [64]. The *in-situ* polymerization pathway of PI/FGS composites is shown in **Fig.2.2**. Firstly, graphene oxide (GO) was achieved by the traditional Hummer's

method and modified with ethyl isocyanate (iGO), which is readily dispersed in N,N'-dimethylformamide (DMF). Then the iGO dispersion in DMF was used as media for the synthesis of poly(amic acid) (PAA). In the following, the PAA/iGO solution was casted and heat-treated at high temperature under nitrogen, forming the PI/iGO composites. The results indicated that iGO had good dispersion in the PAA/iGO solution and the conductivity of composites with only 0.38 wt% iGO was $1.7 \times 10^{-5}$ S·m$^{-1}$, which was much increased as compared to neat PI ($1.2 \times 10^{-13}$ S·m$^{-1}$).
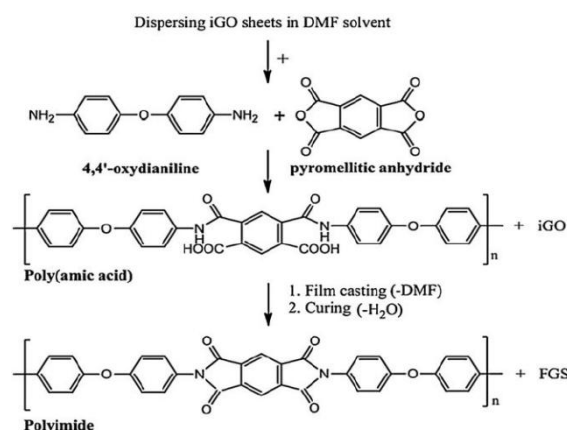


**Fig. 2.2** *In-situ* polymerization procedures of PI/iGO composites. Reused with the permission from Elsevier [64].

The advantage of *in-situ* polymerization is its suitability for large-scale production of composites with high filler loadings. Excellent filler dispersion can be achieved if the used monomers or solvents are well interacting with the (functionalized) fillers. However, sometimes the electrical conductivities are reduced if the polymer wrapping effect onto the fillers (especially on CNTs) is strong. The highly wrapped polymer layer reduces the electrical tube-tube (CNTs) or plate-plate (graphene) contact. This disadvantage of the approach should not be ignored.

**2.2.4 Solution mixing**

Regarding solution mixing, conductive fillers are dispersed in a solvent and the polymer is dissolved in the same or another solvent. Subsequently, the two solutions are mixed under strong agitation or sonication. Then the solution mixture is casted and dried to get the CPC. Solution mixing is regarded as a facile method to give CPCs with higher conductivity because conductive fillers typically have better dispersion in an organic solvent than e.g. in a melt. The entangled CNTs or stacked graphene layers can be disentangled or exfoliated in the solution, which improves the filler dispersion and resulting conductivity of the CPCs. Nevertheless, some characteristics of the fillers, such as the sp$^2$ hybridized structure

of nanotubes, makes these fillers insoluble in common solvents [65]. Therefore, introducing functional groups onto the filler surface can not only improve the filler solubility in a solvent but also strengthen the interaction between fillers and polymer during processing. Ma et al. investigated the mechanical and electrical properties of PI based CPCs containing hybrid carbon fillers [66]. In their study, reduced graphene oxide (rGO) and CNTs were functionalized by 4,4'-oxydianiline (ODA). ODA was selected because it has good interaction with the PI matrix and can achieve homogeneous filler dispersion in solution. Then the functionalized fillers were mixed with the polymer in DMF. These functionalized fillers exhibited good dispersion in CPCs, and the electrical percolation was achieved at a low hybrid filler content (0.3 wt%). The filler dispersion state in the solution just after preparation and after one month is shown in **Fig. 2.3**. It can be seen that hybrid graphene/CNTs with different ratios are precipitated after a long time standing, but the CNTs functionalized by ODA show a homogeneous dispersion in DMF solution even after one month of storage, indicating that the functionalized CNTs had better dispersion stability in the solvent.



**Fig. 2.3** Digital photographs of functionalized CNTs or rGO and different CNT/rGO solutions after preparation and one month standing. Reused with the permission of John Wiley & Sons [66].

Solution mixing is typically used on laboratory scale and the achieved dispersion is much better than that achieved by other processing methods [67]. However, it is only applicable to those polymers, which can be dissolved. To some extent, this method is not suitable for industrial production, as large amounts of solvent are needed to dissolve the polymer, which poses great threat to environment. In addition, solvent mixing requires relatively long time to shape the CPCs by the film-casting method after solution mixing. Thus, spin coating and electrospinning are more favored shaping method because of their fast drying

and energy saving characteristics. Before shaping, the composites are prepared by solution mixing.

### 2.2.5 Melt compounding

Melt compounding is an effective method for incorporating conductive fillers into a viscous polymer melt. The advantage of this method is that the conductive filler can be directly dispersed in a matrix. Another advantage of this approach is that no chemical modifications are required and the dispersed fillers are hindered in their tendency to re-reagglomerate by the viscous polymer matrix [18, 65]. A large number of studies have been reported on CPCs prepared either by direct melt mixing or by masterbatch dilution. This fast and economic mixing method uses different kinds of compounders such as (single or twin screw) extruders or internal mixer [68-71]. During melt mixing, the polymer is melted immediately after being fed into the hot mixing chamber of the compounder and the applied shear stresses in the compounder help to break up the primary filler agglomerates in the viscous polymer melt. Kasaliwal et al. systematically investigated the agglomerate dispersion mechanism of MWCNTs during melt mixing with PC [72]. A high cohesive strength of the 'as produced' primary MWCNT agglomerates restrict their dispersion into individualized tubes within polymer matrix during melt compounding, which leads to many un-dispersed MWCNT agglomerates in composites. The dispersive mixing operation during melt compounding consists of two stages: 1) filler incorporation, wetting and infiltration by the polymer melt; 2) filler dispersion and distribution in the polymer melt resulted from rupture and erosion mechanisms as shown in **Fig. 2.4**.
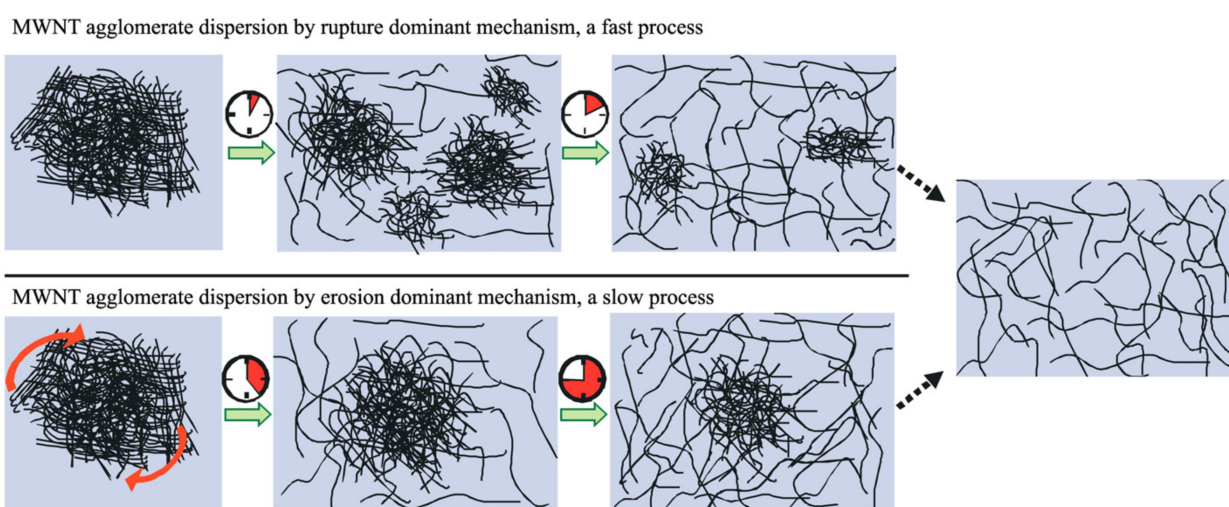


**Fig. 2.4** Schematic illustration of MWCNT agglomerates dispersion mechanisms. Reused with the permission of Elsevier [72].

Regarding the rupture dominant mechanism, the large agglomerates are broken down quickly into small pieces, which can be further reduced in size with time. However, the cohesive strength of agglomerates itself could be a limiting factor. In the erosion dominant mechanism, the size of agglomerates is reduced in longer time and dispersion is mainly driven by melt infiltration. Whereas the rupture mechanism is fast but may result in undesired breakage of tubes, the erosion mechanism is slower but leads to well infiltrated agglomerates and is not expected to cause damage to the tubes. Overall, these two dispersion mechanisms are influenced by processing parameters [73], polymer viscosity [74, 75], filler polarity [76], and chemical functionalization of fillers [7, 77]. It seems that melt compounding is the most effective method to prepare CPCs due to their controllable processing parameters, low cost and readiness for large-scale production. One limitation is the restriction to relatively low filler loadings, since a high filler loading of the CPCs can lead to a limitation regarding the possible torque values in extruders.

## 2.3 Most commonly used carbon fillers and their properties

### 2.3.1 Carbon black

Carbon black (CB) is a material produced by the incomplete combustion of petroleum products such as coal tar or ethylene cracking tar. CBs are nano- and micro-sized spherical carbon particles and their morphology can be range from individual spherical particles to a complex chain like-structure which depends on how they are manufactured [78]. CB is a type of carbon material with widespread applications such as reinforcing compounds in rubbers [79, 80], electrically conductive fillers in polymers [11, 81], and as catalyst support in proton exchange membrane fuel cells [82]. During the combustion process, the thermodynamically unstable network becomes carbonaceous and aromatic as carbon atoms readjust their positions and approximate to the six membered ring systems that are building blocks of the graphite-like lamellar constituent molecules (see **Fig. 2.5a**). The morphology of CB depends on the structural details of lamellar constituent molecules that are strongly affected by specific production conditions [78, 83]. **Fig. 2.5b** illustrates the morphology of primary CB particles. A single spherical CB particle is called primary spherical particle with a size range of 20-50 nm, which tends to form aggregates within the size range of 100-200 nm. When the aggregates interact with each other driven by van der Waals forces, a secondary structure named agglomerates is formed (ranged in size of $10-10^3$ µm). Finally, a cluster will be formed when a group of agglomerates get together [78, 84].
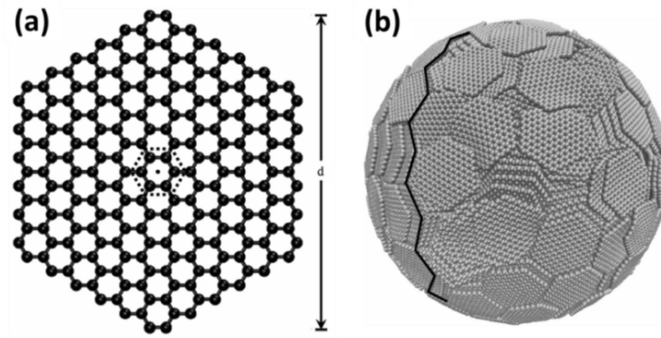
**Fig. 2.5** Model of (a) hexagonal graphite unit with *d*=2.7 nm and (b) morphology of primary CB particles with shell units *d*=2.7 nm. Reused with permission of Elsevier [78].

In the early stages of the development of CPCs, CB was the most frequently chosen filler due to its availability and low cost. In order to realize electrical percolation, a relatively high CB content is needed (5 wt.% - 15 wt.%), and such high filler contents also impair the mechanical properties [11, 85]. In order to reduce such the percolation concentration, super conductive CB is synthesized by manipulating the manufacture process, whose conductivity is 100 times higher than the commercial CB. In addition, such CB materials are highly structured meaning that the agglomerates show highly branched structures. Super conductive CBs play a critical role in improving the electrical properties of CPCs. In general, CPCs with CB have lower mechanical properties such as tensile strength and stiffness as compared to composites filled with high aspect ratio fillers such as CNTs. This is attributed to the spherical morphology of CB aggregates.

### 2.3.2 Carbon nanotubes

Carbon nanotubes (CNTs) are another allotrope of carbon material. They were firstly described by Iijima et al. in 1991 [86]. CNTs are produced by three main methods: laser ablation, arc discharge method, and e chemical vapor deposition (CVD). CVD is the only truly scalable method as compared to the other methods, with the advantage that purity can be controlled by carefully controlling the synthesis process [87]. CNTs are rolled up sheets of $sp^2$ bonded graphene with no surface broken bonds. Single-walled carbon nanotubes (SWCNT) and MWCNT are the two main kinds of CNTs, which are synthesized as a single cylinder or multiple coaxial cylinders of graphene sheets with a hollow core. The electrical properties of CNTs are closely related to their geometric arrangement. **Fig. 2.6** illustrates the structural representations of SWCNT and MWCNT. The SWCNT chirality determines the material to be metallic or semiconducting (**Fig. 2.6a**), while MWCNTs are considered to be

always metallic (**Fig. 2.6b**). In MWCNTs, the distance between two neighboring layers is assumed to be the same as the spacing between adjacent graphene sheets in graphite, i.e. 0.34 nm [88].
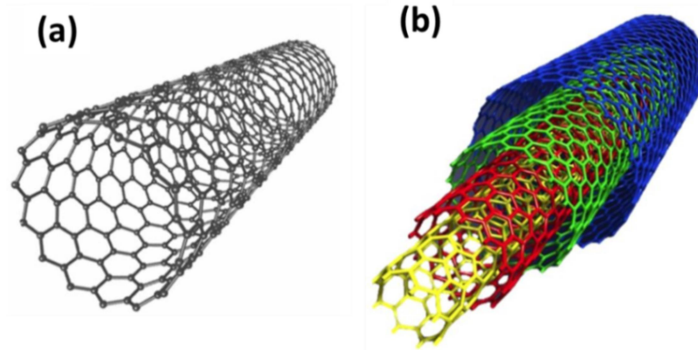


**Fig. 2.6** Images of (a) SWCNT and (b) MWCNT [89].

The addition of CNTs into polymer matrices to fabricate CPCs has been a facile way to achieve electrical conductive polymer materials, whereby at the same time mechanical properties can be improved. This is attributed to the excellent electrical and mechanical properties of CNTs. Krause et al. investigated the electrical properties of polyamide 6.6/MWCNT and PP/SWCNT composites prepared by melt mixing [90, 91]. Both of the two composite systems exhibit outstanding electrical properties and the $\varphi_c$ of them are 0.04 wt% and 0.075 wt%, respectively. They assumed that the ultralow $\varphi_c$ can be assigned to the high aspect ratio of CNTs.

### 2.3.3 Graphite and graphene derivatives

Graphite is a soft material on which the carbon atoms have hybrid $sp^2$ bonds forming planar hexagonal rings in layers parallel to each other. It occurs naturally in this form and is the most stable form of carbon under standard conditions. Under high pressures and temperatures it converts to diamond. There are many types of graphite such as expanded and graphite oxide, which have different bonding or Van der Walls forces between graphite planes. Therefore, these graphite materials have different electrical, mechanical, and thermal properties [92]. In 2004, Geim and Novoselov from Manchester University firstly reported the preparation of graphene material [93]. Graphene is a single layer of hexagonal arrangement of carbon atoms with $sp^2$ hybridization. There are many different kinds of graphene related materials, which are named according to the size of particles and amount of layers. To address this problem, an editorial was made to clarify the nomenclature for two-dimensional carbon

materials from the perspective of graphene layer and morphology [94]. The graphene materials such as bilayer/trilayer graphene, multi-layer graphene, few-layer graphene, graphite nanoplates, graphite nanosheets and graphite nanoflakes are clearly defined and demonstrated. Since 2004, many studies have been carried out to investigate the physical and electrical properties of graphene related materials [93, 95]. All these properties make graphene related material a suitable choice for many engineering applications such as rechargeable batteries, supercapacitors, gas sensors, etc. [96-99]. Furthermore, polymer/rGO composites have low electrical percolation threshold [14, 100]. Improving the graphene dispersion either in solutions or polymer matrices is still a big challenge to obtain good electrical and mechanical properties of graphene based CPCs.

## 2.4 Conductive polymer nanocomposites

### 2.4.1 Electrical conductivity of CPCs

Most of the polymers are insulating, which for many applications is an advantage over e.g. metallic parts. To achieve CPCs, the conductivity of CPCs is enabled by the addition of percolated conductive fillers. To enable this percolated state, a certain amount of conductive fillers is required to be added into the insulating polymer matrix so that these fillers can either directly connected or get close enough to each other to allow conductive pathways by hopping or tunneling processes. The filler content at which the conductivity of CPCs has the maximum conductivity increase is regarded as the percolation threshold $\varphi_c$. A typical 'S-shape' percolation curve of CPCs is shown in **Fig. 2.7**. At low filler contents ($\varphi < \varphi_c$), the conductivity of CPCs remains nearly the same as the neat polymer, which indicates that the fillers are isolated or in small isolated clusters distributed throughout the matrix. With the increase of filler content in matrix, those isolated fillers start connecting with neighboring fillers and form conductive pathways ($\varphi = \varphi_c$). There is a drastic conductivity increase of several orders of magnitude in the electrical percolation region. Upon further increasing the filler contents, the conductivity of CPCs levels off at certain filler content. The conductivity of CPCs remains the same indicating that a dense conductive network has been constructed ($\varphi > \varphi_c$).
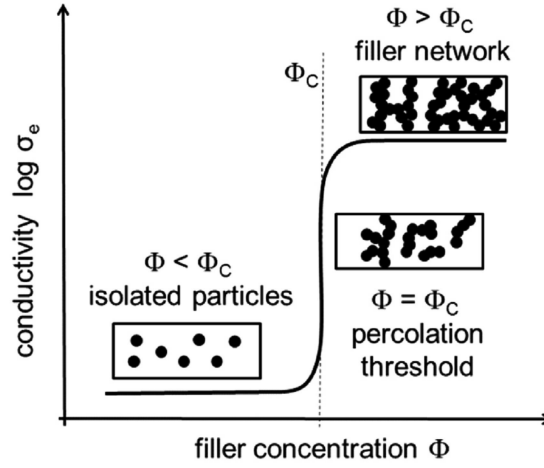
**Fig. 2.7** Schematic percolation curve for electrical conductivity of CPCs and composite morphologies in different distinguished regions [101].

Until now, various models have been proposed to describe the electrical percolation behavior. Two of the early percolation models often referenced were organically proposed by Kirkpatrick [102] and Zallen [103]. The $\varphi_c$ of composites can be estimated using the power-law of the classical percolation theory by **Eq. 2.1**,

$$\sigma = \sigma_0(\varphi - \varphi_c)^t \qquad (2.1)$$

where $\sigma$ represents the conductivity of the composite at a given filler content, $\sigma_0$ is a scaling factor [104], $\varphi$ is the filler volume content, $\varphi_c$ is the percolation volume concentration of filler, and the exponent $t$ is a parameter which depends on the dimensionality of the conductive network. The exponent $t$ is expected to vary for different materials with values of $t \approx 1.3$ and $t \approx 2.0$ for 2D and 3D conductive networks, respectively [105, 106].

## 2.4.2 Manipulating the percolation threshold

### 2.4.2.1 Processing condition

Kim et al investigated correlations between electrical percolation thresholds and CNTs agglomerate distributions [107]. They found that the $\varphi_c$ varied from 0.1 wt% to 1.0 wt% with different processing methods for CNT/epoxy composites. For the CPCs prepared by shear mixing for 30 at 3000 rpm, the mean CNT particle size was 136 μm (**Fig. 2.8a**) and the $\varphi_c$ was 0.4 wt.%. The mean particle size was decreased to 34.7 μm for the CPCs prepared by ultrasonication for 2 h at 60 °C. Its $\varphi_c$ was 0.1 wt.%, which was resulted from the breakage of CNT agglomerates by ultrasonication (**Fig. 2.8b**). For the third CPCs, CNTs were UV/O$_3$ treated for 1 h and ultrasonicated for 2 h in acetone/epoxy solution, the mean particle size was

further reduced to 0.29 µm and the $\varphi_c$ of CPC was 0.25-0.3 wt.% (**Fig. 2.8c**). They concluded that the processing method had great influence on CNT disentanglement, which in turn determined the electrical percolation of CPCs.
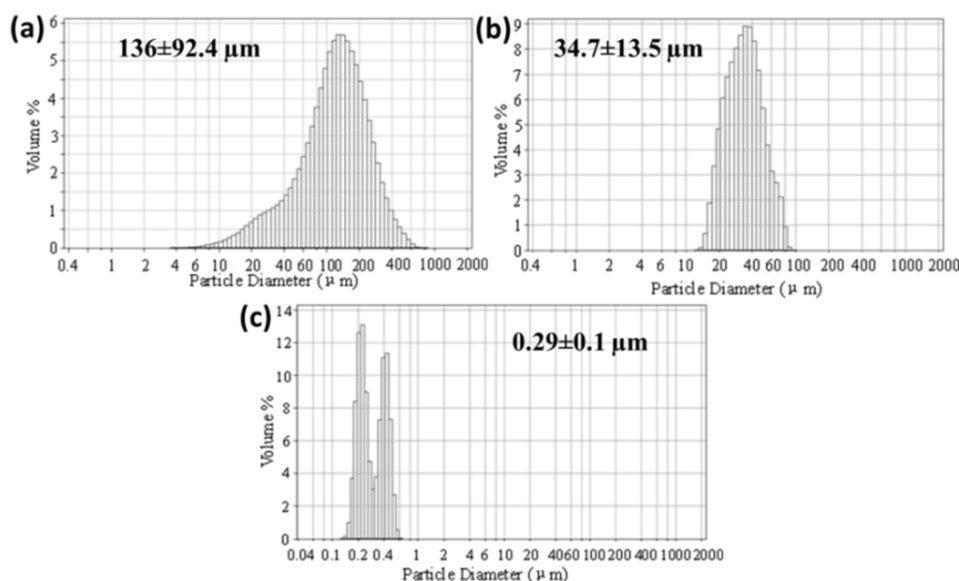


**Fig. 2.8** Size distribution of CNT agglomerates produced by different processing methods. Reused with permission of John Wiley & Sons [107].

Generally, high nanofiller loading will impair the mechanical properties and processability as well as raise the cost of composites. Hence, reducing $\varphi_c$ of CPCs without sacrificing the mechanical properties is still an important issue to be investigated. Therefore, much work has been done in achieving CPCs with desirable electrical properties at low filler content [108-111]. Up to now, many methods have been reported regarding modulating the conductive network and resulted $\varphi_c$. In the following section, these methods will be introduced.

### 2.4.2.2 Hybrid filler method

In recent years, incorporating hybrid fillers into polymer matrices has become a facile technique to fabricate conductive polymer nanocomposites with a good combination of excellent electrical and mechanical properties as well as price. For example, Ma et al. [20] used hybrid fillers of MWCNT and CB and studied the electrical conductivity of epoxy based nanocomposites. The $\varphi_c$ of epoxy/MWCNT composites was about 0.3 wt%. In comparison, when adding 0.2 wt% CB into the nanocomposites containing 0.2 wt% MWCNT, a remarkable conductivity increase by 6 orders of magnitude was observed, even if at that MWCNT content the epoxy/MWCNT was not conductive. It was confirmed that CB

nanoparticles could effectively fill the gaps between MWCNTs and link them together which gave rise to the conductivity enhancement of the nanocomposites. Socher et al. [21] studied melt-mixed composites based on polyamide 12 (PA12) containing hybrid filler systems of CB and MWCNT by the weight ratios of 50/50 and 25/75. No synergistic effects were observed regarding the electrical percolation threshold. However, at loadings well above the $\varphi_c$, higher volume conductivities were obtained for samples containing MWCNT/CB, especially by the weight ratio of 50/50, as compared to samples filled with only MWCNT or CB. Furthermore, the addition of CB reduced the MWCNT agglomeration in the PA12 matrix.

Oh et al. investigated the electrical network formed by MWCNT/graphene hybrid fillers in PDMS [112]. CNTs and graphene are desirable fillers for CPCs because of their high electrical conductivity and high aspect ratio, but agglomeration of CNTs and restacking of graphene sheets can hinder the electrical performance of CPCs. Therefore, they compared the electrical conductivity with different hybrid filler ratios. They found that MWCNTs could effectively prevent graphene sheets from restacking and increase the contact area during processing as shown in **Fig. 2.9**. An enhanced conductive network and conductivity was observed for MWCNT/graphene/PDMS composites as compared to MWCNT/PDMS and graphene/PDMS composites at small filler loadings. From this work, it proves that filler with different geometries can generate synergistic effect in electrical conductivity of CPCs due to the improved filler dispersion in the polymer matrix.
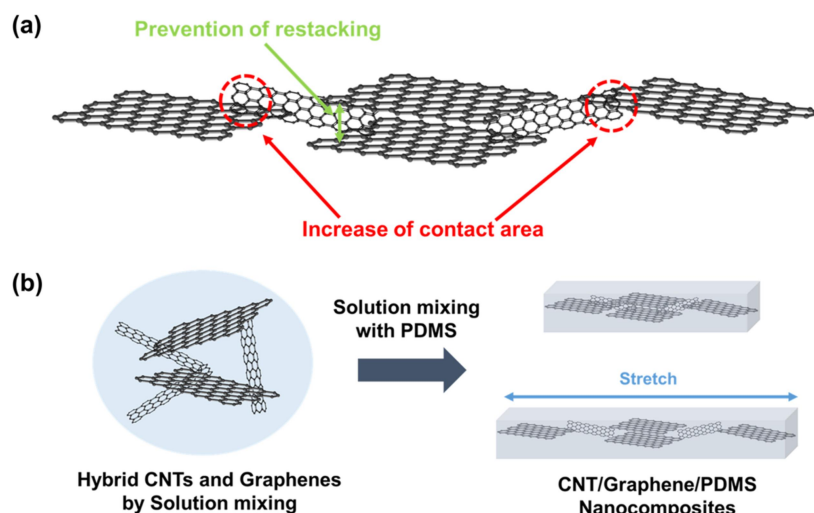


**Fig. 2.9** (a) Schematic illustration of the interaction between MWCNT and graphene. (b) MWCNT/graphene/PDMS nanocomposite fabrication. Reused with permission from American Chemical Society [112].

### *2.4.2.3 Double percolation method*

Another facile method in lowering $\varphi_c$ is the double percolation structure. Sumita et al. found that CB preferentially localizes in one polymer component or at the interface of immiscible polymer blends with co-continuous structure. At such condition, a low $\varphi_c$ of CPCs was achieved [28, 113]. Based on such novel phenomenon, they proposed the double percolation concept with percolation of filler in one component which itself is continuous (percolated). The conductivity of CPCs based on multiphase polymer blends is largely influenced by localization of the filler as well as the blend morphology. The filler localization in polymer blends at equilibrium is determined by thermodynamic driving forces, which result from the interfacial energy minimization to arrange the fillers in the energetically preferred polymer component. The wetting coefficient $\omega_a$ is used to estimate the thermodynamic preference of fillers in immiscible polymer blends, which is defined by **Eq. 2.2**,

$$\omega_a = \frac{\gamma_{filler-polym} - \gamma_{filler-polymer}}{\gamma_{polymer1-polymer2}} \tag{2.2}$$

where $\gamma_{filler-pol}$ is the interfacial tension between polymer 1 and filler, $\gamma_{filler-polymer2}$ is the interfacial tension between polymer 2 and filler, and $\gamma_{polymer1-polymer}$ is the interfacial tension between polymer 1 and polymer 2. The filler tends to be localized in polymer 1 if $\omega_a$ is less than -1 and tends to be located in polymer 2 if $\omega_a$ is greater than 1. The filler is more likely located at the interface between polymer components if $\omega_a$ is between -1 and 1.

The interfacial tension between different components can be calculated via the Harmonic-mean equation **Eq. 2.3**:

$$\gamma_{12} = \gamma_1 + \gamma_2 - 4\left(\frac{\gamma_1^d \gamma_2^d}{\gamma_1^d + \gamma_2^d} + \frac{\gamma_1^p \gamma_2^p}{\gamma_1^p + \gamma_2^p}\right) \tag{2.3}$$

or the Geometric-mean equation by **Eq. 2.4**:

$$\gamma_{12} = \gamma_1 + \gamma_2 - 2\left(\sqrt{\gamma_1^d \gamma_2^d} + \sqrt{\gamma_1^p \gamma_2^p}\right) \tag{2.4}$$

where $\gamma_i$ is the surface energy of component i, and $\gamma_i^d$ and $\gamma_i^p$ represent the dispersive and polar contribution to the interfacial tension of component *i*, respectively.

This method has been implemented for a large number of polymer blend systems with various kinds of conductive fillers. Gubbels et al. reported the conductivity of CB filled polyethylene (PE)/PS composites. A co-continuous structure was found at the blend ratio of 45/55 PE/PS by weight. By tuning the CB to locate at the interface of blends, CPCs exhibited higher conductivity than the composites in which CB was localized in one polymer

component. In addition, they also studied the best conditions in achieving higher conductivity by adjusting the blend morphology or manipulating CB to localize at the interface of the blends [11, 114, 115].

In addition to thermodynamic prediction, kinetic factors such as mixing time, compounding sequence and shear stresses are also influencing factors which determine the filler localization in polymer blends. Much work has been done to localize the conductive filler at the blend interface as at the same filler loading higher conductivity is expected in that case [109, 116-119]. Shi et al. premixed CNTs with unfavorable ethylene-*co*-vinyl acetate (EVA) for EVA/PLA blends. SEM results indicated that CNTs migrated from EVA to the interface of the blend during compounding, and the electrical percolation occurred at lower filler content as compared to CPCs fabricated by premixing CNTs and PLA [120]. Zhu et al. designed PS/PMMA/MWCNT composites with ultralow $\varphi_c$ (0.017 wt%) by incorporating MWCNTs with carboxyl functional groups. The MWCNTs were localized at the interface of PS/PMMA, which was attributed to the balance of $\pi$-$\pi$ interactions between PS and MWCNT surfaces and dipole-dipole interactions between PMMA and MWCNT carboxylic groups [108]. Hoseini et al. investigated the electrical conductivity of polyamide-6 (PA6)/PS/MWCNT composites with different blend morphologies [121]. A co-continuous structure was formed when the blend ratio was 50/50 by weight. The electrical conductivity of PA6/PS/MWCNT (50w/50w) composites was higher than in PA6/MWCNT composites with the same MWCNT loading.

### 2.4.2.4 Segregated network

Forming a segregated filler network structure in CPCs is also a feasible method to achieve low $\varphi_c$. In CPCs with segregated networks, the conductive filler are primarily located at the interfaces between the polymeric matrix particles instead of being randomly arranged throughout the entire CPC [17]. For instance, Gupta et al. prepared acrylonitrile-butadiene-styrene (ABS) based CPCs with a segregated conductive CB network and the $\varphi_c$ of CPCs was only 0.0054 vol%, which is the lowest reported value for CB filled CPC systems [16]. **Fig 2.10a** shows an image of the used ABS pellets, whereas **Fig. 2.10b** illustrates the morphology of compression molded ABS/CB composites prepared by the mechanical mixing method. i.e., the ABS pellets and CB powder were placed in a zip-lock bag and shook by hands for at least 10 min at room temperature; then the mixture was compression molded using a press machine. It can be seen clearly that the CB material is located around the ABS pellet boundaries. The mechanism for the formation of segregated structure relies on a polymer matrix with an

exclusionary microstructure in which conductive fillers are arranged in a constrained space, subsequently increasing the effective density of the conductive pathways at certain filler contents. The segregated structure provides an efficient paradigm for forming a well-established conductive network with minimal filler loading. The drawback of CPCs with such structure is the structure cannot be maintained well during shaping process, like injection molding or pressing at high processing temperature.
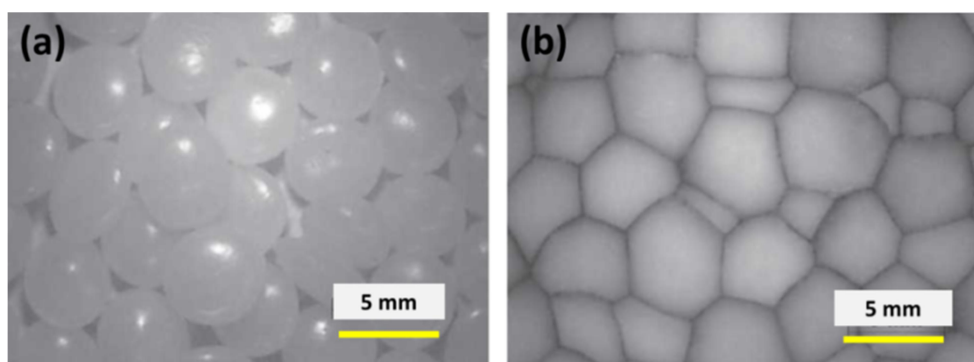


**Fig. 2.10** (a) ABS pellets and (b) surface of a 1 phr ABS/CB composite fabricated by hand mixing and compression molding. Reused with permission from Springer [16].

In terms of segregated CPCs, high melt viscosity polymers such as ultra-high molecular weight polyethylene (UHMWPE), PS, and natural rubber are widely selected because conductive fillers have a high affinity to higher viscous polymer [122-124]. Three main approaches are widely used to prepare segregated CPCs as shown in **Fig. 2.11** [17]. The first one involves compressing a mixture of polymer pellets decorated with conductive fillers via dry or solution mixing to construct the segregated conductive network (**Fig. 2.11a**); the second approach is to disperse conductive filler within a polymeric latex in which the conductive fillers are retained within the interstitial space between the latex particles while freeze-drying the polymer emulsion (**Fig. 2.11b**) [125]; the third one is the selective localization of fillers at the interface of immiscible polymer blends through melt compounding, which has been illustrated in last section (**Fig. 2.11c**).
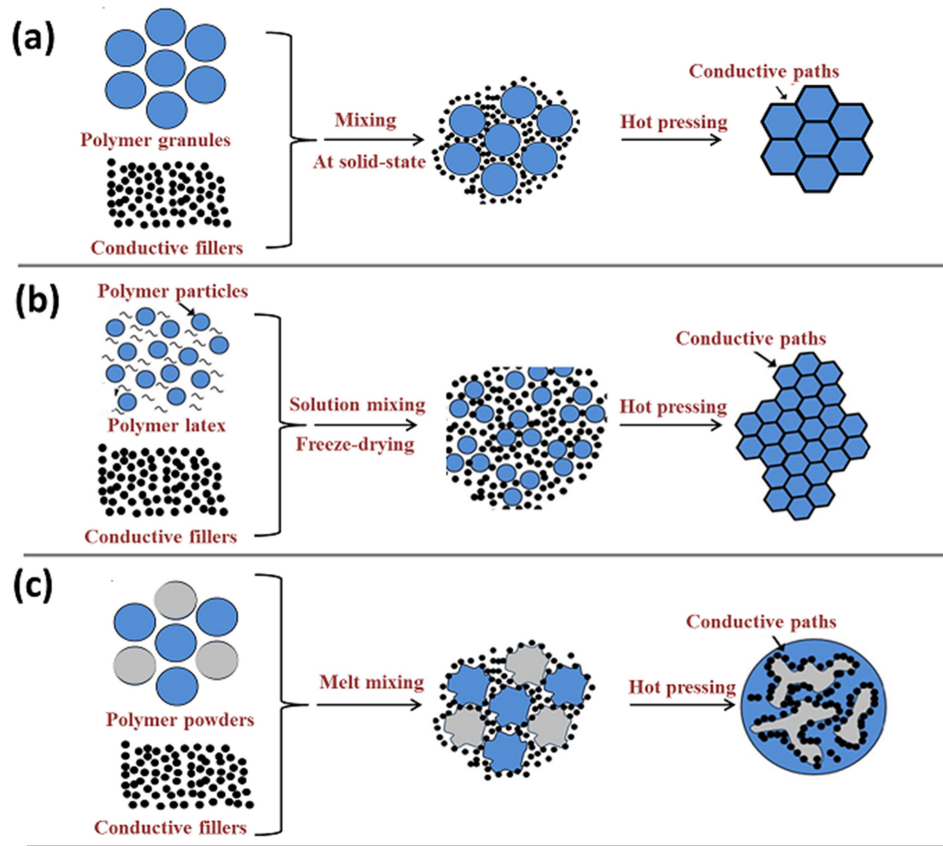
**Fig. 2.11** Schematic for the fabrication of the segregated CPCs with different processing approaches: (a) dry or solvent mixing; (b) latex technique; (c) melt compounding. Reprinted with permission from Elsevier [17].

### *2.4.2.5 Thermal annealing*

Thermal annealing involves the heating of CPCs above their glass transition or melting temperature at quiescent conditions. Recently, researchers found that the electrical conductivity of CPCs could be improved by thermal annealing, which was ascribed to the filler particle re-agglomeration (secondary agglomeration) and conductive network reconstruction in polymer matrices [126-129]. Li et al. investigated the electrical properties of poly(ethylene-*co*-hexene) (PEH)/MWCNT composites under different annealing treatments [130]. The electrical conductivity of PEH/MWCNT composites increased obviously under annealing for 40 min at 160 ºC, and a maximum conductivity increase of 3 orders of magnitude was achieved by 120 min annealing at the same temperature. SEM results revealed that MWCNT agglomerates were broken down and a more loosely packed MWCNT network was formed due to thermal annealing. Cipriano et al. made a comparison of electrical properties of PS/MWCNT and PS/carbon nanofiber (CNF) composites after annealing treatment [128]. The effect of annealing temperature on the conductivity of PS/MWCNT and PS/CNF composites for 30 min annealing is shown in **Fig. 2.12**. It can be observed that the conductivity of both composites is improved after thermal annealing above the glass transition

34

temperature of PS (~100 ºC). Such behavior involves a transition from unconnected particles prior to annealing to an interconnected network after annealing through viscoelastic relaxation of polymer chains.
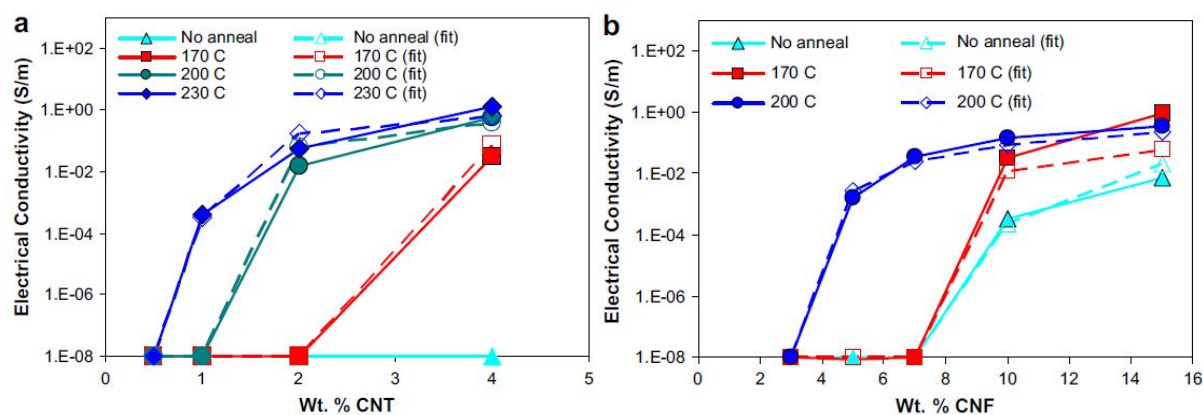


**Fig. 2.12** Effect of annealing temperature on the conductivity of (a) PS/MWCNT and (b) PS/CNF nanocomposites, these samples were annealed for 30 min. Fits from a model of the time- and temperature-dependent electrical conductivity is used to predict the conductivity of CPCs at different annealing times and temperatures. Reprinted with permission from Elsevier [128].

## 2.5 CPCs as chemical sensors

### 2.5.1 Material selection and sensing mechanism of CPCs for chemical sensing

Since the first research in this field with CB it is known that CPCs are sensitive to external stimuli. Environmental factors such as the presence of organic liquids or vapors were found to significantly influence the electrical resistivity of CPCs [131]. Therefore, CPCs are regarded as promising candidates for chemical sensing materials to detect leakages of chemicals or diagnose health of human beings [56]. Taking vapor sensors as an example, the relative resistance change ($R_{rel}$) of CPCs caused by vapors can be assigned to two mechanisms: (1) Resistance change caused by vapor absorption: The absorbed vapor molecules may influence the electrical properties of carbon filler. Some researchers suggested that the vapor adsorption in the sample forms non-conductive layers around carbon fillers, which decrease the contact of adjacent fillers and increase the macroscopic resistance [53, 132]; (2) Resistance change caused by polymer swelling: The adsorption of vapor molecules causes polymer swelling and thus increase in the volume of the polymer matrix, which increases the distance of neighbored filler nanoparticles above the tunneling distance and disrupts direct contacts between adjacent nanoparticles. This reduces the conductive network's density resulting in increased resistance. Whereas the first mechanism is the mechanism in vapor sensors based on pure conductive carbon materials, the second one is the dominant

mechanism in CPCs with only little contribution of absorption/desorption to resistance changes.

**Fig. 2.13** illustrates the relationship between the electrical percolation curve and $R_{rel}$ of CPCs. The response of CPCs towards chemicals becomes higher as the filler content is closer to $\varphi_c$. Therefore, it can be assumed that CPCs whose filler content is only slightly higher than the percolation content are more sensitive to external stimulation than those with higher filler contents. At the narrow percolation region, any slight external stimulation can significantly change the conductive network of the CPCs, which gives rise to large resistance changes. This is due to the fact, that the conductive network formed by conductive fillers at such filler loading is not stable and can be damaged easily under even slight external stimuli. Therefore, the $R_{rel}$ of CPCs slightly above the percolation concentration is normally high and fluctuated because of the dynamically disconnection and reconnection of conductive network during sensing tests. On the contrary, the conductive network in the conductor region is in a well percolated state, which means the network is formed by densely interconnected particles. As a result, the conductive network change of CPCs induced by polymer swelling is weak. Hence, the $R_{rel}$ of CPCs whose filler content is much higher than $\varphi_c$ is lower than that of composites near the percolation region.
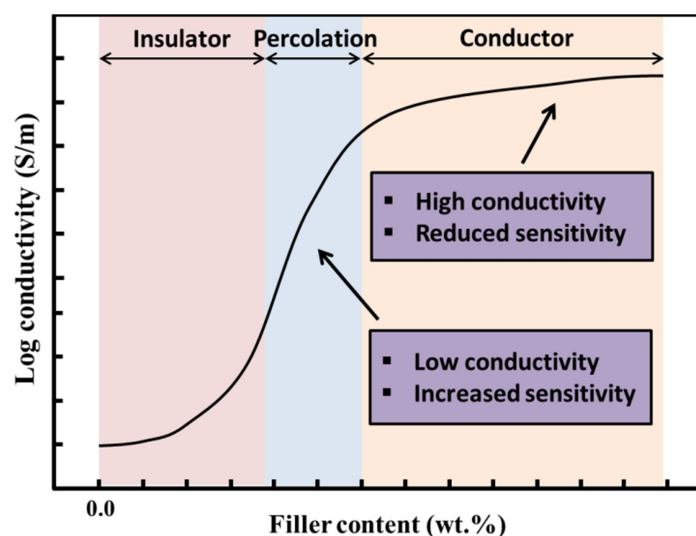


**Fig. 2.13** Relation between electrical conductivity and relative resistance change of CPCs.

Great efforts are currently being made to use CPCs in chemical sensing fields. CPC based chemical sensors were fabricated for the detection of organic solvents and volatile organic compounds (VOCs) [34, 56, 133, 134] and there are also some attempts for detecting biological compounds related to disease of human beings [49, 135, 136]. For instance, Pötschke et al. prepared liquid sensors based on MWCNT/polymer composites capable of

identifying different solvents such as n-hexane and methanol [36]. Similarly, Rentenberger et al. fabricated PLA/PCL/MWCNT fibers by melt spinning for liquid sensing application [58]. These multifilament fiber sensors showed very fast response and high $R_{rel}$ to ethyl acetate and acetone. However, the response to ethanol was less pronounced which was due to the poor interaction between polymer and ethanol. Wang et al. discussed the vapor sensing behavior of poly(styrene-butadiene-styrene) (SBS)/MWCNT fiber based sensor towards VOCs. SBS is a triblock copolymer consisting of soft non-polar butadiene (PB) domains and hard polar PS domains. According to the rule of 'like dissolve like' [137], non-polar PB segments and polar PS segments can be swollen when being exposed to non-/low- polar and polar vapors, respectively. Therefore, such flexible fiber sensor exhibited good discriminability to different VOCs [133]. Apart from detecting the chemicals, CPC based sensors are also investigated and used for disease diagnose of human beings. Chatterjee et al. developed an e-nose composed of several polymer/MWCNT composites. MWCNTs were dispersed in polymer solutions (PC, PCL, PLA, PS and PMMA), respectively. Then these solutions were cast and dried as composite films. These CPCs showed different sensitivity to polar vapors and non-polar vapors, which could be a good choice as biomarkers for lung cancer detection [49].

In a previous study, we presented the conductive network changes of PLA/CB and PLA/MWCNTs composites towards organic vapors as shown in **Fig. 2.14** [68]. Since CB nanoparticles are zero-dimensional and MWCNTs are one-dimensional nanoparticles, the conductive network change of these two CPCs towards organic vapors is different. **Fig. 2.14a** shows a schema of the initial CB conductive network in the PLA matrix. After being immersed in xylene vapor, the conductive network change is shown in **Fig. 2.14a'.** Some CB particles start losing contact to neighboring nanoparticles under the polymer swelling. Subsequently, the conductive network reconstructs with polymer de-swelling when the sample is taken out from the testing chamber (**Fig. 2.14a''**). In case of MWCNT/PLA, it is a similar process but the disconnection and reconnection of MWCNT network is not as easy as in the case of CB particles, which is attributed to the large aspect ratio of MWCNTs and the entanglement of the nanotubes (**Fig. 2.14b**). Therefore, given both samples having slightly higher filler contents than the their own percolation concentration, PLA/CB exhibits higher $R_{rel}$ but poor reversibility and PLA/MWCNT exhibits lower $R_{rel}$ but better reversibility during vapor sensing tests.
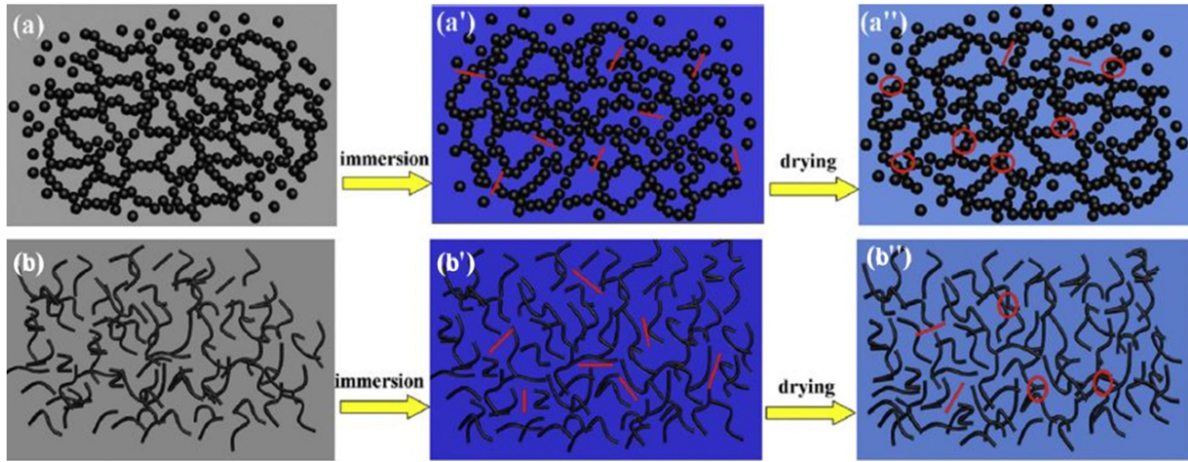
**Fig. 2 14** Schematic of conductive network formed by CB or MWCNT in PLA matrix during vapor sensing tests. The red line and circles represent changes of conductive paths. Reprinted with the permission from Elsevier [68].

Several studies have been reported to achieve improved sensing performance by tailoring the conductive network of CPCs. Mondal et al. selected MWCNTs to tailor the CB conductive network of CB/poly(dimethylsiloxane) (PDMS) composites. With the addition of MWCNTs, the conductive network becomes more perfect and both networks overlap. A decrease in $R_{rel}$ of CPCs towards xylene vapor can be seen from 270 % for CB/PDMS to *ca.* 35 % for MWCNT/CB/MWCNT. They concluded that MWCNTs made the CB network more perfect and more stable to vapor stimulation. The conductivity of CPCs was increased at the expense of reduced $R_{rel}$ towards VOCs [46].

How to select the right polymers and chemicals for the sensing test is another important topic for CPC sensing tests. The Hansen solubility parameters (HSP) were proposed by Charles M. Hansen in 1967 as an attempt to predict the solubility of polymers in solvents. The principle is based on the idea that 'like dissolves like', meaning that if a solvent has HSP similar to those of a polymer, there will be a stronger interaction between them [59]. The HSP are composed of the dispersion solubility parameter ($\delta_d$), the polar solubility parameter ($\delta_p$) and the hydrogen bonding solubility parameter ($\delta_h$) as shown in **Eq. 2.5**,

$$\delta^2 = \delta_d^2 + \delta_p^2 + \delta_h^2 \tag{2.5}$$

In the beginning Hansen et al. used the solubility sphere model to distinguish good from bad solvents for the polymer, whereby all good solvents are included within a sphere in $\delta_d$, $\delta_p$, and $\delta_h$. All the bad solvents are excluded from the sphere. **Fig. 2.15** illustrates the HSP sphere model. The red and green dots represent 'bad' and 'good' solvents, respectively. Clearly, 'good' solvents are located in the HSP sphere, while 'bad' solvents are excluded

from the sphere. According to this theory, good solvents are more likely to dissolve or swell polymer.
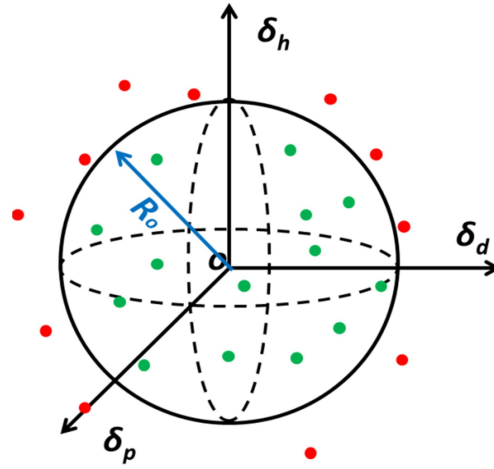


**Fig. 2.15** Hansen solubility sphere with 'good' and 'poor' solvent-polymer interactions marked as green dots and red dots, respectively.

The radius for this sphere is known as the interaction radius, $R_o$, and is considered a a fourth parameter in the HSP value determination. The advantage of the solubility sphere is that once an interaction radius is determined, solvents that have not yet been experimentally tested for the desired interaction can be quickly screened and used for further study. This solubility sphere evaluation is aided by an equation developed for determining the straight-line distance, $R_a$, in a plot of $\delta_d$ vs. $\delta_p$ vs. $\delta_h$ between two materials based on their respective HSP values as shown in **Eq. 2.6**,

$$(R_a)^2 = 4(\delta_{d2} - \delta_{d1})^2 + (\delta_{p2} - \delta_{p1})^2 + (\delta_{h2} - \delta_{h1})^2 \qquad \textbf{(2.6)}$$

where $\delta_{d2}$, $\delta_{p2}$, and $\delta_{h2}$ are associated with a given solvent and $\delta_{d1}$, $\delta_{p1}$, and $\delta_{h1}$ with the center of the optimized solubility sphere [59]. Therefore, if the solvent has strong interaction with polymer, $R_a$ should be less than $R_o$, and vice versa. A convenient index, relative energy difference (*RED*), is proposed, which is defined as the ratio of $R_a$ and $R_o$ in **Eq. 2.7**,

$$RED = R_a/R_o \qquad \textbf{(2.7)}$$

For an individual solvent, a value of *RED* < 1 indicates good polymer-solvent interaction, a value of *RED* > 1 indicates poor polymer-solvent interaction, and *RED* ≈ 1 represents a boundary condition between good and bad. By employing these parameters, it is possible to predict polymer-solvent interactions. This approach has been already successfully employed to estimate in advance if a composite will react to a certain solvent [36].

In terms of vapor sensing behavior of CPCs, also the vapor volume should be taken into consideration as it is related to the vapor penetration and diffusion in the polymer matrix. To better illustrate the polymer-vapor interaction, the Flory-Huggins interaction parameter $\chi_{12}$ is introduced, which was proposed by Flory and Huggins [138, 139]. Flory-Huggins solution theory is mathematical model of the thermodynamics of polymer solutions which takes account of the great dissimilarity in molecular sizes in adapting the usual expression for the entropy of mixing. The polymer-vapor interaction can be well predicted using $\chi_{12}$ calculated by **Eq. 2.8**,

$$\chi_{12} = \frac{V_1^0}{RT}(\delta_1 - \delta_2)^2 \qquad \textbf{(2.8)}$$

where $V_1^0$ is the solvent molar volume (cm$^3$·mol$^{-1}$), $R$ is the universal gas constant (8.314 J·mol$^{-1}$·K$^{-1}$), $T$ is the temperature ($K$), and $\delta_1$ and $\delta_2$ are the solubility parameters of solvent and polymer (J$^{1/2}$·cm$^{-3/2}$), respectively. Typically, a low $\chi_{12}$ indicates that polymer and vapor have high solubility. Moreover, Hansen et al. proposed that if $\chi_{12} \leq 0.5$ the vapor or liquid can be regarded as good vapor/solvent to the selected polymer, and values much above 0.5 indicate nonsolvency [59].

Additional aspects, which influence the solubility of polymers, are the solvent/vapor molecule size and the testing temperature. Smaller molecule sizes or molar volumes can result in promoted swelling processes [56]. In cases, where the sensing experiments are not carried out at room temperature, there is a volume change of the solvent and its cohesive energy density with temperature. The change of the $\delta_d$, $\delta_p$, and $\delta_h$ parameters for solvents with temperature, $T$, can be estimated using following equations **Eq. 2.9-2.11**, where $\alpha$ is the thermal expansion coefficient:

$$d\delta_d/dT = -1.25\alpha\delta_d \qquad \textbf{(2.9)}$$

$$d\delta_p/dT = -0.5\alpha\delta_p \qquad \textbf{(2.10)}$$

$$d\delta_h/dT = -\delta_p(1.22\times10^{-3}+0.5\alpha) \qquad \textbf{(2.11)}$$

For instance, Li et al. investigated the vapor sensing behavior of PLA/CB composites towards several kinds of vapors at 40 ºC. They deduced the $\delta$ and volume of vapors at 40 ºC using those equations mentioned above [140]. The influence of temperature on the resulting vapor sensing behavior of graphene/TPU composites was another work by Liu et al. and it was found that the sensitivity of the CPCs increased with temperature due to higher absorption activation at higher temperature [141].
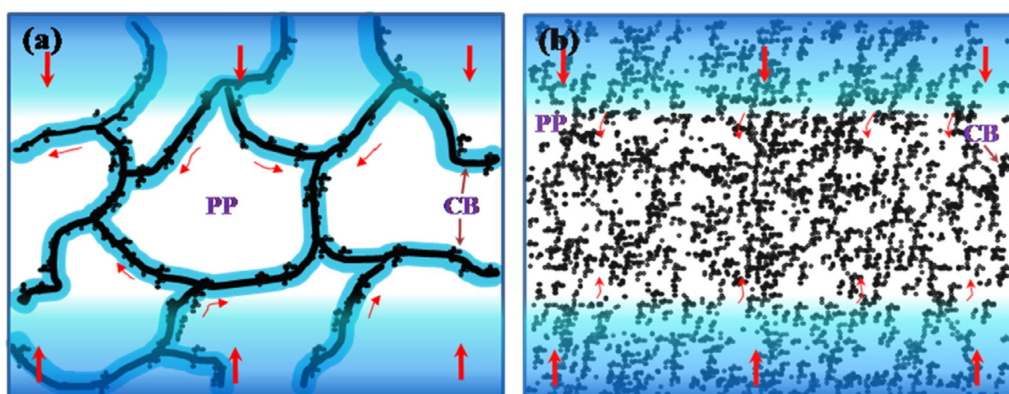
**2.5.2 Liquid sensing behavior of CPCs**

Organic solvents are widely used in industries and laboratories. However, most of organic liquids are toxic and harmful to the environment and human health. Sometimes they may cause disastrous accidents. Thus, real-time detection of organic liquids and efficient emergency intervention to solvent leakage is of great importance. CPCs, with the merits of lightweight, good processability and low cost, have been considered as potential liquid sensing materials. As mentioned in the introduction section, sensing detection is fulfilled via electrical resistance changes of CPCs when they are immersed in an organic liquid. More specifically, solvent absorption leads to polymer swelling and causes disconnection of percolated conductive pathways, thus resulting in electrical resistance increase. When the absorbed liquids are removed, the disconnected conductive networks are reconstructed and resistance decreases.

In the past several years, the liquid sensing behavior of CPCs has been intensively investigated and discussed. Kobashi et al. [37, 38, 142] studied the liquid sensing behavior of PLA/MWCNT composites fabricated by melt compounding. They studied the liquid sensing mechanism of PLA/MWCNT films from the viewpoints of MWCNT loading, solvent solubility parameters, solvent transportation behavior, as well as the crystallization of PLA. It was found that lower filler loading led to the higher $R_{rel}$ of CPCs, indicating that the conductive network tended readily to disconnect due to the less dense network structure as compared to higher filler loadings. In addition, the liquid sensing behavior of neat CPCs and annealed CPCs ($T_{g,PLA}$ is 64.0 ºC and annealing temperature is 105 ºC) was compared. Results demonstrated that $R_{rel}$ of annealed samples is significantly reduced. This is due to increased crystallinity which resulted in a confined molecule chain mobility of PLA, leading to a less changeable network when exposed to solvents.

Concerning CPCs with CB, Narkis et al. reported that the interfaces play an important role in the liquid sensing behavior of CB filled immiscible polymer blend composites [131, 143-145]. For instance, CB was found to be located in EVA component of HIPS/EVA/CB composites. Due to the possible accumulation of methanol at the interface of blends, CPCs exhibited higher sensitivity in liquid sensing tests. Furthermore, Pötschke et al. compared the $R_{rel}$ of PCL/MWCNT and PCL/PP/MWCNT composites in liquid sensing tests. MWCNTs were found selectively localized in the PCL component of blend composites. Interestingly, the blend composite (PCL/PP/MWCNT-3.0 wt%) yielded the largest $R_{rel}$ in methanol as compared to PCL/MWCNT-1.0 wt.% and PCL/MWCNT-3.0 wt.% composites, which was attributed to the blend interface that promoted the ethanol molecule penetration in the PCL

component. Such behavior is more efficient in increasing the distance between neighboring MWCNTs than in PCL/MWCNT-3.0 wt.% composites [36].

Dai et al. studied the liquid sensing behavior of CPCs by constructing a segregated structure in CB/PP composites [146, 147]. They utilized a dissolving-smashing method, i.e. dissolving PP pellets in hot xylene and smashing the dried PP bulks into powders (PP particle size is ca. 30 μm). Subsequently, CB particles and PP powder were mixed by solution mixing in ethanol. After drying, the composites were compression molded by a hot press machine. When being immersed in an organic solvent, CPCs with segregated structure exhibited much higher $R_{rel}$ than CB/PP composites without segregated structure. The authors proposed a scheme to illustrate such phenomenon as shown in **Fig. 2.16**. By controlling the localization of CB at the interface of PP particles, the conductive network is just localized at the interface of PP granules. Once the solvents penetrate the interfaces, the CB conductive networks between adjacent polymer particles are severely damaged, leading to a high $R_{rel}$ of CPCs. Similar studies were reported by Pang et al. for CB/UHMWPE/PMMA composites [111] and Wang et al. for CB/PA6/HDPE composites [148].



**Fig. 2.16** Schematic illustration of the mechanisms of liquid sensing behavior of (a) segregated CB/PP and (b) CB/PP without segregated structure. The red arrows represent the penetration direction of the solvent. Reprinted with permission from Elsevier [147].

In addition to organic solvent detection, CPCs can also be used as water sensors. Cellulose extracted from natural plants has been used for clothes and fabrics manufacturing for a long period. As a renewable alternative to petrochemical substrate, cellulose has many advantages such as flexibility, low cost and biodegradability. Furthermore, cellulose is a hygroscopic polar molecule and good affinity to water; on the other hand, hydrogen bonding between cellulose chains results in the insolubility to water. Thus, cellulose is a good candidate as matrix for CPC based water sensors. Qi et al. prepared cellulose/CNT composites using solution mixing and investigated their water sensing behavior [149-151]. The CPCs

were made by adding CNTs into a NaOH/urea/water aqueous system, and then the mixtures were casted and degassed. **Fig. 2.17** illustrates the morphology of such composite and their water-sensing scheme. The CNTs have good dispersion in the cellulose matrix in the cellulose/CNT-3.0 wt% composite which is attributed to the hydrogen bonding between the functional group (-OH) of CNTs and the cellulose chains. The $R_{rel}$ of the composite film reached up to *ca.* 550% when being immersed in water and decreased to its initial value when the sample was taken out from the water (see **Fig. 2.17d**). The main sensing mechanism is explained by swelling effects, which involves a fast and large disconnection of the CNT network induced by the strong cellulose swelling in water. Similar work was reported by Dichiara et al., who fabricated hydroxyl-functionalized CNT/cellulose composites by solution mixing, with the $R_{rel}$ of CPCs with 10 wt% CNTs reaching a maximum of 3100 % when immersed in water. In addition, they compared the thickness of CNT/cellulose microfibers after immersing in air, ethanol and water. The fiber diameter of 10 μm increased to 100-140 μm when the fiber was immersed in water. Immersion in air or ethanol resulted in fiber diameters of 20-60 μm. Such results indicate that CNT/cellulose composites have good swelling property in water and are good candidates for water sensing application [152].
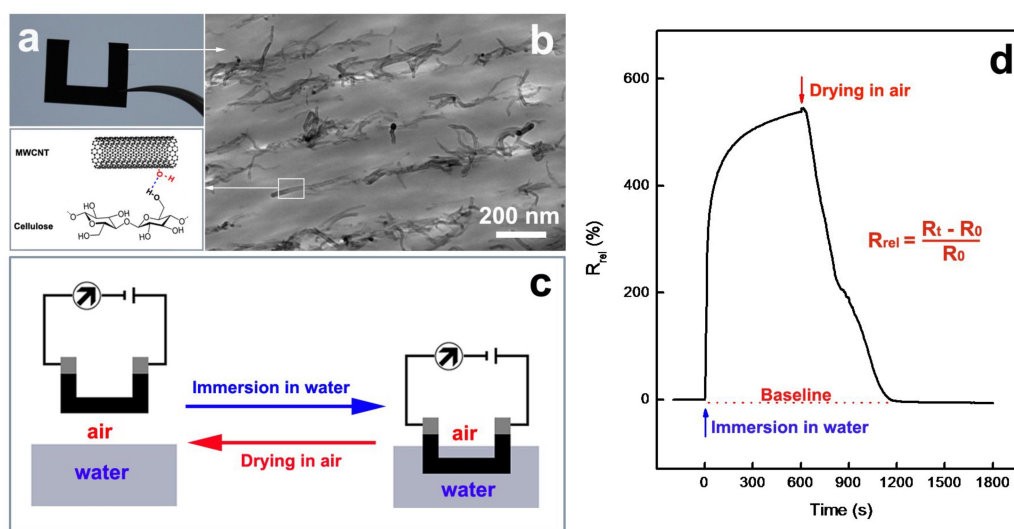


**Fig. 2.17** Cellulose/CNT composite film (with 3% CNTs) as water sensor: a) photo and (b) TEM image of the U-shape sample; (c) schematic of liquid sensing test; (d) $R_{rel}$ of the sample during immersion/drying (600 s/1200 s) cycle in water at 20 ºC, where $R_0$ and $R_t$ are the initial resistance and transient resistance upon exposure to water. Reused with permission from Elsevier [150].

### 2.5.3 Vapor sensing behavior of CPCs

Leakage of VOCs especially toxic vapors has posed a great threat to the environment and human health. Currently, many kinds of vapor sensor materials such as metal oxides

(MO), carbonaceous material, conjugated polymer (CP) and CPCs have been intensively investigated and reported. All of these sensors have their own advantages and disadvantages, which will be briefly summarized in the following.

MO semiconductor material is a kind of commonly used gas/vapor sensors because of their unique sensing characteristics such as low temperature dependence, rapid recovery kinetics and high thermal stability. The sensing signal results from the electron transfer from the electrode to the MO layers. Despite many advantages of MO materials, the detection range is limited and they can only detect a small group of gases such hydrogen ($H_2$) and nitrogen dioxide ($NO_2$), while for organic solvent vapors, MO sensors are usually not fully applicable. Furthermore, the adhesive force between the MO layer and the sensor substrate (e.g. silicon wafer) is weak, resulting in a poor stability and reversibility during sensing tests [153]. In addition to MO sensors, electronic sensors based on field-effect transistors (FETs) are developed due to their ultrahigh sensitivity at extremely low vapor concentration, rapid response, low power consumption, room temperature operation and good reversibility. Amongst these nanostructured sensing systems, nano-carbon based materials are more promising;, the electrical properties of nano-carbon materials such as CNTs and graphene are highly sensitive to changes in the chemical environment [154]. During sensing tests, the adsorption of gas or vapor molecules onto the surface of nano-carbon materials results in conductivity changes of the sensor device. These adsorbates act as donors or acceptors. For example, CNTs are p-type under ambient conditions; therefore the electron donation into the valence band will lead to charge-carrier ($h^+$) recombination, causing a decrease in conductivity [155, 156]. The strong Van der Waals force between neighboring nanotubes or graphene plates make them easily agglomerated. Therefore, the current difficulties for nano-carbon sensors are how to improve the sensitivity, selectivity and anti-jamming capability. Conjugated polymers (CPs) have continuous delocalization along the chain axis, thus leading to excellent electrical and optical properties. CPs have unique material properties that make them promising for a wide range of applications. Polyaniline (PANI), polypyrrole (PPy), polythiophene (PT) are the conjugated polymers most commonly used as chemical sensor materials. Their π-electron delocalization makes these polymers readily interacting with vapor analytes. Apart from π-π interaction, hydrogen-bonding, π-dipole interaction and even van der Waals interaction are the main interactions between CP and vapor analytes, which make CPs a good candidate for sensor array and e-nose. Pavase et al. published a review on CP nanocomposite-based chemical sensors in food spoilage detection [157]. However, these sensing elements are typically conducted at high temperature in order to achieve enhanced

sensing performance. Moreover, poor stability and considerable variations in the synthesized CPs also confine their practical application.

Among those kinds of vapor sensors, CPCs are regarded as the most promising candidate as vapor sensors due to their easy fabrication, lightweight, and tunable conductivity [141, 158]. The resistance increase of CPCs when being exposed to organic vapors is named as positive vapor coefficient (PVC). In addition, negative vapor coefficient (NVC) i.e. the resistance decrease when the sample is exposed to vapors, was also reported, e.g. by Chen et al. [159]. They found that a NVC phenomenon occurred for CB/PU composites whose filler contents are near or lower than the percolation content of CPCs. This is due to damages of the hydrogen bonding between carbonyl and ether of PU during vapor penetration, thus facilitating the agglomeration of separated CB particles leading to resistance decrease of the CPCs. Zhang et al. explored the vapor sensing behavior of amorphous PS composites filled with CB or MWCNTs [160-162]. The sensitivity of vapor sensors is related to the vapor concentration, vapor polarity, and mixed vapor compositions. For instance, CPCs with non-polar PS showed low responsivity towards polar vapors such as ethanol and methanol, but high responsivity to non-polar (cyclohexane and butanone) or low polar (tetrahydrofuran and acetone) vapors. These results demonstrated that the responsivity of CPCs is not only related to the solubility parameters, but also to the polarities of vapors and polymers. Kumar et al. reported the chemo-resistive properties of MWCNT/PLA composites prepared by a layer-by-layer technique [55]. The sensitivity and selectivity of CPCs corresponded to the ranking of the Flory-Huggins interaction parameters $\chi_{12}$. In addition, the increase in crystallinity of PLA (a semi-crystalline polymer) weakened the sensing performance in terms of sensitivity and selectivity of the CPCs.

Recently, researchers aimed to develop CPC vapor sensors with novel structures. Li et al. selected natural ramie fiber (RF) as a skeleton for CB or MWCNT attachment in PLA based composites. They found that the existence of RF improves the stability of CPCs towards xylene and tetrachloromethane, which are good solvents to PLA. RF stabilized the conductive network in CPCs during sensing tests [68]. Besides, Gao and co-workers investigated the vapor sensing behavior of PU/polystyrene-*b*-poly(ethylene-*co*-butylene)-*b*-polystyrene (SEBS/CNF) with hierarchical structure [163]. A PU/SEBS blend nanofiber mat was prepared by the electrospinning technique and then the mat was immersed in a homogenous CNF/ethanol solution to achieve PU/SEBS/CNF composites. The results proved that the CNT decorated nanofibrous membranes are sensitive to both polar and non-polar

vapors. Moreover, testing temperature and conductive filler loading also had great influence on the sensing performances of these CPCs as shown in **Fig. 2.18**.
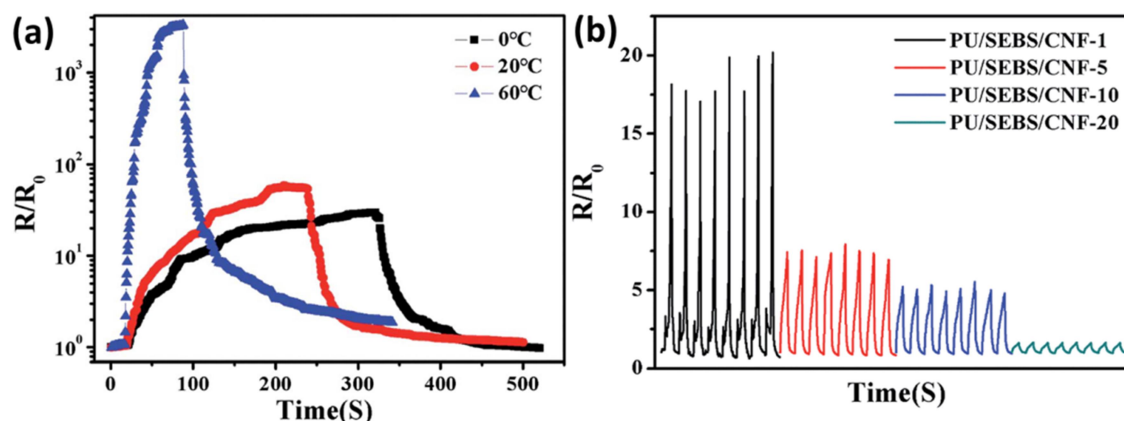


**Fig. 2.18** (a) Influence of toluene temperature on the relative resistance change of PU/SEBS/MWCNT-10 and (b) cyclic sensing behavior of PU/SEBS prepared at different ultra-sonication times against toluene vapor. Reprinted with permission from Royal Society of Chemistry [163].

Furthermore, fiber-based sensors developed from CPCs were reported by Zhu and co-workers [133, 164]. SBS/MWCNT fibers and SBS/few layer graphene fibers were prepared by wet spinning. SBS is a triblock copolymer consisting of soft non-polar PB domains and hard polar PS domains, which enable SBS based CPC sensors to response to both low or high polar VOCs. Both of these two CPC sensors showed high sensitivity, fast response as well as good reversibility to both polar and non-polar VOCs. For instance, the sensitivity of a SBS/MWCNT fiber-based sensor to 10 % acetone and cyclohexane was 19 % and 256 %, respectively. The response time was less than 40 s (response time is defined by the time taken by the sensor to reach 90 % of the maximum resistance in presence of the analyte vapor).

Humidity sensors are another application of vapor sensing of CPCs. With respect to humidity sensors, polyvinyl alcohol (PVA) [165, 166], poly(acrylic acid) (PAA) [167], and chitosan [168] are the most commonly used polymers. Li et al. fabricated MWCNT/PVA composite yarns by immersing a MWCNT yarn in a PVA solution and then collecting yarns using a rotating motor. The humidity sensing was carried on different saturated salt solutions in its equilibrium to achieve the desired humidity values. **Fig. 2.19** shows the sensitivity (ratio of resistance change to the initial resistance at a given relative humidity) of the MWCNT/PVA composite yarn at different humidity. It was found that the composite dipped in 5 % PVA solution exhibits the highest sensitivity (ca. 1.89) as compared to other samples. The authors concluded that the humidity sensing behavior is related to the swelling property

of PVA. At high humidity, rapid increase of intermolecular distances occurs in PVA due to de-bonding of hydrogen bonds [169].
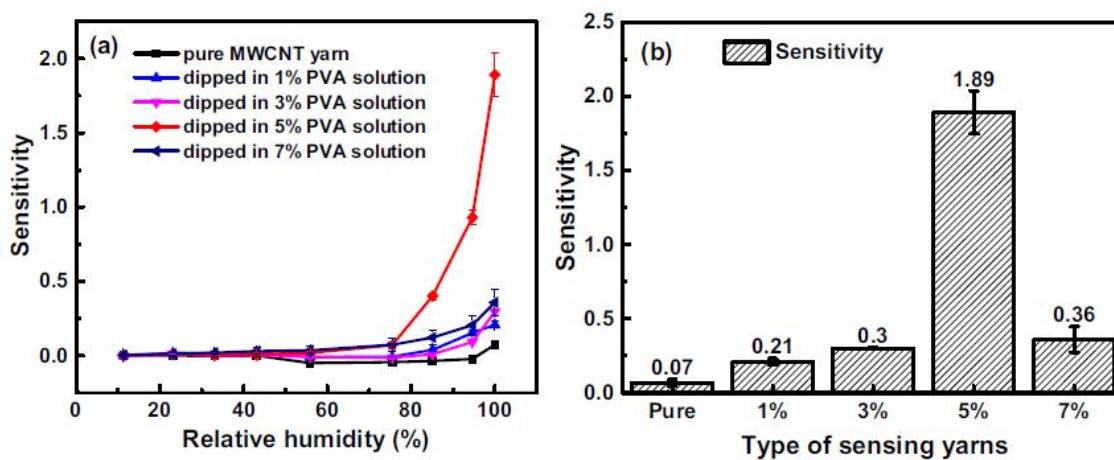


**Fig. 2.19** (a) Sensitivity-humidity curves and (b) sensitivity at 100 % humidity of pure MWCNT yarn and MWCNT/PVA composite yarns. Reprinted with permission from Elsevier [165].

## 3. Experimental

### 3.1 Materials

Bisphenol A based PC was used to perform most of the experiments in this work. As PCs, a high viscosity grade Makrolon 3108 ($M_w$=29800 g·mol$^{-1}$), a medium viscosity grade Makrolon 2600 ($M_w$=26200 g·mol$^{-1}$), and a low viscosity grade Makrolon 2205 ($M_w$=20100 g·mol$^{-1}$) were purchased from Bayer MaterialScience AG, Germany. All these PCs have a density of 1.2 g·cm$^{-3}$. PVDF pellets (Kynar 720) with a polydispersity of 6.08 and a density of 1.78 g cm$^{-3}$ were supplied by Arkema S.A., France. PLA (4043D) with a density of 1.24 g·cm$^{-3}$ was obtained from NatureWorks Co. Ltd. USA. PS (145D) with a density of 1.05 g·cm$^{-3}$ was received from BASF AG, Germany. Highly electrically conductive CB (Printex XE2B) with a carbon purity of more than 99%, a BET value of 400 m$^2$ g$^{-1}$, a buck density of 100-400 kg·m$^{-3}$, and a primary particle size of 30-35 nm was obtained from Evonik Degussa GmbH, Germany [21]. Commercially available MWCNTs (NC3100$^{TM}$) with an average length of *ca.* 1.5 µm and an average diameter of 9.5 nm were obtained from Nanocyl S.A., Belgium. The carbon purity is higher than 95 % and the density of MWCNT is 2.1 g·cm$^{-3}$ [170]. Acetone, dichloromethane (DCM), tetrahydrofuran, toluene, ethyl acetate and cyclohexane were of analytical grade (purity > 99.9%) and obtained from Sigma-Aldrich, Germany. All chemicals were used as received.

### 3.2 Sample preparation

Prior compounding, all the polymer granules and carbon fillers were dried in a vacuum oven at 70 °C for 16 h to avoid trace water. The CPCs were fabricated using a twin-screw micro-compounder (DSM Xplore, capacity 15 cm$^3$, The Netherlands) as shown in **Fig. 3.1a**. Different processing parameters are applied for different composite systems, which will be introduced in the specific following chapters. After mixing the polymer melt was extruded through the die (2 mm diameter) without any additional cooling. In the following, the extruded strands were pelletized and compression molded into circular plates (60 mm diameter and 0.3 mm thickness) using a hot press machine (Model-PW40EH, Paul-Otto Weber GmbH, Germany) as shown in **Fig. 3.1b**.
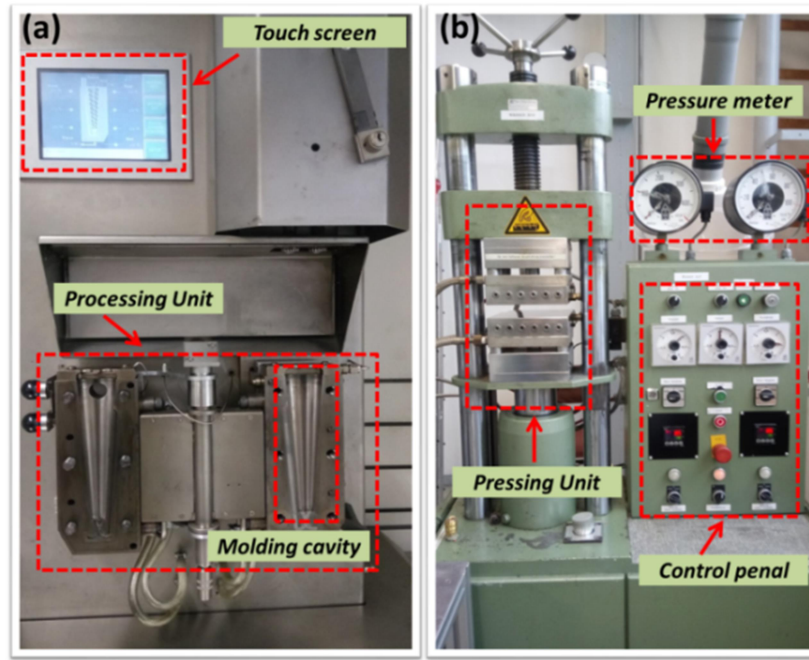
**Fig. 3.1** Photograph of (a) DSM Xplore15 micro-compounder and (b) PW40EH hot press machine.

### 3.3 Characterization of the CPCs

### 3.3.1 Electrical resistivity measurement

The electrical volume resistivity measurements were performed either on the circular plates or on strips, depending on sample's resistivity values. For the compression molded circular plates whose resistivity is above $10^7$ $\Omega \cdot$cm, the Keithley Electrometer 6517A (Keithley Instruments Inc., USA) combined with a Keithley 8009 Resistivity Test Fixture equipped with ring electrodes was applied. In this case, at least two samples were measured on both sides to achieve the mean value of resistivity. For samples with resistivity values lower than $10^7$ $\Omega \cdot$cm, the measurements were performed on strips (cut from the circular plates) with a dimension of $30 \times 5 \times 0.3$ mm$^3$ using a four-point probe combined with a Keithley Multi-meter DMM 2000. The four-point test fixture has gold contact wires with a distance of 16 mm between the source electrodes and 10 mm between the measuring electrodes. At least 4 strips were measured per sample to get the arithmetic mean value and standard deviation. The images of the resistivity measuring devices are shown in **Fig. 3.2**
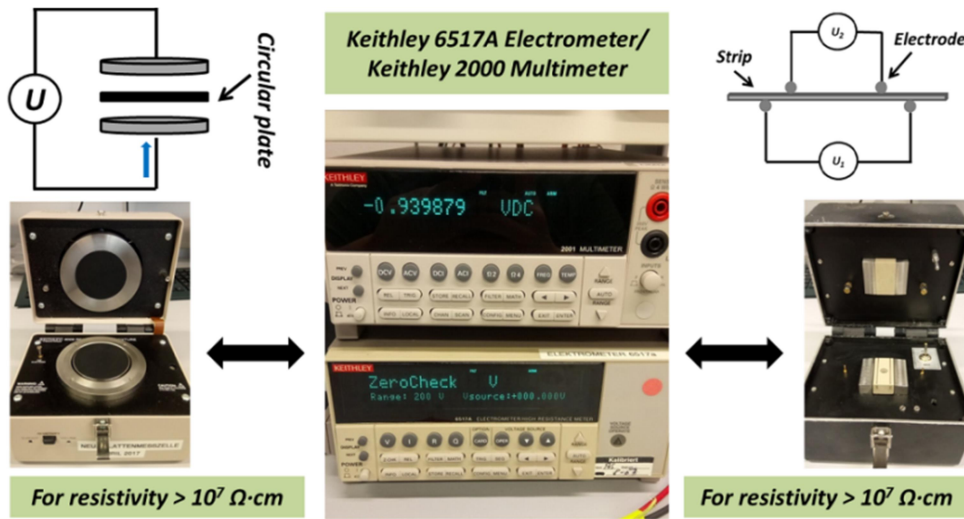
**Fig. 3.2** Photographs and schematic diagrams of resistivity measuring devices.

### 3.3.2 Transmission light microscopy (TLM)

The state of MWCNT dispersion in polymer matrix was evaluated using TLM. For each sample a series of thin sections with 5 μm thickness were prepared from extruded strands (perpendicular to the extrusion direction) using a Leica RM2265 microtome (Leica, Germany) at room temperature. These sections were observed using an Olympus BX-53 (Olympus Deutschland GmbH, Germany) combined with a DP71 video camera in transmission mold. The area ratio of remaining nanotube agglomerates ($A_{agg}$) was determined from the TLM images using the software of Stream Motion 1.9.4 by calculating the ratio between the area of remaining MWCNT agglomerates ($A$) and the total area of the images ($A_0$) [74, 76], whereby the total area of each image was 16.9 mm$^2$. According to the ISO-18553 standard only agglomerates with circle equivalent diameter > 5 μm were regarded [75, 171]. At least 12 images from different sections of the strands were used for $A_{agg}$ calculation.

### 3.3.3 Scanning electron microscopy (SEM)

The morphology of the cross-section of the composites was investigated using an ULTRA-55 electron microscope (Carl Zeiss AG, Germany) with an accelerating voltage of 3 kV. Different kinds of samples for SEM investigation had different preparation methods. For single polymer based CPCs, the strips cut from compression-molded circular films were cryo-fractured after 30 min immersion in liquid nitrogen and sputtered with a thin platinum layer using a sputter coater (Leica EM SCD 500) to avoid electrical charging. For polymer blend based CPCs, the surfaces of the extruded strands were firstly smoothed by a Leica RM2265 microtome (Leica, Germany), then these smoothed strands were immersed into a certain

solvent to extract one component of the blends. Afterwards, the extracted strands samples were cleaned again using the pure solvent, air-dried, and coated with a thin platinum layer (thickness is 3 nm).

### 3.3.4 Transmission electron microscopy (TEM)

TEM was performed using a LIBRA120 (Carl Zeiss AG, Germany) with the acceleration voltage of 120 kV. Ultrathin sections with a thickness of approximately 60 nm were obtained by using Leica UC7 ultra-microtome at -40 ºC (Leica, Germany).

### 3.3.5 Solvent extraction

Solvent extraction is used to determine the component continuity of polymer blends. For the extraction experiment, the extruded strand samples were cut along the extrusion direction, and the cut area along extrusion direction is ca. 1 cm$^2$ (length is 2 cm and width is 0.5 cm). The extracted polymer content $C_{extract}$ of CPCs is calculated based on the initial mass and the change in mass of the blend during extraction using **Eq. 3.1** [172]**.**

$$C_{extract} = \frac{m_{0,CPC} - m_{r,CPC}}{m_{0,CPC}} \times 100\% \tag{3.1}$$

where $m_{0,CPC}$ is the sample mass before extraction and $m_{r,CPC}$ is the remaining sample mass after the solvent extraction.

### 3.3.6 Rheological characterization

The rheological measurements were conducted on an ARES oscillatory rheometer (Rheometric Scientific Inc., USA) with parallel-plate geometry (diameter 25 mm, gap 2 mm) under the protection of liquid nitrogen. Angular frequency sweeps from 0.1 rad/s to 100 rad/s and back were accomplished with fixed strain amplitude of 1 %, which was located in the linear viscoelasticity regime of the composites. The testing temperature varied for different composite systems, which would be introduced in the corresponding chapters. The rheological results presented in the thesis derive from the measurements from 100 rad/s to 0.1 rad/s. The samples with 25 mm diameter and 2 mm thickness were compression molded from the as received polymer pellets or the extruded strands under the processing conditions given in the respective chapters.

### 3.3.7 Differential scanning calorimetry (DSC)

The melting and crystallization behavior of components and composites was investigated with a differential scanning calorimeter (TA Q2000, TA Instruments, USA) at a scanning rate of +/− 10 K·min$^{-1}$ under nitrogen atmosphere. About 5 mg of the samples (compression molded samples) were first heated from room temperature to 200 °C and kept isothermally for 3 min to eliminate the thermal history. Then the samples were cooled from 200 °C to room temperature followed by a second heating to 200 °C. The cooling and the first heating runs were used for evaluation of the thermal transitions in the materials.

### 3.3.8 Vapor sensing tests

The vapor sensing behavior of CPCs were investigated by *in-situ* recording electrical resistance change of CPCs upon alternating exposure to cyclic flows of (diluted) organic vapors and dry air. A self-made sensing set-up connected with a digital multi-meter (Keithley 2400, USA) is shown in **Fig. 3.3**.
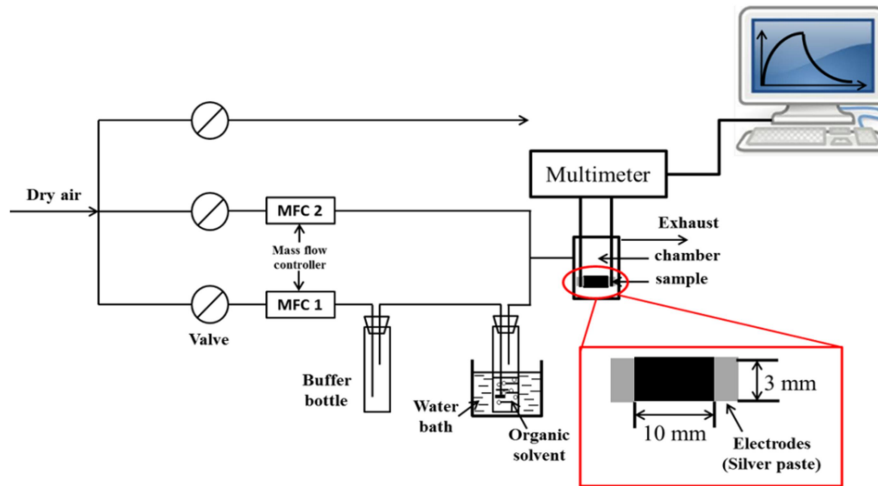


**Fig. 3.3** Schematic set-up diagram for the vapor sensing behavior measurements of CPCs towards organic vapors.

The strips with the dimension of 10×3×0.3 mm$^3$ for sensing test were cut from the circular films, and both sides at the two ends of the specimen were coated with electrically conductive silver paste to ensure good contact between specimen and electrodes. For better comparison, the relative resistance change ($R_{rel}$) was calculated by means of **Eq. 3.2**,

$$R_{rel} = \frac{R - R_o}{R_o} \times 100\ \% \qquad\qquad (3.2)$$

where $R_o$ is the initial resistance of specimen in dry air and $R$ is the actual resistance during experiments. The vapor concentration ($C$) was adjusted to the desired value by tuning the flow

rates (L·h$^{-1}$) of the two mass flow controllers (MFC1 for VOC and MFC2 for dry air). $C$ is calculated by **Eq. 3.3**,

$$C = \frac{P_i}{P} \times \frac{f}{(f+F)} \times 100\% \tag{3.3}$$

where $P$ is the atmospheric pressure, $P_i$ is the saturated partial pressure of organic solvent at 25 °C, and $f$ and $F$ are the mass flow rate of MFC1 and MFC2, respectively. Atmospheric pressure is applied in all tests and the temperature is 25 °C. The vapor mixture was derived from the mixed solvents at given volume ratios.

## 4. Results and Discussion

### 4.1 Electrical and vapor sensing behavior of PC composites containing hybrid carbon fillers[*]

### 4.1.1 Introduction

As it was shown in previous work and discussed before, the use of mixed filler systems, especially consisting of 2 carbon based fillers with different dimensionalities, can result in synergistic effects concerning electrical percolation threshold and achievable conductivity. In addition, it is a way to tune the sensing response in vapor sensing. Therefore, a hybrid fillers system consisting of MWCNT and CB was selected to be melt-mixed with PC by varying the amount of filler and MWCNT/CB ratio. PC was selected as the polymer matrix for fabricating CPCs for the vapor sensing tests since it showed high affinity with many commercial organic solvents as well as high and fast volume change upon vapor immersion. The detailed processing condition during melt mixing was 270 °C, 250 rpm and 5 min. Compression molding was performed under the conditions of 270 °C, 20 kN, 5 min The obtained PC/MWCNT/CB composites with different filler contents are denoted as N$x$B$y$, where $x$ and $y$ represent the MWCNT and CB content in wt%. For instance, N01B05 indicates that the MWCNT and CB loading in composites are 0.1 wt% and 0.5 wt%, respectively.

In this chapter, the morphological and electrical properties of the CPCs with different hybrid filler contents are analyzed and discussed in detail. In order to investigate the electrical and vapor sensing behavior of CPCs, two MWCNT contents were chosen, which were respectively lower and higher than the electrical percolation threshold of PC/MWCNT composites. In the following, three CB contents were selected to mix with MWCNT mutually. The conductive network is either composed of MWCNT or hybrid CB/MWCNT in composites. By using such combined fillers, a fine-tuning of the structure and conductivity of the filler networks was aimed which was expected to broaden the range of detectable vapors. The sensing properties of PC/MWCNT/CB composites were evaluated by exposing them to different VOCs in several successive VOC/dry air cycles. The relationships between the structure of the differently composed electrically conductive networks and their electrical response when exposing them to varied concentrations of the organic vapors were comprehensively investigated.

---

[*] The results presented in chapter 4.1 are published as "*Electrical and vapor sensing behavior of polycarbonate composites containing hybrid carbon fillers*" (**European Polymer Journal 108(2018) 461-471**) with the co-authors Petra Pötschke, Jürgen Pionteck, and Brigitte Voit.

### 4.1.2 Electrical properties of PC/MWCNT/CB composites

To evaluate the influence of MWCNT, CB, and hybrid carbon nanofillers on the electrical properties of the nanocomposites, the volume conductivity versus the carbon filler loadings (in wt%) is plotted in **Fig. 4.1.1**. The electrical percolation curves of the composites were fitted by the non-linear fitting function **Eq. 2.1**, whereby only the compositions above the percolation were used for the fitting. For PC/MWCNT, there is a drastic increase in conductivity between 0 and 0.2 wt% MWCNT and the percolation concentration was fitted to be 0.11 wt%. The percolation threshold of CB in PC is located between 1.0 wt% and 1.5 wt% CB and $\varphi_c$ was fitted to be 1.38 wt%. It is obvious that a significantly lower MWCNT content is needed for constructing the conductive networks compared to CB.
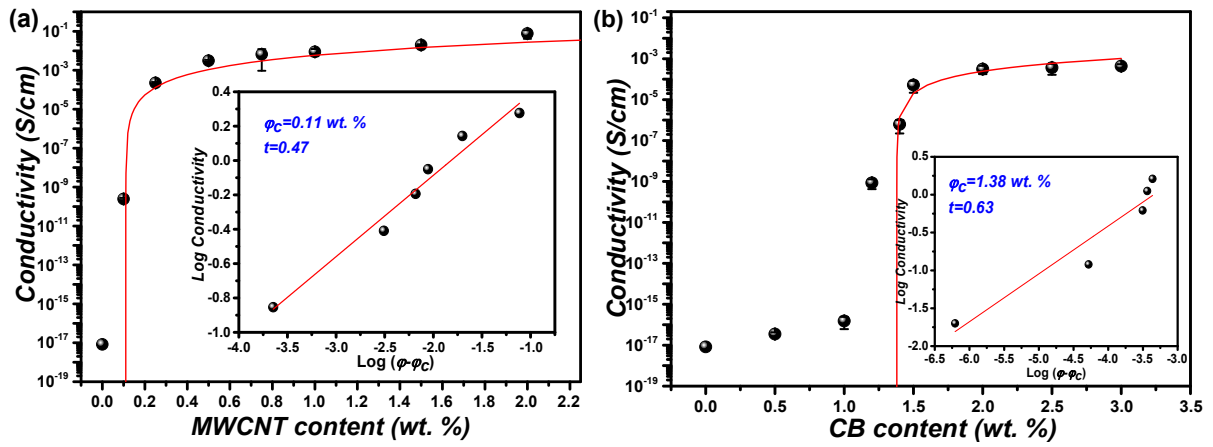


**Fig. 4.1.1** Electrical volume conductivity as function of carbon nanofiller content for (a) PC/MWCNT and (b) PC/CB.

Before discussing the results on the hybrid filler systems, the occurrence of "synergy" concerning the electrical percolation threshold should be regarded. Sun and Xiong et al. proposed a model based on the excluded volume theory to calculate the percolation concentration of hybrid filler composites from both the percolation concentrations of the CPCs filled with one of the fillers [173, 174]. If the fillers do not interfere with each other, percolation is reached when

$$\frac{m_{MWCNT}}{\varphi_{c,MWCNT}} + \frac{m_{CB}}{\varphi_{c,CB}} = 1 \tag{4.1}$$

$m_{MWCNT}$ and $m_{CB}$ are the weight fractions of carbon fillers, and $\varphi_{c,MWCNT}$ and $\varphi_{c,CB}$ are the corresponding electrical percolation concentrations of MWCNT filled CPCs and CB filled CPCs, respectively. The equation was developed for volume fractions, however, for the convenience of practical use and the avoidance of the fillers' density uncertainty, the formula

was also expressed in weight fractions [173, 175]. Based on **Eq. 4.1**, the PC/MWCNT/CB composites are theoretically conductive for

$$\frac{m_{MWCNT}}{\varphi_{c,MWCNT}} + \frac{m_{CB}}{\varphi_{c,CB}} > 1 \qquad (4.2)$$

and insulative when

$$\frac{m_{MWCNT}}{\varphi_{c,MWCNT}} + \frac{m_{CB}}{\varphi_{c,CB}} < 1 \qquad (4.3)$$

If the experimental percolation concentration is lower than the calculated one, a synergistic effect of both fillers can be deduced. This would be the case if composites with calculated ratios > 1 are conductive.

In this study, MWCNTs are regarded as the basic conductive filler for creating the conductive network within the composites. Based on the $\varphi_{c,MWCNT}$ of 0.11 wt% in PC/MWCNT composites, two MWCNT contents, namely of 0.10 wt% and 0.50 wt%, were selected as basis for the preparation of hybrid filler composites. PC/MWCNT-0.1 wt% is non-conductive (volume conductivity *ca.* $2\times10^{-10}$ S/cm) without CB addition, while PC/MWCNT-0.5 wt% can be regarded as conductive composite already without CB addition (volume conductivity $3\times10^{-3}$ S/cm). To evaluate the effect of CB content on the conductivity, three different weight contents of CB are incorporated into these two PC/MWCNT composites as the second conductive filler. **Fig. 4.1.2** shows the electrical volume conductivity vs. CB content for these composites.
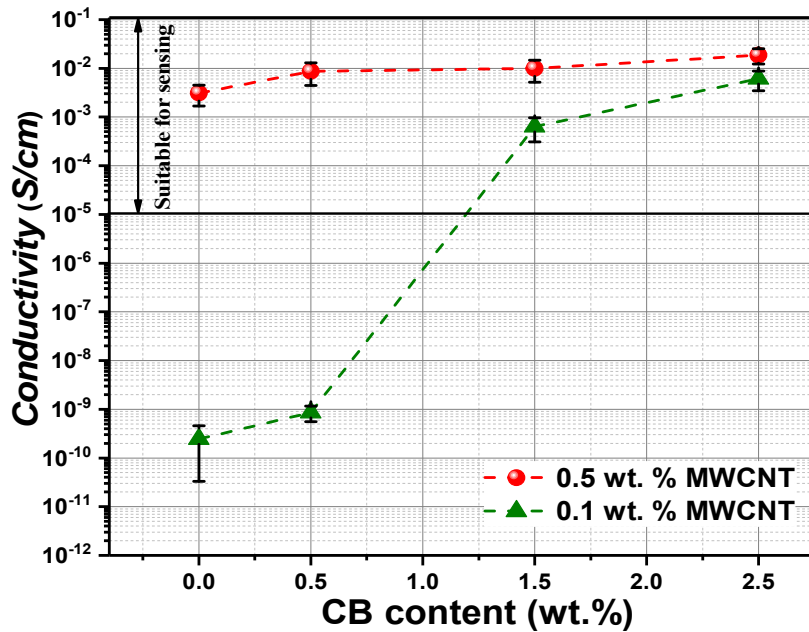


**Fig. 4.1.2** Electrical conductivity as function of CB content for PC/MWCNT/CB composites with two fixed MWCNT contents.

In case of the N01B05 hybrid composite, the calculation according to **Eq. 4.1** results in $\frac{m_{MWCNT}}{\varphi_{c,MWCNT}} + \frac{m_{CB}}{\varphi_{c,CB}} = 1.26$ . This value indicates that this hybrid composite should be conductive; however, the measured conductivity of N01B05 is *ca.* $10^{-9}$ S/cm, indicating that no conductive network is formed in this composite. Thus, one can conclude that during the mixing process the formation of the conductive network is mutually interfered by the two different fillers and that no synergistic effect occurs concerning electrical percolation. When the CB content is increased to 1.5 wt% (N01B15), the calculation results in $\frac{m_{MWCNT}}{\varphi_{c,MWCNT}} + \frac{m_{CB}}{\varphi_{c,CB}} = 1.99$. The conductivity of this sample is *ca.* $6\times10^{-4}$ S/cm, which is about 6 orders of magnitude higher than that of N01B05, illustrating an electrically percolated sample. In N01B15, the MWCNT content is slightly lower than $\varphi_{c,MWCNT}$ (0.11 wt%), whereas the CB content is slightly above the percolation concentration of PC/CB composites ($\varphi_{c,CB}$ 1.38 wt%). Therefore, it can be concluded that CB forms the main skeleton of the conductive network in N01B15. When the CB loading is 2.5 wt% (N01B25), the conductivity is *ca.* $6\times10^{-3}$ S/cm, which is 20 times higher than that of N01B15. This also manifests that CB plays an important role in forming the conductive network in CPCs containing 0.1 wt% MWCNT. For the PC/MWCNT/CB composites with 0.5 wt% MWCNT, the influence of CB on the conductive network structure of PC/MWCNT/CB composites is not so obvious. Comparing the conductivity values of the composites N05B00, N05B05, N05B15 and N05B25, it can be observed that the conductivity increases only very slightly (less than one decade) manifesting that a perfect conductive network has been built in these composites. For the sensing tests, all the prepared carbon hybrid composites are in the conductivity region suitable for sensing, i.e. above $10^{-5}$ S/cm, as shown in **Fig. 4.1.2**. Thereby, the resistivity of the sample N01B25 is similar to those of N05B15 and N05B25 and differs only by half a decade.

### 4.1.3 Morphology of PC/MWCNT/CB composites

In order to investigate the contribution of CB as the second filler on the electrical network formation and to the vapor sensing characteristics of CPCs, the morphology of PC/MWCNT/CB with different hybrid filler contents was studied. **Fig. 4.1.3** shows SEM micrographs of fractured surfaces of conductive composites containing either 0.5 wt% MWCNT or 1.5 wt% CB. As seen in **Figs. 4.1.3a** and **b** the MWCNTs appear to be individually dispersed and homogeneously distributed in the PC matrix. The fracture surface of the CB containing composite (**Fig. 4.1.3c** and **d**) shows evenly distributed grape-like small clusters of CB particles. The filler content in both composites is above the corresponding

electrical percolation concentrations, thus 3D-conductive networks must have been formed (which cannot be seen in 2D-images) either from individualized MWCNTs or small agglomerates of CB.
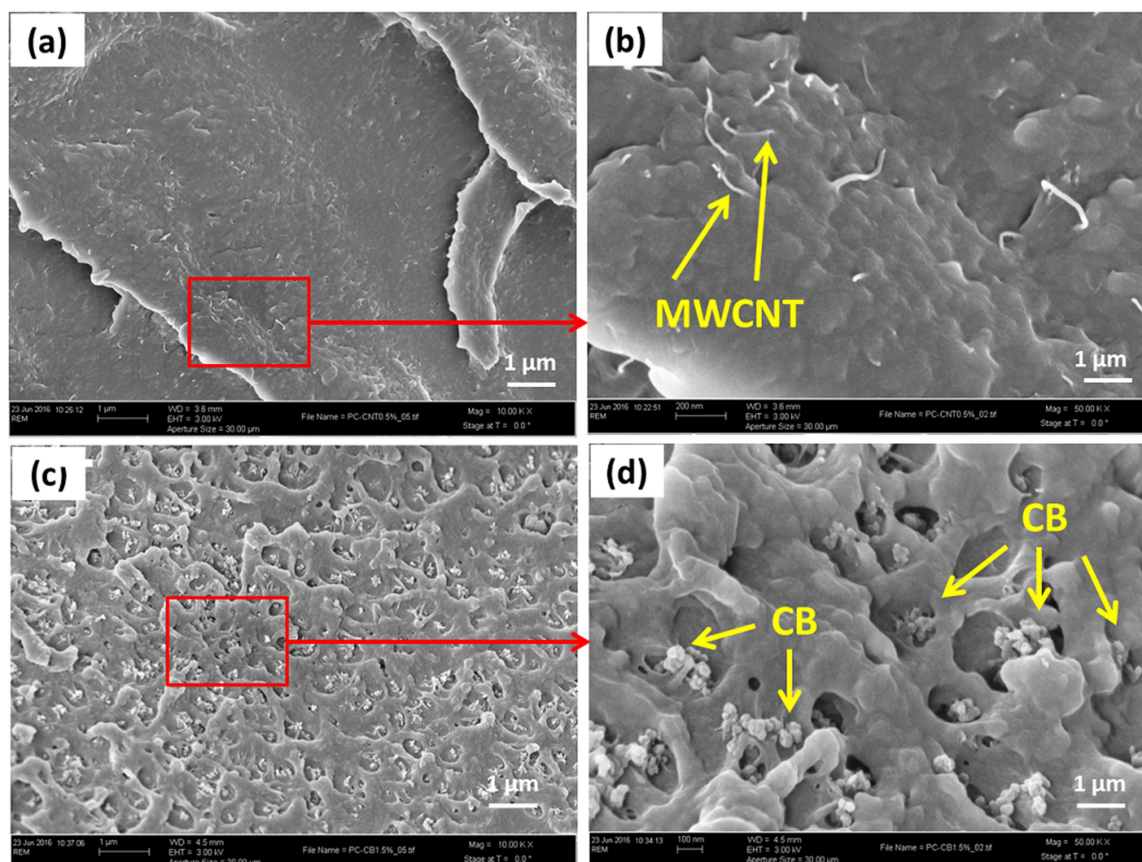


**Fig. 4.1.3** Scanning electron microscopic (SEM) images of fracture surfaces of (a, b) PC/MWCNT-0.5 wt% and (c, d) PC/CB-1.5 wt% composites.

The morphology of N01B15 and N05B15 is shown in **Fig. 4.1.4**. As discussed above, in N01B15 the conductive network is mainly formed by CB particles, and this can be verified in **Figs. 4.1.4a** and **b**. In **Fig. 4.1.4a**, several CB clusters can be seen in polymer matrix whereas MWCNTs can hardly found due to the very low loading. In higher magnification (**Fig. 4.1.4b**), it is obvious that there are enough CB particles which gather together to construct the conductive network, and only a few MWCNTs are dispersed partially bridging such CB clusters. The corresponding conductivity values (see **Fig. 4.1.2**) indicate that the presence of additional MWCNTs make the percolated CB conductive networks more perfect resulting in 20 times higher conductivity values. In N05B15, both compact CB clusters and MWCNTs can be found at the fracture surface (see **Fig. 4.1.4c** and **d**). The MWCNT and CB contents are both slightly higher than the percolation thresholds of the single filler systems, so it can be concluded that the conductive networks in N05B15 are formed by the hybrid fillers

together. Since the MWCNT network at 0.5 wt% filler content is already quite perfect, the addition of CB only slightly increases the conductivity of the hybrid filler composites.
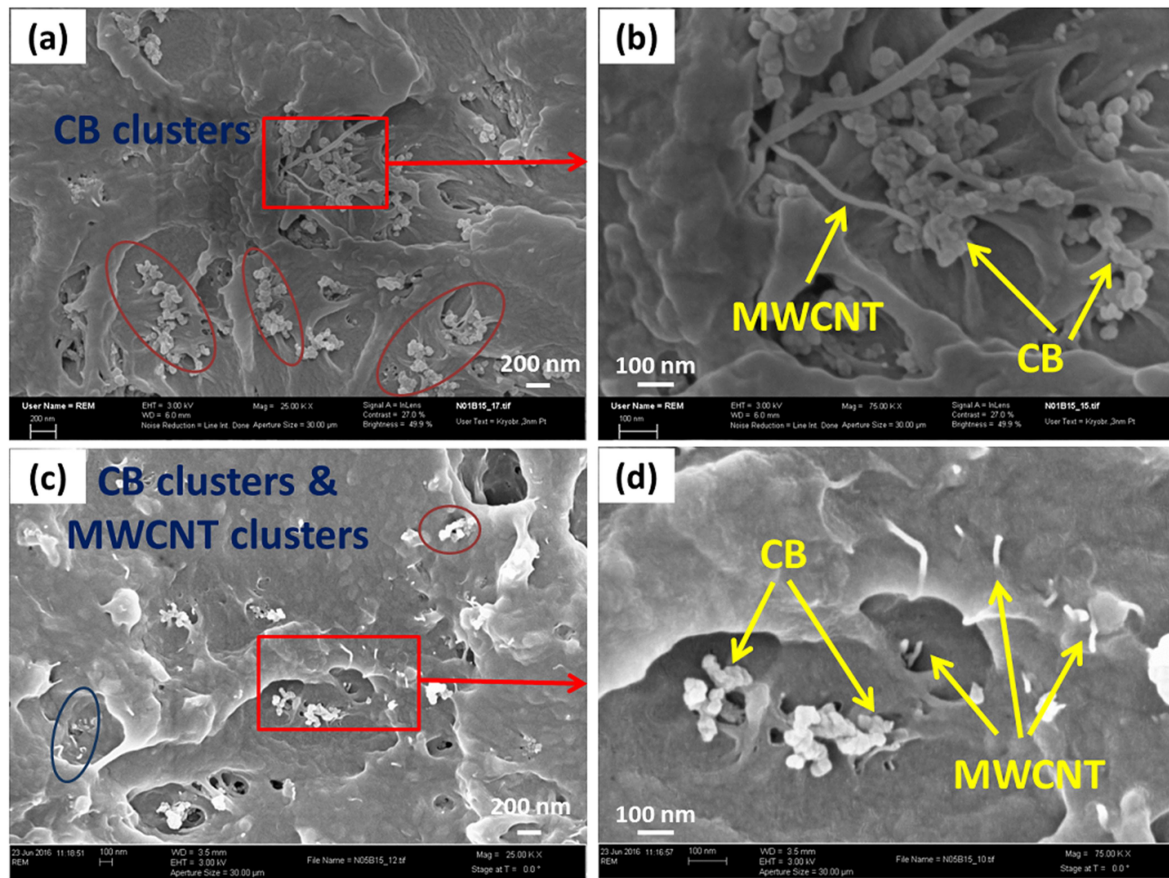


**Fig. 4.1.4** Scanning electron microscopic (SEM) images of fracture surfaces of (a, b) N01B15 and (c, d) N05B15.

Despite the fine dispersion observed in SEM on cryofractures, optical microscopy on much larger observed areas revealed some filler agglomerates as well in the composites with the individual fillers as in the hybrid composites (**Fig. 4.1.5**). In general, the electrical conductivity of CPCs is related to the dispersion of the carbon fillers in the polymer matrix, as only dispersed fillers can take part effectively in the conductive network formation. To characterize the state of filler dispersion, the agglomerate area ratio $A/A_0$ of PC/MWCNT/CB composites is calculated and shown in **Fig. 4.1.5**. The MWCNTs show better dispersibility than CB in the PC matrix; the $A/A_0$ value of PC/MWCNT-0.5 wt% is 0.05 %, which is lower than 0.24 % for PC/CB-0.5 wt%. In addition it can be seen that the addition of low amounts of MWCNTs (0.1 wt% in N01B05) improves the CB dispersion (B05), but this effect vanishes at the higher MWCNT loading of 0.5 wt%.
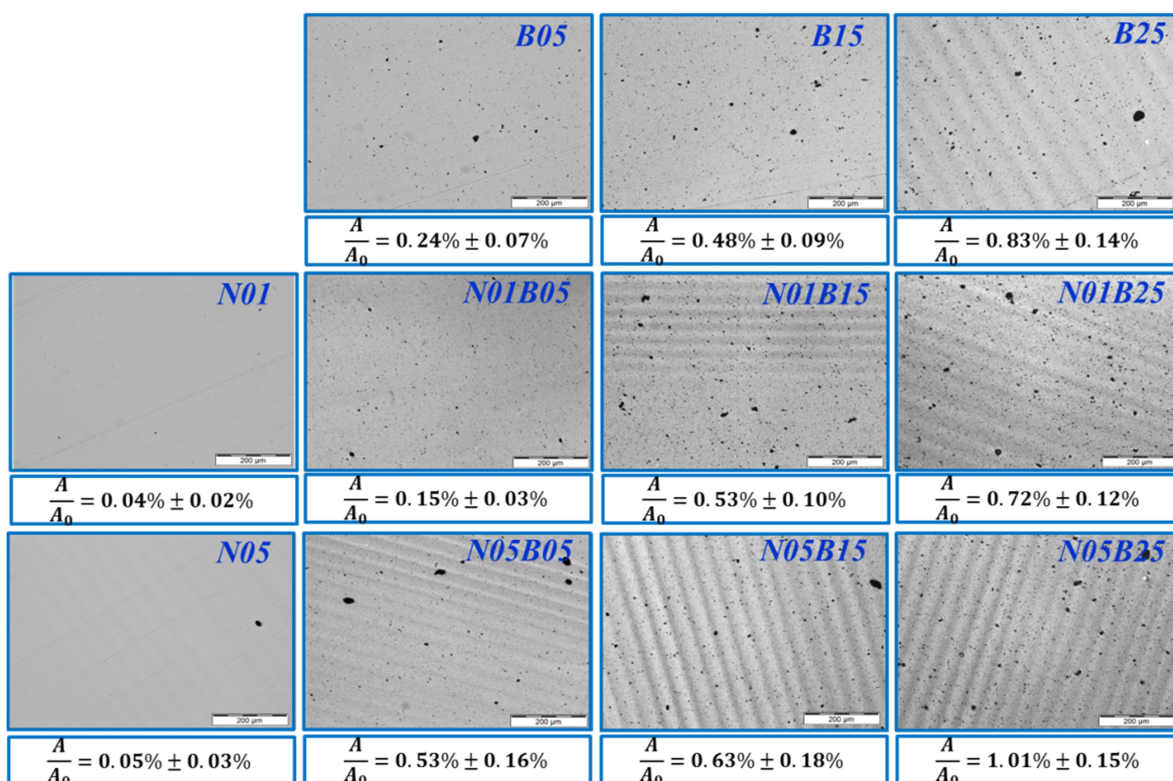
**Fig. 4.1.5** Optical microscopy images of PC/MWCNT, PC/CB, and PC/MWCNT/CB composites with different carbon filler loadings together with their agglomerate area ratios $A/A_0$.

## 4.1.4 Vapor sensing behavior of PC/MWCNT/CB composites

### 4.1.4.1 Sensing mechanism and selection of solvents

For organic vapor sensing, the most important features of a CPC sensor are its discriminability and sensitivity towards organic vapors. As mentioned above, the $R_{rel}$ derives from the changes in the conductive network structure when the polymer swells. This is regarded as the main sensing mechanisms of CPC vapor sensors and was described as "key-lock" theory [55]. In this study, three representative organic solvents were selected for the vapor sensing tests. The interaction between the CPC samples and the vapor analyte has a direct correlation with the polymer chain relaxation and the analyte molecule diffusion, which can be expressed in term of the Flory-Huggins interaction parameter ($\chi_{12}$) [55, 176] as shown in **Eq. 2.8**. A high $\chi_{12}$ value stands for a low solubility between polymer and solvent. The calculated interaction parameters of PC with the tested organic analytes are listed in **Table 4.1.1** They rank as follows: acetone (0.003) < toluene (0.172) < cyclohexane (0.507), showing a decreasing solubility of PC with increasing polarity and hydrogen bonding of the organic solvents.

**Table 4.1.1** Partial vapor pressure $P_i$ [177] and Hansen solubility parameters [59] of PC and different VOCs and their Flory-Huggins interaction parameter with polycarbonate

| Materials | Molar volume ($cm^3 \cdot mol^{-1}$) | $P_i$ (kPa, 25 °C) | $\delta_D$ (MPa)$^{1/2}$ | $\delta_P$ (MPa)$^{1/2}$ | $\delta_H$ (MPa)$^{1/2}$ | $\delta$ (MPa)$^{1/2}$ | $\chi_{12}$ with PC |
|---|---|---|---|---|---|---|---|
| Acetone | 74.0 | 30.6 | 15.5 | 10.4 | 7.0 | 19.9 | 0.003 |
| Toluene | 106.8 | 3.8 | 18.0 | 1.4 | 2.0 | 18.2 | 0.172 |
| Cyclohexane | 108.7 | 13.0 | 16.8 | 0 | 0.2 | 16.80 | 0.507 |
| Polycarbonate | | | 18.1 | 5.9 | 6.9 | 20.2 | |

For the cyclic vapor sensing of CPCs, an acetone concentration ($C$=30.0 %) was chosen, which is approximating to the acetone saturation concentration ($C$=30.6 %). For toluene and cyclohexane, their saturation concentration (3.8 % for toluene and 13.0 % for cyclohexane) was selected. Generally, the stress within polymer composites resulted from processing may relax during first vapor exposure, which is ascribed to the high mobility of polymer chains in the swollen state. Thus, the first exposure can be considered as conditioning and was ignored during discussing even if all cycles are shown in the plots. The sensing behavior is compared based on the sensing curves from the second cycle to the fifth cycle. In order to compare the efficiency of sensing in the regarded cycles, the sensing response was calculated for each cycle $i$ according **Eq. 4.4** and plotted over the cycle number.

$$Response_i = \frac{R_{i,t} - R_{i,0}}{R_{i,0}} \qquad (4.4)$$

where $R_{i,t}$ represents the terminal resistance value at the end of the cycle $i$ and $R_{i,0}$ the starting resistance value of cycle $i$. The average response (second cycle to fifth cycle, mean value and standard deviation) of different CPCs upon exposure to acetone, toluene, and cyclohexane vapor versus $\log(1/\chi_{12})$ is shown in **Fig. 4.1.6**. It can be seen that the response of all CPCs exhibits a positive correlation with the increase of $\log(1/\chi_{12})$, i.e. the highest response is for acetone ($\log(1/\chi_{12})$ =2.44) followed by toluene ($\log(1/\chi_{12})$ =0.74), and the lowest is for cyclohexane ($\log(1/\chi_{12})$ =0.28). Thus, we define these used solvents as good solvent (acetone), moderate solvent (toluene), and poor solvent (cyclohexane).
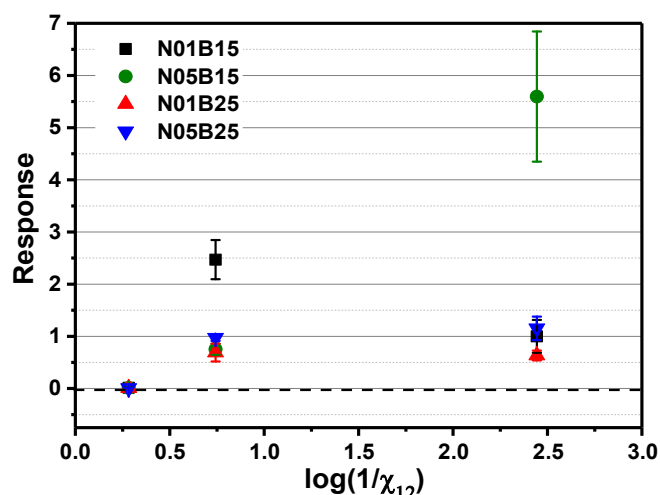
**Fig. 4.1.6** Sensing response of PC/MWCNT/CB composites (mean value and standard deviation of responses in cycles 2-5) vs. the interaction parameter $\log(1/\chi_{12})$ (the $\log(1/\chi_{12})$ for cyclohexane is 0.28, for toluene is 0.74, and for acetone is 2.44).

As expected, cyclohexane vapor has weakest interaction with PC, and the conductive network in all CPCs is nearly unchanged during exposure to cyclohexane. With the increase of $\log(1/\chi_{12})$, toluene as a moderate vapor has stronger interaction with PC and the responses for N01B15 are 2.47 and between 0.7 and 1.0 for the other three composites. It can be assumed that the conductive network density is crucial for the CPC response towards moderate vapor. If the conductive network is mainly constructed by CB, like in N01B15, this CB network can be damaged easily by the polymer swelling due to the low aspect ratio of CB so that a significant response can be observed. For the samples N01B25, N05B15 and N05B25 the filler loadings are much higher than the filler percolation concentration. Thus, the denser conductive networks are more stable under polymer swelling induced by the toluene vapor penetration.

Acetone has the strongest interaction with PC; therefore, all CPCs show higher response values towards acetone vapor as compared to cyclohexane and toluene vapor. The composite N05B15 exhibits the outmost response (*ca.* 5.6), and response values of the other three composites are in the range of 0.6-1.2. Based on the criterion of good, moderate, and bad solvent, the vapor sensing behavior of CPCs towards these three organic vapors was analyzed in detail in cyclic sensing tests.


### 4.1.4.2 Sensing behavior of PC/MWCNT/CB composites towards acetone

Due to the strong interaction between PC and acetone vapor, it is hard to reach the equilibrium state of the $R_{rel}$ when the samples are exposed to acetone vapor. Such behavior

also has been discussed in previous work on PLA based composites, which show strong interaction with dichloromethane [68]. When the PLA/MWCNT composites were exposed to dichloromethane, the samples damaged gradually with time and could not reach the equilibrium state even after long time immersion. Therefore, in our study a controlled immersion and drying time protocol with immersion and drying times of 50 s and 100 s, respectively, was applied to investigate the vapor sensing performance of CPCs.
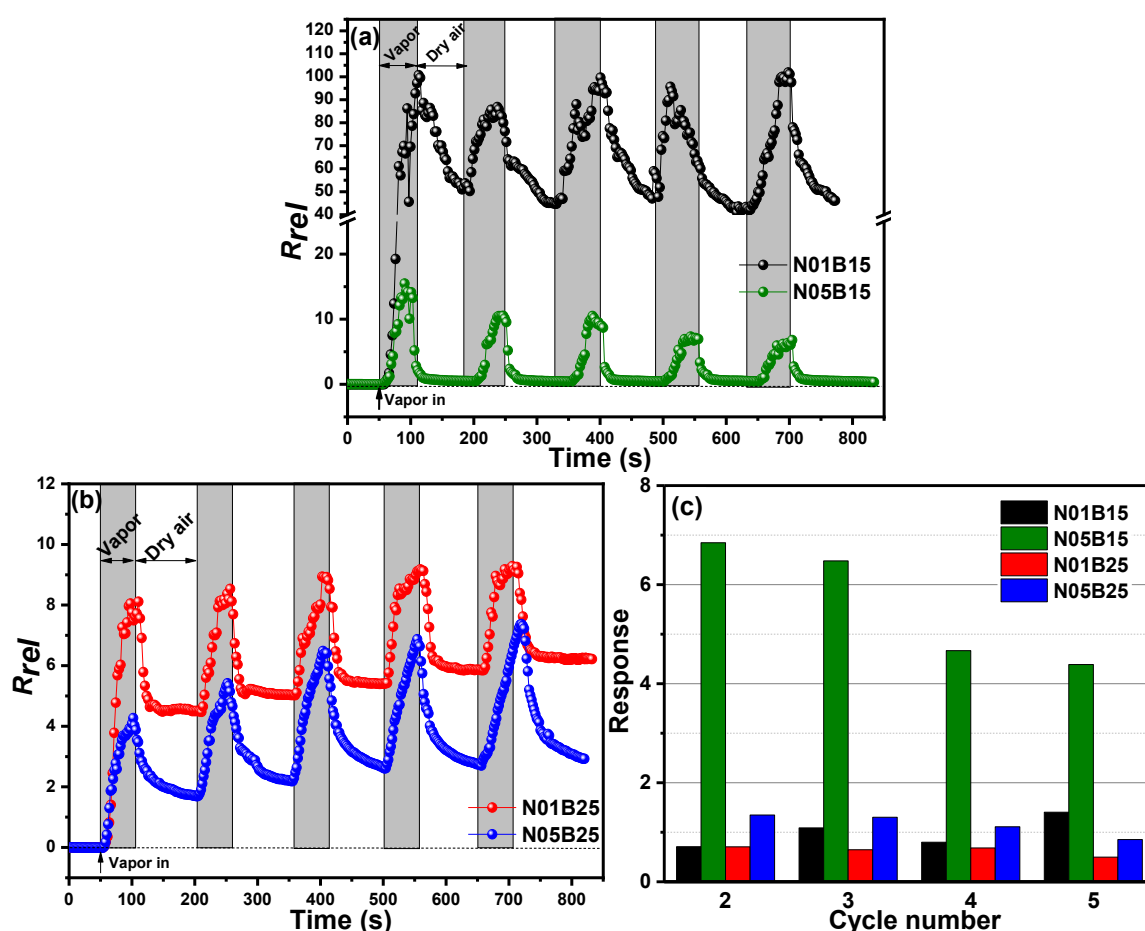


**Fig. 4.1.7** Relative resistance changes ($R_{rel}$) of PC/MWCNT/CB composites towards acetone vapor: (a) comparison of N01B15 and N05B15; (b) comparison of N01B25 and N05B25; (c) sensing responses of different CPCs at consecutive sensing cycles.

**Fig. 4.1.7** shows the electrical resistance response of CPCs exposed to 5 successive immersion-drying runs. The sensing behavior of the two composites with lower CB content N01B15 and N05B15 show an instant sharp increase of $R_{rel}$ immediately after being exposed to acetone (**Fig. 4.1.7a**). In the immersion period of the first sensing cycle, the maximum $R_{rel}$ of N05B15 is only 15.5, while for N01B15, the $R_{rel}$ reaches 100.7 (see **Fig. 4.1.7a**), whereby the values are comparatively more fluctuating. Such strong increase is related to the relatively low density of the percolated network structures at the lower MWCNT loading, which is

reflected in the lowest initial conductivity (see **Fig. 4.1.2**). Thus, the destruction or formation of only few network contacts leads to high relative resistance changes and a more pronounced fluctuation tendency. During the first equilibration cycle of N01B15, the resistance increased from $6.5 \times 10^2$ Ω to $6.7 \times 10^6$ Ω and recovered just to ca $3.3 \times 10^6$ Ω. It increased to $5.7 \times 10^6$ Ω in the second exposure, which is a similar resistance than that obtained in the first cycle. The calculated response values after equilibration were only about 0.7 (**Fig. 4.1.7c**) in the $2^{nd}$ to $5^{th}$ cycle. This behavior indicates that this conductive network reaches a steady state after the equilibration process and does not change much during the following immersion cycles. In other words, after drying the original conductive network is not reconstructed and a less dense network was formed. Acetone molecules occupy during following exposures same sites without causing increased swelling compared to the first one so that at the end of every cycle similar states are reached.

The sample N05B15 exhibits better reproducibility during the first drying, indicating that the conductive network can be easily reconstructed. Related to this better recovery behavior, higher responses are achieved (ca. 6.8-4.3) during the $2^{nd}$ to $5^{th}$ cycle. The sensing behavior of N01B25 and N05B25 exposed to acetone vapor is compared in **Fig. 4.1.7b**. The maximum $R_{rel}$ of the first equilibration cycle of these composites are much smaller than those with 1.5 wt% loading, namely 8.1 for N01B25 and 4.3 for N05B25. When increasing the CB amount from 1.5 wt% to 2.5 wt%, more CB particles take part in the formation of the conductive network (at 0.1 wt% MWCNT) or completing the imperfect conductive paths formed by MWCNTs (at 0.5 wt% MWCNT), thus leading to more perfect conductive networks which are more resistant to the polymer swelling induced by vapor adsorption.

Concerning the recovery behavior of the composites in the drying periods of the cycles, the relative resistance changes of the composites show different behavior. While N05B15 recovers completely during all drying cycles, all other composites show poor recovery especially in the first cycle. In the following cycles the recovery is nearly completed in N01B15, while in N01B25 and N05B25 the starting resistance values increase after the drying period due to the effects discussed above. Such behavior of incomplete recovery was also found by other authors. For example, Liu et al. [141] reported that TPU/reduced graphene oxide composites could hardly go back to their initial state during the drying step when they were exposed towards good solvent vapors. This was ascribed to the strong polymer/vapor interaction which leads to the partially unrecoverable polymer swelling and permanent destruction of conductive networks. Also for the PC composites under investigation here, the complete solvent vapor desorption in the drying processes was not reached.
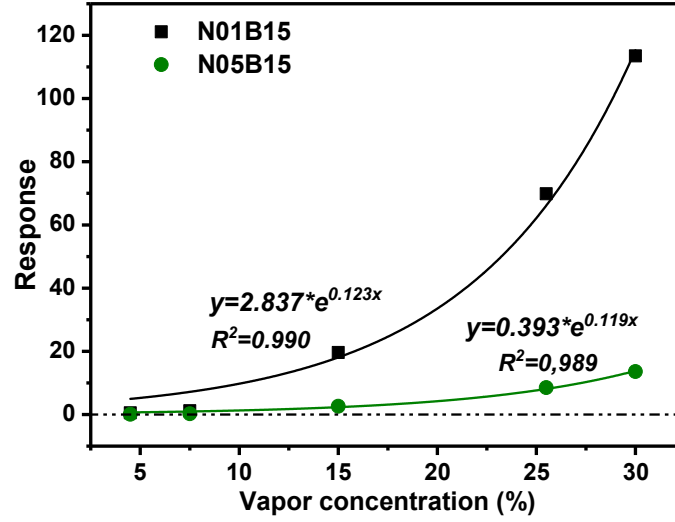
**Fig. 4.1.8** Response of N01B15 and N05B15 to different acetone vapor concentrations.

In the following, the sensing behavior of CPCs towards different acetone vapor concentrations was studied as shown in **Fig. 4.1.8.** Fresh samples were exposed for 50 s to the given vapor concentrations and the responses of N01B15 and N05B15 were determined. The responses increase exponentially with the acetone vapor concentration and N01B15 exhibits higher values than N05B15. The response values can be fitted by an exponential model proposed by Mondal et al. [46] (**Eq. 4.5**):

$$Response = a * e^{bf} \qquad\qquad (4.5)$$

where $a$ and $b$ are constants and $f$ is the vapor concentration. As seen on the fit parameters added in **Fig. 4.1.8** the value of the parameter $b$ is lower at the higher MWCNT content. This clearly points out that N01B15 is more sensitive to the vapor concentration than N05B15.

### 4.1.4.3 Sensing behavior of PC/MWCNT/CB composites towards toluene

**Fig. 4.1.9a** illustrates the vapor sensing behavior of the CPCs with the lower CB content of 1.5 wt% for 5 successive cycles. Both N01B15 and N05B15 exhibit rapid response during exposure to toluene vapor. In the first cycle, the maximum $R_{rel}$ after 50 s immersion for N01B15 and N05B15 are 0.5 and 1.0, respectively (see **Fig. 4.1.9a**). Interestingly, the maximum $R_{rel}$ of N01B15, the sample with the lowest initial conductivity, increases sharply with each cycle and reaches 17.5 in the fifth cycle, which is almost 35 times higher than the response in the first cycle. For N05B15, the $R_{rel}$ values display a lower increase with the sensing cycles, and the ratio of maximum relative resistance change between the fifth and the second cycle is only 2.4. Unlike for the good solvent acetone, the interaction between toluene and the PC matrix is not so strong resulting in lower maximal $R_{rel}$ changes than in acetone.

Once the toluene vapor penetrates the CPCs, whose conductive networks are mainly formed by CB, the conductive networks can be torn easily with the PC swelling. Again, it seems to be very difficult to achieve complete desorption of the solvent vapor in the selected drying period, so that the $R_{rel}$ values increase after each drying process, also enhancing the maximum $R_{rel}$ values in the following immersion cycles. Similarly as discussed above for acetone, the network of N01B15 is more difficult to reconstruct during the toluene vapor evaporation, which leads to a poor repeatability. N05B15 exhibits lower response than N01B15 but the $R_{rel}$ values are more stable and the cycles show better repeatability due to the much more perfect conductive networks constructed by CB and the higher MWCNT content.

**Fig. 4.1.9b** shows the sensing performance of N01B25 and N05B25. The $R_{rel}$ after 50 s immersion also increases with the cycle number. The maximum $R_{rel}$ of N01B25 in the fifth cycle is 3.1, which is much lower than that of N01B15, indicating that the higher content of CB makes the conductive network more stable towards the toluene induced matrix swelling. Another interesting point is the comparison of $R_{rel}$ between N05B15 and N01B25 (see **Fig. 4.1.9a**), both having similar initial volume conductivity values (compare **Fig. 4.1.2**). For N01B25, the conductive network is dominated by CB; while for N05B15, the conductive network is dominated by MWCNTs and CB jointly. It can be seen that the $R_{rel}$ of N01B25 is slightly higher than that of N05B15, manifesting that CB is more easily to loose contact under polymer swelling. Moreover, for N05B15 and N05B25, the even more perfect conductive networks in these composites are less influenced by the toluene stimulation as compared to the networks with 0.1 wt% MWCNTs. Again, the recovery in the drying periods of 100 s in air is incomplete; the $R_{rel}$ values after each cycle steadily increase resulting in increased $R_{rel}$ values also in the following exposure steps. The variations of the response achieved after each immersion cycle are summarized in Fig. **4.1.9c**. It can be seen the responses of N01B15 are in the range of 2.0 to 2.9 for the four regarding cycles, which is higher than those of the three other composites whose responses are all less than 1.0. This indicates that the composite with the lowest density of the conductive network has higher response when being exposed to moderate vapor (toluene).
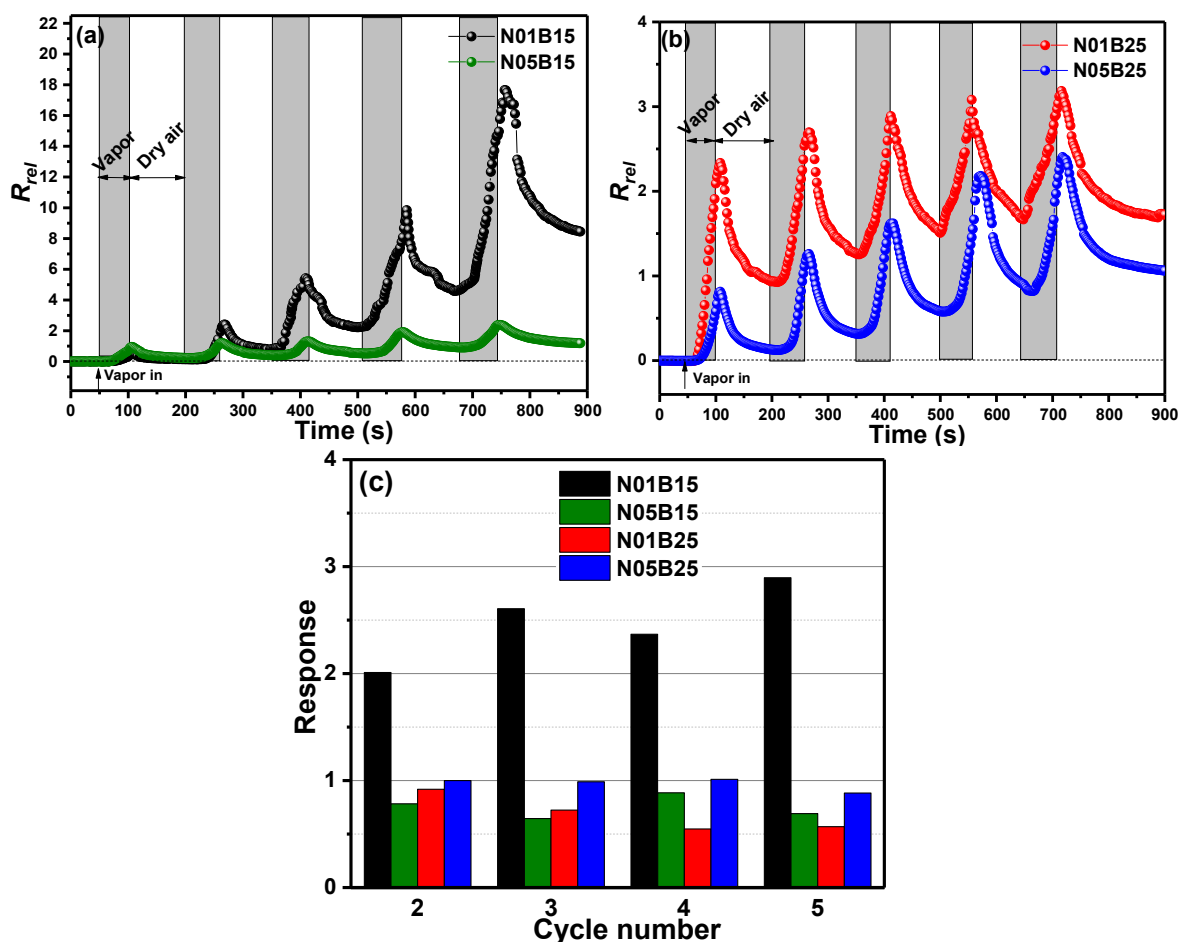
**Fig. 4.1.9** Relative resistance changes ($R_{rel}$) of PC/MWCNT/CB composites towards toluene vapor: (a) comparison of N01B15 and N05B15; (b) comparison of N01B25 and N05B25; (c) sensing responses of different CPCs at consecutive sensing cycles.

### 4.1.4.4 Sensing behavior of PC/MWCNT/CB composites towards cyclohexane

Cyclic sensing behavior of CPCs towards cyclohexane vapor was studied and is shown in **Fig. 4.1.10a**. As expected much lower values of the $R_{rel}$ (maximum 0.018) are observed than for good and moderate solvent vapors (maxima 100 and 18, respectively). As for the other solvent vapors, in every exposure-drying run, the $R_{rel}$ of the CPCs increases when they are exposed to the cyclohexane vapor and decreases when exposed to dry air. During the five successive cycles, the CPCs exhibit the same sensing tendency, whereby the sample N01B15 again shows the highest response. It should be also noticed that the maximum response of the CPCs demonstrates a stepwise decrease with the sensing cycle and that for all samples except N01B15 the values after drying reach negative $R_{rel}$ values. This drift may be assigned to the poor solubility between PC and cyclohexane. In every sensing cycle, the resistance increases with the immersion time, which resulted from the disconnection of conductive networks, however, only a slight polymer swelling can be achieved due to the

weak interaction of PC and cyclohexane. When the samples are taken from cyclohexane atmosphere, the distance of enlarged neighboring fillers come to contact again upon vapor evaporation. The soft swelling improves the particle mobility and may allow their rearrangement to a slightly more perfect conductive network than former sensing cycle. Therefore, the resistances of the composites decrease gradually with each sensing cycle. The response of N01B25 is lower than for N01B15 which is due to the higher CB loading and the resulting higher initial conductivity. **Fig. 4.1.10b** summarizes the responses of all composites during the cyclic sensing in cyclohexane. It can be seen that N01B15 and N05B15 exhibits higher response than the composites with higher CB loadings. In summary, the very low $R_{rel}$ of CPCs towards cyclohexane is mainly caused by the poor interaction between PC and cyclohexane. The responses are very low and the drift with cycle number is comparatively high, so that the selected systems can be regarded as not suitable for sensing of cyclohexane.
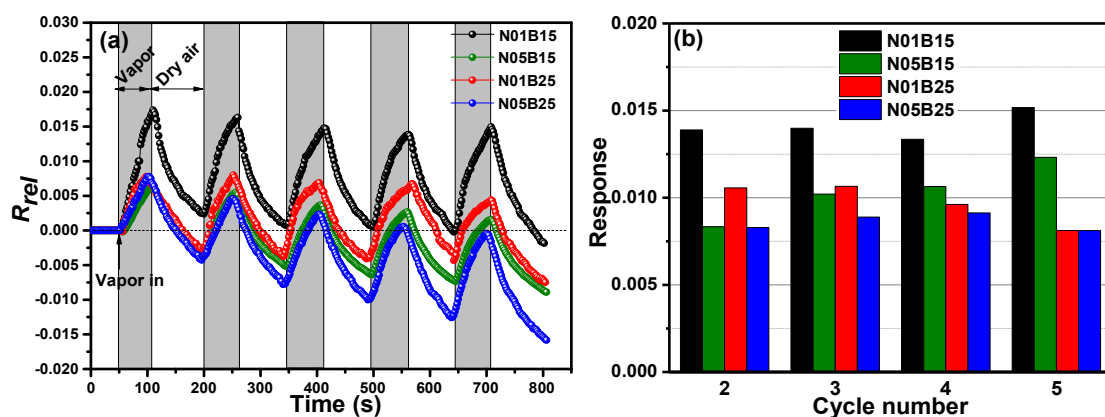


**Fig. 4.1.10** (a) Relative resistance changes ($R_{rel}$) of PC/MWCNT/CB composites towards cyclohexane vapor; (b) sensing responses of different CPCs at consecutive sensing cycles.

### 4.1.5 Summary

In this chapter, the vapor sensing behavior vs. different solvent vapors was studied for melt-mixed PC based nanocomposites containing hybrid fillers of MWCNT and CB. By using such combined fillers a fine-tuning of the structure and conductivity of the filler networks was aimed which was expected to broaden the detectable vapors. On compression molded samples, the percolation thresholds $\varphi_c$ of the fillers were measured to be 0.11 wt% for MWCNTs and 1.38 wt% for CB. Two MWCNT loadings (0.1 wt% and 0.5 wt%) are selected for the nanocomposites, which are lower and higher than $\varphi_{c,MWCNT}$, respectively. Based on this, three CB contents (0.5 wt%, 1.5 wt% and 2.5 wt%) are chosen as second filler to prepare the PC/MWCNT/CB composites. The electrical conductivity measurements implied that at 0.1 wt% MWCNT the conductive networks are mainly formed by the added CB; while for the CPCs

with 0.5 wt% MWCNT, the conductive MWCNT networks are already quite perfect and the addition of CB does not increase the conductivity much.

When being exposed to good vapor acetone, all CPCs exhibit high relative resistance change because of the very strong polymer/vapor interaction. The maximum $R_{rel}$ of first cycle (equilibration cycle) for N01B15 and N05B15 reached 100.7 and 15.5, respectively. However, N01B15 has lower response than N05B15 regarding the following four cycles, which is ascribed to the bad recovery of conductive network formed by CB and MWCNT in N01B15, especially in the first drying cycle. With the increase of CB content to 2.5 wt%, the maximum $R_{rel}$ of the first equilibration cycle are much smaller than those for composites with 1.5 wt% CB loading, namely 8.1 for N01B25 and 4.3 for N05B25. More CB particles take part in forming the conductive network or completing the imperfect conductive network, thus making the perfect network more resistive to the polymer swelling.

In the moderate solvent toluene, all the four CPCs display an increase in $R_{rel}$ with the sensing cycle and the recovery in the drying periods of 100 s in air is incomplete; the $R_{rel}$ values after each cycle steadily increase resulting in increased responses also in the following exposure steps. It can be seen that the responses of N01B15 are in the range of 2.0 to 2.9 for the four regarded cycles, which is higher than those of the three other composites whose responses are all less than 1.0. This indicates that the composites with lowest conductive network density have higher responses when being exposed to moderate toluene vapor.

For cyclohexane, very low $R_{rel}$ for all CPCs were found. The responses of the regarded cycles for N01B15 are higher than those of the other three composites, manifesting again that networks with low density can be changed easier than networks with higher density.

In summary, the network quality could be tuned by the selection of the composition of MWCNT and CB. Among the selected samples, that one with the lowest CB and MWCNT concentration, also showing the lowest starting initial conductivity, namely N01B15, performed best. However, one should consider that very strong interactions between the solvent and the PC matrix, as in the case of acetone, may irreversibly destruct the sample by dissolving parts of the polymer matrix This may be the case in the sample N01B15, having the lowest network density and highest change in $R_{rel}$, and may be related also to the significant non-recovery of $R_{rel}$ in the first drying cycle. Thus, this work provides first results using a suitable concept for designing chemo-resistive sensors by adjusting amount and ratio of mixed carbon nanofillers in melt-mixed polymer composites.

**4.2 Vapor sensing behavior of PC/PS/MWCNT composites with different blend structures[†]**

**4.2.1 Introduction**

Up to now, many polymer based vapor sensors have been investigated, but seldom work has been done on vapor sensors based on conductive polymer blends. In our previous study, we prepared poly(lactic acid)/polypropylene/MWCNT (PLA/PP/MWCNT) composites with different blend ratios [35]. It was found that CPCs with high PLA content displayed a higher $R_{rel}$ to dichloromethane vapor, which is a good solvent to PLA. Similarly, CPCs with high PP content exhibited a higher $R_{rel}$ towards xylene vapor, which is good solvent to PP. In another example, Gao et al. fabricated polyurethane (PU)/polystyrene-*block*-poly(ethylene-*co*-butylene)-*block*-polystyrene (SEBS)/carbon nanofiber mats via electrospinning [163]. Due to the existence of polar PU and non-polar SEBS, the CPC nanofiber mats were sensitive to both polar and non-polar solvent vapors and showed excellent reversibility. Therefore, the use of blend systems is a promising method to extent the detectable vapor analyte range.

In order to study the polymer blend structure on the vapor sensing behavior of CPCs, a suited polymer blend pair should be used. PC and PS are immiscible polymer blend component and they have different affinity to the selected acetone, cyclohexane, toluene, ethyl acetate, and dichloromethane (DCM) vapors. For PS all the selected vapors can be regarded as good solvents, whereas for PC acetone and DCM are good solvents, toluene and ethyl acetate are moderate ones, and cyclohexane is a poor solvent. Therefore, PC/PS blends were selected and the PC/PS/MWCNT composites were fabricated by melt mixing. The melt mixing of the PC/PS/MWCNT blend composites was carried out at 240 °C for 5 min at the screw rotation speed of 250 rpm. The obtained extruded strands were compression molded (240 °C, 20 kN, 5 min). The PC/PS/MWCNT composites with different polymer blend ratios and filler contents are denoted as C*x*S*y*M*z*, where *x*, *y* and *z* represent the weight fraction of PC, PS and MWCNT, respectively. For instance, C50S50M0.75 means that the PC/PS blend ratio is 50/50 wt%), and the MWCNT loading is 0.75 wt%. The MWCNT dispersion and localization in the polymer blends was analyzed by optical microscopy and scanning electron microscopy. The vapor sensing behavior of CPCs was investigated by cyclic exposure to the chosen vapors and dry air. The effects of blend morphology on the vapor sensing performances of CPCs towards different organic vapors are discussed in detail.

---

[†] The results presented in chapter 4.2 are published as "*Organic vapor sensing behavior of polycarbonate/polystyrene/multi-walled carbon nanotube blend composites with different microstructures.*" (***Materials & Design 2019, 107897***) with the co-authors Jürgen Pionteck, Petra Pötschke, and Brigitte Voit.

## 4.2.2 Estimation of MWCNT localization in PC/PS blends from the thermodynamic point of view

The filler localization in polymer blends at equilibrium is determined by the thermodynamic driving force which results from the tendency of interfacial energy minimization to arrange the filler in an energetically preferred polymer component. The wetting coefficient $\omega_a$ is used for predicting the thermodynamic preference of the MWCNTs in PC/PS blend. As the surfaces energy of the components should be used at melt processing temperature (240 °C), they were deduced from values at 20 °C using the relations $-\frac{d\gamma}{dT} = K_T$ and $-\frac{dXp}{dT} = 0$. Here $K_T$ is the temperature coefficient and $X_p$ represents the polarity of the components ($\gamma_i^p/\gamma_i$). The calculated surface energy of PC, PS, and MWCNTs at 20 °C and 240 °C are given in **Table 4.2.1**. For the surface energy parameters of MWCNTs, two sets of data reported by Nuriel et al. [178] and Barber et al. [179] using different nanotubes and measuring techniques were applied.

**Table 4.2.1** Surface energy parameters of PC, PS, and MWCNT at 20 °C and 240 °C

| Material | 20 °C | | | 240 °C | | | Temp. coefficient | Citation |
|---|---|---|---|---|---|---|---|---|
| | $\gamma$ (mJ/m$^2$) | $\gamma^d$ (mJ/m$^2$) | $\gamma^p$ (mJ/m$^2$) | $\gamma$ (mJ/m$^2$) | $\gamma^d$ (mJ/m$^2$) | $\gamma^p$ (mJ/m$^2$) | | |
| MWCNT | 45.3 | 18.4 | 26.9 | 45.3 | 18.4 | 26.9 | - | [178] |
| MWCNT | 27.8 | 17.6 | 10.2 | 27.8 | 17.6 | 10.2 | - | [179] |
| PS | 40.7 | 34.5 | 6.1 | 24.9 | 21.1 | 3.8 | -0.072 | [180] |
| PC | 34.2 | 27.7 | 6.5 | 24.0 | 19.4 | 4.6 | -0.04 | [181] |

After obtaining the surface energy values of the polymer components at 240 °C, the wetting coefficient calculated by the Harmonic-mean and Geometric-mean equations were calculated according to **Eq.2.2-2.4** (see **Page 30**) mentioned above and listed in **Table 4.2.2** and **Table 4.2.3**.

**Table 4.2.2** Calculated interfacial energies $\gamma$ of composites and blends using Harmonic and Geometric mean equations

| Materials | $\gamma$ (mJ/m$^2$) | $\gamma$ (mJ/m$^2$) | Source of surface energy values for CNTs |
|---|---|---|---|
| | Harmonic-mean equation | Geometric-mean equation | |
| PC/MWCNT | 15.53 | 9.04 | |
| PS/MWCNT | 17.57 | 10.57 | [178] |
| PC/PS | 0.12 | 0.06 | |
| PC/MWCNT | 2.18 | 1.12 | |
| PS/MWCNT | 3.24 | 1.71 | [179] |
| PC/PS | 0.12 | 0.06 | |

**Table 4.2.3** Calculated wetting coefficients $\omega_a$ using interfacial energies from Table 4.2.2

| Composites | $\omega_a$ Harmonic-mean equation | $\omega_a$ Geometric-mean equation | Source of surface energy values for CNTs |
|---|---|---|---|
| PC/PS/MWCNT | -17.0 | -25.5 | [178] |
| PC/PS/MWCNT | -8.83 | -9.83 | [179] |

According to the $\omega_a$ values calculated in **Table 4.2.2** and **4.2.3**, it can be predicted that MWCNT are preferentially localized within the PC component during melt mixing.

## 4.2.3 Electrical and morphological properties of PC/PS/MWCNT composites

To illustrate the electrical properties of PC/PS/MWCNT composites with different blend ratios, the percolation behavior of the CPCs was investigated. **Fig. 4.2.1** demonstrates the volume conductivity of PC/PS/MWCNT composites as a function of MWCNT content. For C70S30 (**Fig. 4.2.1a**), there is a sharp conductivity increase by 10 orders of magnitudes when the MWCNT loading increases from 0.25 wt% to 0.5 wt% (corresponding to 0.14 vol. % to 0.29 vol. %), which indicates the formation of conductive networks. CPC with the blend ratio of C60S40 (**Fig. 4.2.1b**) and C50S50 (**Fig. 4.2.1c**) exhibits electrical percolation at much lower MWCNT contents as compared to C70S30M$z$ composites. The fitted $\varphi_c$ of C70S30M$z$ using **Eq.2.1** is 0.30 vol. %. With the increase of PS content in the blend, the $\varphi_c$ decreases to 0.15 vol. % for C60S40M$z$ and 0.13 vol. % for C50S50M$z$ composites. At 0.75 wt% MWCNTs (approx. 0.43 vol. %), the content used for the following sensing tests, the electrical conductivity values are $6.5 \times 10^{-4}$ S·cm$^{-1}$ for C70S30, $5.9 \times 10^{-4}$ S·cm$^{-1}$ for C60S40, and $1.2 \times 10^{-4}$ S·cm$^{-1}$ for C50S50M. This indicates that although the C70S30 based sample is closer to the corresponding percolation threshold it has the highest conductivity value compared to the other two samples. The highest conductivity despite the lowest MWCNT content related to the PC (0.75 wt. % MWCNTs in 70 wt. % PC) part can be explained by the blend composite morphology as discussed later.
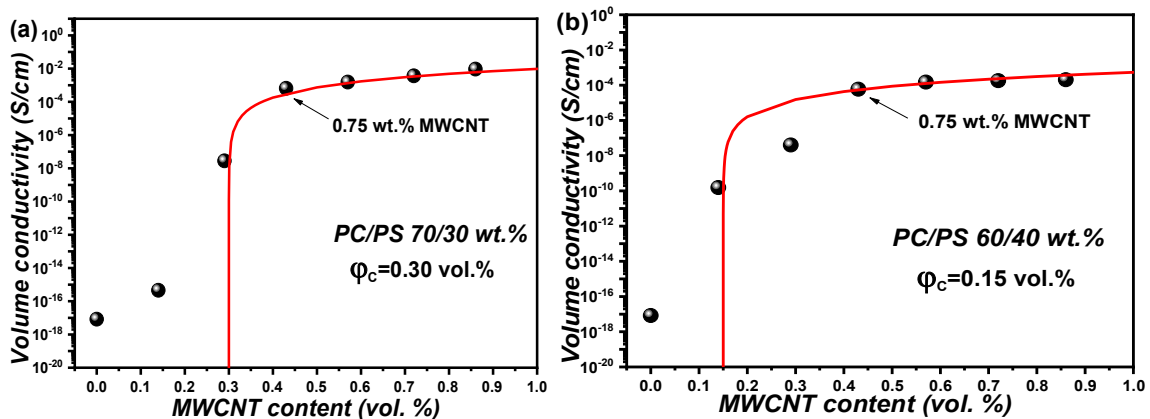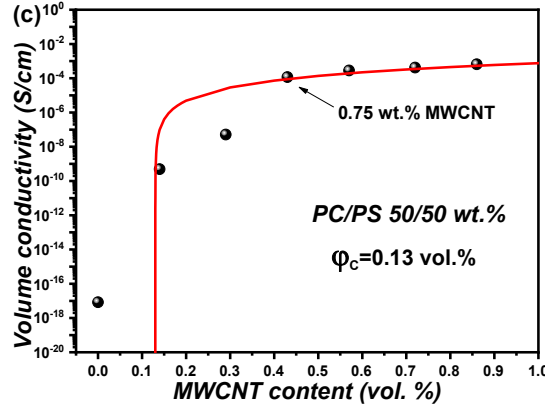
**Fig. 4.2.1** Electrical conductivity as a function of MWCNT content for PC/PS/MWCNT composites with different PC/PS blend ratios: (a) 70/30 wt%, (b) 60/40 wt%, and (c) 50/50 wt%.

Optical micrographs of blend composite thin sections with 0.75 wt% MWCNT are shown in **Fig. 4.2.2.** The MWCNT agglomerate area $A_{Agg}$ increases with rising PS content in the blends. For example, the $A_{Agg}$ of C70S30M0.75 is 0.65 %, while the values for C60S40M0.75 and C50S50M0.75 are 1.56 % and 2.19 %, respectively. These are 2.4 and 3.4 times greater than the value of C70S30M0.75, respectively. It can be deduced that MWCNTs have a better dispersion in PC/PS blend with high PC content, in which the relative filler content in the PC component is lower because of the filler selectivity. Regarding the CPCs with co-continuous structure (see below), the MWCNT content in the PC component is relatively higher than that of C70S30M0.75 due to the reduced PC content in blends. Therefore, there are larger MWCNT agglomerates in composites because of overloading in the PC component.
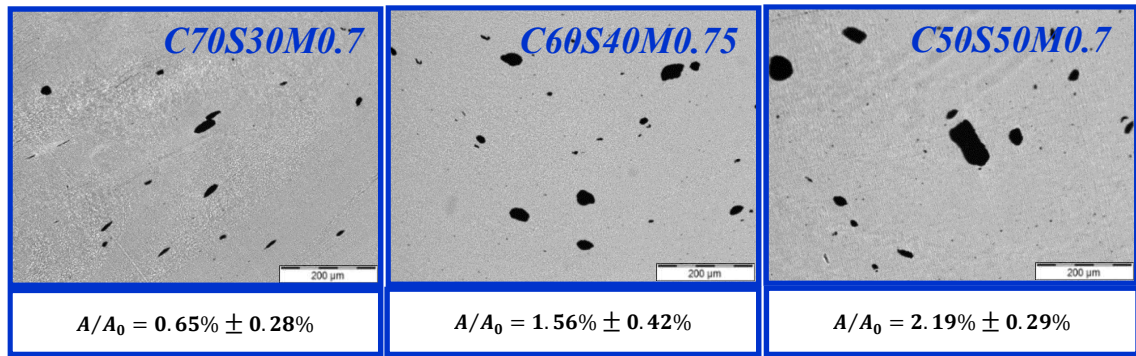


**Fig. 4.2.2** Optical micrographs of the blend composites with 0.75 wt% MWCNT illustrating the different dispersion states of MWCNT in polymer blends.

**Fig. 4.2.3** presents the SEM micrographs of PC/PS/MWCNT-0.75 wt% strand cross-sections. The cut surface of the strands was immersed in cyclohexane to extract PS component. For C70S30M0.75, it can be observed that the PS component, which appears as holes after extraction, forms some spherical particles embedded in the PC matrix, which is

73

characteristic for a sea-island structure (**Fig. 4.2.3a-c**). At higher magnification (**Fig. 4.2.3c**), it is found that MWCNTs are dispersed in the PC matrix, which is in accordance with the thermodynamic prediction. For C60S40M0.75 (**Fig. 4.2.3d**), the composite morphology is quite different from that of C70S30M0.75. The elongated PS structures have started to connect with each other and form a continuous structure [27]. PC is still the major component in C60S40M0.75; however, PS is already seen to be thoroughgoing in these cuts. In the high magnification micrographs of C60S40M0.75 (**Fig. 4.2.3e and 4.2.3f**), it can be seen that some isolated MWCNTs laying on the surface of the PC component remain after the etching process. In C50S50M0.75 (**Fig. 4.2.3g-i**), the co-continuity is further evolved. The remained PC component is finer and the co-continuous structure is clearly seen (see **Fig. 4.2.3g**). The co-continuous structure together with the selective localization of the MWCNTs within PC and the attainment of percolation in the PC component represents double percolation in the CPCs and is the reason for the observed significantly lower $\varphi_c$ as compared to C70S30 blends. Interestingly, MWCNTs are not only found in the cross-section of the remaining PC component but also seen at the interfaces of the PC/PS blend. This indicates that most of the MWCNTs were localized in the PC component, but there are also some MWCNTs expelled to the interfaces of PC/PS blend or PS component because of the relative low PC content in C50S50M0.75 composites.
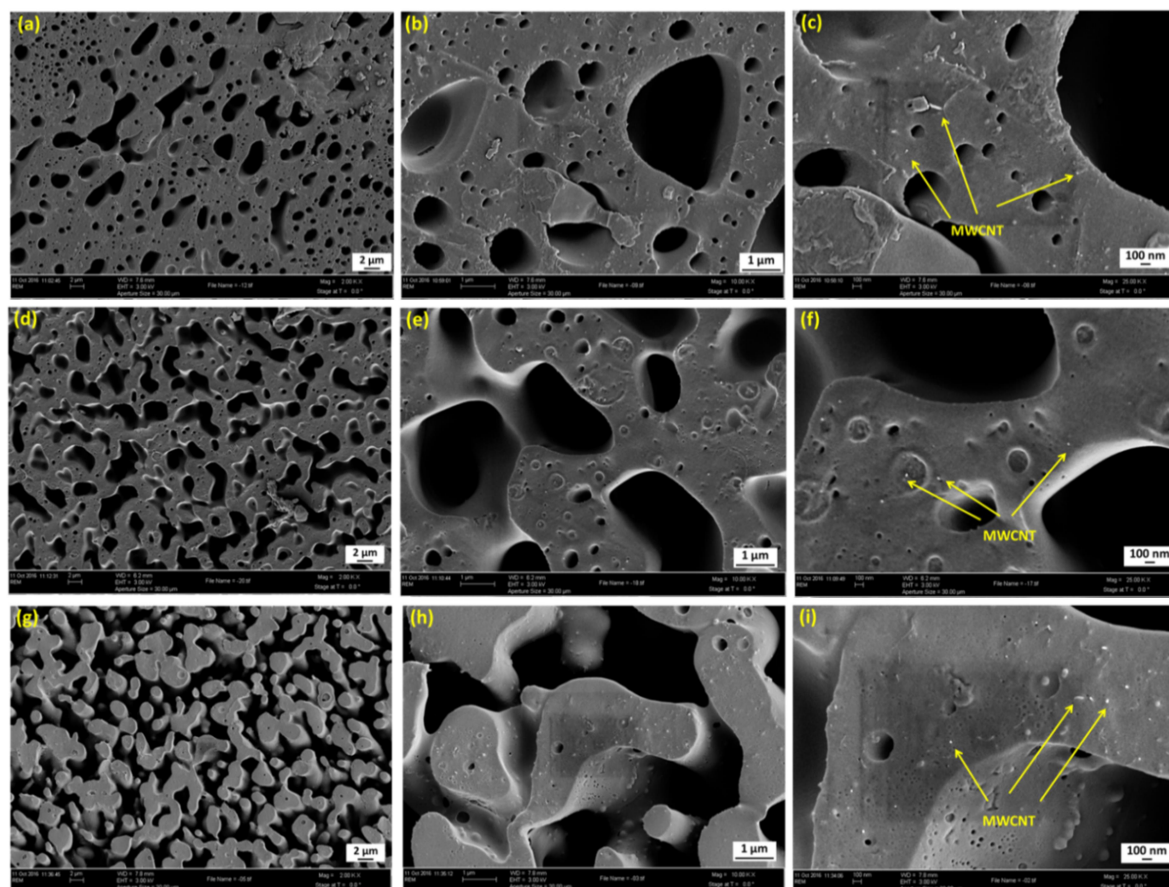
**Fig. 3** SEM images of the PC/PS/MWCNTs composites containing 0.75 wt% MWCNT. (a), (c) and (e) are C70S30M0.75, C60S40M0.75 and C50S50M0.75, respectively. (b), (d) and (f) are high magnifications of partial enlarged images corresponding to the three composites, respectively.

To further investigate the blend structure of CPCs, solvent extraction using cyclohexane (dissolving PS) was performed. **Fig. 4.2.4** shows the weight loss of the CPCs with 0.75 wt% MWCNT caused by the PS extraction. About 5 wt% of C70S30M0.75 is extracted, which is far lower than the actual PS content of 30 wt% in the blend. Due to the isolated spherical PS domains in the PC matrix, the PS imbedded within the sample is only partially accessible to cyclohexane. For C60S40M0.75, the extracted part increases to 25 wt%, which is still lower than the actual PS content in the blend (40 wt%). 40 wt% PS was extracted for C50S50M0.75, which is only slightly lower than the actual content in the blend (50 wt%) and illustrates a nearly perfect co-continuous structure. The inset photos in **Fig. 4.2.4** show the cyclohexane solvent after extraction. The solvent becomes more turbid with increasing PS content in the blends. Furthermore, the relatively dark extracted solution of C50S50M0.75 shows that obviously some MWCNTs were extracted as well. In this blend, the PC-related MWCNT content is highest (1.5 wt%) and the MWCNT agglomerates are the largest. This suggests that some MWCNTs may be located in the PS component or near the interface and caused by the filler saturation in the PC component. The excess MWCNTs are expelled to the PS component.
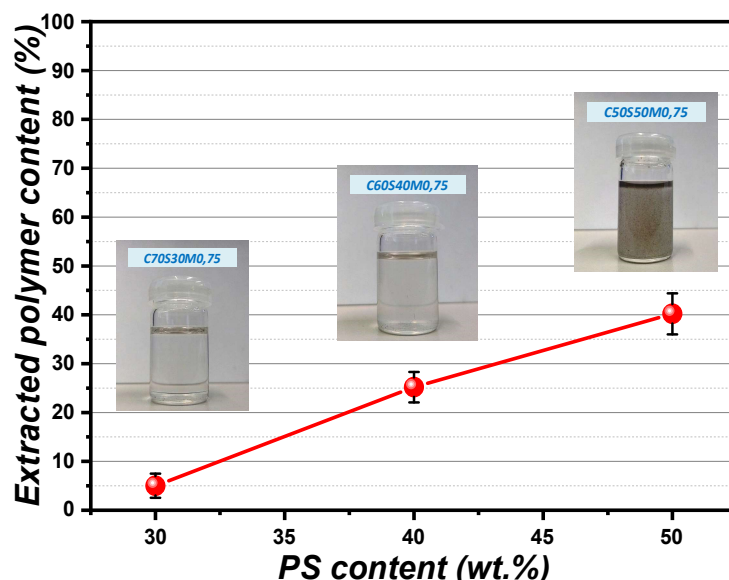


**Fig. 4.2.4** Extracted part for PC/PS/MWCNT-0.75 wt% with different blend ratios, inset graphs are the cyclohexane solutions after extraction.

### 4.2.4 Rheological characterization of PC/PS/MWCNT composites

The melt rheological behavior of conductive polymer blend composites is sensitive to their inner microstructure. The storage modulus ($G'$) is a sensitive measure of the microstructure in the melt state, especially at the low frequency regime where time does not limit molecular relaxation processes. Higher $G'$ values at low frequencies relate to a more elastic structure where molecular motion is inhibited by structural features in immiscible polymer blends and filler network formation in nanocomposites [27, 182, 183]. In filled polymer blends both effects may be overlapped, which makes an unambiguous discussion difficult. [184]. To better understand the rheological behavior of conductive polymer blend composites, the effect of increasing amount of MWCNTs in the PC/PS blends (70/30 wt% and 50/50 wt%) was investigated at 240 ºC. Liebscher et al. found that a co-continuous structure leads to higher $G'$ at low frequency than the sea-island structure for PA6/SAN blends [183]. **Fig. 4.2.5a** shows the $G'$ of PC/PS/MWCNT composites (70/30 wt%) with different MWCNT loadings as a function of angular frequency ($\omega$). A significant increase of $G'$ at low frequency can be observed when the MWCNT content increases from 0 to 0.5 wt%. The occurrence of the low frequency plateau indicates the formation of interconnected networks formed by nanotubes or by nanotubes together with polymer chains in the composite and is referred to as rheological percolation threshold [185]. This rheological percolation is in agreement with the above-mentioned electrical percolation threshold of 0.29 vol% (ca. 0.50 wt%). PC/PS/MWCNT composites (50/50 wt%) have a similar tendency of $G'$ increase when compared to PC/PS/MWCNT (70/30 wt%) composites (see **Fig. 4.2.5b**), even if the unfilled blends start at a lower level due to the increased content of the lower viscous blend component PS.
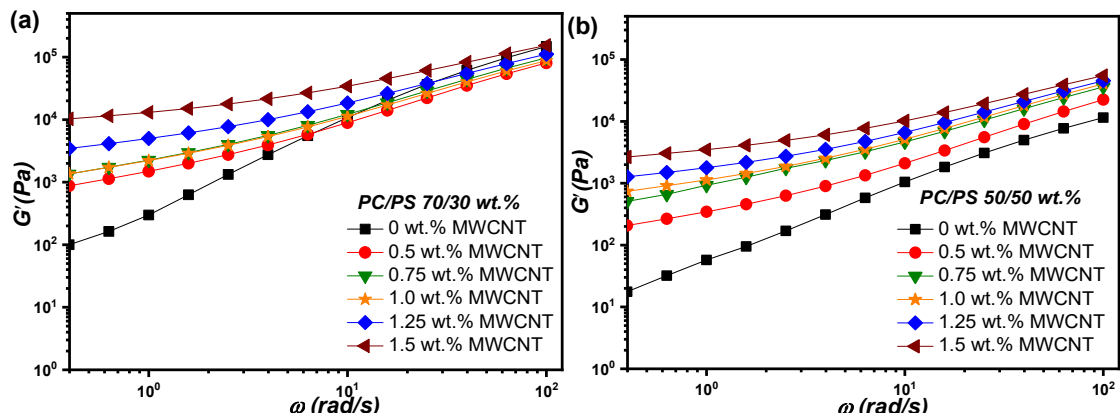


**Fig. 4.2.5** Storage modulus ($G'$) as a function of frequency ($\omega$) for (a) PC/PS 70/30 and (b) PC/PS 50/50 with varied MWCNT content.

**Fig.4.2.6a** shows the $G'$ of neat PC and PS as a function of $\omega$. The $G'$ of neat PC is slightly higher than that of PS at low frequencies, so the increase of PS content in polymer blend will also reduce the $G'$ of CPCs. **Fig. 4.2.6b** presents $G'$ of PC/PS blends with different polymer blend ratios containing 0.75 wt% MWCNT, the content for the following sensing study, as function of $\omega$. It can be seen that in the low frequency region the $G'$ of C70S30M0.75 is the highest. However no difference is found between C60S40M0.75 and C50S50M0.75, despite the higher content of the component with the lower melt viscosity in C50S50M0.75. This could be either due to the better developed co-continuous blend morphology or by improved dispersion when increasing the PS content.
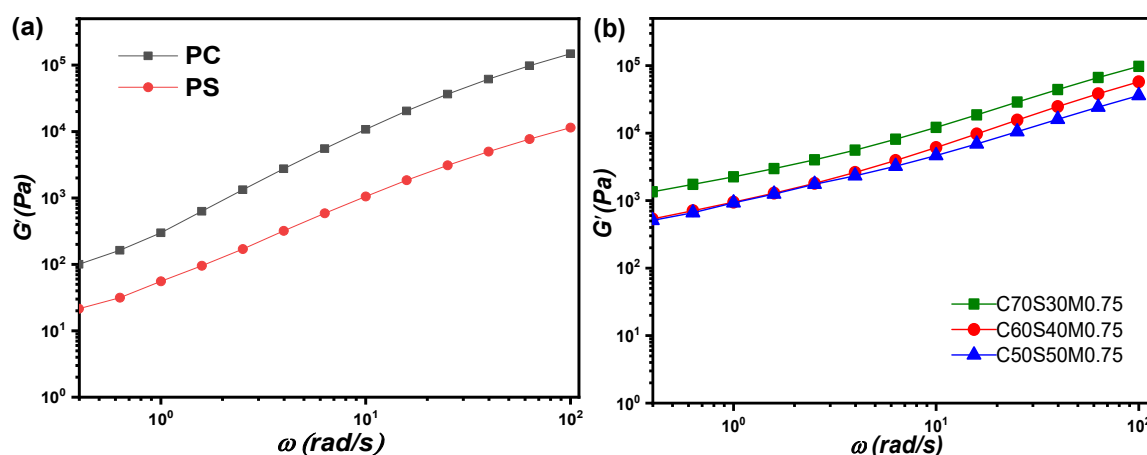


**Fig. 4.2.6** Storage modulus ($G'$) as a function of frequency ($\omega$) for (a) neat PC and PS and (b) PC/PS/MWCNT-0.75 wt% composites with different blend ratios.

### 4.2.5 Vapor sensing behavior of PC/PS/MWCNT blend composites

As reported, the vapor sensor behavior of CPCs is influenced by the filler loading, polymer-vapor interaction, and filler dimensionality [140, 142, 168]. However, the effect of composite microstructure on the vapor sensing behavior has not yet been investigated in detail. In this study, five organic solvents namely acetone, ethyl acetate, DCM, toluene, and cyclohexane were chosen (see **Table 4.2.4**). The composites C70S30M0.75, C60S40M0.75, and C50S50M0.75 were selected for the vapor sensing studies because their initial resistances and those at solvent vapor exposition were below the upper resistance limit (200 MΩ) of the electrometer used. The calculated $\chi_{12}$ values between polymers and organic vapors are listed in **Table 4.2.4**. According to the definition of polymer-vapor interaction proposed by Hansen et al. [59], $\chi_{12} < 0.5$ is considered to be a strong polymer-vapor interaction. Thus, it can be concluded from **Table 4.2.4** that acetone and DCM are good solvents for PC, while ethyl acetate and toluene should cause moderate swelling of PC. Cyclohexane poorly interacts with

PC due to their large $\chi_{12}$ value. In terms of PS, the small $\chi_{12}$ values give cause to suspect that all the selected vapors have good interaction with the PS component.

**Table 4.2.4** Molar volume ($V_{mol}$), saturated partial pressure ($P_i$), solubility parameters ($\delta$), and Flory-Huggins interaction parameters ($\chi_{12}$) of polymers and organic solvents at 25 °C [59]

| Materials | $V_{mol}$ (cm³·mol⁻¹) | $P_i$ (kPa, 25°C) | $\delta_D$ (MPa)$^{1/2}$ | $\delta_P$ (MPa)$^{1/2}$ | $\delta_H$ (MPa)$^{1/2}$ | $\delta$ (MPa)$^{1/2}$ | $\chi_{12}$ PC | $\chi_{12}$ PS |
|---|---|---|---|---|---|---|---|---|
| Acetone | 74 | 30.6 | 15.5 | 10.4 | 7.0 | 19.9 | 0.003 | 0.011 |
| Ethyl acetate | 98.5 | 12.6 | 15.8 | 5.3 | 7.2 | 18.2 | 0.159 | 0.048 |
| DCM | 67.8 | 53.0 | 18.2 | 6.3 | 6.1 | 20.2 | 0.0003 | 0.022 |
| Toluene | 106.8 | 3.8 | 18.0 | 1.4 | 2.0 | 18.2 | 0.172 | 0.052 |
| Cyclohexane | 130.6 | 13.0 | 16.8 | 0 | 0.2 | 16.8 | 0.507 | 0.274 |
| Polycarbonate | | | 18.1 | 5.9 | 6.9 | 20.3 | - | - |
| Polystyrene | | | 18.5 | 4.5 | 2.9 | 19.3 | - | - |

In the beginning of vapor sensing measurement, the samples were immersed in dry air for 50 s to get a stable initial resistance value before exposing them to the organic vapors. Then the samples were exposed to four successive cycles of alternating vapor and dry air. **Fig. 4.2.7a** shows the $R_{rel}$ of PC/PS/MWCNT blend composites towards saturated ethyl acetate vapor. When comparing the cyclic sensing curves of the CPCs, it can be observed that C70S30M0.75 has a higher $R_{rel}$ than those of C60S40M0.75 and C50S50M0.75 composites. For C70S30M0.75 there is a significant $R_{rel}$ increase when the sample is exposed to ethyl acetate vapor and the final $R_{rel}$ of the first cycle after 100 s exposure is approximately 1100 %. Afterwards, during the drying phase the $R_{rel}$ decreases rapidly and reaches a plateau. However, the final $R_{rel}$ value after the first drying is 300 %, which cannot recover to the initial state, indicating that the conductive network of CPCs is damaged and cannot be fully reconstructed. For C60S40M0.75 and C50S50M0.75 the maximum $R_{rel}$ after the first exposure is only 175 % and 100 %, respectively. However, these samples show a good reversibility and the $R_{rel}$ values returned to their initial states after the drying time. When comparing with the maximum $R_{rel}$ of each cycle for C70S30M0.75, it can be seen that the values are between 1100 % and 1300 %, which shows that the conductive network in C70S30M0.75 is highly susceptible to polymer swellings when exposed to ethyl acetate vapor. For C60S40M0.75, its maximum $R_{rel}$ shows a significant increase from 150 % (first cycle) to of 325 % (fourth cycle), and a similar trend is seen for C50S50M0.75, whose $R_{rel}$ is in the range of 100% to 220% during these consecutive cycles. The big difference of sensing behavior of these three CPCs is attributed to the blend microstructure. The co-continuous structure with larger interfaces facilitates vapor evaporation from the blend matrix [68], which leads to better reversibility compared to the blend composite with sea-island structure.

**Fig. 4.2.7b** shows the cyclic vapor sensing behavior of CPCs towards saturated toluene. Although toluene and ethyl acetate have similar $\chi_{12}$ values to PC, the CPCs show a much lower $R_{rel}$ compared to toluene than compared to ethyl acetate. For C70S30M0.75 the maximum $R_{rel}$ in the first immersion step reaches 125 %, followed by an $R_{rel}$ decrease to about 70 % during drying. Based on the results of the C70S30M0.75 cyclic scan curve, the conductive network is gradually damaged with the sensing cycles resulting in poor reversibility. In comparison, the maximum $R_{rel}$ of C60S40M0.75 and C50S50M0.75 show a decreasing tendency with the sensing cycle. First, the maximum $R_{rel}$ of both samples is 60 %, in the fourth cycle the $R_{rel}$ of C60S40M0.75 is only 52 %, while in C50S50M0.75 it is only 35 %. This shows that the toluene vapor penetration makes the conductive network especially of C50S50M0.75 more perfect during the sensor test and thus less sensitive to further cycles. In summary, it can be said that the blend structure of the CPCs plays an important role in vapor sensor technology of moderate organic vapors such as ethyl acetate and toluene. CPCs with co-continuous structures have a lower $R_{rel}$ due to the following reasons: because of the selective localization of the CNTs in PC, the lower PC content in the composite leads to a higher local MWCNT concentration and thus denser conductive network in this component compared to CPCs with higher PC loading and the same MWCNT content. Furthermore, the co-continuous structure has larger interfaces that can increase vapor penetration and evaporation during sensor testing.

In general, the strong interaction between a polymer and its good solvents results in strong polymer swelling and complete damage to the conductive network. Therefore, CPCs in saturated good solvent vapors always exhibit poor reversibility as the conductive network is irreversibly damaged. For this reason, the vapor concentration of dichloromethane, a good solvent to PC, was reduced to 23.5 % (saturation concentration 52.3 %) by adjusting the mass flow controllers. **Fig. 4.2.7c** shows the cyclic vapor sensing behavior of CPCs towards DCM vapor. Although it is an unsaturated DCM vapor, each CPC shows a conditioning effect in the first cycle due to the strong interaction between PC and DCM vapor. Starting with the second cycle, C70S30M0.75 and C60S40M0.75 have a gradually increased maximum $R_{rel}$ with the sensing cycle. The gradually increasing $R_{rel}$ after each immersion and drying cycle is attributed to two reasons: 1) The irreversible damage to the conductive network in contact with the good vapor DCM; 2) The difficulty of good vapor evaporation. For C50S50M0.75, $R_{rel}$ and its changes with the cycles have the lowest values. It can therefore be assumed that C50S50M0.75 has the densest conductive network, which is rather stable under polymer swelling. In addition, the poor reversibility of CPCs to dichloromethane is due to the strong

polymer-vapor interaction, which hampers the drying process. In general, the stresses generated within the polymer composite during the melt shaping process can relax during the first vapor load due to the increased mobility of the polymer chains in the swollen state. Thus, the first exposure is considered as conditioning cycle and the following cycles should be regarded for evaluation of the sensing behavior. In order to compare the efficiency of sensing, the mean $R_{rel}$ of the regarded cycles (second cycle to fourth cycle) of CPCs towards ethyl acetate, toluene, and DCM vapors are plotted and shown in **Fig. 4.2.7d**. In this plot, $R_{rel}$ is calculated based on the initial resistance of each cycle and the error bars indicate the standard deviation of the three regarded cycles. The mean $R_{rel}$ values of the CPCs for these considered cycles are mainly related to the polymer interaction. CPC sensors have a higher $R_{rel}$ in saturated ethyl acetate vapor than saturated toluene vapor, which corresponds to the polymer-vapor interaction ranking given in **Table 4.2.4**. In addition, the diluted DCM vapor induces a lower $R_{rel}$, although it exhibits a very strong interaction with the PC. When comparing the $R_{rel}$ of CPCs with different blend ratio, C70S30M0.75 composites always have the highest $R_{rel}$, followed by C60S40M0.75 and C50S50M0.75, where the difference of the mean $R_{rel}$ is less pronounced. The reason for this is that the diluted DCM vapor can diffuse and evaporate easier in the co-continuous structure as compared to that of sea-island structure.
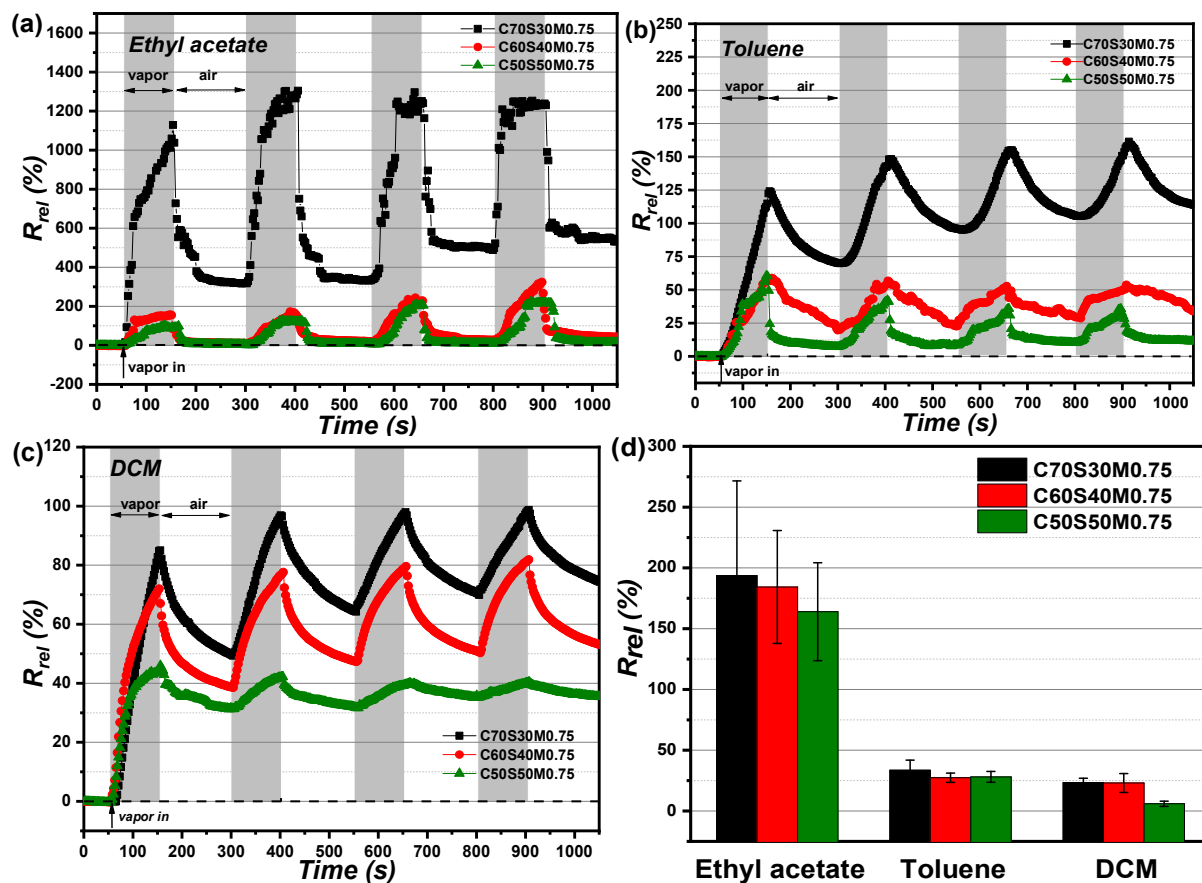
**Fig. 4.2.7** Cyclic sensing behavior of PC/PS/MWCNT composites with different blend ratios towards (a) ethyl acetate, (b) toluene, (c) diluted DCM vapor (23.5 % vapor concentration). (d) Mean values of relative resistance change for CPCs from second cycle to fourth cycle towards different vapors. $R_{rel}$ is calculated based on the initial resistance value before each cycle, error bars show the standard deviation of the three regarded cycles.

To investigate the sensitivity of CPCs towards organic vapors, **Fig. 4.2.8** illustrates $R_{rel}$ values of CPCs at different acetone vapor concentrations. Acetone is a good solvent for both PC and PS (see **Table 4.2.4**). In this study an exponential model given in [46] is used to describe the sensor response vs. vapor concentration ( **Eq.4 5**)

$$R_{rel} = a * e^{bx} \tag{4.5}$$

where *a* and *b* are constants and *x* is the vapor concentration. **Fig. 4.2.8** confirms such exponential relationship of the sensor response ($R_{rel}$ values are taken after 100 s immersion in the first cycle) with the vapor concentration. When the vapor concentration is below 15%, all three kinds CPCs have almost the same low $R_{rel}$ and the $R_{rel}$ increases only slightly with the increase of acetone vapor concentration. When the vapor concentration is 18.5%, the $R_{rel}$ of CPCs is several times higher than at lower vapor concentrations. In particular, C70S30M0.75 shows the highest $R_{rel}$ at 18.5 % acetone vapor concentration compared to the other concentrations, even if this sample has the highest initial conductivity, indicating the best network quality. However, with this blend composition, the selected 0.75 wt% MWCNT loading is closer to the corresponding percolation threshold than with the other blend compositions, leading to the expectation of higher sensitivity. In summary, the blend structure in which MWCNTs are dispersed in good quality in the matrix component of the sea-island structure allows better accessibility to vapors and thus reacts more sensitively to the stimulation by higher concentration of good organic solvent vapors.
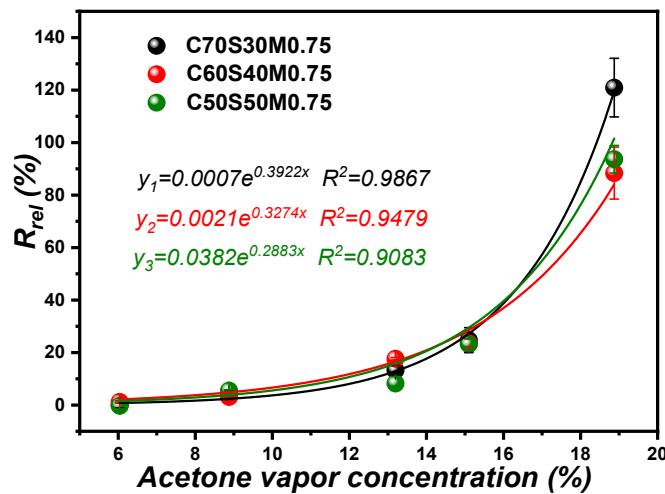


**Fig. 4.2.8** Relative resistance changes for different composites under dynamic flow conditions. The lines are drawn by the exponential fitting model $y = a * e^{bx}$.

**Fig. 4.2.9a** demonstrates the sensing performance of CPCs for the long-term exposure towards saturated cyclohexane vapor. As discussed above, cyclohexane is a poor solvent for PC and a good solvent for PS. All three CPCs reach an equilibrium state after the long-term immersion (500 s) in cyclohexane vapor, however, the $R_{rel}$ are very low due to the weak interaction between PC and cyclohexane. For C70S30M0.75, its equilibrium $R_{rel}$ is only 1%, and the $R_{rel}$ of C60S40M0.75 and C50S50M0.75 are ca. 3% and 5%, respectively. This is related to the sorption-desorption behavior of CPCs with different microstructures. For C70S30M0.75, the conductive network variations are mainly resulted from the cyclohexane penetration into PC that causes the only mild swelling of PC. In case of the co-continuous C50S50M0.75 composite, cyclohexane can penetrate into the PC and PS phase simultaneously. From the point of view of MWCNT localization, it has been proved by the morphological micrographs and extraction results that in this composite some MWCNTs are localized in the PS component. Therefore, the conductive network change in the PS component induced by cyclohexane in C50S50M0.75 is more pronounced, leading to a higher $R_{rel}$ as compared to other CPCs when they were exposed to cyclohexane vapor.
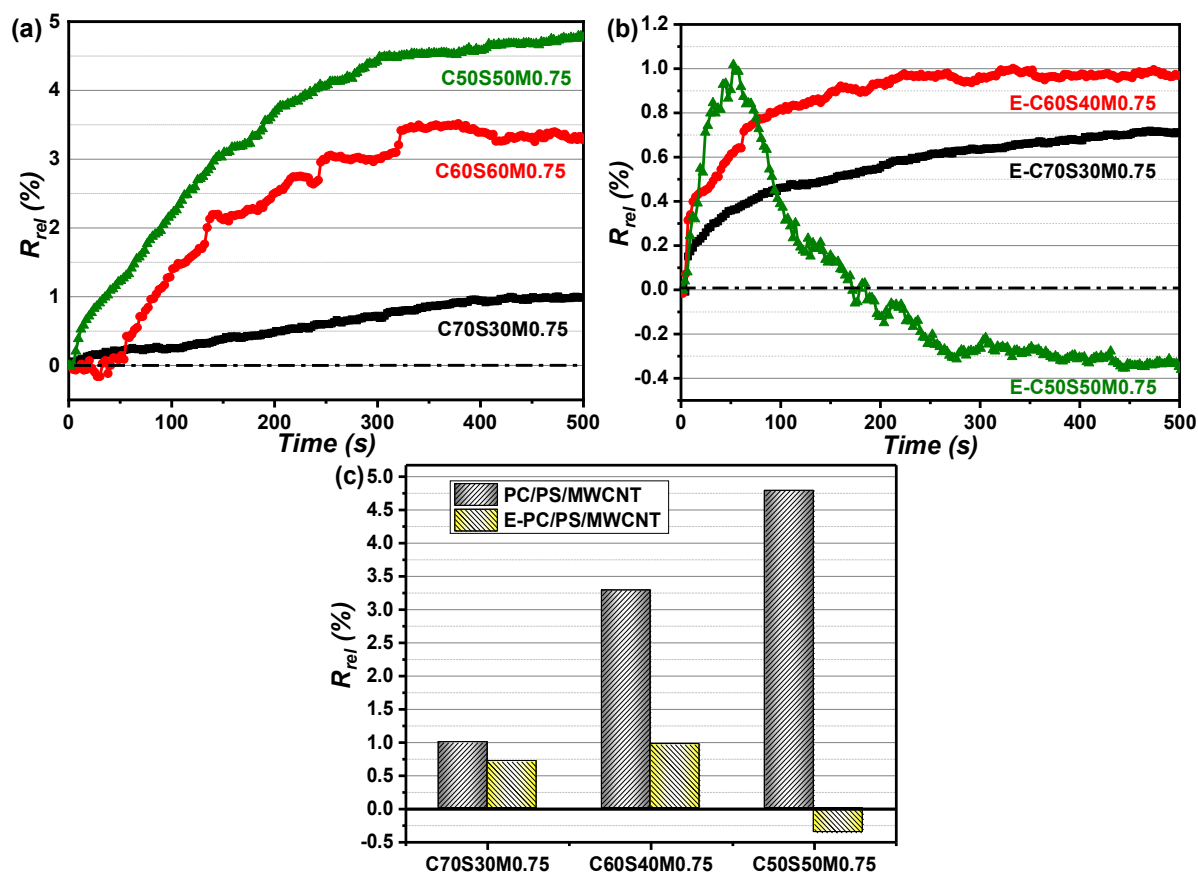


**Fig. 4.2.9** Long-term immersion towards cyclohexane vapor of (a) PC/PS/MWCNT composites, (b) PS etched PC/PS/MWCNT composites, and (c) comparison of terminal $R_{rel}$ of CPCs after 500 s exposure to cyclohexane vapor.

To further illustrate the effect of PS in polymer blends on the sensing behavior in cyclohexane, the PS part of the CPC samples was extracted using cyclohexane. **Fig. 4.2.9b** shows the sensing curves of the etched CPCs during long-term exposure to cyclohexane vapor. Obviously, the extracted CPCs E-C70S30M0.75 and E-C60S40M0.75 show a similar sensor tendency as the untreated samples, but lower $R_{rel}$ values, whereas the E-C50S50M0.75 $R_{rel}$ increases strongly up to the peak value of 1 % after 50 s immersion and then gradually decreases and even reaches negative changes (increase of conductivity). The terminal $R_{rel}$ of compact CPCs and PS extracted CPCs are compared in **Fig. 4.2.9c** showing that the terminal $R_{rel}$ of the compact CPCs increases with rising PS content, which proves that CPCs with co-continuous structure are more sensitive to the vapor of poor solvents because of their microstructure. Interestingly, an obvious terminal $R_{rel}$ distinction is observed for the PS extracted CPCs. After extraction, E-C70S30M0.75 and E-C60S40M0.75 show lower $R_{rel}$ as compared to corresponding compact CPCs. This can be explained by the fact that the remaining PC matrix is less swellable to cyclohexane as compared to PS and the conductive network can be better maintained during the vapor exposure. Since PS is only partially extracted for E-C70S30M0.75, the extracted content as shown in Fig 4.2.4 is only 5 wt%, indicating there are still 25 wt% PS remained in composites. The remaining PS is willing to interact with cyclohexane, causing a pressure to the conductive PC resulting in higher resistance. In case of E-C50S50M0.75, less PS is remained. In the beginning, the strong increase of $R_{rel}$ may be explained by the blend interface effect. In the following, the reduction of $R_{rel}$ indicates a polymer relaxation process which allows regeneration of conductive network.

A scheme is proposed in **Fig. 4.2.10** to illustrate this phenomenon. **Fig. 4.2.10a** shows the microstructure of C70S30M0.75 before and after PS extraction. It can be seen that the composite has the typical sea-island structure and the MWCNTs are homogeneously distributed in the PC matrix component. After cyclohexane extraction, partial isolated PS domains are extracted and the conductive networks are still present due to the weak interaction of PC and cyclohexane. For C50S50M0.75 composites (see **Fig. 4.2.10b**), the major part of the PS component has been extracted by cyclohexane due to interconnection of PS in this co-continuous structure composite. In this process, some MWCNTs distributed in PS are also extracted, which partially destroys the conductive networks in the composite material and causes a strong $R_{rel}$ increase when C50S50M0.75 is exposed to cyclohexane vapor. In the following, further diffusion of cyclohexane in etched PS domains and

penetration into PC domains leads to a rearrangement of the conductive network, leading to a decrease in resistance of E-C50S50M0.75.
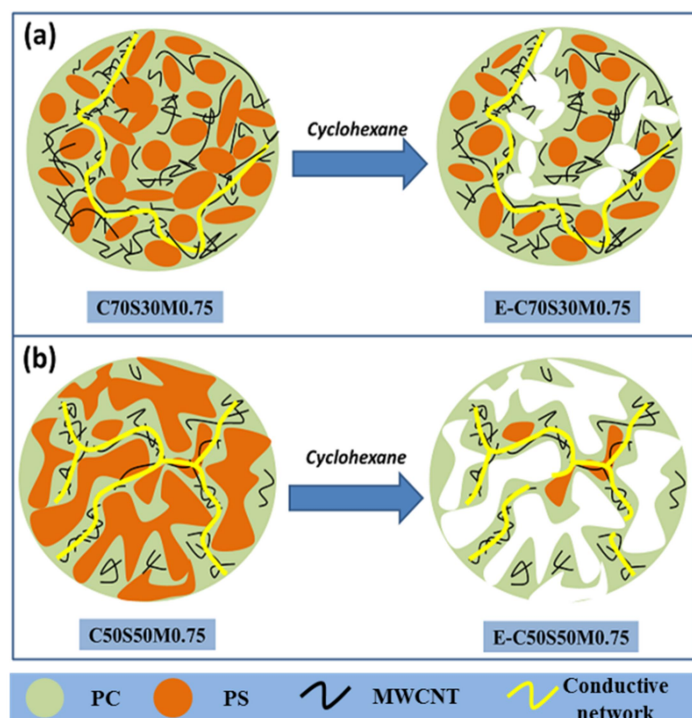


**Fig. 4.2.10** Schematic of morphology changes and MWCNT distribution of PC/PS/MWCNT composites extracted by cyclohexane; (a) is C70S30M0.75 composites and (b) is C50S50M0.75 composites.

As a summary, immiscible polymer blend based CPCs give rise to abundant electrical signals. According to the discussion above, CPCs with co-continuous structure improve the reversibility of swelling with good solvent vapors and prolong the lifespan of sensor materials. Moreover, they are also sensory to poor solvent vapors that broaden the detectable analyte ranges for the sensing tests. Thus, the vapor sensing behavior of CPCs can be tuned by adjusting the blend structure and filler distribution state of CPCs.

**4.2.6 Summary**

This chapter investigated the morphological and electrical properties of melt-mixed PC/PS/MWCNT composites with different polymer blend ratios. The MWCNTs are preferably localized in the PC component, which corresponds to the thermodynamic prediction. The MWCNT percolation threshold of the composites with co-continuous structure (PC/PS 50/50 wt%) is 0.13 vol. %, which is lower than that of 0.30 vol. % of the composites with sea-island structure (PC/PS 70/30 wt%). The sensing behavior was studied on blend composites having 0.75 wt% (approx. 0.43 vol%) MWCNTs, whereby the composite based on PC/PS 70/30 wt% showed the highest electrical conductivity value and

the best state of macrodispersion of MWCNTs. The three kinds of CPCs exhibit different sensing behavior towards different organic vapors. Under the influence of moderate solvent vapors such as ethyl acetate and toluene, the CPC with sea- island structure showed a higher relative resistance change ($R_{rel}$) and poor reversibility; whereas CPCs with co-continuous structure showed a lower $R_{rel}$ but excellent reversibility. All CPCs showed poor reversibility towards the good solvent vapor DCM due to their strong interaction with the two polymers. The CPCs sensors show an exponential relationship between $R_{rel}$ and vapor concentration, as shown for acetone sensing. If the CPCs were exposed to poor solvents such as cyclohexane, the PC/PS 50/50 wt% blend with 0.75 wt% has a higher $R_{rel}$ equilibrium than the other CPCs due to the microstructural differences of the blend composites. With respect to blend structure, CPCs with co-continuous structure show better reversibility towards good and moderate solvent vapors and higher $R_{rel}$ towards poor solvent vapors, which is attributed the larger blend interfaces that facilitate the vapor diffusion process. The results indicate that conductive polymer blends are promising vapor sensors, especially due to their tunable blend structures.

**4.3 Vapor sensing behavior of PLA/PS/MWCNT composites**

**4.3.1 Introduction**

In order to improve the sensing response and especially the reversibility of the sensing response in the drying cycle, in this chapter the effect of polymer crystallinity on these properties was studied. For this, a blend system containing a crystallizable blend component, namely semi-crystalline PLA, was used and combined with amorphous PS. PLA can change its degree of crystallinity during thermal annealing. PLA/PS blend pair is selected as they show different swelling behavior to the solvent vapors of acetone and cyclohexane. Moreover, for polymer blends, the generated microstructures during processing are usually in a non-equilibrium state after the melt mixing of the composites [186, 187]. Therefore, the morphologies and resulting properties of the polymer blends are unstable and may alter when being further processed, e.g. during compression or injection molding. In order to achieve a more stable structure of blends, thermal annealing is an effective method. Without mechanical stress, such treatment leads to coarsening of the blend structure if the polymer molecular chains are mobile (above the glass transition temperatures or in the molten state). In conductive polymer blends, thermal annealing can not only enhance the conductivity of the composites [188, 189] but the nanofiller presence also can suppress the coarsening process [186]. Bai et al. investigated the evolution of the co-continuous morphology of PLA/PS (50/50 wt%) blends containing reduced graphene oxide (rGO) after annealing for different times at 180 °C [100]. It was found that rGO was trapped at the interface of PLA/PS after melt compounding and annealing. If the rGO content was above 0.028 vol%, rGO effectively suppressed the coarsening of the composite morphology during thermal annealing.

For PLA/PS/MWCNT composites, the melt processing parameters in the one-step mixing process were set as 190 °C, 250 rpm and 8 min. The extruded strands were pelletized and compression molded at 190 °C, 50 kN, 5 min. In order to explore the effect of annealing on the electrical and vapor sensing behavior of CPCs, strip samples cut from pressed circular plates were placed in between two copper plates and annealed in the vacuum oven at 150 °C for 30 min, 60 min and 120 min, respectively. For abbreviation, the PLA/PS/MWCNT composites with different polymer blend ratios and filler loadings are denoted as A$x$S$y$M$z$, where $x$ and $y$ represents the weight composition of the blend, and $z$ give the weight content of MWCNTs in the blend composites. For instance, A50S50M1.0 is short for the PLA/PS blend ratio of 50/50 by wt containing 1.0 wt% MWCNT; thus the overall composition is 49.5 wt% PLA, 49.5 wt% PS, and 1.0 wt% MWCNT. In this section, only A50S50M1.0 composites

were selected for annealing studies. They were referred as A-*t*, where *t* represents the annealing time in min.

The effect of blend composite annealing at 150 °C for different times on the thermal and morphological characteristics and the resulting vapor sensing behavior is studied. The state of MWCNT dispersion and distribution in the PLA/PS blends is analyzed by SEM and TEM. DSC is used to characterize the thermal properties of the CPCs. Consecutive exposure-drying cycles and long-term exposure protocols were applied to evaluate the sensing performance of the CPC based sensors against acetone vapor (good solvent for PS and PLA) and cyclohexane vapor (good solvent for PS but poor solvent for PLA). In addition, the sensing behavior of CPCs towards different acetone/cyclohexane vapor mixtures is investigated.

### 4.3.2 Estimation of MWCNT localization in PLA/PS blends from the thermodynamic point of view

As discussed in the last chapter, wetting coefficient $\omega_a$ is used for predicting the thermodynamic preference of the MWCNTs in polymer blends. As the surface energy of the components should be used at melt processing temperature, the surface energy of components at 190°C were deduced from literature values given for 20 °C using the relations $-\frac{d\gamma}{dT}=K_T$ and $-\frac{dXp}{dT}=0$. Here $K_T$ is the temperature coefficient and $X_p$ represents the polarity of the components ($\gamma_i^p/\gamma_i$). The calculated surface energies of PLA, PS, and MWCNTs at 20 °C and 190 °C are shown in **Table 4.3.1**.

**Table 4.3.1** Surface energy of PLA, PS, and MWCNT at 20 °C and 190 °C.

| Material | 20 °C | | | 190 °C | | | Temp. coefficient | Citation |
|---|---|---|---|---|---|---|---|---|
| | $\gamma$ (mJ/m$^2$) | $\gamma^d$ (mJ/m$^2$) | $\gamma^p$ (mJ/m$^2$) | $\gamma$ (mJ/m$^2$) | $\gamma^d$ (mJ/m$^2$) | $\gamma^p$ (mJ/m$^2$) | | |
| MWCNT | 45.3 | 18.4 | 26.9 | 45.3 | 18.4 | 26.9 | - | [178] |
| PLA | 40.2 | 29.7 | 10.5 | 27.4 | 20.2 | 7.2 | -0.074 | [190] |
| PS | 40.7 | 33.9 | 6.8 | 28.5 | 23.7 | 4.8 | -0.072 | [187] |

In the following, these deduced surface energy parameters at the processing temperature (190 °C) were used to calculate $\omega_a$ using Harmonic-mean Equation and Geometric-mean Equation as shown in **Table 4.3.2**. According to the calculation, $\omega_a$ are -6.6 (Harmonic-mean) and -7.5 (Geometric-mean). Thus, it can be predicted that the MWCNTs are preferentially localized in the PLA component.

**Table 4.3.2** Interfacial energy and wetting coefficient at 190 °C

| Components | $\gamma_{PLA-MWCNT}$ (mJ·m$^{-2}$) | $\gamma_{PS-MWCNT}$ (mJ·m$^{-2}$) | $\gamma_{PLA-PS}$ (mJ·m$^{-2}$) | $\omega_a$ |
|---|---|---|---|---|
| Harmonic-mean Equation | 11.5 | 16.1 | 0.7 | -6.6 |
| Geometric-mean Equation | 6.3 | 9.3 | 0.4 | -7.5 |

### 4.3.3 Electrical properties and morphological observation of PLA/PS/MWCNT composites

In terms of filler localization in immiscible polymer blend composites, two scenarios are mainly observed, i.e. preferentially localization in one component of the polymer blend or at the blend interface [108, 116, 188, 191]. The electrical properties are strongly dependent on the morphology of the conductive polymer blend composites as conductivity of the sample requires continuity of the filled conductive component or at the interface [117, 192]. Therefore, the electrical properties of composites can be varied by tuning the microstructure of the polymer blends. The electrical resistivities of the PLA/PS/MWCNT composites with different blend compositions containing 0.5 wt% or 1.0 wt% MWCNT are shown in **Fig. 4.3.1**. At 0.5 wt% MWCNTs, the resistivity of the composite with the lowest PLA content (A30S70M0.5) is *ca.* $2\times10^8$ Ω·cm. With increasing PLA content in the composites, the resistivity decreases slightly to *ca.* $5\times10^7$ Ω·cm for A40S60M0.5, and for A50S50M0.5 a distinct minimum with almost 3 orders of magnitude lower resistivity is found. As the PLA content continues to increase, the resistivity increases back to $1.4\times10^8$ Ω·cm for A60S40M0.5 and even to $2\times10^9$ Ω·cm for A70S30M0.5, the composite with the highest PLA content.
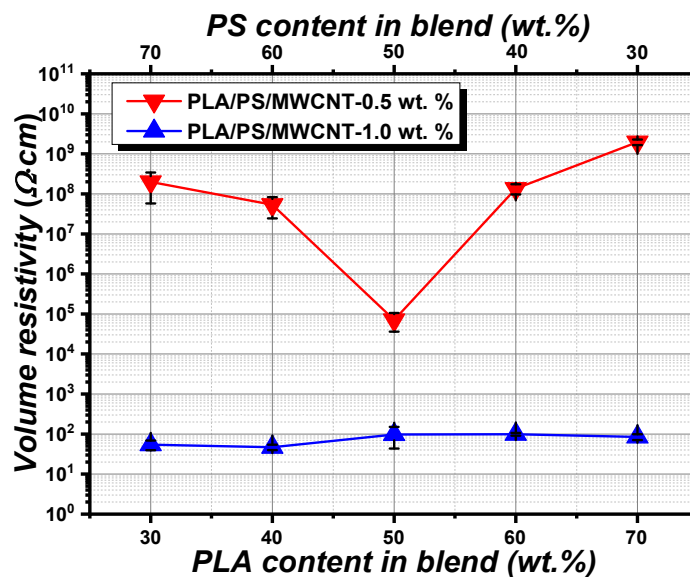


**Fig. 4.3.1** Electrical volume resistivity of PLA/PS/MWCNT-0.5 and PLA/PS/MWCNT-1.0 composites with different blend compositions.

The dependence of the resistivity on the blend composition is caused by the morphology of the blend composites which is shown in **Fig. 4.3.2**. The PS component was extracted with cyclohexane, leaving holes in its original positions. The remaining visible structure is the PLA component. The SEM micrographs show that the A40S60M0.5 (**Fig. 4.3.2a**) already forms a connective structure of the remaining PLA component thus leading to the measurable conductivity. Under the same extraction condition, the A30S70 blend composites disintegrated completely because PS forms the matrix and the insoluble PLA remains in the PS solution as particle dispersion after dissolution. These morphological differences also explain why the resistivity is nearly one decade lower in the co-continuous blend.
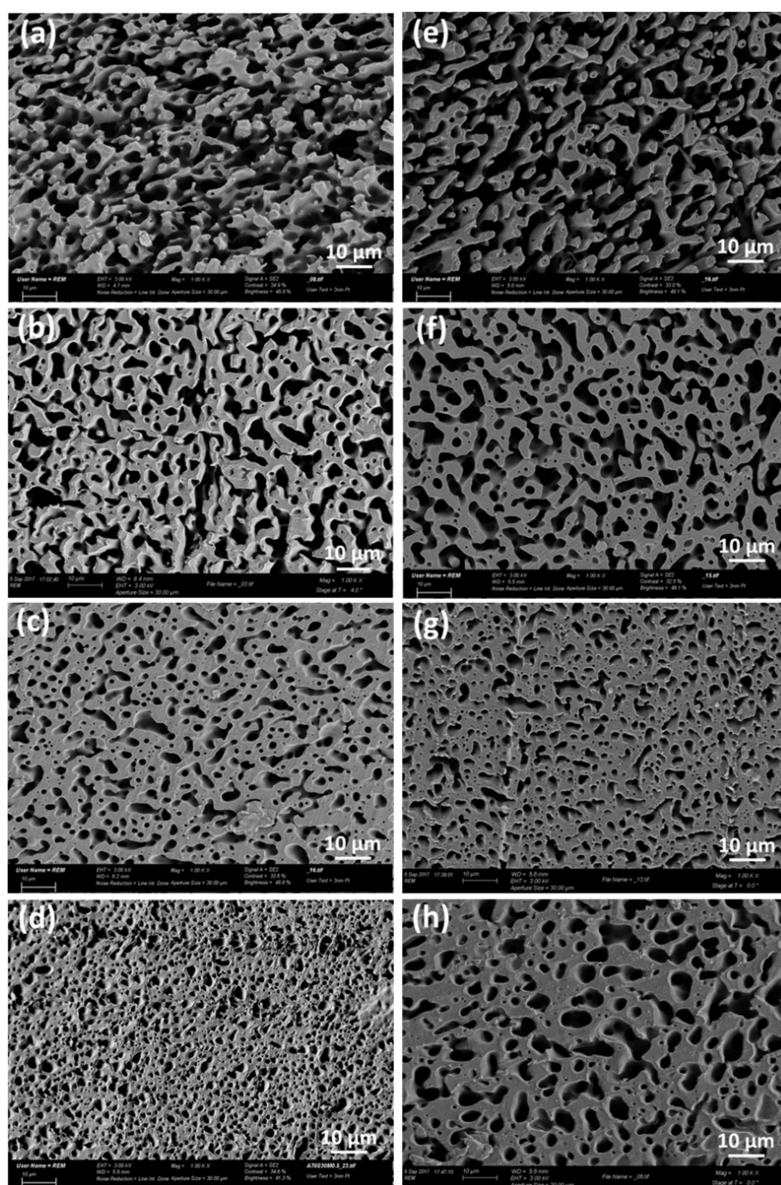


**Fig. 4.3.2** SEM micrographs of (a-d) PLA/PS/MWCNT-0.5 and (e-h) PLA/PS/MWCNT-1.0 blend composite extruded strands with different blend composition: (a, e) A40S60, (b, f) A50S50, (c, g) A60S40, and (d, h) A70S30 (PS has been extracted by cyclohexane).

The sample A50S50M0.5 (**Fig. 4.3.2b**) exhibits a well-developed co-continuous structure in which the remaining PLA as well as the volumes created by PS extraction are continuous. As expected from thermodynamic considerations (**Tables 4.3.1** and **4.3.2**), a selective localization of the MWCNT in PLA component occurs, which was proven by TEM investigations. It can be observed that MWCNT are selectively localized in the PLA component for A50S50M0.5 and A50S50M1.0 composites as shown in **Fig. 4.3.3**. Moreover, the PS continuity is 97 % for A50S50M0.5, which is verified by extraction experiments (see **Fig. 4.3.4**). The high PS continuity also indicates that a perfect co-continuous structure is formed in the blend composite.
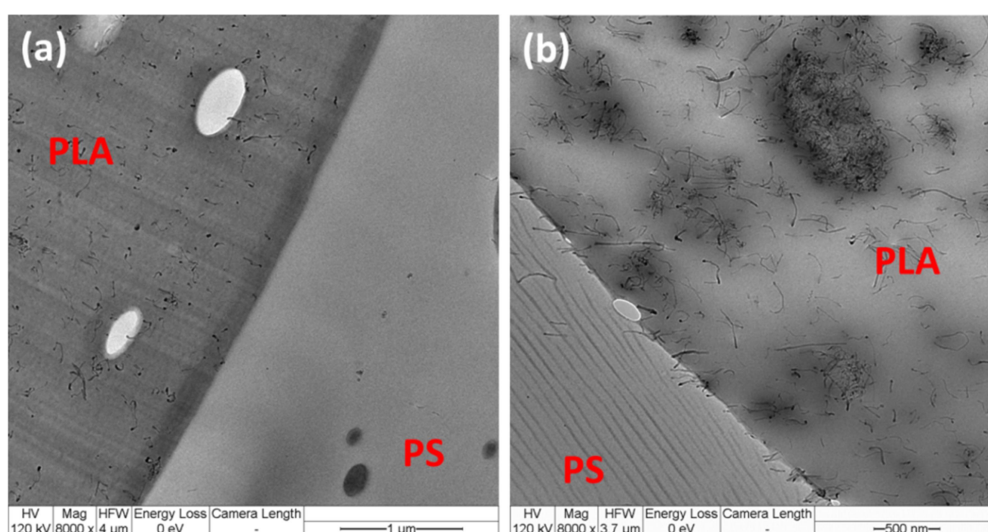


**Fig. 4.3.3** TEM images of PLA/PS/MWCNT composites with different MWCNT loading at the blend composition of 50/50 wt%. (a) A50S50M0.5, (b) A50S50M1.0.

To further investigate the filler localization in these polymer blends during the melt mixing, extraction experiments were carried out. The compression molded samples (10×3×0.3 mm$^3$) of A50S50M0.5 and A50S50M1.0 were put into the vials containing cyclohexane at the room temperature for 24 h. Every 6 hours, the vials were sonicated for 5 min. Photographs of the vials after 24h treatment are shown in **Fig. 4.3.4a**. Finally, the extracted samples were washed by distilled water in an ultrasonic bath for another 15 min, dried, and weighed in order to calculate the extracted part of the blends. The extracted PS component was studied by quantitatively determining the relation between the extracted amount of PS and the original PS content in the CPC. As the part extracted from the blends (the extracted PS part) was ca. 48 wt% (see **Fig. 4.3.4b**), the continuity of PS is ~97% in both composites, meaning that PS could be nearly completely etched out by cyclohexane.
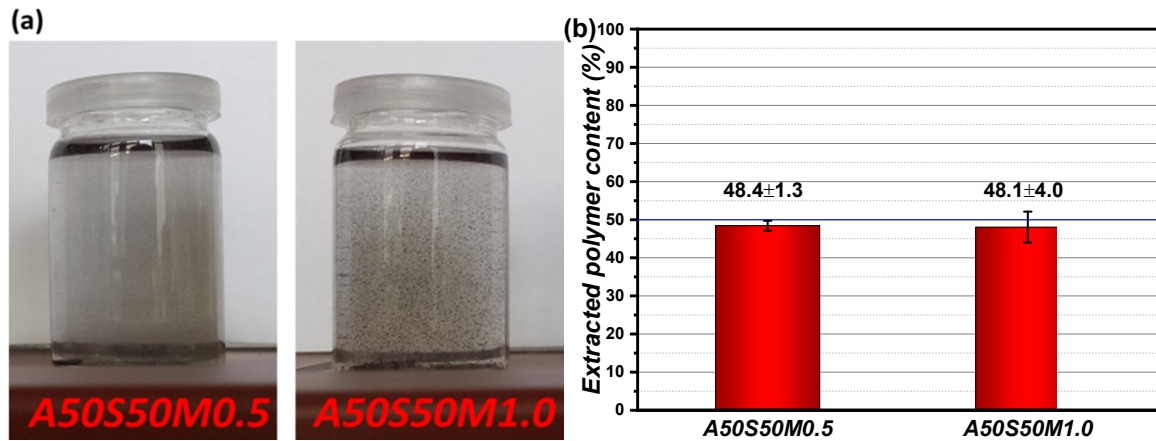
**Fig. 4.3.4** (a) photographs of A50S50M0.5 and A50S50M1.0 after extraction with cyclohexane, and (b) extracted polymer content of the composites.

Based on an almost perfect co-continuous structure and the selective localization of the MWCNTs, the blend composite A50S50M0.5 has the lowest resistivity of only $8 \times 10^4$ $\Omega$·cm of all blends with 0.5 wt% MWCNT. In A60S40M0.5 (**Fig. 4.3.2c**), the continuous morphology of PLA is clearly visible, while the PS domains appear to be somehow isolated. This indicates the beginning of the transition towards a matrix-dispersed component structure in blends from 60 wt% PLA on. At the PLA content of 70 wt% (A70S30M0.5, **Fig. 4.3.2d**), a matrix-dispersed component structure is present although the visible holes are not yet spherical. The resistivity increase with PLA excess is due to the reduced local MWCNT concentration in the PLA component compared to the blend composition of 50/50 wt%, resulting in a less dense conductive network.

When the MWCNT content of the composites is increased to 1.0 wt%, their resistivity is much lower and largely independent of the blend composition. The resistivity range of 50 to 100 $\Omega$·cm is 3 to 7 orders of magnitude lower than that of the corresponding composites containing 0.5 wt% MWCNTs. Compared to PLA/PS/MWCNT-0.5 wt% composites (**Fig. 4.3.2a-4.3.2d**), the composites containing 1.0 wt% MWCNTs (**Fig. 4.3.2e-4.3.2h**) exhibit similar morphology changes with the increase of the PLA content. Again, at the PLA/PS blend ratio of 50/50 wt%, a nearly perfect continuity of PS is reached as seen in a continuity degree of 97% (**Fig. 4.3.4b**). At higher PLA contents, especially at 70 wt% PLA, the blend morphology is coarsened at the higher MWCNT content. Since the 1 wt% MWCNT loading is well above the electrical percolation threshold, the resistivity changes only slightly when the mixture composition is changed. Slightly lower values are obtained when the PLA content is 30 wt% and 40 wt% because the local MWCNT concentration in this continuous component is higher due to the selective localization in this component.

Based on the above findings, the conductive polymer blend composites with the composition PLA/PS 50/50 wt% were selected for further investigation due to their excellent electrical property and their almost perfect co-continuous structure. **Fig. 4.3.5** shows the volume conductivity as a function of MWCNT content for A50S50M$z$ composites. A drastic jump in conductivity of about 9 orders of magnitude occurs when the MWCNT content increases from 0.1 wt% to 0.5 wt%, proving the formation of a conductive network in the composites. The $\varphi_c$ is non-linearly fitted using **Eq. 2.1** (see **Page 27**) whereby only the conductivity values above the percolation region were considered. This procedure is repeated until the lowest value of the root mean square error is achieved for $\varphi_c$, which is determined to be 0.4 wt%.
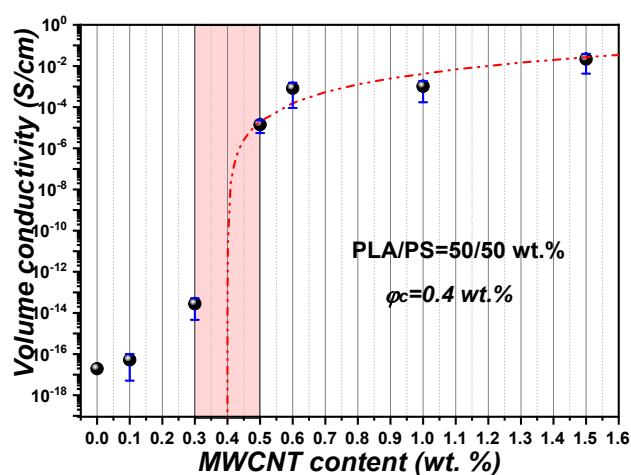


**Fig. 4.3.5** Electrical volume conductivity of PLA/PS(50/50 wt%)/MWCNT composites at different MWCNT loadings.

**Fig. 4.3.6** shows the micrographs of the cross-sections of compression molded specimens of PS-extracted A50S50M1.0 composites. It has to be mentioned that there is a strong phase coarsening after compression molding at 190 °C of neat PLA/PS extruded strands, while the co-continuity remains (see **Fig. 4.3.7**). Such a coarsening process has also been reported for other blend systems [186, 193-195]. For instance, Bai et al. compared the domain size of PLA/PS blends after different annealing times at 180 °C. The neat PLA/PS blend showed a nearly linear increase in domain size from *ca.* 2 *μm* to 77 *μm* with the annealing time up to 60 min [100]. When a small amount rGO (0.028 vol%) was added into the PLA/PS blend, the phase coarsening rate was significantly reduced, which indicated that the addition of rGO was effective to suppress the coarsening and stabilize the co-continuous structure.
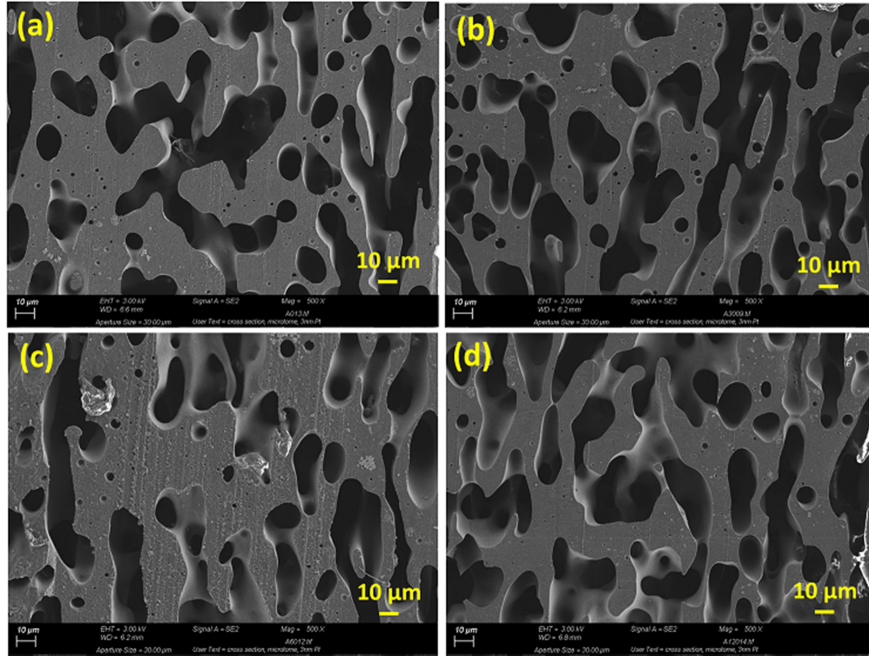
**Fig. 4.3.6** SEM micrographs of PS extracted A50S50M1.0 compression molded plates (a) without annealing and annealed at 150 °C for (b) 30 min, (c) 60 min, (d) 120 min.
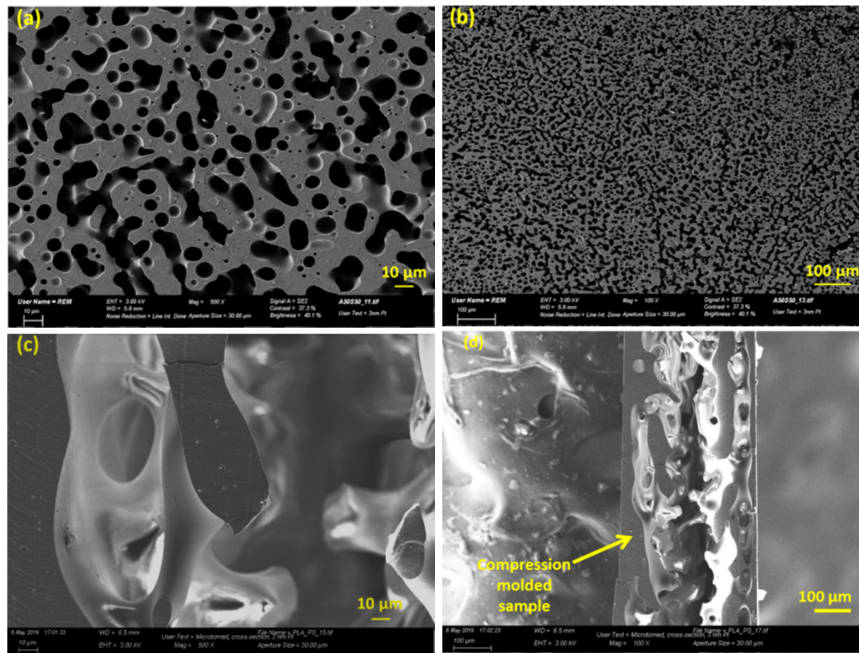


**Fig. 4.3.7** SEM micrographs of PS extracted PLA/PS blends without CNTs (blend raito is 50/50 wt%) for (a and b) extruded strands and (c and d) compression molded plates.

As seen in **Fig. 4.3.6**, the morphology type and the blend domain size are almost the same for the non-annealed and annealed samples. As a measure for coarseness degree the length of the blend interface per area unit was determined from SEM images shown in **Fig. 4.3.6**. The relative length of interface of the extracted blend composites was traced using the ImageJ software. The resulted relative length of interface has a slight increase from 0.598 μm /μm$^2$ for A0 to 0.648 μm/μm$^2$ for A120 (see **Fig. 4.3.8**), indicating that the addition of

93

MWCNT somehow suppresses the coarsening process of A50S50M1.0 composites during the annealing at 150 °C. However, the annealing process may increase the crystallinity of semi-crystalline polymers such as PLA, which will be discussed in the following. Crystalline regions of polymers are less swellable, which is expected to make CPC sensors more resistant to vapor stimulation.
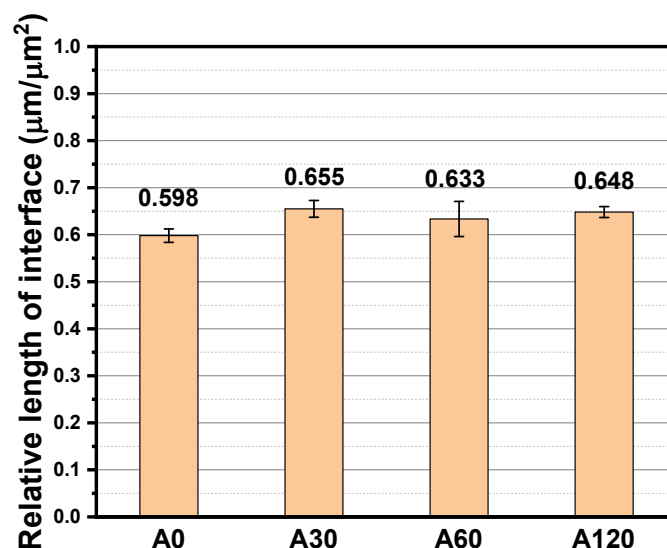


**Fig. 4.3.8** Relative length of interface for A50S50M1.0 under different annealing times.

**Fig. 4.3.9** illustrates the morphology changes of PLA/PS/MWCNT composites with the increase of MWCNT content. Without MWCNT incorporation, the domain size of remaining PLA is 40-50 μm. there is an obvious difference between the PLA/PS blend and the PLA/PS/MWCNT composites. It can be seen clearly that the PLA domain size is decreased significantly when 0.5 wt% MWCNTs are mixed with the polymer blend (5 μm). When further increasing the MWCNT loading to 1.0 wt%, no big difference regarding the PLA domain size is observed for A50S50M1.0 as compared to A50S50M0.5. Thus, it can be concluded that the addition of MWCNTs to the polymer blend effectively controls the blend coarsening behavior and makes the blend structure much finer.
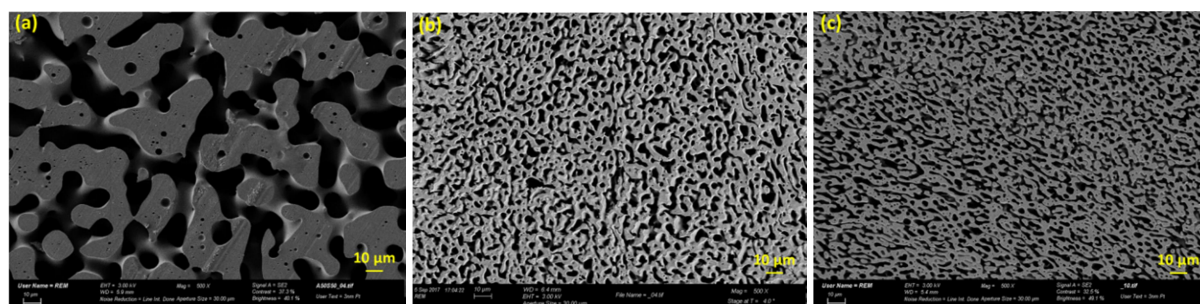


**Fig. 4.3.9** SEM micrographs of extruded strand surfaces (PS extracted using cyclohexane) of (a) A50S50, (b) A50S50M0.5, and (c) A50S50M1.0.

### 4.3.4 Thermal transitions and crystallinity of PLA/PS/MWCNT composites

In the following, the effect of annealing on the crystallinity and crystallization behavior of CPCs was studied. The first heating run of the DSC measurement was followed by a controlled cooling run that showed no exothermal crystallization peak. The glass transition temperature ($T_g$), cold crystallization temperature ($T_{cc}$), melting temperature ($T_m$) of PLA, as well as the cold crystallization and melting enthalpies, were determined in the first heating run (**Fig. 4.3.10a** and **b**) as well as the $T_g$ of the amorphous PS component. The first heating run is used for the evaluation because its thermal information reflects the state of the samples after compression molding (as used for the sensing experiments). The second heating run is also influenced by the cooling conditions in the DSC measurement and therefore gives less information about the state of the composites as used in the sensing trials (**Fig. 4.3.10c** and **d**). The thermal information is summarized in **Table 4.3.3.** The crystallinity ($X_c$) of the composites is calculated using **Eq. 4.7** [196]:

$$X_c = \frac{\Delta H}{\Delta H_m^0 \cdot PLA\ wt.\%} \cdot 100\% \tag{4.7}$$

Here, $\Delta H = \Delta H_m - \Delta H_{cc}$ is the melting enthalpy. $\Delta H_m^0$ is the melting enthalpy of a 100% crystalline polymer matrix (for PLA 93.7 J·g$^{-1}$) [197], $\Delta H_m$ is the measured melting enthalpy and $\Delta H_{cc}$ is the enthalpy of cold crystallization appearing during the heating below the beginning of melt transition.

**Table 4.3.3** Phase transition temperatures and crystallinity ($X_{c,PLA}$) of PLA at the blend ratio of 50/50 wt. % of PLA/PS and PLA/PS/MWCNT blend composites

| PLA/PS/MWCNT | $T_{gPLA}$ (°C) | $T_{gPS}$ (°C) | $T_{cc}$ (°C) | $T_{mPLA}$ (°C) | $\Delta H$ (J/g) | $X_{c,PLA}$ (%) |
|---|---|---|---|---|---|---|
| A50S50 | 63.9 | - | 105.8 | 169.8 | 9.3 | 19.9 |
| A50S50M0.1 | 61.9 | 100.2 | 127.4 | 153.6 | 4.2 | 9.0 |
| A50S50M0.3 | 62.5 | 100.0 | 126.2 | 153.4 | 4.0 | 8.6 |
| A50S50M0.5 | 62.5 | 100.0 | 128.6 | 154.4 | 4.6 | 9.9 |
| A50S50M0.6 | 62.9 | 100.0 | 129.4 | 154.2 | 2.9 | 6.3 |
| A50S50M1.0 = A-0 | 63.1 | 100.2 | 125.4 | 154.4 | 3.2 | 6.9 |
| A-30 | 63.7 | 98.1 | 123.4 | 150.8 | 3.6 | 7.8 |
| A-60 | 63.9 | 97.5 | - | 144.7/155.2 | 14.1 | 30.4 |
| A-120 | 64.2 | 97.1 | - | 149.5/155.5 | 16.3 | 35.1 |
| A50S50M1.5 | 63.7 | 100.2 | 124.5 | 154.7 | 2.4 | 5.2 |

As **Fig. 4.3.10a** shows, there is a big difference in the melting behavior between the blends without and with MWCNTs. The $T_m$ of neat blend A50S50 is 169.8 °C and its

crystallinity is 19.9 %. With the MWCNT addition the melting peak of PLA shifts $T_m$ to lower temperature with values between 153.4 °C to 154.7 °C and the crystallinity decreases to below 10 %. Interestingly, there are double melting peaks for A60 and A120 because of the formation of different crystal structures [198] or lamellar populations with different perfection degrees [199]. The $T_g$ values of PLA and PS in A50S50Mz are almost equal, while the $T_m$ of the PLA component gradually shifts to higher temperatures with increasing MWCNT content. With increasing filler content, the cold crystallization, which is very pronounced at 0.1 wt% MWCNT loading, is impeded and the overall crystallinity reduced. The DSC first heating runs of the A50S50M1.0 composites after the annealing treatment are shown in **Fig. 4.3.10b**. All composites have similar $T_g$ and $T_m$ values. The crystallinities of A-0 and A-30 are 6.9 % and 7.8 %, respectively. There is only a slight crystallinity increase of the sample after 30 min annealing. With increasing annealing time, the crystallinity increases reaching values of 30.4 % for the sample A-60 and 35.1 % for A-120 illustrating that the crystallinities of the CPCs are increased significantly after 60 min or even longer annealing. The corresponding second heating runs of the composites are shown in **Fig. 4.3.10c** and **d**.
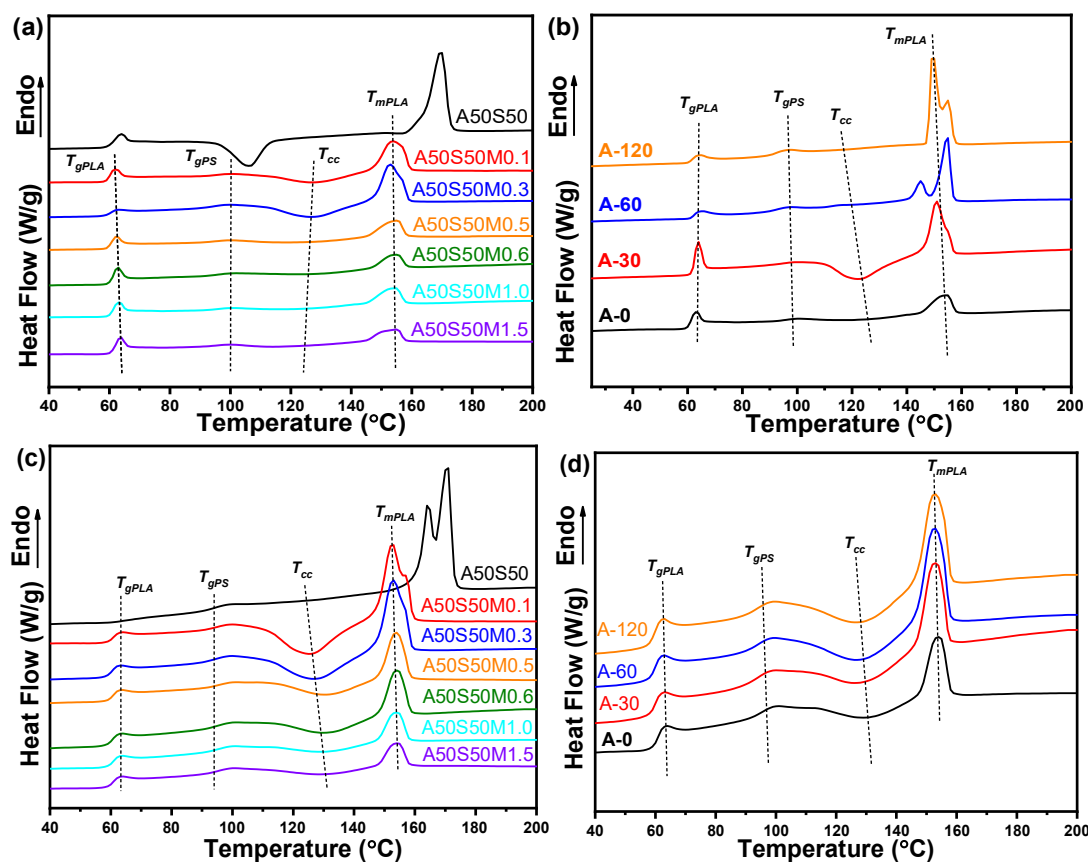


**Fig. 4.3.10** DSC first heating run of (a) PLA/PS (50/50 wt%) with different MWCNT contents and (b) A50S50M1.0 composites after different annealing times; the second heating run of (c) PLA/PS (50/50 wt%) with different MWCNT contents and (d) A50S50M1.0 composites after different annealing times

**4.3.5 Vapor sensing behavior of PLA/PS/MWCNT blend composites**

As mentioned earlier, the exposure of CPCs towards vapors induces polymer swelling due to vapor absorption which increases the composite volume thus reducing the filler volume concentration and increasing the filler-filler distances. The resulting contact resistance increases and finally partial destruction of the conductive network is considered as the main mechanism for CPC based chemiresistors [37, 56, 168, 200, 201]. When the swollen CPCs are dried, their volumes shrink and neighboring nanofiller contacts are reconstructed, thus decreasing the resistance of CPCs. In ideal cases, this process of filler network disconnection and reconstruction caused by the swelling/shrinking is completely reversible.

In this study, acetone and cyclohexane are selected as test vapors. Their $\chi_{12}$ values with PLA and PS are listed in **Table 4.3.4**. It can be concluded that acetone ($\chi_{acetone,PLA}$ = 0.050) is a good solvent and cyclohexane ($\chi_{cyclohexane,PLA}$ = 1.020) is a poor solvent for PLA. However, both acetone ($\chi_{acetone,PS}$ = 0.010) and cyclohexane ($\chi_{cyclohexane,PS}$ = 0.329) are good solvents for PS.

**Table 4.3.4** Molar volume ($V_{mol}$), saturated partial pressure ($P_i$), solubility parameters ($\delta$), and Flory-Huggins interaction parameters ($\chi_{12}$) of polymers and organic solvents at 25 °C [59, 177]

| Materials | $V_{mol}$ (cm$^3$mol$^{-1}$) | $P_i$ (kPa, 25°C) | $\delta$ (MPa)$^{1/2}$ | $\chi_{12}$ PLA | PS |
|---|---|---|---|---|---|
| Acetone | 74 | 30.6 | 19.9 | 0.050 | 0.011 |
| Cyclohexane | 130.6 | 13.0 | 16.8 | 1.020 | 0.329 |
| PLA | - | - | 21.2 | - | - |
| PS | - | - | 19.3 | - | - |

Considering the upper limit (200 MΩ) of the multi-meter used for vapor sensing tests, A50S50M0.5 composites are not suitable for the sensing tests as their loose conductive network (just percolated) will be changed drastically and results in huge resistance change that surpass the upper limit of the multi-meter. Based on their resistivity values and the expected changes, the differently annealed A50S50M1.0 composites were selected for the sensing tests. **Fig. 4.3.11** shows the $R_{rel}$ of those CPCs under cyclic exposure to acetone vapor of different concentration. At the lowest analyzed acetone concentration of 18.1 % a sharp resistance increase with a maximum $R_{rel}$ of 17 % (**Fig. 4.3.11a**) is observed in the first exposure cycle for non-annealed A50S50M1.0 (A-0), but the recovery is poor with a remaining $R_{rel}$ of > 8 %. In the following sensing cycles, the maximum $R_{rel}$ are slightly reduced and almost constant at about 15 % combined with $R_{rel}$ values of about 11 % after recovery relative to the initial values of the first cycle. Thus, the first sensing cycle can be considered as a conditioning process after which the composite exhibits good reversibility. At

higher acetone concentrations (**Fig. 4.3.11b-c**), there is no such concompactation phenomenon and the sensing response leads to higher $R_{rel}$ values after each sensing cycle and the corresponding drying cycle. The maximum $R_{rel}$ of A-0 at 30.2% acetone vapor is higher than 1500%, indicating an unstable conductive network under strong polymer swelling. In contrast to the non-annealed sample, the annealed blends show lower $R_{rel}$ but better reversibility (**Fig. 4.3.11d**), especially after annealing of 60 and 120 min (A-60 and A-120).
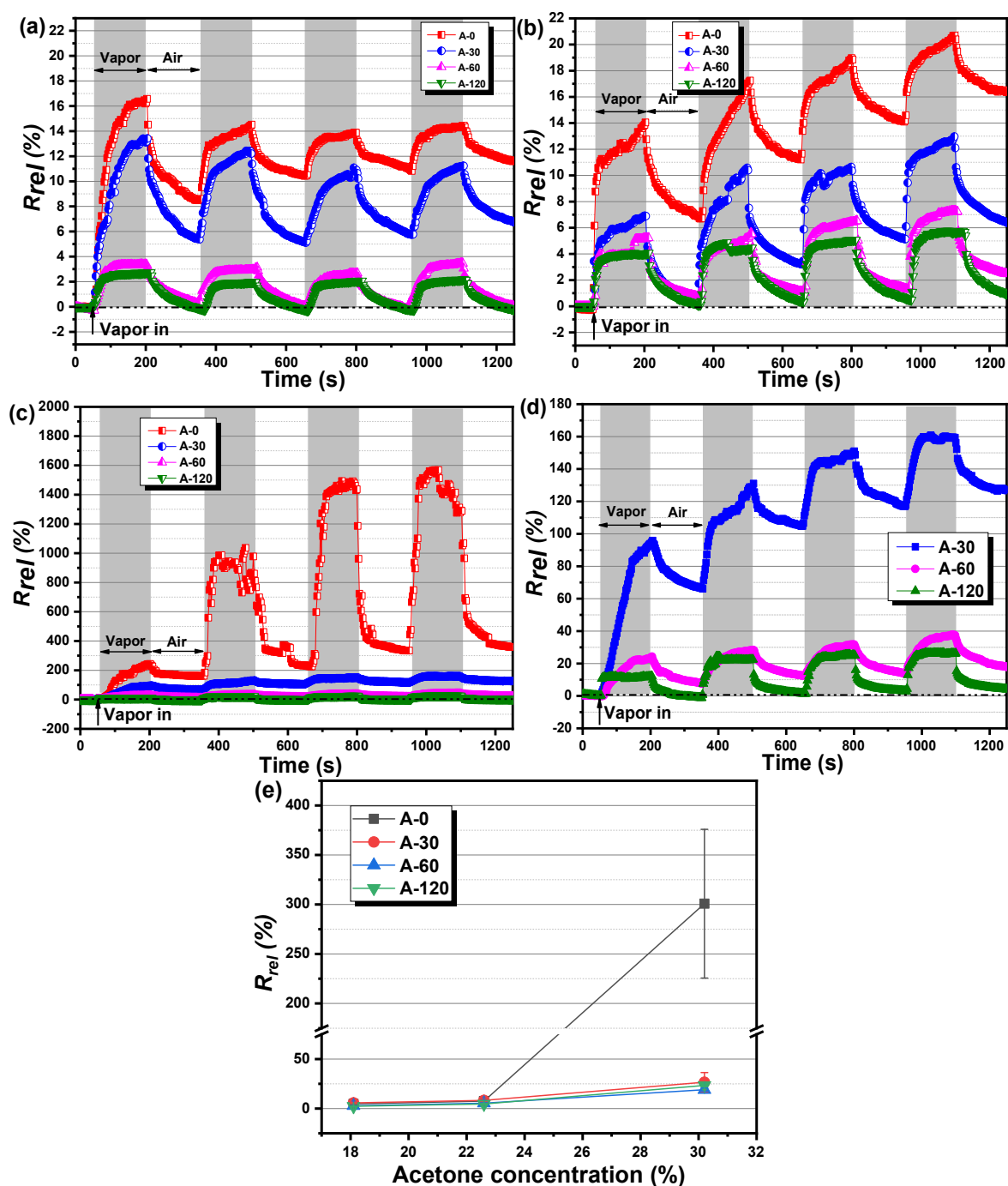


**Fig. 4.3.11** Effect of annealing on the vapor sensing behavior of A50S50M1.0 composites towards acetone vapors. The acetone vapor concentrations are (a) 18.1%, (b) 22.6%, and (c,d) 30.2%. (e) $R_{rel}$ (calculated based on the initial resistance value before each cycle) of CPCs after 150 s of immersion at different acetone vapor concentrations, mean values and standard deviations of the 2$^{nd}$ to 4$^{th}$ cycle are shown

There are two possible main reasons for the reduced sensing response in case of the annealed samples. The first one is that annealing is known to lead to secondary agglomeration of the nanotubes which helps to form conductive pathways and make the samples more conductive. However, as shown in **Figure 4.3.12**, the electrical resistivity of about 55 S/cm remains nearly constant after annealing so that this factor is neglectable. The second reason can be seen in the increased crystallinity of the PLA component after annealing, which rose from 6.9 % to 35.1% as shown before. The only very slightly coarsened morphology due to annealing could allow somehow faster vapor diffusion, but the formed crystals are hardly accessible for vapor diffusion and, more importantly, the increased crystallinity confines some volume of the amorphous part, thus hampering the vapor diffusion. For the non-annealed or short time annealed CPCs, the larger free volume in the amorphous PLA regions allows faster vapor penetration and results in higher $R_{rel}$ towards acetone vapor. **Fig. 4.3.11e** shows the sensitivity of CPCs with vapor concentrations with the values based on the second to fourth cycle by taking the corresponding starting values in each cycle as base for the $R_{rel}$ calculation. It can be observed that the sensitivity of CPCs increases with the acetone vapor concentration. The non-annealed sample is the most sensitive to saturated acetone vapor, but with unstable sensing signal. The annealed samples show a significantly lower sensitivity towards acetone vapor, however with $R_{rel}$ values of about 25% at 30 % vapor concentration the materials are is also suitable to sense acetone vapor concentrations. In addition, they show good sensing reversibility, which is a good aspect for cyclic use of CPC sensors.
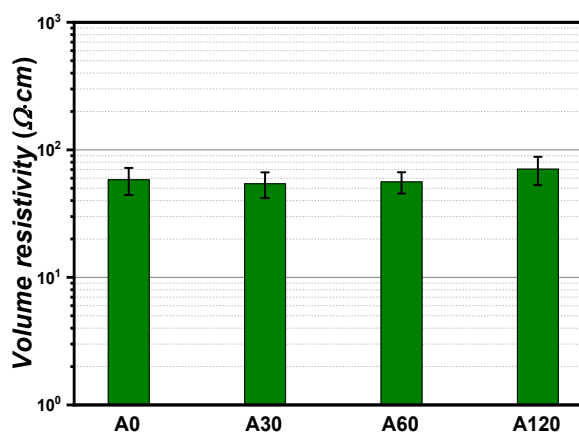


**Fig. 4.3.12** The electrical volume resistivity of A50S50M1.0 composites before annealing (A0) and after annealing (A30, A60 and A120).

Sensing with cyclohexane, which according to the $\chi_{12}$ calculations is a good solvent for PS but a poor solvent for PLA, was performed on the same differently annealed samples. **Fig. 4.3.13** shows the $R_{rel}$ of the composites towards saturated cyclohexane vapor ($C = 13\%$).

Again, the non-annealed A50S50M1.0 sample (A-0) gives the highest response (up to 40%) and the responses decrease with annealing time **(Fig. 4.3.13a)**. In each cycle performed with A-0, as well the $R_{rel}$ value after vapor exhibition as after recovery increase. This is similar for the samples annealed at 30 and 60 min (A-30 and A-60) **(Fig. 4.3.13a and b)**. Only the sample annealed for 120 min (A-120) shows relatively constant values after vapor exhibition (about 5%) and full recovery in the air exposure part of the cycles. Compared to the sensing with acetone, the increase in the exposure parts does not lead to an $R_{rel}$ plateau and also the recovery is slower than with all acetone concentrations. The constant sensing response and excellent reversibility of A-120 are expected to be again related to the increased crystallinity of the PLA component. Since cyclohexane has only strong interaction with PS, mainly the PS component swells while the CNT filled PLA tends to restrict the swelling. For the composites with co-continuous structure, PS swelling may cause stresses on the PLA part resulting in small deformations so that the conductive network in PLA is affected. With the increased crystallinity of PLA after annealing, the PLA component is more stable and less affected by the PS swelling.
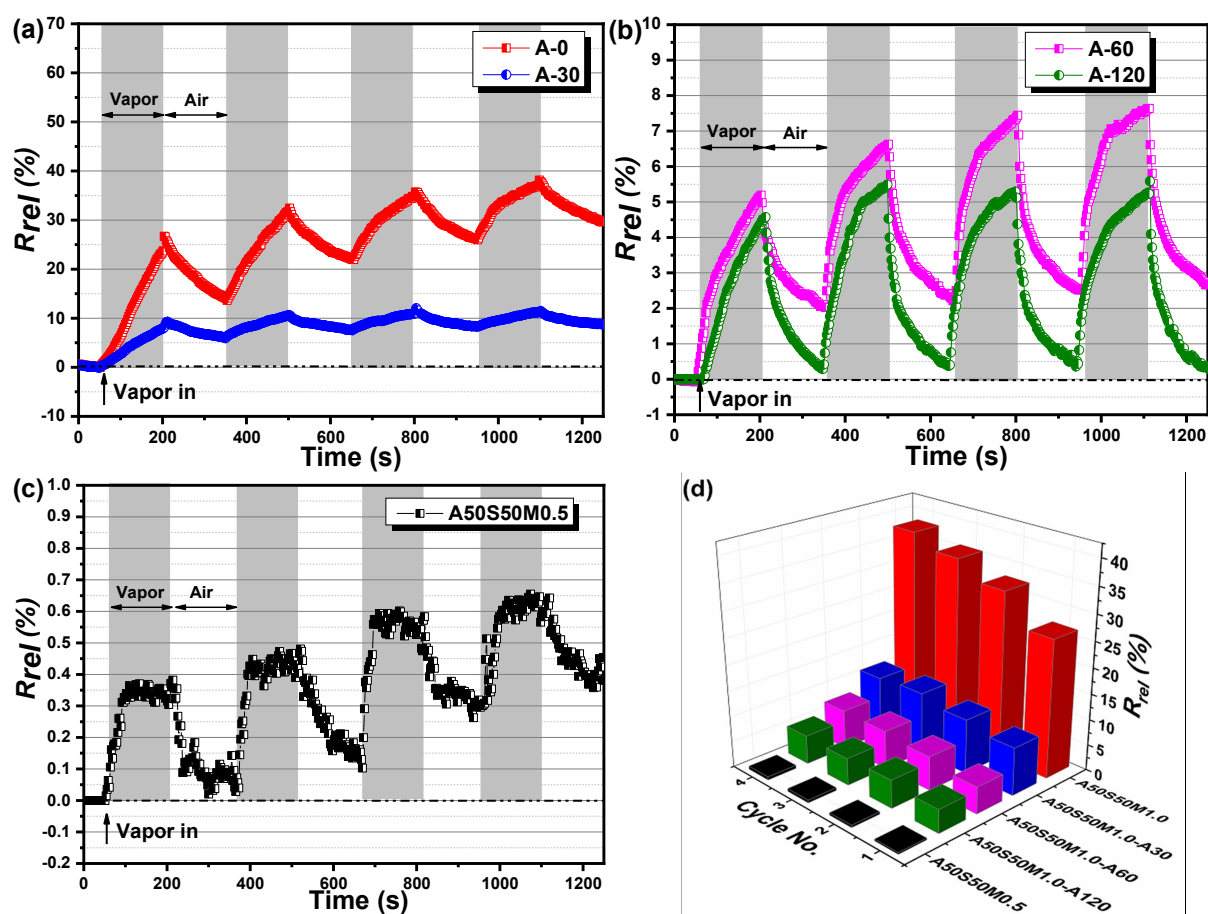


**Fig. 4.3.13** Cyclic sensing behavior of (a,b) differently annealed A50S50M1.0 composites and (c) A50S50M0.5 in saturated cyclohexane vapor (concentration 13%). (d) Comparison of relative resistance change $R_{rel}$ of the

composites after 150 s exposure to cyclohexane vapor (values based on the initial resistance before the first cycle).

In order to get deeper insight in the sensing mechanism of PLA/PS/MWCNT composites towards cyclohexane, also the sample A50S50M0.5, whose MWCNT content is with 0.5 wt% just slightly above $\varphi_c$ (0.4 wt%) was selected for an additional sensing test. As seen from **Fig. 4.3.13c**, the maximum $R_{rel}$ of this sample towards saturated cyclohexane vapor is in the range between 0.35 % and 0.65 %, which is much lower than that of A50S50M1.0 composites. This is an unexpected behavior since composites with filler concentrations closer to the percolation threshold are generally expected to react more strongly than composite materials with higher filler concentrations [158].

**Fig. 4.3.13d** summarizes the maximum $R_{rel}$ of each cycle for A50S50M0.5 and A50S50M1.0 composites towards cyclohexane showing that the blend with 0.5 wt% CNT has an even lower response than the blend with 1.0 wt% CNT annealed for 120 min. The reason for this behavior can be related to the blend structure of the sample and the differences at different CNT loadings. In A50S50M0.5, the conductive network formed by MWCNTs is mainly localized in the continuous, thermodynamically favored PLA component. When the sample is exposed to cyclohexane vapor, the vapor selectively penetrates into the PS component, while the conductive network in PLA is hardly swollen by cyclohexane. Therefore, the $R_{rel}$ of A50S50M0.5 is low. The still observed $R_{rel}$ of A50S50M0.5 may be caused by stress transferred from the swollen PS component to the PLA component, thus affecting the conductive MWCNT network present in PLA. With increasing MWCNT loading, it can be expected that some nanotubes also localize at or near the interface or even cross the interface, as it is indicated in **Fig. 4.3.3**. At a blend loading with 1 wt% CNTs, the local concentration within PLA is 2 wt%, which is well above the percolation threshold (about 0.4 wt%) [38]. Such CNTs partially localized in PS are directly affected under PS swelling induced by cyclohexane, thus $R_{rel}$ is higher for A50S50M1.0 than for A50S50M0.5.

The effect of partial migration of CNTs into PS is supported by the observation of photographs taken from the cyclohexane solution after PS extraction of A50S50M0.5 and A50S50M1.0 as shown in **Fig. 4.3.4a**. The darker color and the larger particles seen in case of A50S50M1.0 are indicative for a higher MWCNT fraction located in the dissolved PS. On the other hand, the PS extraction is nearly quantitative, as shown in **Fig. 4.3.4b**.

As the $R_{rel}$ caused by cyclohexane indicated, the exposure time was not sufficient to reach plateau values. Therefore, the long-term exposure of these differently annealed A50S50M1.0 composites towards saturated acetone (30.2%) and saturated cyclohexane (13%)

was studied and results are shown in **Fig. 4.3.14**. When being exposed to acetone vapor, the non-annealed sample (A-0) and that one annealed for 30 min (A-30) display unsteady behavior and achieve after 650 s of exposure very high $R_{rel}$ of 5500 % and 3500 %, respectively (**Fig. 4.3.14a**). The shape of the $R_{rel}$ vs. time curves suggests that the sensing process has two stages whereby in the first 300 s of exposure the $R_{rel}$ shows almost a linear increase (see **Fig. 4.3.14b**), which is due to the gradually destruction of the conductive network under polymer swelling. With increasing vapor penetration into the blend composites in the following sensing stage, the conductive network change is affected by PLA swelling and PS swelling. Therefore, a sharp $R_{rel}$ increase and a sensing plateau can be found during this stage, which is the result of simultaneous PLA and PS swelling.

For A-60 and A-120, the sensing response is comparatively small and homogeneously increasing with time. The terminal $R_{rel}$ values are 414 % and 20 %, respectively, showing their better stability under long-term exposure to saturated acetone vapor. For cyclohexane, all samples show a slow but continuous $R_{rel}$ increase with exposure time, which slows down with time and seems to approach a plateau value after 600 s (**Fig. 4.3.14c**). The response rate again depends on the annealing time and thus on crystallinity of the PLA component. The terminal $R_{rel}$ of A-0 is 32.5 % and for A-120 it is only 10 %. This also proves that annealing plays an important role in improving the stability of CPCs in vapor sensing application.
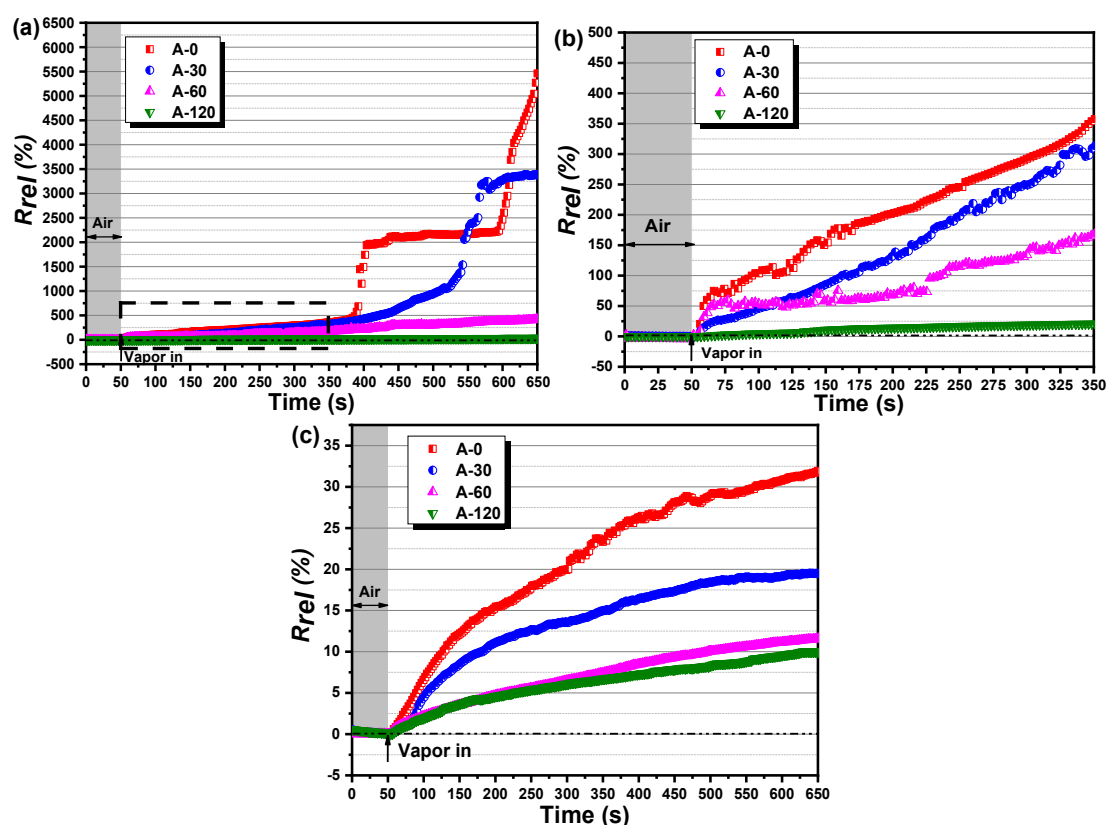


**Fig. 4.3.14** Relative resistance changes of differently annealed A50S50M1.0 composites when exposed towards (a, b) saturated acetone vapor (30.2 %) and (c) saturated cyclohexane vapor (13 %).

To explore the sensing selectivity of PLA/PS/MWCNT, vapor mixtures prepared from different acetone/cyclohexane solvent volume ratios were used for sensing tests. Li et al. investigated the sensing behavior of PS/CB composites towards mixtures of ethanol and tetrahydrofuran (THF) [160]. The results indicated that the $\Delta t_{max}$ (time to the maximum $R_{rel}$) decreased significantly when the ethanol/tetrahydrofuran volume ratio decreased from 4/1 to 2/1. Otherwise, the response rate increased accordingly, implying that the THF concentration is crucial for the PS/CB vapor sensing performance. This is due to the fact, that PS has much lower interaction with ethanol, but better interaction with THF. In this study, immiscible polymer blends with components having different interactions with the two solvents of the solvent mixture are applied. PLA has better interactions to acetone than cyclohexane, whereas PS has good interactions to both solvents. The sensing responses of A50S50M1.0 for long-term exposure in mixed vapors are shown in **Fig. 4.3.15**. A fast resistance increase can be observed once the samples are immersed in the testing chamber during the first 50 seconds, followed by a continuous slow $R_{rel}$ increase up to the end of the test. Similar to the test for single vapor, the non-annealed blend composite (A-0) shows the highest sensing response compared to the annealed samples. The terminal $R_{rel}$ after 600 s exposure to acetone/cyclohexane vapor mixtures of 1v/4v and 1v/1v are 425% and 375%, respectively, with this sample reaching only 150% in 4v/1v acetone/cyclohexane vapor (**Fig. 4.3.15a**). When comparing the sensing curves of the annealed samples (**Fig. 4.3.15b-d**), in accordance to the previous findings all of them show much lower terminal $R_{rel}$ than those of A-0. Interestingly, all annealed samples are most sensitive towards vapor mixtures prepared from 1v/1v mixed solvents. Perhaps this acetone /cyclohexane vapor ratio results in similar swelling of both polymers. Thus, there is no mutual confinement effect suppressing the swelling of the other polymer component.
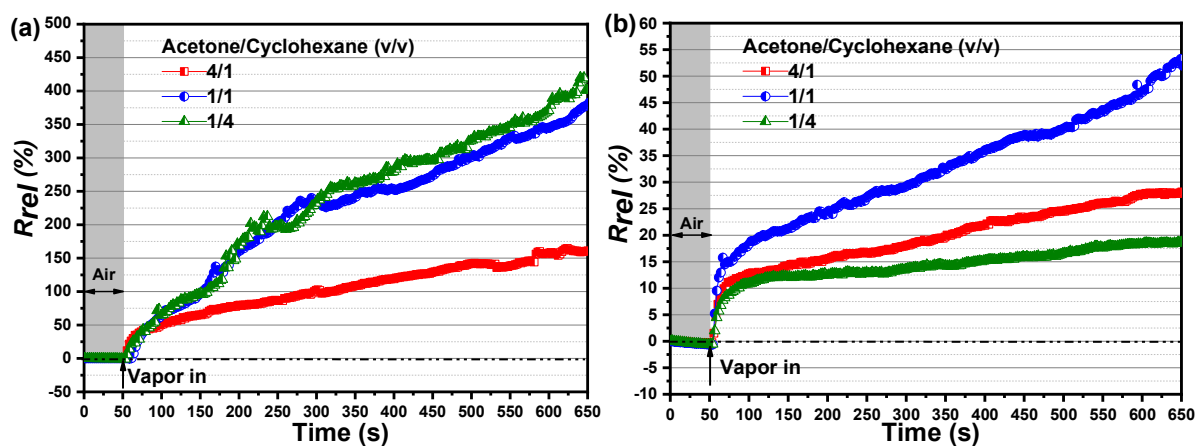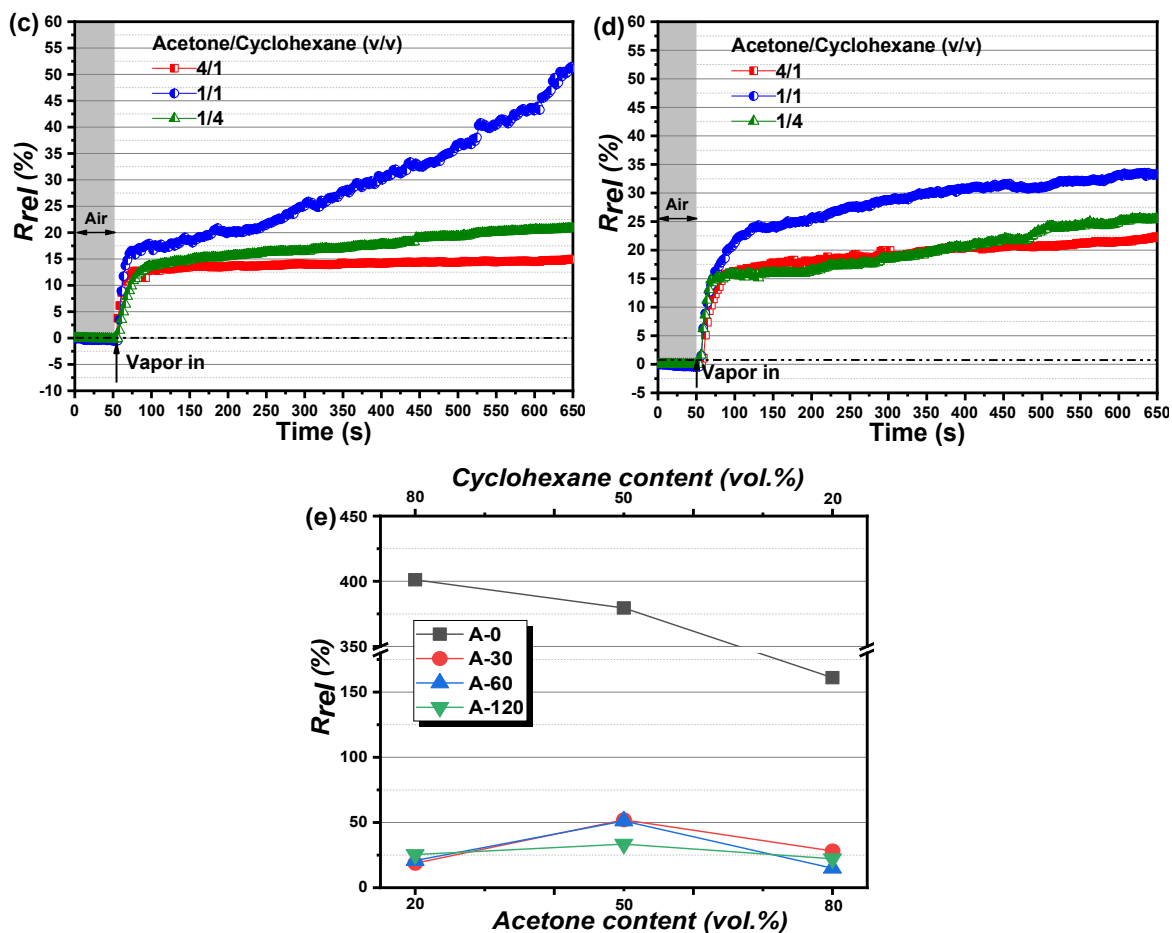
**Fig. 4.3.15** Effect of different annealing time of A50S50M1.0 composites on relative resistance changes when exposed towards vapors generated from different solvent compositions: (a) A-0, (b) A-30, (c) A-60, and (d) A-120. (e) The terminal $R_{rel}$ after 600s immersion of CPCs towards different vapor mixtures.

To compare the sensing response of CPCs towards different vapor mixtures, the terminal $R_{rel}$ after 600 s exposure are plotted in **Fig. 4.3.15e**. It can be clearly seen that the terminal $R_{rel}$ of the non-annealed composites decreases with the acetone content in the solvent mixture, indicating that the network is mainly influenced by acetone vapor penetration. The annealed samples exhibit low $R_{rel}$ towards vapor mixtures because of the increased crystallinity, which hampers the vapor penetration. Interestingly, in all annealed samples highest $R_{rel}$ are achieved in vapors of acetone/cyclohexane 50/50 vol% solvent mixtures. This proves that the electrical signal is generated from both the PLA and PS component simultaneously. According to such phenomenon, it is acknowledged that polymer swelling and filler distribution are two key issues in determining the $R_{rel}$ of PLA/PS/MWCNT composites.

### 4.3.6 Summary

In this chapter, PLA/PS/MWCNT blend composites were fabricated by melt mixing. Different blend ratios containing 0.5 wt% and 1.0 wt% MWCNTs were prepared and their morphologies were studied. A co-continuous structure is formed when the PLA/PS blend ratio is 50/50 wt%. At this composition, the blend composite containing 0.5 wt% MWCNTs shows a significantly higher conductivity than at other blend compositions. At 1.0 wt% MWCNT addition all blend composites are percolated and show nearly the same conductivity, which is about 3 decades higher than that of the PLA/PS=50/50 wt% blend with 0.5 wt% MWCNTs. The MWCNTs preferentially localize within the PLA component and the $\varphi_c$ of MWCNTs in PS/PLA=50/50 wt% blends is 0.4 wt%. Because of the suitable resistivity range and the nearly perfect co-continuous structure, this blend composition filled with 1.0 wt% MWCNTs (A50S50M1.0) was selected for cyclic vapor sensing tests. When being exposed to acetone vapor, A50S50M1.0 shows higher sensing responses with the increase of vapor concentration. At the same time, the reversibility of the swelling deteriorates during drying after exposure to higher vapor concentrations. The crystallinity of non-annealed A50S50M1.0 increases from 6.9 % to 35 % for 120 min annealed A50S50M1.0 at 150°C. Annealing of these blend composites min can significantly improve the reversibility but on the expense of the sensing response. The stabilization is ascribed to increased crystallinity of PLA after annealing. Crystalline regions are hardly accessible for vapor diffusion. Moreover, the increased crystallinity confines some volume of the amorphous part, thus hampering the vapor diffusion. Interestingly, blend composites with higher MWCNT content (1.0 wt%) display higher $R_{rel}$ when exposed towards cyclohexane vapor than those of the CPC with lower MWCNT loading (0.5 wt%). This suggests that A50S50M1.0 where the local concentration in the PLA component is 2.0 wt%, some nanotubes cross the interphase and are also located in the unfavorable PS component. This assumption is supported by extraction experiments.

When using solvent vapor mixtures of acetone/cyclohexane for sensing, the $R_{rel}$ of the non-annealed composites decreases with the acetone content in the solvent mixture. Otherwise, in case of annealed samples, the crystallinity is increased resulting in low $R_{rel}$ as compared to non-annealed samples. The solvent volume ratio of 1/1 resulted in the higher $R_{rel}$ than 1/4 or 4/1 volume ratios, which is attributed to the simultaneous swelling of the PLA and PS component. In summary, the morphology, filler distribution and the resulting vapor sensing behavior of CPCs were systematically investigated. The annealing process significantly improves the sensor stability and durability towards good solvent vapors.

## 4.4 Vapor sensing behavior of compact and porous PC/PVDF/MWCNT blend composites with different PC viscosities

### 4.4.1 Introduction

In chapter 4.2 and 4.3, the electrical, morphological, and vapor sensing behavior of MWCNT filled immiscible polymer blend composites were discussed. By comparing the vapor sensing performance of CPCs, it was found that PC/PS/MWCNT composites with co-continuous structure exhibited lower $R_{rel}$ but better reversibility as compared to CPCs with sea-island structure. It was concluded that the larger interface of co-continuous structure composites facilitate the vapor penetration and evaporation processing during sensing tests. Therefore, PLA/PS/MWCNT composites with co-continuous structure were selected for the following investigations. There was an obvious distinction in $R_{rel}$ for CPCs after different thermal annealing time. This was due to the fact that the MWCNTs were selectively localized in the PLA component and the different crystallinity of the PLA affected the conductive network change under vapor stimulation. However, conductive polymer blend composites, even annealed, still exhibited poor reversibility towards good solvent vapors, which is an issue to be improved.

In this chapter, the conductive network changes in a blend matrix and the vapor sensing behavior of CPCs with co-continuous structure will be further investigated. Therefore, the blend system of PVDF and PC was selected as a third blend system. This blend system was chosen as it contains two polymer components with completely different solubility behavior. For PC, good swelling towards most vapors is expected at room temperature, while PVDF is much more difficult to swell. Thus, PC/MWCNT acts as sensing component and PVDF should stabilize the blend structure of the composites during the vapor sensing tests. This study will focus on the influence of the blend viscosity ratio on MWCNT dispersion and localization in the blends, as well as on the morphological, rheological, electrical, and vapor sensing behavior. In addition, the successive cyclic sensing of compact sensors is compared with that of porous sensors in which the PC component is extracted.

Three PCs with different molecular weights were selected and compounded with PVDF and MWCNTs using the DSM Xplore15 at 260 °C with a rotation speed of 250 rpm for 10 min. The blend ratio of PC/PVDF was set as 40/60 wt% for all CPCs. At this composition a co-continuous structure was formed. The pellets cut from the obtained extruded strands were also compression molded using the same hot press machine under the pressing condition of 260 °C, 50 kN for 5 min. Next to these compact films, samples with a porous structure were prepared. For this, the compression molded samples were immersed in DCM

for 24 hours for dissolving the PC blend component, rinsed several times by fresh by DCM and dried in the oven.

### 4.4.2 Melt viscosity ratio between PCs and PVDF

Since it is known that, in addition to the blend composition, the melt viscosity ratio determines the type and fineness of the composite structures, the viscosity ratio between PC and PVDF was varied by using three different PC with high, middle, and low molecular weights hereinafter referred to as hPC, mPC, and lPC, respectively. To determine the viscosity ratios, the complex viscosity $|\eta^*|$ of the neat PCs and PVDF at the processing temperature of 260°C were measured (**Fig. 4.4.1a**) and the frequency dependent viscosity ratios were calculated (**Fig. 4.4.1b**). PVDF shows the strongest shear thinning effect and its complex viscosity lies between that of low and middle molecular PC. Due to the different frequency dependencies of PVDF and PCs an increase in viscosity ratio was found with increasing frequency. At the highest measured frequency, namely 100 rad/s, the viscosity ratios of lPC, mPC and hPC to PVDF are 0.7, 2.0 and 2.8, respectively..
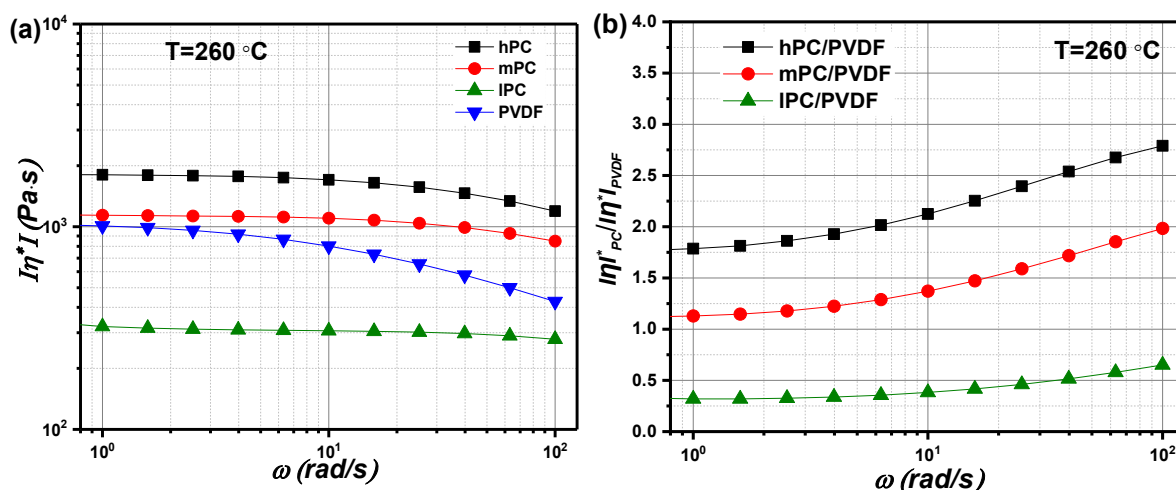


**Fig. 4.4.1** (a) Complex melt viscosity $|\eta^*|$ of neat PCs and PVDF and (b) viscosity ratios PC/PVDF versus angular frequency.

### 4.4.3 Morphological characterization

**Fig. 4.4.2a-c** shows the SEM micrographs of extruded PC/PVDF blends in which PC has been extracted. It can be observed that the domain size of remaining PVDF increases with the decrease of PC/PVDF viscosity ratio. **Fig. 4.4.2d-f** displays the SEM micrographs of extruded PC/PVDF/MWCNT-1.0 wt% composite strands in which PC has been extracted. With decreasing PC viscosity in the composites, the domain size of the structural elements increases and the blend morphology coarsens. As a measure for the degree of coarseness the

length of the blend interface per area unit was determined from the SEM images, which resulted in values of 2.19 µm/µm$^2$, 1.98 µm/µm$^2$, and 1.33 µm/µm$^2$ for composites containing hPC, mPC and lPC, respectively (see **Fig. 4.4.3**). The highest relative length of interface in lPC indicates the finest co-continuous structure. These values correspond to values of a characteristic domain size $\zeta$, a measure introduced by Bai et al. [100], of 0.46 µm, 0.50 µm and 0.75 µm (reciprocal value of length of the blend interface per area unit).
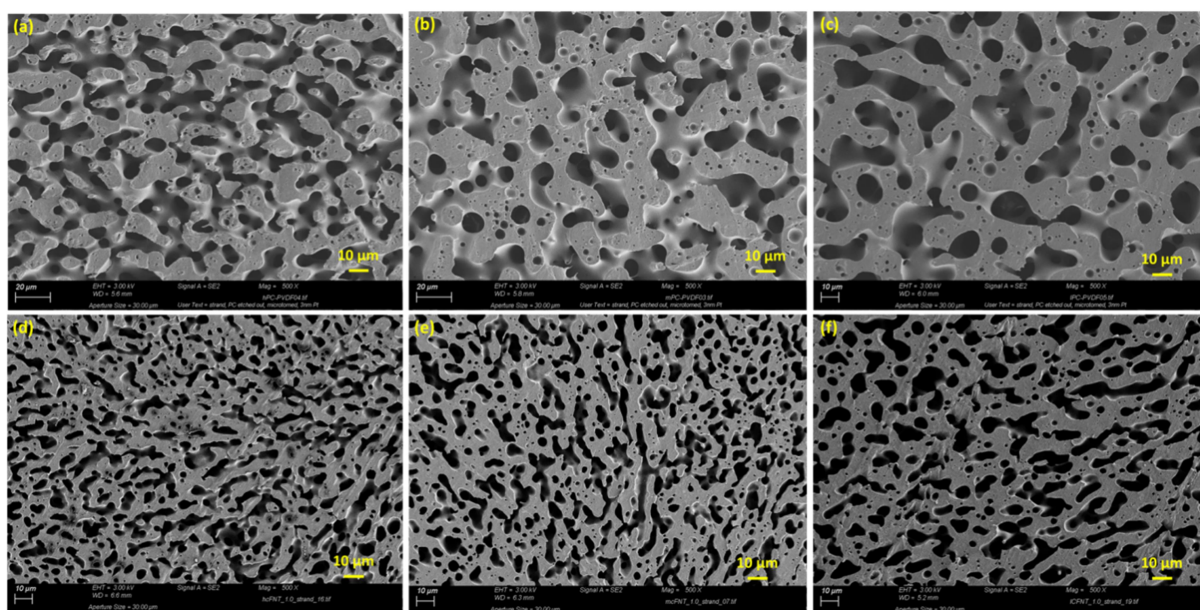


**Fig. 4.4.2** SEM micrographs of PC/PVDF blend (blend ratio is 40/60 wt%) strands with (a) high viscosity PC (hPC), (b) medium viscosity PC (mPC), and (c) low viscosity PC (lPC). (d-f) are the corresponding PC/PVDF/MWCNT-1.0 wt% composites. The PC component has been extracted out by dichloromethane.
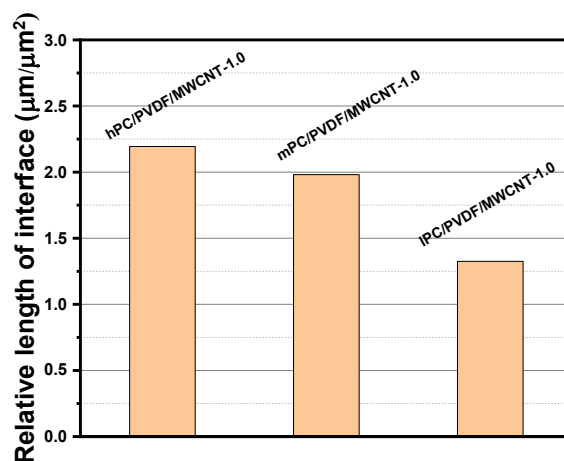


**Fig. 4.4.3** Relative length of the interface for PC/PVDF/MWCNT-1.0 wt% composites with different blend viscosity ratios.

The degree of continuity of the PC component was studied by quantitatively determining the proportion between the extracted polymer content and the added PC content

of CPCs. As the extracted polymer content was nearly exactly 40 wt% for all three PCs (see **Fig. 4.4.4**), the continuity of PC is ~100%, meaning that PC can be completely etched out by DCM. Interestingly, the remaining strand pieces appear grayish after PC extraction even if the MWCNTs were mainly localized in PC, which indicates that there are still some nanotubes in the PVDF component after the extraction.
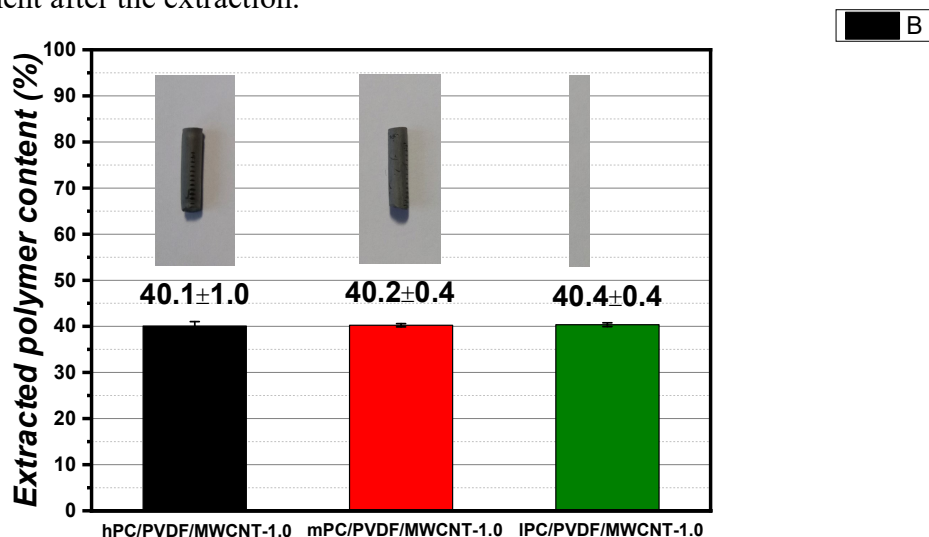


**Fig. 4.4.4** Extracted polymer content of PC/PVDF/MWCNT-1.0 blend composites after immersion of strand pieces in dichloromethane solvent for 48 h, insets show the extracted strand samples.

SEM on cut surfaces (**Fig. 4.4.5a-c**) without etching indicates that the MWCNT are localized in the PC, appearing as white areas in the darker PC component. This was confirmed by TEM investigations (**Fig. 4.4.5d-f**) performed on the sample containing low viscous PC. According to these micrographs taken at different magnifications, most of MWCNTs are selectively localized in the PC component and have a homogeneous dispersion. Interestingly, there are also some nanotubes that are located at the interface of the blends where they somehow connect both components (**Fig. 4.4.5f**), which can be an explanation for the grayish appearance of the extracted strands (**Fig. 4.4.4**).
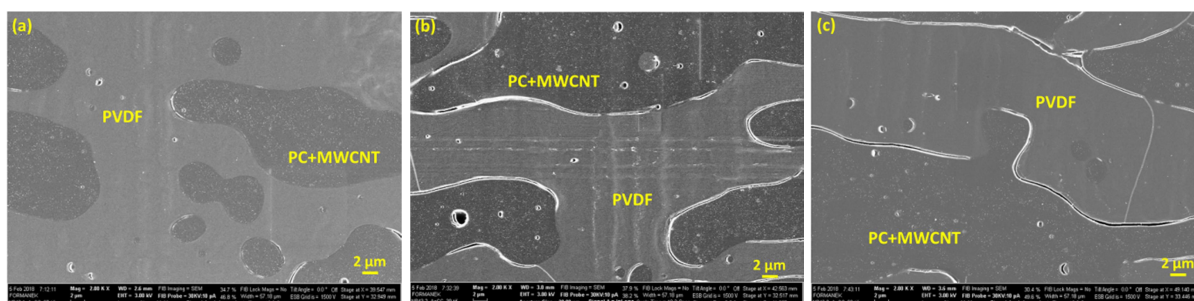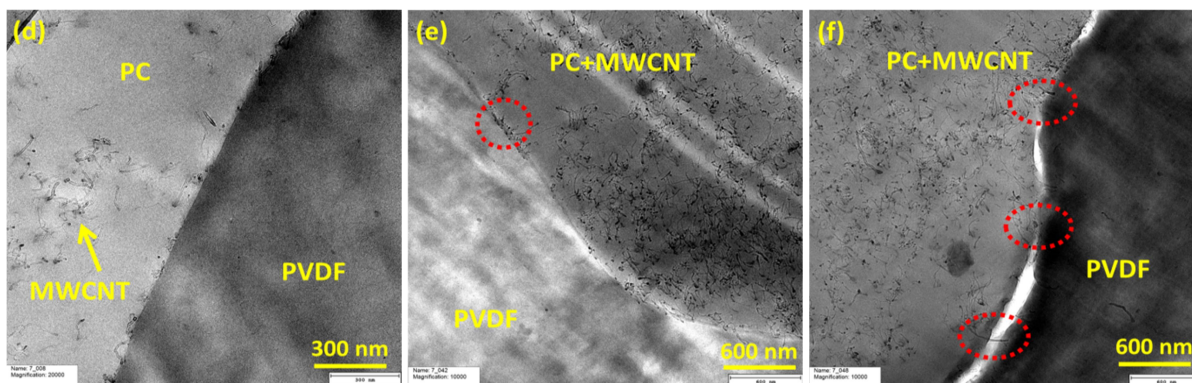
**Fig. 4.4.5** SEM micrographs of (a) hPC/PVDF/MWCNT-1.0, (b) mPC/PVDF/MWCNT-1.0, (c) lPC/PVDF/MWCNT-1.0; (d-f) TEM micrographs of lPC/PVDF/MWCNT-1.0 at different locations and magnifications.

In selectively filled co-continuous blends high electrical conductivity of the composites is only achieved if the filled component is continuous and conductive at the same time. The conductivity is related to the state of dispersion of the nanofillers in the filled component. To quantify the MWCNT dispersion in the blend composites, transmission light microscopy was performed on thin sections of blend composites with 1 wt% MWCNTs. The images are shown in **Fig. 4.4.6** for two locations at different magnifications and the agglomerate area ratio of $A/A_0$ was calculated. Even in the light microscopy images the co-continuous structure can be observed as the filled PC component appears to be darker. However, next to nicely dispersed nanotubes also large MWCNT agglomerates are seen as black areas in the blend matrix. For the blend composite with high viscous PC their number and agglomerate area ratio are the highest and $A/A_0$ shows a value of 1.52 %. With decreasing blend viscosity ratio, the agglomerate area ratio decreases and is 0.57 % for mPC/PVDF/MWCNT-1.0 and 0.25% for lPC/PVDF/MWCNT-1.0. This finding illustrates the importance of the infiltration of polymer chains in the primary agglomerate structures as the first step of the dispersion. The PC with lower melt viscosity can easier enter into the space existing within the nanotubes in the as supplied CNT material, thus reducing the agglomerate strength which enables easier disagglomeration and dispersion [202].

| hPC/PVDF/MWCNT-1.0 | mPC/PVDF/MWCNT-1.0 | lPC/PVDF/MWCNT-1.0 |

$\frac{A}{A_0} = 1.52\% \pm 0.57\%$

$\frac{A}{A_0} = 0.57\% \pm 0.16\%$

$\frac{A}{A_0} = 0.25\% \pm 0.15\%$
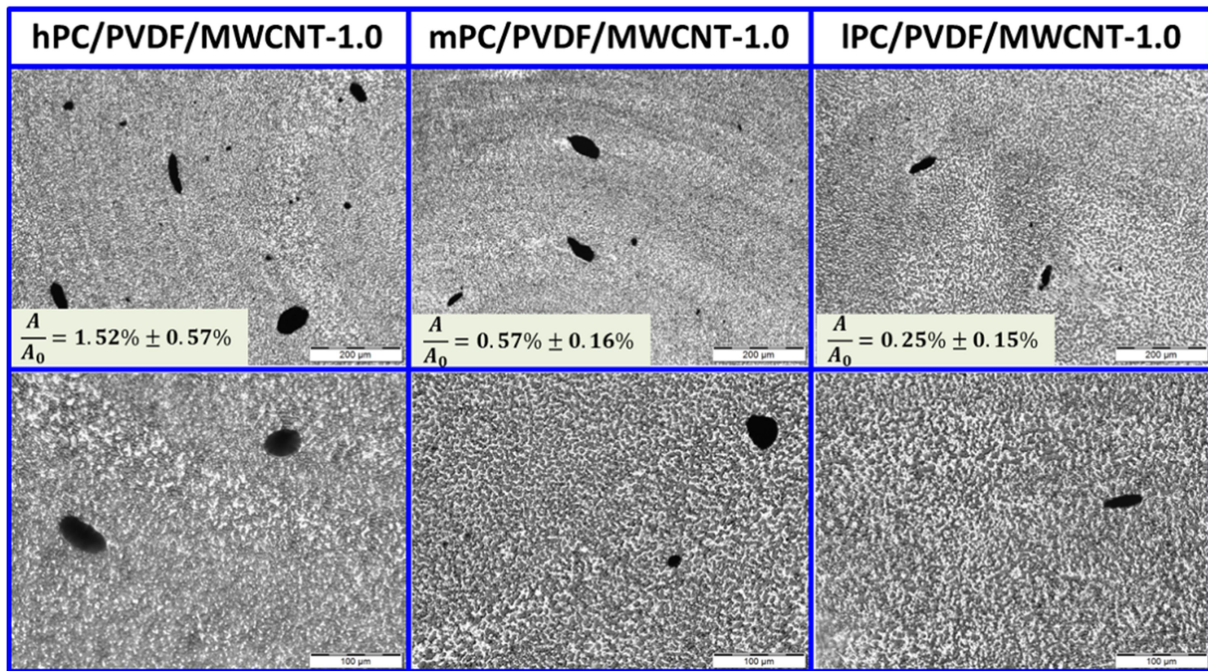
**Fig. 4.4.6** Optical micrographs of the blend composite strands with the blend ratio of 40/60 wt% showing different states of MWCNT dispersion and fineness of the co-continuous blend morphology.

In order to get more detailed blend morphology information of the porous composites as used for sensing, higher magnification SEM was performed on cryo-fractured extracted compression molded films of PC/PVDF/MWCNT-1.0 composites (**Fig. 4.4.7a-f**) as they were later used for the sensing trials. The empty darker areas represent the etched PC component area. The continuous structure of the remaining PVDF component is clearly seen, however it is significantly roughened as compared to the extruded strands illustrating that the compression molding step resulted in morphology coarsening. In addition it can be observed that there are also some MWCNTs kept at the surface of PVDF after extraction, visible in all the three composites (see **Fig. 4.4.7b, d and f**). The nanotubes wrapped onto PVDF have better dispersion for low viscous PC based CPCs as compared to the blend composites with higher viscous PCs. This finding can be attributed to the similar viscosity of lPC and PVDF.
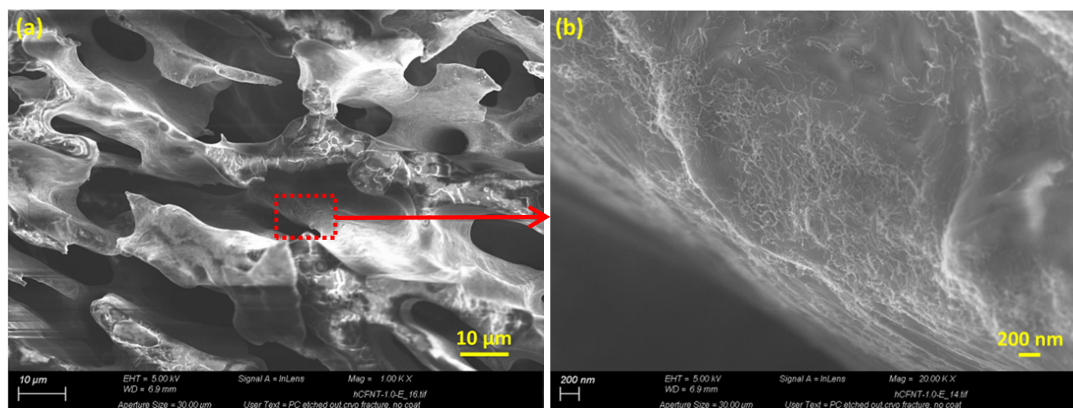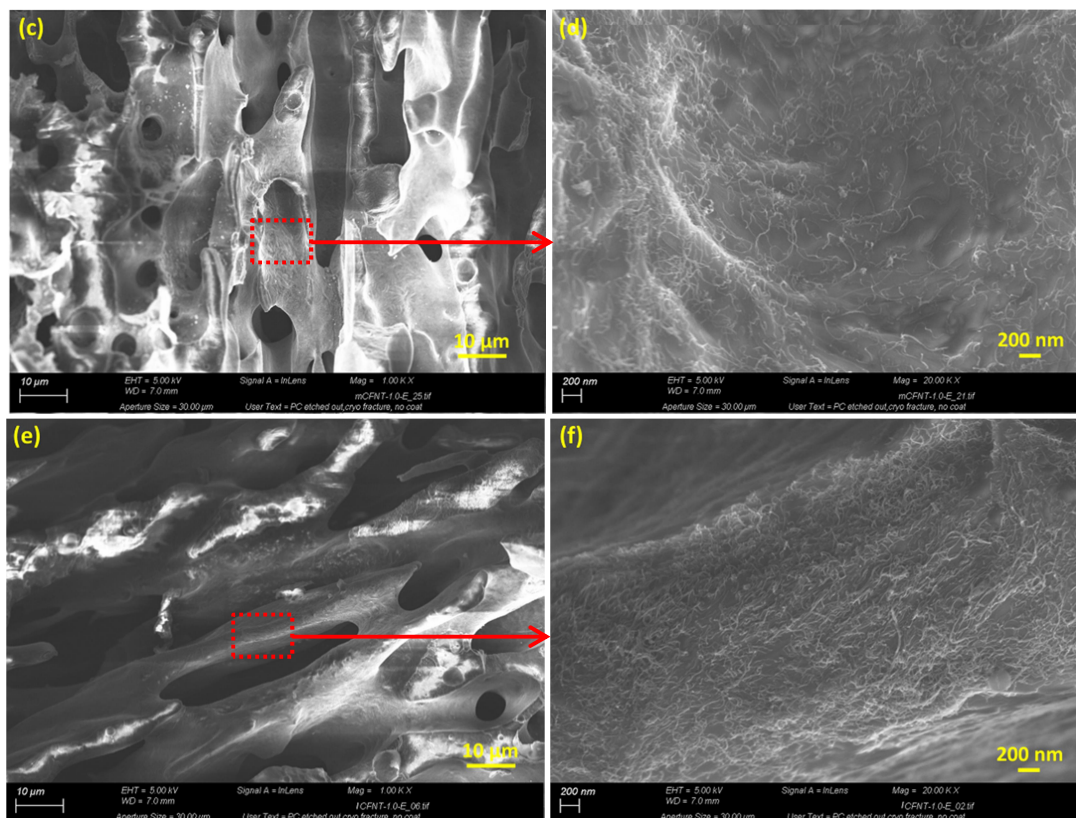
**Fig. 4.4.7** SEM micrographs of cryofractured extracted compression molded films of (a, b)hPC/PVDF/MWCNT-1.0, (c, d) mPC/PVDF/MWCNT-1.0, and (e, f) lPC/PVDF/MWCNT-1.0 composites.

### 4.4.4 Rheological behavior of PC/PVDF/MWCNT blend composites

Next to those of the neat blend components, the rheological properties of the prepared blends and blend composites were investigated. **Fig. 4.4.8** shows a comparison of storage modulus ($G'$), loss modulus ($G''$) and complex viscosity ($|\eta^*|$) versus angular frequency for the neat blends and the conductive blend composites containing 1.0 wt% MWCNT. It can be seen that the $G'$ and $G''$ of the composites decreases with angular frequency. The addition of 1.0 wt% MWCNT increases the $G'$ and $G''$ of PC/PVDF/MWCNT composites significantly especially at high frequency as compared to those of PC/PVDF blends (**Fig. 4.4.8a** and **b**). $G'$ is a sensitive measure of microstructure in the melt state, especially in the low frequency regime where time does not limit molecular relaxation processes. Higher $G'$ values at low frequencies relate to a more elastic structure where molecular motion is inhibited by structural feature in immiscible polymer blends and filler network formation in nanocomposites [27, 182, 183]. Otherwise, if we look at $|\eta^*|$ of CPCs, it can be seen clearly that 1.0 wt% MWCNT addition increases the $|\eta^*|$ of PC/PVDF/MWCNT composites significantly at low frequencies (**Fig. 4.4.8c**). This is attributed to the blend microstructure change and conductive network formation after MWCNT addition. Moreover, both lPC/PVDF and lPC/PVDF/MWCNT-1.0

display stronger shear thinning effect at higher frequency as compared to hPC and mPC based CPCs, which is attributed to better dispersion of MWCNTs in lPC matrix that makes conductive network more sensitive to damages induced by external stress.
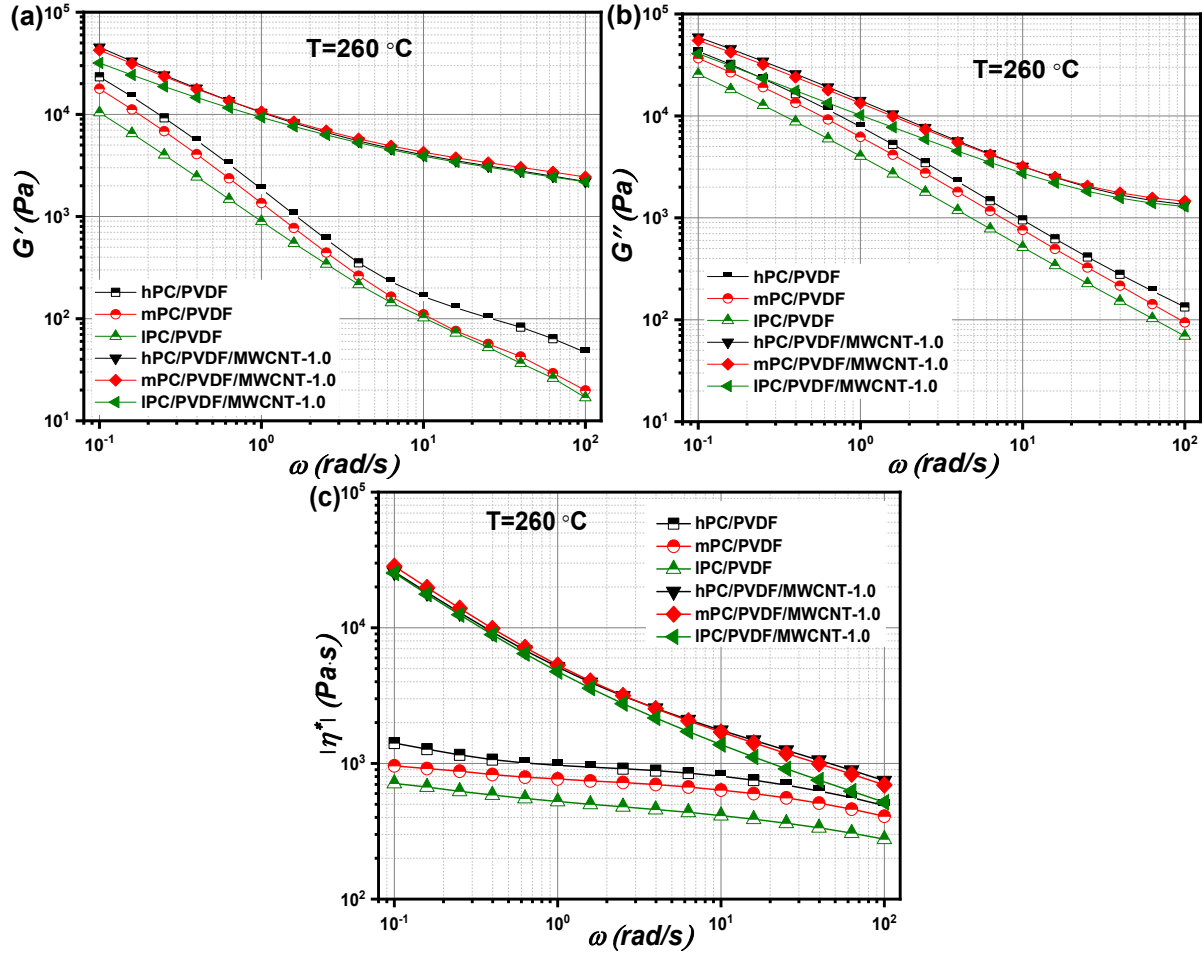


**Fig. 4.4.8** (a) Storage modulus $G'$, (b) loss modulus $G''$, and (c) complex viscosity $|\eta^*|$ of neat PC/PVDF and PC/PVDF/MWCNT-1.0 wt% composites versus oscillation frequency at 260 °C.

To better understand the rheological behavior of conductive polymer blend composites, the effect of increasing MWCNT amount on the rheological behavior of lPC/PVDF blends was investigated. The $G'$, $G''$ and $|\eta^*|$ versus frequency at 260 °C for lPC/PVDF/MWCNT with different MWCNT contents is plotted in **Fig. 4.4.9**. It can be observed that as little as 0.05 wt% MWCNT incorporation into the blend matrix causes an obvious increase in $G'$, $G''$ and $|\eta^*|$ at low frequencies. Taking $|\eta^*|$ as an example, with increasing MWCNT content, the increase in viscosity at lower frequencies becomes higher and also at higher frequencies the viscosity values increase starting at 0.3 wt% MWCNT loading. This phenomenon is associated with the MWCNT-MWCNT interactions and the formation of combined networks of MWCNTs and polymer chains [185, 203, 204]. With increasing MWCNT loading in lPC/PVDF blends, $G'$ increases monotonously over the entire frequency. Similar behavior is

113

observed for $G''$. The increase of all investigated rheological parameters is due to a combined effect of changes in the blend morphology and the contribution of the filled PC component, in which the percolated CNT network becomes denser with increasing CNT content.
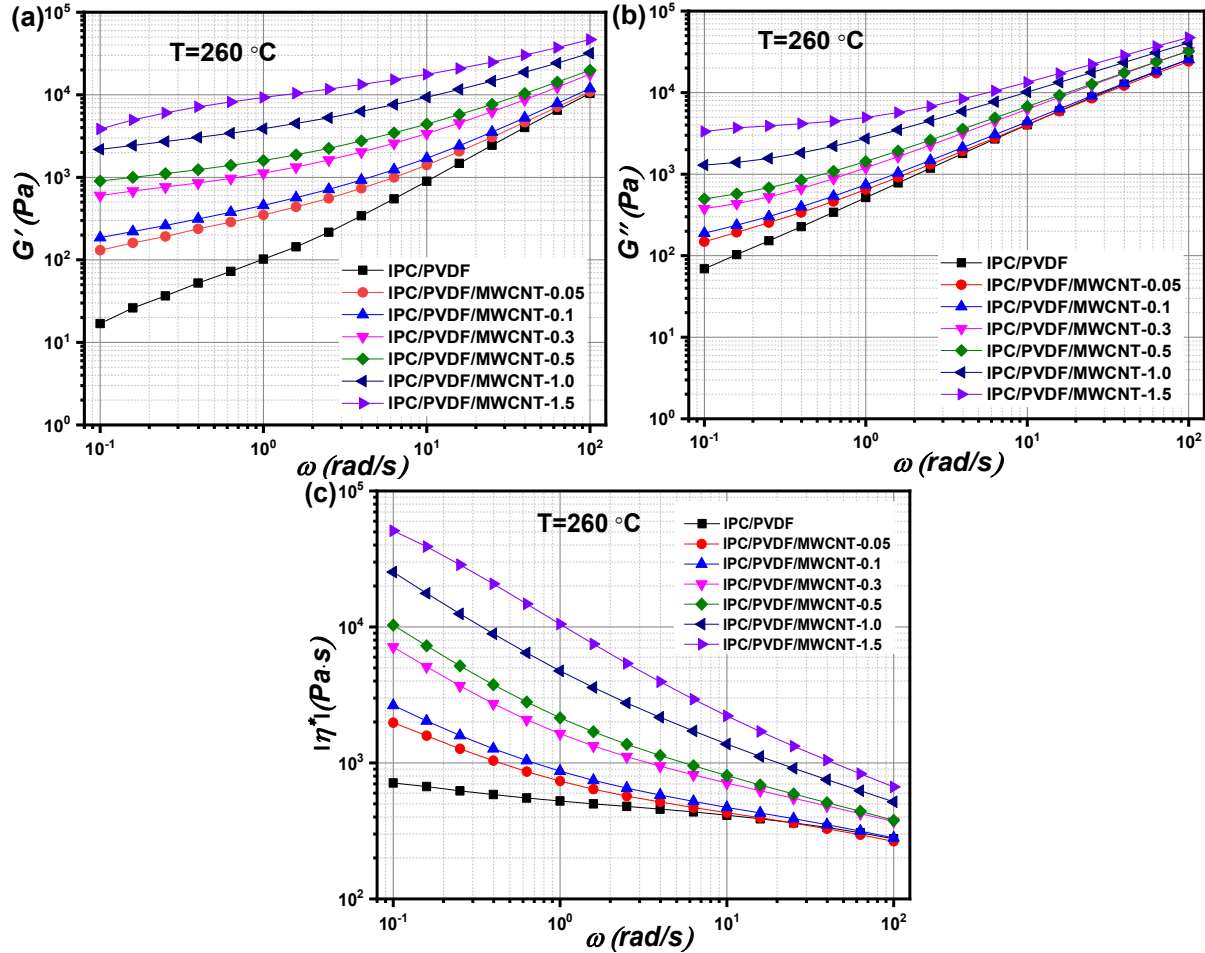


**Fig. 4.4.9** (a) Storage modulus $G'$, (b) loss modulus $G''$, and (c) complex viscosity $|\eta^*|$ of neat lPC/PVDF and lPC/PVDF/MWCNT composites versus oscillation frequency at 260 °C.

### 4.4.5 Electrical properties of PC/PVDF/MWCNT blend composites

The electrical volume conductivity of the PC/PVDF/MWCNT blend composites as a function of MWCNT content is shown in **Fig. 4.4.10a**. The electrical conductivity of the neat PC/PVDF blends is *ca.* $5 \times 10^{-15}$ S/cm. When adding 0.05 wt%, hPC/PVDF/MWCNT and mPC/PVDF/MWCNT composites show a slight increase in conductivity to $10^{-14}$ S/cm, while in lPC/PVDF/MWCNT the conductivity significantly increases to approx. $10^{-7}$ S/cm, showing the occurrence of electrical percolation. For hPC/PVDF/MWCNT and mPC/PVDF/MWCNT percolation takes place at filler loadings between 0.1 wt% and 0.3 wt% with fitted values of 0.25 wt% and 0.18 wt%, respectively (see **Fig. 4.4.10b** and **c**). Comparing the three CPC systems (**Fig. 4.4.10b** and **c**), the lPC/PVDF/MWCNT system exhibits higher electrical conductivity than the other two kinds CPCs at low MWCNT loadings and its $\varphi_c$ is only 0.03

114

wt.%. At MWCNT contents of 0.3 wt% and higher, the three composite systems have similar volume conductivity with plateau values in the same order. The inset in **Fig. 4.4.10a** shows the conductivity comparison of three CPCs with 1.0 wt% MWCNT. Obviously, all the composites have similar volume conductivity values of about $2 \times 10^{-4}$ S/cm. This means that CPCs with 1.0 wt% MWCNT are all percolated with conductivity values high enough to avoid surpassing the upper limit of the multi-meter in the following sensing measurements.
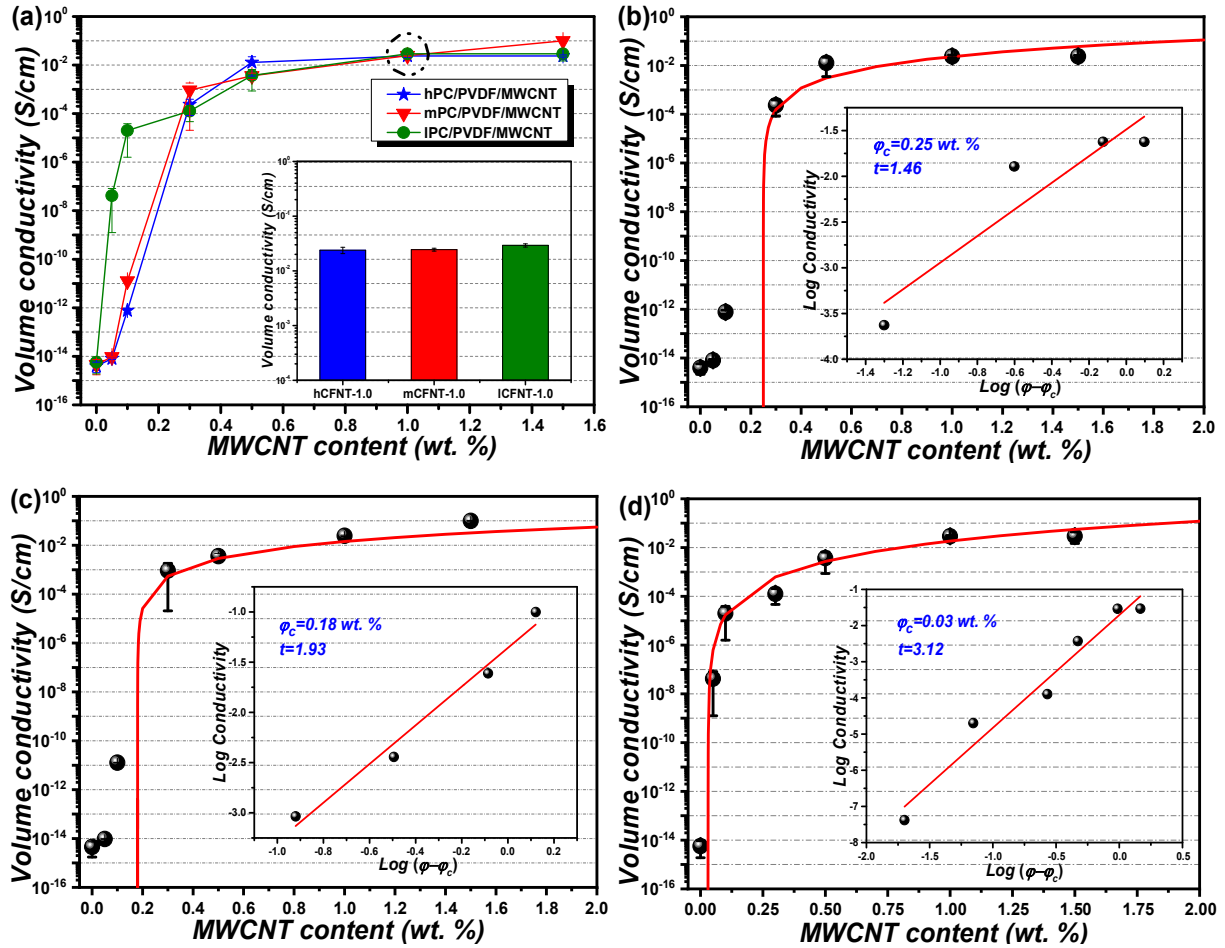


**Fig. 4.4.10** (a) electrical volume conductivity of hPC/PVDF/MWCNT, mPC/PVDF/MWCNT and lPC/PVDF/MWCNT as a function of MWCNT content, the inset is the conductivity comparison of three CPCs with 1.0 wt% MWCNT; (b-d) non-linear fitted percolation curves of hPC/PVDF/MWCNT, mPC/PVDF/MWCNT and lPC/PVDF/MWCNT composites.

Next to the compact CPCs, the electrical conductivity of the porous materials, obtained by extraction of PC, was also measured. **Fig. 4.4.11** shows the electrical conductivity comparison between compact and porous composites. For these selected composites, the MWCNT loading are all fixed at 1.0 wt. %, which is far higher than the $\varphi_c$ of the PC/PVDF/MWCNT composites. Therefore, the conductivities for compact CPCs are almost the same (**Fig. 4.4.11a**). However, the PC extraction causes a significant conductivity

decrease. The conductivities of porous CPCs are 4 or 5 orders of magnitude less than those of the corresponding compact CPCs (**Fig. 4.4.11b**). Since MWCNTs are selectively localized in the PC component, most MWCNT have been extracted with PC by DCM, which results in the sharp decrease of the conductivity. However, it can be seen that the porous lPC/PVDF/MWCNT sample has the highest conductivity among these three porous materials, which might be attributed to the better dispersion of MWCNTs in the low viscous PC polymer matrix and a more homogeneous dispersion of remaining MWCNTs at the surface of the non-dissolved PVDF component.
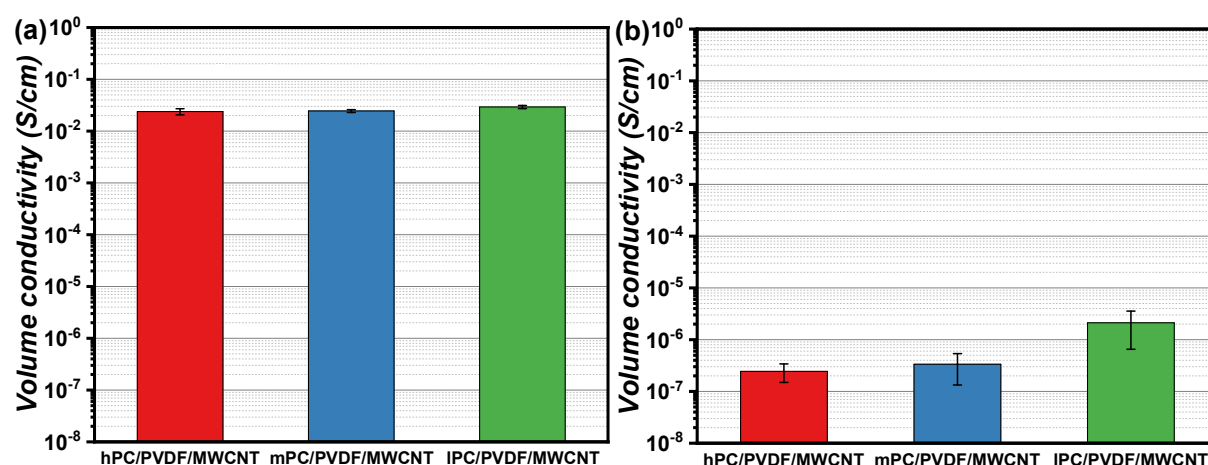


**Fig. 4.4.11** Electrical volume conductivity of hPC/PVDF/MWCNT-1.0, mPC/PVDF/MWCNT-1.0 and lPC/PVDF/MWCNT-1.0 (a) compact samples before extraction and (b) porous samples after extraction of PC.

## 4.4.6 Vapor sensing behavior of PC/PVDF/MWCNT blend composites

To achieve a good understanding of the vapor sensing behavior of PC/PVDF/MWCNT, the vapor sensing performance of composites with different blend viscosity ratios towards different vapors was investigated. It has been generally accepted that the resistance changes of CPCs are resulting from the conductive network changes under polymer swelling and de-swelling. In this chapter, vapors of dichloromethane (DCM), acetone, teteahydrofurane (THF) and ethyl acetate (EA) were selected as analytes. The solubility parameters of these solvents and the polymers are given in **Table 4.4.1**.

**Table 4.4.1** Hansen solubility parameters of polymers and solvents [59].

| Materials | $\delta_D$ (MPa)$^{1/2}$ | $\delta_P$ (MPa)$^{1/2}$ | $\delta_H$ (MPa)$^{1/2}$ | $\delta$ (MPa)$^{1/2}$ |
|---|---|---|---|---|
| DCM | 18.2 | 6.3 | 6.1 | 20.2 |
| Acetone | 15.5 | 10.4 | 7.0 | 19.9 |
| THF | 16.8 | 5.7 | 8.0 | 19.5 |
| EA | 15.8 | 5.3 | 7.2 | 18.2 |
| PC | 18.1 | 5.9 | 6.9 | 20.2 |
| PVDF | 17.2 | 12.5 | 9.2 | 23.2 |

116

As discussed above, the Flory-Huggins interaction parameter $\chi_{12}$ is an important indicator to predict the vapor sensing performance of CPCs during sensing tests [168, 205]. Typically, two materials tend to be miscible if the difference between their solubility parameter is small, i.e. the lower the $\chi_{12}$ value, the stronger interaction between polymer and vapor. From the values given by Hansen (see **Table 4.4.1)**, the $\chi_{12}$ values between the solvents and polymers were calculated and listed in **Table 4.4.2**. It can be concluded that all the selected solvents can be regarded as good solvents to PC due to their very low $\chi_{12}$ values. These vapors are called "good vapors" in the following. In terms of PVDF, EA is regarded as poor vapor and the other organic vapors as medium vapors.

**Table 4.4.2** Molar volume ($V_{mol}$), saturated partial pressure ($P_i$), solubility parameters ($\delta$), and Flory-Huggins interaction parameters ($\chi_{12}$) of polymers and organic solvents at 25 °C.

| Materials | $V_{mol}$ (cm$^3$·mol$^{-1}$) | $P_i$ (kPa, 25°C) | $\delta$ (MPa)$^{1/2}$ | $\chi_{12}$ | |
|---|---|---|---|---|---|
| | | | | PC | PVDF |
| DCM | 63.9 | 13.0 | 20.2 | 0 | 0.232 |
| Acetone | 73.5 | 30.6 | 19.9 | 0.003 | 0.325 |
| THF | 81.0 | 23.5 | 19.5 | 0.016 | 0.451 |
| EA | 97.9 | 12.6 | 18.2 | 0.159 | 0.993 |
| PC[59] | - | - | 20.2 | | |
| PVDF[206] | - | - | 23.2 | | |

Although many studies on CPC sensors have been performed, the sensor durability towards good solvent vapors is still a big challenge [36, 38, 68, 158]. Most of single polymer based CPC sensors exhibit poor reversibility when being exposed to good solvent vapors. The conductive networks are usually damaged irreversibly under polymer swelling because of the strong vapor/polymer interaction. Therefore, improving the CPC sensor reversibility to good solvent vapors is of great importance to enhance the cyclic use of sensors. Adopting immiscible PC/PVDF blends seems to be a promising choice. As a kind of polyester polymer, PC has good swelling to most of organic vapors [201]. PVDF, a solvent resistive polymer, is a good candidate in achieving good reversibility of CPC sensor upon exposure to good solvent vapors of the sensing polymer component (which in this case is PC) [207].The vapor sensing performances of PC/PVDF/MWCNT towards good solvent vapors for PC are discussed below.

### 4.4.6.1 Cyclic sensing behavior of PC/PVDF/MWCNT blend composites towards good vapors for PC

For the sensing tests, the cyclic sensing protocol was controlled as 100 s in saturated vapor of acetone, THF or EA and 150 s in dry air and 4 cycles were performed for each

solvent vapor. The $R_{rel}$ of CPCs towards cyclic vapor/air exposure is shown in **Fig. 4.4.12. Fig. 4.4.12a** illustrates that in acetone vapor the blend composite hPC/PVDF/MWCNT-1.0 exhibit much higher $R_{rel}$ for each cycle as compared to the corresponding CPCs with mPC or lPC. Once being exposed to acetone vapor, the $R_{rel}$ of hPC/PVDF/MWCNT-1.0 increases immediately to *ca.* 30000 % in less than 50 s, followed by a fluctuation of $R_{rel}$ in the rest of immersion time. After dry air injection, the $R_{rel}$ decreases immediately, demonstrating a good reversibility of the composite. In the following cycles, the composite shows similar sensing performance as in the first cycle. For mPC/PVDF/MWCNT-1.0 and lPC/PVDF/MWCNT-1.0, the average maximum $R_{rel}$ are around *ca.* 3500 % and 1250 %, respectively, which manifests the higher stability of their conductive networks. Moreover, all these three CPCs show excellent sensing reversibility, and the sample resistance of mPC/PVDF/MWCNT-1.0 and lPC/PVDF/MWCNT-1.0 could even go back to their initial resistance after drying in air. Such good reversibility may be attributed to the perfection of the co-continuous structure. The continuous interface promotes the vapor diffusion and evaporation from the blend components during drying. This good de-swelling behavior leads to the better reversibility of CPCs.
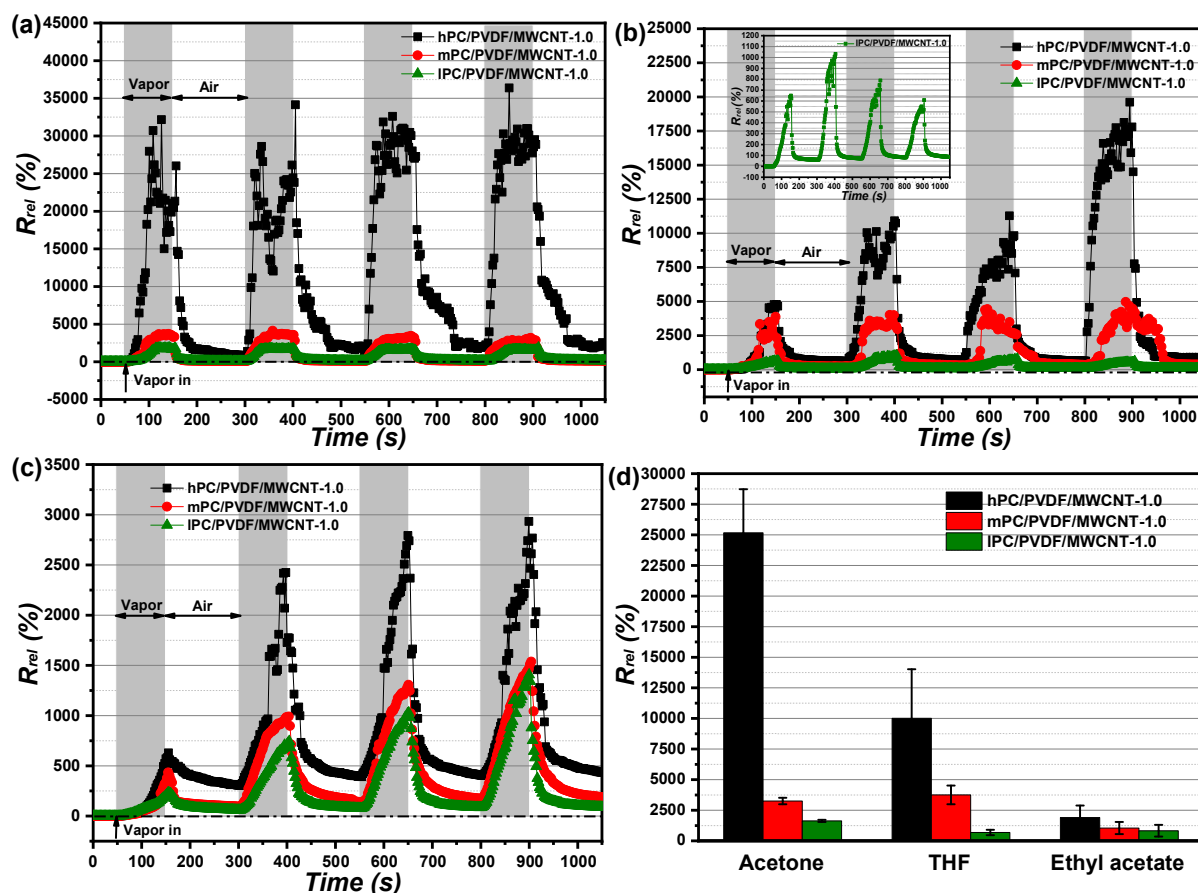


**Fig. 4.4.12** Cyclic vapor sensing behavior of hPC/PVDF/MWCNT-1.0, mPC/PVDF/MWCNT-1.0, and lPC/PVDF/MWCNT -1.0 towards saturated (a) acetone, (b) THF and (c) ethyl acetate. (d) Mean values of

maximum relative resistance change for CPCs from first cycle to fourth cycle towards different vapors, error bars show the standard deviation of the four regarded cycles.

**Fig. 4.4.12b** illustrates cyclic vapor sensing performances of CPCs towards THF. The $\chi_{12}$ of PC/THF and PVDF/THF are 0.016 and 0.451, respectively, which is higher than their corresponding $\chi_{12}$ values towards acetone. Unlike acetone, hPC/PVDF/MWCNT-1.0 shows an increased maximum $R_{rel}$ with sensing cycles. The maximum $R_{rel}$ in the first cycle is ca. 5000 %, while it reaches nearly 20000 % in the fourth cycle related to the initial value before the first cycle. Besides, the composites also exhibit unstable sensing during immersion due to the worse MWCNT dispersion in the hPC matrix. In comparison, mPC/PVDF/MWCNT-1.0 and lPC/PVDF/MWCNT-1.0 exhibit much more stable sensing signals towards THF vapor, and their average maximum $R_{rel}$ for the cyclic sensing are 3750 % and 750 %, respectively (**Fig. 4.4.12d**). The cyclic vapor sensing behavior of CPCs towards EA is shown in **Fig. 4.4.12c**. As predicted, EA has the weakest interaction with PC compared with the other selected vapors. As seen in **Fig. 4.4.12c**, hPC/PVDF/MWCNT-1.0 displays an increasing maximum $R_{rel}$ from the first cycle of 700 % to the fourth cycle of 3000 %. mPC/PVDF/MWCNT-1.0 and lPC/PVDF/MWCNT-1.0 show much lower responses, but also increasing $R_{rel}$ values with each cycle.

As is shown in **Table 4.4.2**, the $\chi_{12}$ of PC and DCM is 0, which indicates that DCM is the best solvent for PC. The cyclic sensing curves of CPCs upon exposure to DCM vapor are shown in **Fig. 4.4.13**. The maximum $R_{rel}$ of hPC/PVDF/MWCNT-1.0 in the first cycle is only 175 %. When dry air is injected into testing chamber, the sample maintains stable $R_{rel}$ values without any sign of resistance recovery. In the following three cycles, the $R_{rel}$ keeps increasing. In the case of good vapor, Wang et al. reported vapor sensing behavior of wet-spinning SBS/MWCNT fiber composites that the poor reversibility is attributed to the irreversible damage of the conductive network [133]. For the mPC/PVDF/MWCNT-1.0 blend composite, it can be seen that the $R_{rel}$ in first cycle is 400% and exhibits a slight $R_{rel}$ decrease during the drying cycle. The terminal $R_{rel}$ of each cycle increases gradually with the cycle number, which proves that the conductive network during the drying periods is only partially reconstructed. Regarding lPC/PVDF/MWCNT-1.0, the maximum $R_{rel}$ in the first cycle is ca. 500 %, followed by an $R_{rel}$ decrease to 300 %. After this conditioning effect of first cycle, the terminal $R_{rel}$ of each cycle goes back to its initial $R_{rel}$ from the second cycle on. For the better reversibility of lPC/PVDF/MWCNT-1.0 towards DCM as compared to the blend composites with mPC and hPC, two possible reasons can be assumed. On one hand, lPC based composites have larger domain sizes that can facilitate the penetration and evaporation of

119

vapor. On the other hand, despite comparable electrical conductivities of the three samples, the MWCNTs have best dispersion in the lPC matrix, so that the conductive network is more homogeneous as compared to the other two composites at the same filler loading. Therefore, the conductive network can be more easily damaged and rebuilt under polymer swelling and de-swelling.
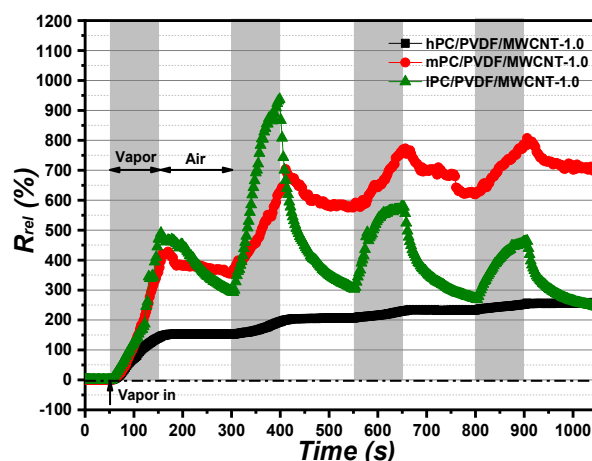


**Fig. 4.4.13** Cyclic vapor sensing behavior of PC/PVDF/MWCNT composites with different blend viscosity ratios towards saturated DCM vapor.

To further investigate the mechanism of vapor sensing, lPC/PVDF/MWCNT composites with different MWCNT loadings were selected for additional cyclic vapor sensing tests. **Fig. 4.4.14a** displays the $R_{rel}$ of lPC/PVDF/MWCNT with different MWCNT contents upon exposure to saturated DCM vapor. For lPC/PVDF/MWCNT-0.5, a sharp $R_{rel}$ increase is observed to *ca.* 2500 % after DCM vapor injection, followed by a fluctuated $R_{rel}$. When dry air is delivered into the testing chamber, $R_{rel}$ decreases instantly. From the second cycle, the maximum $R_{rel}$ of composites has a slight decrease with cycles. Nevertheless, the composites still exhibit good reversibility. For the lPC/PVDF/MWCNT-1.0 blend composite, already described before, a similar but more stable sensing tendency is observed, which is attributed to the more perfect conductive network in the composites. lPC/PVDF/MWCNT-1.5 exhibits the comparatively lowest $R_{rel}$ upon exposure to DCM vapor. This sample has the densest MWCNT network and reacts weakest to the DCM vapor exposition. These results also confirm that higher filler loading of the blend composites improves the sensing stability at the expense of $R_{rel}$.

**Fig. 4.4.14b** demonstrates the cyclic vapor sensing behavior of the selected lPC based blend composites CPCs towards saturated ethyl acetate vapor. All three CPCs do not reach a sensing plateau within the 100 s immersion caused by the comparatively weaker interaction between PC and EA vapor that makes the polymer chain relaxation process slower compared

to the other studied solvents, resulting in less pronounced change in the conductive network structure. Taking lPC/PVDF/MWCNT-0.5 and lPC/PVDF/MWCNT-1.5 as an example, both of them have a similar maximum $R_{rel}$ in the first cycle of about 625 %, while in the fourth cycle $R_{rel}$ are 2500 % and 750 %, respectively. Also these results indicate that the $R_{rel}$ of lPC/PVDF/MWCNT composites is related to the filler loading of the composites. Lower filler loadings result in higher $R_{rel}$, while higher filler loading provides composites with better sensing stability. From the comparison of the vapor sensing curves in DCM and EA, it can be concluded that the different conductive network states in lPC/PVDF/MWCNT composites with different MWCNT contents result in different sensing behavior when the composites are exposed to different vapors.
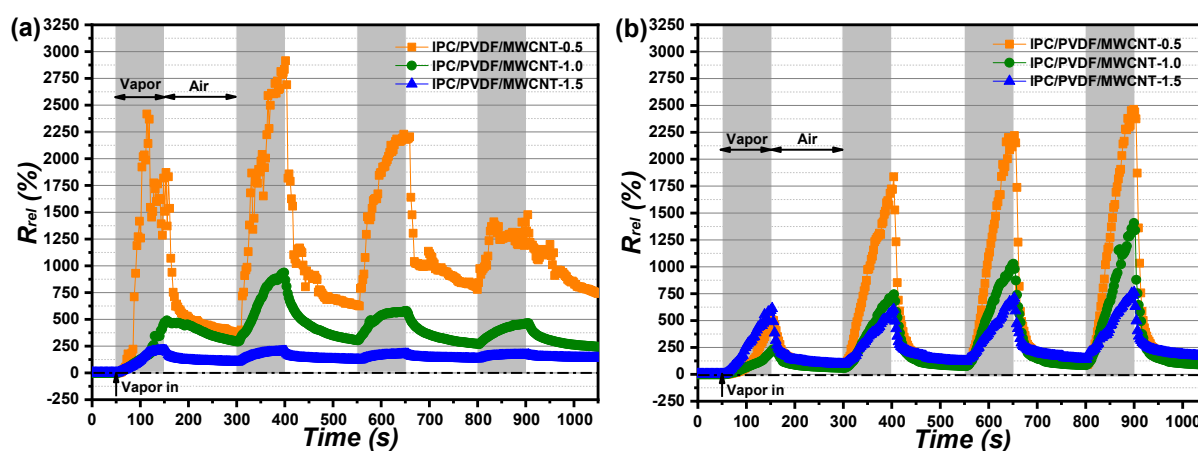


**Fig. 4.4.14** Cyclic vapor sensing behavior of lPC/PVDF/MWCNT composites towards saturated (a) DCM vapor and (b) ethyl acetate vapor.

### 4.4.6.2 Long-term immersion sensing behavior of PC/PVDF/MWCNT blend composites towards good vapors for PC

Long-term vapor stimulation was performed using a sensing protocol of 300 s immersion in vapor and 300 s drying in dry air. The $R_{rel}$ curves of lPC/PVDF/MWCNT-1.0 blend composites upon exposure to different organic vapors are shown in **Fig. 4.4.15a**. When being exposed to organic vapors, the selected blend composite experience an $R_{rel}$ increase followed by a steady $R_{rel}$ during vapor exposure. Interestingly, the sensing curve of lPC/PVDF/MWCNT-1.0 towards DCM is different from that in the other three vapors. With DCM vapor the $R_{rel}$ increase is slower and the equilibrium state is reached in *ca.* 150 s. For the other three vapors, the initial $R_{rel}$ increase is much sharper. The sensing equilibrium time is *ca.*75 s for acetone and ca. 25 s for THF and EA, whereas the terminal $R_{rel}$ are 1250 %, 500 %, and 350 %, respectively. This $R_{rel}$ ranking is accordance with the $\chi_{12}$ ranking, i.e. low $\chi_{12}$ results in high $R_{rel}$ of CPCs. In addition, the samples exposed to acetone, THF, and EA

exhibit a better reversibility during drying process than the sample exposed to DCM. This is ascribed to the strong interaction between PC and DCM that leads to irreversible conductive network damage during polymer swelling and a decreased evaporation process of this good solvent vapor. **Fig. 4.4.15b** compares the vapor sensing behavior of PC/PVDF/MWCNT-1.0 based on PCs with different viscosity towards saturated acetone vapor, in difference to **Fig. 4.4.12a**, now it is 300 s immersion (instead of cycling sensing with only 100 s immersion). hPC/PVDF/MWCNT-1.0 again displays a rather fluctuated sensing process and the terminal $R_{rel}$ is *ca.* 25000 % combined with a relatively bad recovery in the drying step. Lower $R_{rel}$ is achieved for mPC/PVDF/MWCNT-1.0 (*ca.* 2250%) and lPC/PVDF/MWCNT-1.0 (ca. 1400 %), accompanied with a much more pronounced recovery during exposure in air.

Therefore, it can be concluded that the blend microstructure has a great effect on the sensing performance of CPCs. According to the long-term sensing result, the composite with poor filler dispersion shows an unstable sensing signal, which is due to the inhomogeneous conductive network. In terms of composite with good filler dispersion, the conductive network is homogeneous, thus leading to a stable sensing signal [36, 38].
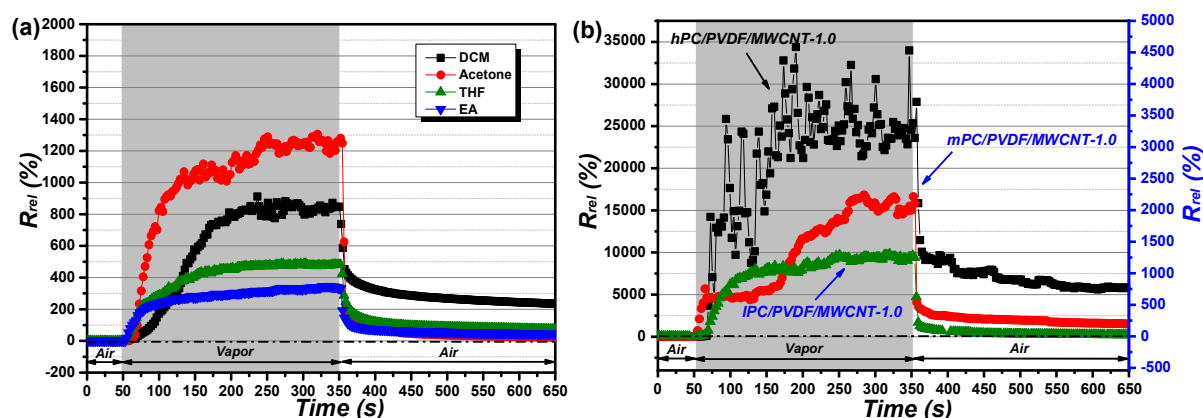


**Fig. 4.4.15** Long-time immersion of (a) lPC/PVDF/MWCNT-1.0 towards different saturated organic vapors and (b) PC/PVDF/MWCNT-1.0 composites with different PC viscosities towards saturated acetone vapor.

### 4.4.6.3 Cyclic sensing behavior of porous PC/PVDF/MWCNT blend composites

Next to the sensing on compact samples as described above, the cyclic sensing measurements towards DCM, acetone, THF and EA were carried out on CPC blend composite whose PC component has been extracted by DCM. According to extraction results (see **Fig. 4.4.2**), the weight loss is *ca.* 40% for all the three CPCs, indicating that PC has been totally extracted. Despite the fact that most of the MWCNTs were found to be preferentially localized in the PC component, the TEM study showed that some MWCNTs are located at the surface of the remaining PVDF structures (**Fig. 4.4.7**). These results in the finding that even after the extraction process conductivity values can be found which are high enough to use

these porous structures for vapor sensing (**Fig. 4.4.11**). **Fig. 4.4.16a** shows the cyclic sensing behavior of the porous CPCs towards DCM vapor. The maximum $R_{rel}$ exhibits a decreasing tendency with the sensing cycles which is less pronounced for lPC/PVDF/MWCNT-1.0. In the drying step, always negative $R_{rel}$ values are achieved, manifesting the conductivity increase during drying. Such phenomenon is attributed to the remaining MWCNT network at the surface of PVDF. MWCNT in porous lPC/PVDF/MWCNT-1.0 has better dispersion as compared to the other CPCs and the conductive network is stable under polymer de-swelling, so the negative effect during drying is not so intense. Considering the $R_{rel}$ of CPCs, DCM is not a suitable solvent to be detected for porous PC/PVDF/MWCNT composites. The cyclic vapor sensing of the porous CPCs towards acetone is shown in **Fig. 4.4.16b**. The maximum $R_{rel}$ of lPC/PVDF/MWCNT-1.0 upon acetone exposure is around 1300 %, which is much higher than that of mPC/PVDF/MWCNT-1.0 (*ca.* 500 %) and hPC/PVDF/MWCNT-1.0 (ca. 375 %). A similar sensing tendency but with better recovery can be also observed when exposing mPC/PVDF/MWCNT-1.0 and hPC/PVDF/MWCNT-1.0 porous composites towards THF and ethyl acetate (**Fig. 4.4.16c-16d**). To make a visualized comparison, $R_{rel}$ of CPCs towards acetone, THF and EA are summarized in **Fig. 4.4.16e**. Two main results can be concluded which are a) the maximum $R_{rel}$ increases with the decreased blend viscosity ratio of CPCs towards all tested vapors and b) the $R_{rel}$ is in proportion to $\chi_{12}$, i.e. the lower $\chi_{12}$, the higher $R_{rel}$. Regarding the porous PC/PVDF/MWCNT composites, the sensing signal of the porous CPCs are attributed to PVDF swelling and the interaction between surface MWCNT network and the vapor. Since PVDF has less interaction with the selecting vapors, so the polymer swelling contribution is limited. The absorption of vapor analytes onto the MWCNT networks on the surface of the remaining PVDF structures contributes to network changes. Solvent absorption on the nanotubes may increase the MWCNT-MWCNT junction distance by intercalation or MWCNT network swelling [208, 209]. lPC/PVDF/MWCNT-1.0 whose surface appears to be more homogeneously with MWCNTs is more likely to generate higher resistance change than the other two porous CPCs.
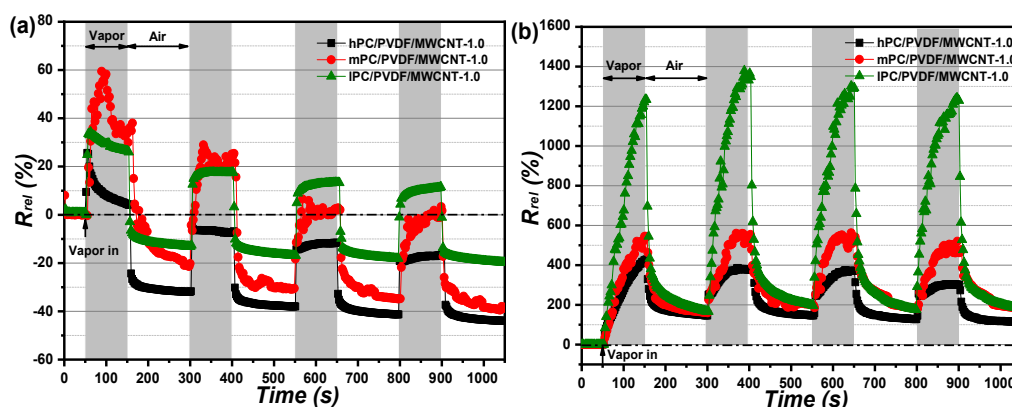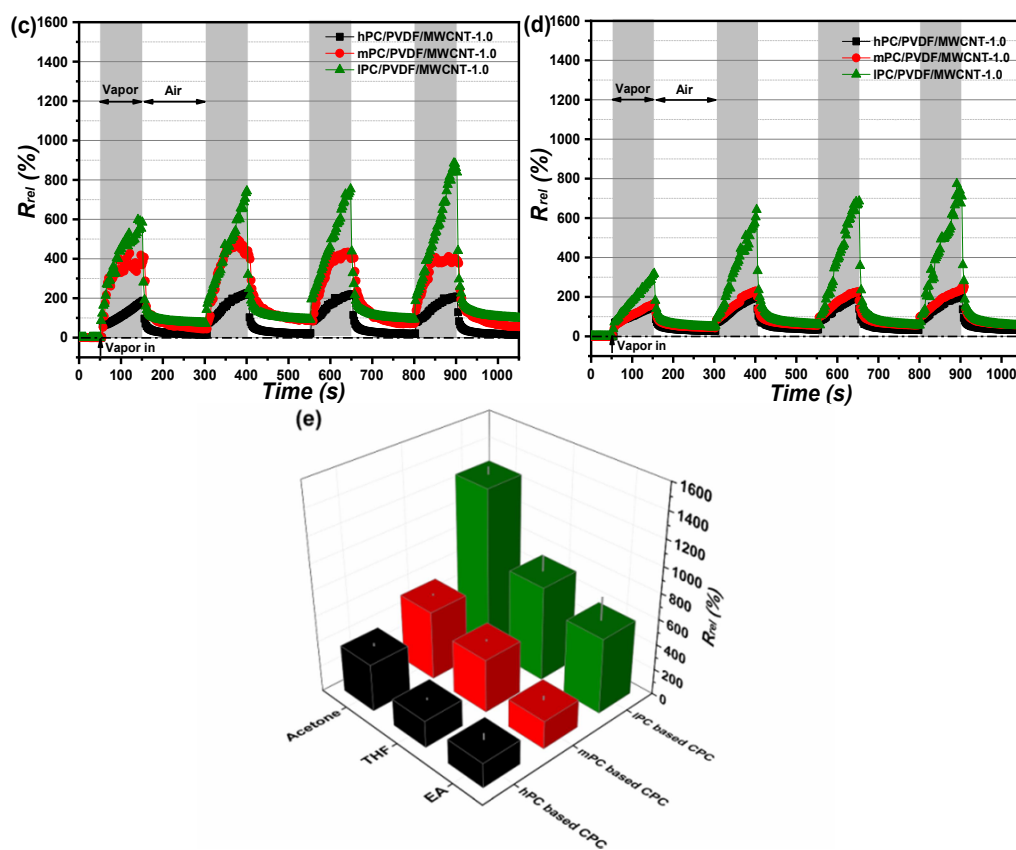
**Fig. 4.4.16** Cyclic sensing of porous PC/PVDF/MWCNT-1.0 blend composites with different viscosity ratios towards (a) DCM, (b) acetone, (c) THF and (d) EA. (e) average $R_{rel}$ comparison of CPCs towards different vapors ($R_{rel}$ calculated based on the initial resistance value before the first cycle).

**Fig. 4.4.17** presents an illustration of the assumed sensing mechanism of porous CPC sensors. As discussed, most of MWCNTs were localized in the PC component in the compact PC/PVDF/MWCNT composites. Thus, after PC extraction, most of MWCNT have been extracted. However, there are still some remaining MWCNT located at the surface of the remaining PVDF structures of these co-continuous blends. Since PVDF is resistive to most of organic vapors, it is expected to swell only slightly when vapor penetrates into the porous blend composites. As a part of the nanotubes is anchored in PVDF, the conductive networks formed at the surface of PVDF can be disconnected and rebuilt during vapor penetration and evaporation, which next to swelling of the PVDF continuous structure results in the resistance changes of the porous CPC sensors. From electrical aspect, porous composites based on lPC/PVDF/MWCNT-1.0 shows higher electrical conductivity as compared to the two other porous CPC sensors, indicating a more dense and homogeneous nanotube network at the PVDF surface. This may be related to the originally better filler dispersion in the low viscous PC polymer blend component. Therefore, the porous lPC/PVDF/MWCNT exhibit higher $R_{rel}$ than porous CPC sensors derived from hPC or mPC based blends.
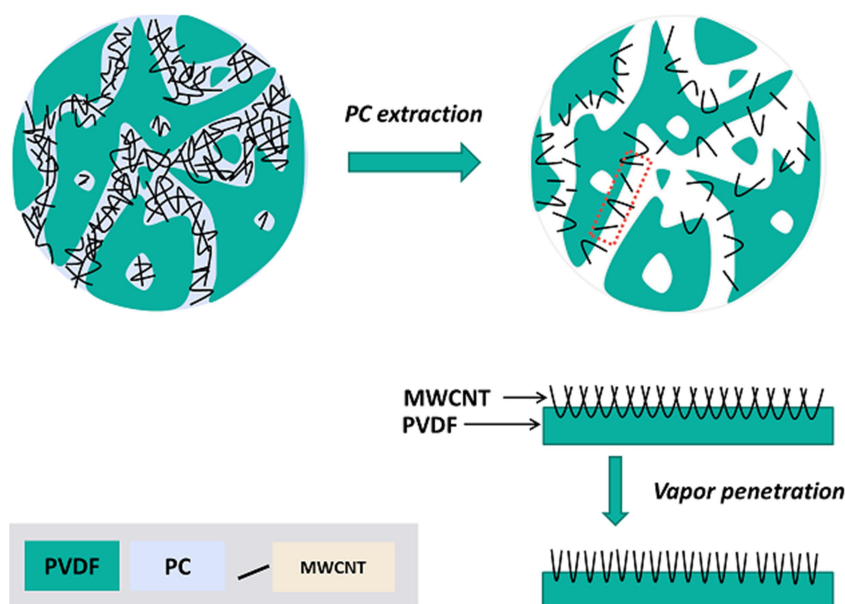
**Fig. 4.4.17** Sensing mechanism illustration of porous sensors based on co-continuous PC/PVDF/MWCNT blend composites in which PC was selectively extracted.

### 4.4.7 Summary

The vapor sensing behavior of compact and porous PC/PVDF/MWCNT blend composites against different solvent vapors was investigated. Initially, three PCs with different molecular weights were selected to be blended with PVDF at the blend ratio of 40w/60w, at which co-continuous structures could be formed. Subsequently, the electrical, morphological, and rheological behaviors of these CPCs were investigated and discussed. The cyclic vapor sensing and long-term immersion vapor sensing of compact CPCs towards solvent vapors which show strong interactions to PC were conducted. In addition, the cyclic sensing behavior of porous PC/PVDF/MWCNT from which the continuous PC part was extracted was investigated. A sensing mechanism scheme was proposed to explain the sensing behavior of such porous sensors. This study provides new thoughts in preparation, characterization, and application of chemiresistors. The main conclusions are summarized as follows:

–       At a PC/PVDF blend ratio of 40w/60w, a co-continuous structure is formed. The percolation threshold of lPC/PVDF/MWCNT is 0.03 wt%, which is much lower than those of mPC/PVDF/MWCNT and hPC/PVDF/MWCNT (range from 0.1 wt% to 0.3 wt%).

–       SEM and TEM images reveal that MWCNT are selectively localized within the PC component. With the decrease of PC viscosity in the blend, the blend morphology becomes coarser. OM results show that lPC/PVDF/MWCNT blend composites have the lowest

MWCNT agglomerate ratio compared to the other CPCs, indicating that the MWCNTs have better dispersion in the low viscous PC component.

– The cyclic sensing behavior towards four solvent vapors is investigated which represent good vapors for the PC component. Except for DCM, all CPCs exhibit very high $R_{rel}$ and good reversibility towards acetone, THF, and ethyl acetate vapors. The $R_{rel}$ response is related to the blend viscosity ratio of the CPCs, i.e. hPC/PVDF/MWCNT-1.0 with the highest viscosity ratio has the highest $R_{rel}$ because of the more susceptible conductive network formed by the non-homogeneously distributed MWCNTs. For the extremely good DCM solvent vapor, the strong interaction between DCM and PC and the medium interactions to PVDF causes very poor reversibility of hPC/PVDF/MWCNT-1.0 due to the irreversible damage of the conductive network and the difficulty of the evaporation process of this good solvent vapor. The sample lPC/PVDF/MWCNT-1.0 exhibit better reversibility even against DCM vapor, which is attributed to the better dispersion of the MWCNTs in PC. Variation of the MWCNT loading in lPC/PVDF/MWCNT blend composites indicated that lower MWCNT loading results in higher but unstable $R_{rel}$, but all of the composites exhibit good reversibility.

– In case of porous CPC sensors obtained after extraction of PC, the $R_{rel}$ is mainly resulted from the change of the parts of the MWCNTs forming a network at the surface of the remaining continuous PVDF component. Thereby, extracted lPC/PVDF/MWCNT-1.0, which has better MWCNT dispersion and is expected to have also a higher amount of nanotubes at the PVDF surface, exhibits the highest $R_{rel}$ compared to extracted mPC/PVDF/MWCNT-1.0 and extracted hPC/PVDF/MWCNT-1.0.

## 5. Summary and conclusions

This work investigates the vapor sensing behavior of conductive polymer composites (CPCs). In connection with the protection of the environment and human beings, sensing of different kinds of chemical vapors is of increasing importance. At the moment, four kinds of vapor sensors are widely investigated and reported, namely semiconducting metal oxide sensors (MO), conjugated polymer sensors, carbonaceous nanomaterial based sensors, and CPC based sensors. Due to their unique component systems, the different sensor types are based on different sensing mechanisms resulting in different potential application ranges.

In consideration of costs and processability, CPC based vapor sensors seem to be a promising candidate owning to their low material costs, excellent processability by well-established methods, and designable compositions. Thus, the vapor sensing behavior of CPCs was studied under the following aspects in this work: 1) The conductive network of CPCs is formed and tuned by utilizing MWCNT/CB hybrid fillers: the relationship between vapor sensing performance and conductive network density is discussed; 2) An immiscible polymer blend system based on two amorphous components, namely PC and PS, is chosen aiming to explain the influence of blend morphology on the sensing performance of CPCs; 3) A blend system containing a semi-crystalline polymer, PLA, is selected and PLA is melt-mixed with PS and MWCNT: annealing effects on the polymer crystallinity and vapor sensing behavior of CPCs is discussed; 4) A blend system containing a solvent resistive polymer, PVDF, is chosen in order to improve the reversibility of PC/PVDF/MWCNT based CPCs: the morphology differences induced by different blend viscosity ratios and the resulting sensing behavior is explored.

The vapor sensing behavior of CPC sensors are determined by many factors. The most important factor is the vapor/polymer interaction. In order to quantify such interaction, the Flory-Huggins interaction parameter ($\chi_{12}$) is used to estimate the interaction between the chosen vapors and polymers. This parameter is related to solvent molar volume, temperature and solubility parameter of solvent and polymer. Generally, a lower $\chi_{12}$ value demonstrates a stronger polymer/vapor interaction. Based on this, the vapors used in this work are characterized as vapors of good, moderate and poor solvent to the specific polymer component. This allows estimating which solvent vapor will swell the polymer and to which extent, as swelling of the polymer matrix is necessary for the effective vapor sensing. The polymer swelling induced by organic vapors influences the conductive network and results in changes of its electrical resistance which is measured as the sensing signal. The experimental findings can be summarized as follows:

1) In the first part, PC based nanocomposites containing hybrid fillers of MWCNT and CB were fabricated by melt mixing. The electrical conductivity of compression molded samples was measured and the percolation threshold $\varphi_c$ is found to be 0.11 wt% for PC/MWCNT composites and 1.38 wt% for PC/CB composites. Two MWCNT loadings (0.1 wt% and 0.5 wt%) are chosen which are lower and higher than the $\varphi_c$ of PC/MWCNT composites, respectively. Based on this, three CB contents (0.5 wt%, 1.5 wt% and 2.5 wt%) are selected as second filler component to prepare PC/MWCNT/CB composites. The different hybrid filler ratios stand for different conductive network patterns and formations in the composites. For instance, PC/MWCNT/CB containing 0.1 wt% MWCNT has the conductive network mainly formed by CB particles as the MWCNT content is lower than the $\varphi_c$ of PC/MWCNT composites.

N01B15, N01B25, N05B15, and N05B25 composites (N$x$ stands for MWCNT content and B$x$ stands for CB content) were selected for the vapor sensing tests. When being exposed to the good vapor acetone, all CPCs exhibit high relative resistance changes because of the very strong polymer/vapor interaction. N01B15 shows much higher $R_{rel}$ and poor reversibility than the other three composites due to its loose conductive network formed by MWCNT and CB, which can be easily damaged under polymer swelling. For N01B25, N05B15, and N05B25 composites, more MWCNT and CB particles take part in forming the conductive network or completing the imperfect conductive network, thus making the network more perfect and more resistive to polymer swelling. In the moderate solvent toluene vapor, all the four CPCs display an increase in $R_{rel}$ with the sensing cycle and the recovery in the drying periods of 100 s in air is incomplete; the $R_{rel}$ values after each cycle steadily increase resulting in increased responses also in the following exposure steps. For this case, N01B15 also shows higher $R_{rel}$ as compared to other composites. For the poor solvent cyclohexane vapor, the $R_{rel}$ is very low for all the CPCs due to the poor interaction between cyclohexane and PC.

In summary, the network quality could be tuned by the MWCNT and CB composition. Among the selected samples, that one with the lowest CB and MWCNT concentration, namely N01B15, performed best. However, one should consider that very strong interactions between the solvent and the PC matrix, as in the case of acetone, may irreversibly destruct the sample by dissolving parts of the polymer matrix. This may be the case in the sample N01B15, having the lowest network density and highest change in $R_{rel}$, as it is indicated by the the significant non-recovery of $R_{rel}$ in the first drying cycle. This part provides first results using a suitable concept for designing chemo-resistive sensors by adjusting amount and ratio of mixed carbon nanofillers in melt-mixed polymer composites.

2) In order to improve the cyclic use of CPC sensors towards vapor, especially vapors of good solvents, immiscible amorphous polymer blends are introduced. In the second part, PC/PS/MWCNT composites with different blend morphologies were achieved by varying the polymer blend ratios using the melt-mixing method. MWCNT are selectively localized in PC component according, which corresponds to the thermodynamic estimation. The $\varphi_c$ of composite with co-continuous structure (PC/PS 50/50 wt%) is 0.13 vol%, which is lower than that of 0.30 vol. % of the composites with sea-island structure (PC/PS 70/30 wt%). The sensing behavior was studied on blend composites having 0.75 wt% (approx. 0.43 vol%) MWCNTs, whereby the composite based on PC/PS 70/30 wt% showed the highest electrical conductivity value and the best state of macro-dispersion of MWCNTs. The three kinds of CPCs exhibit different sensing behavior towards different organic vapors. Under the influence of moderate solvent vapors such as ethyl acetate and toluene, the CPC with sea- island structure shows a higher $R_{rel}$ and poor reversibility; whereas CPCs with co-continuous structure shows a lower $R_{rel}$ but excellent reversibility. All CPCs showed poor reversibility towards the good solvent vapor DCM due to their strong interaction with the two polymers. The CPCs sensors exhibit an exponential relationship between $R_{rel}$ and vapor concentration, as shown for acetone sensing. If the CPCs have been exposed to vapor of poor solventssuch as cyclohexane, the PC/PS 50/50 wt% blend with 0.75 wt% has a higher $R_{rel}$ equilibrium than the other CPCs due to the microstructural differences of the blend composites. With respect to blend structure, CPCs with co-continuous structure show better reversibility towards good solvent vapors and higher $R_{rel}$ towards vapors of poor solvents, which is attributed to the larger and continuous blend interfaces that facilitate the vapor diffusion and thus the sensing process. The results indicate that conductive polymer blends are promising vapor sensors, especially due to their tunable blend structures.

3) As concluded in second part, polymer blend based CPCs with co-continuous structure exhibit better reversibility than of sea-island structure composites. Therefore, CPCs with co-continuous structures are further investigated in the following part. PLA, a semi-crystalline polymer, is selected and melt mixed with PS at the blend ratio of 50/50 wt%, whereby a co-continuous structure is formed. MWCNTs preferentially localize within the PLA phase, and the percolation threshold $\varphi_c$ for A50S50M$z$ composites is 0.4 wt%. For the vapor sensing tests, PLA/PS/MWCNT-1.0 wt% composites are selected because of their suitable resistivity range for the cyclic vapor sensing tests. When being exposed to acetone vapor, A50S50M1.0 shows increasing sensing responses with vapor concentration. At the same time, the reversibility of the swelling deteriorates during drying after the exposure to

higher acetone vapor concentrations. To improve the durability of CPCs towards good solvent vapors, A50S50M$z$ composites are annealed at 150°C for up to 120 min. The results indicate that samples after long time annealing (60 min or 120 min) display improved reversibility but at the expense of the sensing response. The stabilization is ascribed to increased crystallinity of PLA due to the annealing. Crystalline regions are hardly accessible for vapor diffusion. Thus, the increased crystallinity confines some volume of the amorphous part, thus hampering the vapor diffusion. The cyclic sensing behavior of CPCs towards cyclohexane vapor indicated that all the composites show low $R_{rel}$ because of the poor interaction between PC and cyclohexane. Interestingly, blend composites with higher MWCNT content (1.0 wt%) display higher $R_{rel}$ when exposed towards cyclohexane vapor than CPCs with lower MWCNT loading (0.5 wt%). This suggests that some nanotubes of A50S50M1.0 cross the interphase and are also located in the unfavorable PS. This assumption is supported by extraction results. In addition, the vapor sensing behavior of CPCs towards vapor mixtures (acetone and cyclohexane) were compared. Also here, annealed samples show lower $R_{rel}$ as compared to non-annealed samples. Interestingly, the solvent volume ratio of 1/1 resulted in the higher $R_{rel}$ than 1/4 or 4/1 volume ratios, which is attributed to the simultaneous swelling of PLA and PS component. In summary, the PLA crystallinity is increased by thermal annealing in order to tune the vapor sensing behavior of the CPCs. By virtue of this, the sensor stability and durability towards vapors of good solvents is largely improved.

4) In the first three parts, the influence of conductive network density, polymer blend microstructure, and annealing treatment on the vapor sensing behavior of CPC sensors has been investigated systematically. However, one key issue is still open to be solved, i.e. improving the reversibility and durability of CPCs towards good solvent vapors. Therefore, in the fourth part, three PCs with different molecular weights are selected to be melt mixed with PVDF at the blend ratio of 40/60 wt%, at which co-continuous structures are formed. The reason for choosing PC/PVDF blend is that PC has good swelling to most vapors while PVDF is much more difficult to swell under vapor stimulation. Thus, PC/MWCNT acts as sensing component and PVDF can stabilize the blend structure of the composites during the vapor sensing tests.

According to SEM and TEM observation, the MWCNT are mainly selectively localized within the PC component. With the decrease of PC viscosity in blend, the blend becomes coarser. Besides, OM images reveal that lPC/PVDF/MWCNT composites have the lowest MWCNT agglomerate ratio, indicating that the MWCNTs have better dispersion in the low viscous PC component. The cyclic sensing behavior towards four good solvent vapors (to

PC) was investigated. Except for DCM, all CPCs exhibit very high $R_{rel}$ and good reversibility towards acetone, THF, and ethyl acetate vapors. Furthermore, $R_{rel}$ is related to the blend viscosity ratio of the CPCs, i.e. hPC/PVDF/MWCNT-1.0 with the highest viscosity ratio has the highest $R_{rel}$ because of the vulnerable conductive network formed by the non-homogeneous MWCNT dispersion. For the best solvent vapor DCM, the strong interaction between DCM and polymers causes a poor reversibility of hPC/PVDF/MWCNT-1.0 due to the irreversible damage of conductive network and difficult vapor evaporation process. Otherwise, lPC/PVDF/MWCNT-1.0 exhibits good reversibility even against DCM vapor, which is attributed to the good dispersion of the MWCNTs in PC. At changed MWCNT contents in lPC/PVDF/MWCNT composites, low MWCNT loading composites show higher but unstable $R_{rel}$. All of them exhibit good reversibility.

In addition, the cyclic sensing behavior of porous CPCs is discussed. The porous composites are prepared by extracting the PC component using DCM. It is observed that there are still some nanotubes fixed at the surface of remaining PVDF component after extraction, which results in reduced but significant conductivity of the porous composites. lPC based CPCs show higher $R_{rel}$ as compared to the other porous composites, which results from the more homogeneous conductive network at the surface of PVDF.

In conclusion, considering the vapor performance such as high sensitivity and good reversibility among these four CPC systems, PC/PVDF/MWCNT composites are the best choice used as chemiresistor in vapor sensing tests. As the sensing component, PC has strong interaction with many organic solvents/vapors such acetone, THF, DMF and EA. PVDF as a stabilizing component can maintain the composite structure and improve the composite reversibility during sensing tests. Such a blend pair makes CPCs with high sensitivity and good reversibility towards organic chemical, providing more potential applications in chemical detection of human health care in the near future. In this study, the selected polymers are only sensitive to organic vapors and have no interaction with water vapor. Therefore, some hydrophilic polymers such PVA and cellulose could be considered to broaden the fields of vapor sensing applications.

## *6. Outlook*

On the basis of the results presented in this thesis, many opportunities remain for further research in the field of polymer composites and their use as sensing materials. The presented results and discussions in this thesis provide a general understanding of influencing factors that determine the vapor sensing performances of CPCs, such as the hybrid MWCNT/CB network, the immiscible blend structure type, the annealing treatment, and the blend fineness of co-continuous blends as varied by the blend viscosity ratio. Although these factors have been investigated and proposed to improve the vapor sensing performance of CPCs, some specific areas related to this topic need to be investigated in the future.

1. A higher amount of conductive fillers is needed in single polymer based CPCs as compared to polymer blend based CPCs. Considering the poor dispersion in composites with high filler loading it is still a big challenge to improve the filler dispersion in the polymer matrix. Probably second fillers such as clay or ionic liquids can be utilized to facilitate the disentanglement and dispersion of carbon fillers. Moreover, a premixing of the fillers using solution mixing is another possible technique to reduce the filler agglomerate size, and the percolation threshold of CPCs can be reduced significantly because of the better dispersion of the fillers in the polymer matrix.

2. As discussed above, the reversibility of CPCs based sensors towards good solvent vapors is poor because of the strong polymer/vapor interaction that leads to the irreversible damage of conductive network in the polymer matrix and incomplete drying of CPCs. Therefore, the selection of suitable immiscible polymer blend pairs is of great importance in improving the cyclic use of CPC sensors. Our study gives a hint that polymer blend components having completely different physical properties result in better reversibility of CPC sensors towards vapors of good solvents of the sensing polymer component. One component containing the conductive network is acting as sensing part that can react with many vapors; the other component is resistive to most of vapors that can help to maintain the blend structure. However, one disadvantage of immiscible polymer blends based CPCs is that the interface may impair the mechanical properties of CPCs, especially for co-continuous morphologies. In order to combine the advantages of good reversibility and excellent mechanical property, some elastomers such SBS and TPU can be used. For instance, TPU is composed of non-polar segments and polar segments, which should be sensitive to non-polar solvents and polar solvents, respectively. Therefore, TPU based CPCs are a good candidate for chemical sensing. Exploring elastomer based CPCs and their multiple sensing (chemical and mechanical) behaviors are of great importance.

3. Regarding the CPC based vapor sensors, most of the studies focus on the relative resistance change towards vapors, which is related to the conductive network state, vapor concentration and polymer/vapor interaction. However, the sensitivity, meaning the dependence of the resistance change on vapor concentration is rarely reported. Therefore, the electrospinning technique either for the shaping of single polymer based CPCs or polymer blend based CPCs seems to be a good solution. The diameter of as-spun composite fibers is only several hundred nanometers, which is suitable for fast penetration and evaporation of organic vapors to the polymer matrix. In addition, as-spun composite mats can be assembled to clothes for the fast detection of hazardous vapors, giving alarm signals as fast as possible to protect the health of human beings.

4. For the studied PC/PVDF/MWCNT blend composites, it seems to be possible to fabricate composite fibers by the melt-spinning method. The fibers or fabrics of PC/PVDF/MWCNT composites could be used in real applications such as real-time leakage detection and hazardous vapor pollution. Another possible application for fibers is to embed them into flexible polymer thin films such as polydimethylsiloxane, which can be used for many applications such as wearable sensors for human activities and chemical sensor for analyzing sweat information of human while doing exercise. This is possibly a good thought in realizing multifunctional applications of CPCs.

## *Bibliography*

[1] W. Bauhofer, J.Z. Kovacs, A review and analysis of electrical percolation in carbon nanotube polymer composites, Composites Science and Technology 69(10) (2009) 1486-1498.

[2] I. Balberg, A comprehensive picture of the electrical phenomena in carbon black–polymer composites, Carbon 40(2) (2002) 139-143.

[3] J.C. Huang, Carbon black filled conducting polymers and polymer blends, Advances in Polymer Technology: Journal of the Polymer Processing Institute 21(4) (2002) 299-313.

[4] Q. Cao, Y. Song, Y. Tan, Q. Zheng, Conductive and viscoelastic behaviors of carbon black filled polystyrene during annealing, Carbon 48(15) (2010) 4268-4275.

[5] H.L. Tekinalp, V. Kunc, G.M. Velez-Garcia, C.E. Duty, L.J. Love, A.K. Naskar, C.A. Blue, S. Ozcan, Highly oriented carbon fiber–polymer composites via additive manufacturing, Composites Science and Technology 105 (2014) 144-150.

[6] C. Soutis, Carbon fiber reinforced plastics in aircraft construction, Materials Science and Engineering: A 412(1-2) (2005) 171-176.

[7] I. Alig, P. Pötschke, D. Lellinger, T. Skipa, S. Pegel, G.R. Kasaliwal, T. Villmow, Establishment, morphology and properties of carbon nanotube networks in polymer melts, Polymer 53(1) (2012) 4-28.

[8] P. Pötschke, A.R. Bhattacharyya, A. Janke, Melt mixing of polycarbonate with multiwalled carbon nanotubes: microscopic studies on the state of dispersion, European Polymer Journal 40(1) (2004) 137-148.

[9] T. Kuilla, S. Bhadra, D. Yao, N.H. Kim, S. Bose, J.H. Lee, Recent advances in graphene based polymer composites, Progress in polymer science 35(11) (2010) 1350-1375.

[10] M. Fang, K. Wang, H. Lu, Y. Yang, S. Nutt, Covalent polymer functionalization of graphene nanosheets and mechanical properties of composites, Journal of Materials Chemistry 19(38) (2009) 7098-7105.

[11] F. Gubbels, S. Blacher, E. Vanlathem, R. Jérôme, R. Deltour, F. Brouers, P. Teyssie, Design of electrical composites: determining the role of the morphology on the electrical properties of carbon black filled polymer blends, Macromolecules 28(5) (1995) 1559-1566.

[12] J. Zhao, K. Dai, C. Liu, G. Zheng, B. Wang, C. Liu, J. Chen, C. Shen, A comparison between strain sensing behaviors of carbon black/polypropylene and carbon nanotubes/polypropylene electrically conductive composites, Composites Part A: Applied Science and Manufacturing 48 (2013) 129-136.

[13] D.X. Yan, H. Pang, B. Li, R. Vajtai, L. Xu, P.G. Ren, J.H. Wang, Z.M. Li, Structured reduced graphene oxide/polymer composites for ultra-efficient electromagnetic interference shielding, Advanced Functional Materials 25(4) (2015) 559-566.

[14] H. Liu, Y. Li, K. Dai, G. Zheng, C. Liu, C. Shen, X. Yan, J. Guo, Z. Guo, Electrically conductive thermoplastic elastomer nanocomposites at ultralow graphene loading levels for strain sensor applications, Journal of Materials Chemistry C 4(1) (2016) 157-166.

[15] Z. Sang, K. Ke, I. Manas-Zloczower, Interface Design Strategy for the Fabrication of Highly Stretchable Strain Sensors, ACS applied materials & interfaces 10(42) (2018) 36483-36492.

[16] S. Gupta, R. Ou, R.A. Gerhardt, Effect of the fabrication method on the electrical properties of poly (acrylonitrile-co-butadiene-co-styrene)/carbon black composites, Journal of electronic materials 35(2) (2006) 224-229.

[17] H. Pang, L. Xu, D.-X. Yan, Z.-M. Li, Conductive polymer composites with segregated structures, Progress in Polymer Science 39(11) (2014) 1908-1933.

[18] J.Z. Kovacs, B.S. Velagala, K. Schulte, W. Bauhofer, Two percolation thresholds in carbon nanotube epoxy composites, Composites Science and Technology 67(5) (2007) 922-928.

[19] A. Yu, P. Ramesh, X. Sun, E. Bekyarova, M.E. Itkis, R.C. Haddon, Enhanced thermal conductivity in a hybrid graphite nanoplatelet–carbon nanotube filler for epoxy composites, Advanced Materials 20(24) (2008) 4740-4744.

[20] P.-C. Ma, M.-Y. Liu, H. Zhang, S.-Q. Wang, R. Wang, K. Wang, Y.-K. Wong, B.-Z. Tang, S.-H. Hong, K.-W. Paik, Enhanced electrical conductivity of nanocomposites containing hybrid fillers of carbon nanotubes and carbon black, ACS applied materials & interfaces 1(5) (2009) 1090-1096.

[21] R. Socher, B. Krause, S. Hermasch, R. Wursche, P. Pötschke, Electrical and thermal properties of polyamide 12 composites with hybrid fillers systems of multiwalled carbon nanotubes and carbon black, Composites Science and Technology 71(8) (2011) 1053-1059.

[22] E. Bilotti, H. Zhang, H. Deng, R. Zhang, Q. Fu, T. Peijs, Controlling the dynamic percolation of carbon nanotube based conductive polymer composites by addition of secondary nanofillers: the effect on electrical conductivity and tuneable sensing behaviour, Composites Science and Technology 74 (2013) 85-90.

[23] Y. Li, T. Yang, T. Yu, L. Zheng, K. Liao, Synergistic effect of hybrid carbon nantube–graphene oxide as a nanofiller in enhancing the mechanical properties of PVA composites, Journal of Materials Chemistry 21(29) (2011) 10844-10851.

[24] J. Sumfleth, X.C. Adroher, K. Schulte, Synergistic effects in network formation and electrical properties of hybrid epoxy nanocomposites containing multi-wall carbon nanotubes and carbon black, Journal of Materials Science 44(12) (2009) 3241-3250.

[25] M. Trifkovic, A. Hedegaard, K. Huston, M. Sheikhzadeh, C.W. Macosko, Porous films via PE/PEO cocontinuous blends, Macromolecules 45(15) (2012) 6036-6044.

[26] C.W. Macosko, Morphology development and control in immiscible polymer blends, Macromolecular Symposia, Wiley Online Library, 2000, pp. 171-184.

[27] P. Pötschke, D. Paul, Formation of co-continuous structures in melt-mixed immiscible polymer blends, Journal of Macromolecular Science, Part C: Polymer Reviews 43(1) (2003) 87-141.

[28] M. Sumita, K. Sakata, S. Asai, K. Miyasaka, H. Nakagawa, Dispersion of fillers and the electrical conductivity of polymer blends filled with carbon black, Polymer Bulletin 25(2) (1991) 265-271.

[29] H. Wang, G. Xie, M. Fang, Z. Ying, Y. Tong, Y. Zeng, Electrical and mechanical properties of antistatic PVC films containing multi-layer graphene, Composites Part B: Engineering 79 (2015) 444-450.

[30] L.-C. Jia, Y.-K. Li, D.-X. Yan, Flexible and efficient electromagnetic interference shielding materials from ground tire rubber, Carbon 121 (2017) 267-273.

[31] P. Li, D. Du, L. Guo, Y. Guo, J. Ouyang, Stretchable and conductive polymer films for high-performance electromagnetic interference shielding, Journal of Materials Chemistry C 4(27) (2016) 6525-6532.

[32] S.P. Pawar, D.A. Marathe, K. Pattabhi, S. Bose, Electromagnetic interference shielding through MWNT grafted Fe 3 O 4 nanoparticles in PC/SAN blends, Journal of Materials Chemistry A 3(2) (2015) 656-669.

[33] R. Rohini, S. Bose, Electromagnetic interference shielding materials derived from gelation of multiwall carbon nanotubes in polystyrene/poly (methyl methacrylate) blends, ACS Applied Materials & Interfaces 6(14) (2014) 11302-11310.

[34] H. Qi, J. Liu, J. Pionteck, P. Pötschke, E. Mäder, Carbon nanotube–cellulose composite aerogels for vapour sensing, Sensors and Actuators B: Chemical 213 (2015) 20-26.

[35] Y. Li, Y. Zheng, P. Zhan, G. Zheng, K. Dai, C. Liu, C. Shen, Vapor sensing performance as a diagnosis probe to estimate the distribution of multi-walled carbon nanotubes in poly (lactic acid)/polypropylene conductive composites, Sensors and Actuators B: Chemical 255 (2018) 2809-2819.

[36] P. Pötschke, K. Kobashi, T. Villmow, T. Andres, M.C. Paiva, J.A. Covas, Liquid sensing properties of melt processed polypropylene/poly (ε-caprolactone) blends containing multiwalled carbon nanotubes, Composites Science and Technology 71(12) (2011) 1451-1460.

[37] P. Pötschke, T. Andres, T. Villmow, S. Pegel, H. Brünig, K. Kobashi, D. Fischer, L. Häussler, Liquid sensing properties of fibres prepared by melt spinning from poly (lactic acid) containing multi-walled carbon nanotubes, Composites Science and Technology 70(2) (2010) 343-349.

[38] K. Kobashi, T. Villmow, T. Andres, P. Pötschke, Liquid sensing of melt-processed poly (lactic acid)/multi-walled carbon nanotube composite films, Sensors and Actuators B: Chemical 134(2) (2008) 787-795.

[39] Y. Liu, H. Zhang, H. Porwal, W. Tu, K. Wan, J. Evans, M. Newton, J. Busfield, T. Peijs, E. Bilotti, Tailored pyroresistive performance and flexibility by introducing a secondary thermoplastic elastomeric phase into graphene nanoplatelet (GNP) filled polymer composites for self-regulating heating devices, Journal of Materials Chemistry C 6(11) (2018) 2760-2768.

[40] S. Zhao, D. Lou, P. Zhan, G. Li, K. Dai, J. Guo, G. Zheng, C. Liu, C. Shen, Z. Guo, Heating-induced negative temperature coefficient effect in conductive graphene/polymer ternary nanocomposites with a segregated and double-percolated structure, Journal of Materials Chemistry C 5(32) (2017) 8233-8242.

[41] J.-F. Gao, D.-X. Yan, B. Yuan, H.-D. Huang, Z.-M. Li, Large-scale fabrication and electrical properties of an anisotropic conductive polymer composite utilizing preferable location of carbon nanotubes in a polymer blend, Composites Science and Technology 70(13) (2010) 1973-1979.

[42] Z. Tang, S. Jia, F. Wang, C. Bian, Y. Chen, Y. Wang, B. Li, Highly Stretchable Core–Sheath Fibers via Wet-Spinning for Wearable Strain Sensors, ACS Applied Materials & Interfaces 10(7) (2018) 6624-6635.

[43] N.T. Selvan, S. Eshwaran, A. Das, K. Stöckelhuber, S. Wießner, P. Pötschke, G. Nando, A. Chervanyov, G. Heinrich, Piezoresistive natural rubber-multiwall carbon nanotube nanocomposite for sensor applications, Sensors and Actuators A: Physical 239 (2016) 102-113.

[44] R. Zhang, H. Deng, R. Valenca, J. Jin, Q. Fu, E. Bilotti, T. Peijs, Strain sensing behaviour of elastomeric composite films containing carbon nanotubes under cyclic loading, Composites Science and Technology 74 (2013) 1-5.

[45] T. Yamada, Y. Hayamizu, Y. Yamamoto, Y. Yomogida, A. Izadi-Najafabadi, D.N. Futaba, K. Hata, A stretchable carbon nanotube strain sensor for human-motion detection, Nature Nanotechnology 6(5) (2011) 296.

[46] R. Mondal, K. Dubey, Y. Bhardwaj, L. Varshney, Novel hybrid nanocarbons/poly (dimethylsiloxane) composites based chemiresistors for real time detection of hazardous aromatic hydrocarbons, Carbon 100 (2016) 42-51.

[47] R. Mondal, J. Kumar, K. Dubey, Y. Bhardwaj, J. Melo, L. Varshney, Network density tailored standalone-flexible fluorocarbon elastomer/nanocarbon black chemiresistors for 2-propanone field detection, Sensors and Actuators B: Chemical 265 (2018) 193-203.

[48] M. Consales, A. Crescitelli, M. Penza, P. Aversa, P.D. Veneri, M. Giordano, A. Cusano, SWCNT nano-composite optical sensors for VOC and gas trace detection, Sensors and Actuators B: Chemical 138(1) (2009) 351-361.

[49] S. Chatterjee, M. Castro, J.-F. Feller, An e-nose made of carbon nanotube based quantum resistive sensors for the detection of eighteen polar/nonpolar VOC biomarkers of lung cancer, Journal of Materials Chemistry B 1(36) (2013) 4563-4575.

[50] G. Gregis, J.-B. Sanchez, I. Bezverkhyy, W. Guy, F. Berger, V. Fierro, J.-P. Bellat, A. Celzard, Detection and quantification of lung cancer biomarkers by a micro-analytical device using a single metal oxide-based gas sensor, Sensors and Actuators B: Chemical 255 (2018) 391-400.

[51] S.-M. Li, L.-X. Zhang, M.-Y. Zhu, G.-J. Ji, L.-X. Zhao, J. Yin, L.-J. Bie, Acetone sensing of ZnO nanosheets synthesized using room-temperature precipitation, Sensors and Actuators B: Chemical 249 (2017) 611-623.

[52] S. Virji, J. Huang, R.B. Kaner, B.H. Weiller, Polyaniline nanofiber gas sensors: examination of response mechanisms, Nano Letters 4(3) (2004) 491-496.

[53] P. Slobodian, P. Riha, A. Lengálová, P. Svoboda, P. Sáha, Multi-wall carbon nanotube networks as potential resistive gas sensors for organic vapor detection, Carbon 49(7) (2011) 2499-2507.

[54] J.F. Feller, H. Guézénoc, H. Bellégou, Y. Grohens, Smart poly (styrene)/carbon black conductive polymer composites films for styrene vapour sensing, Macromolecular Symposia, Wiley Online Library, 2005, pp. 273-280.

[55] B. Kumar, M. Castro, J.-F. Feller, Poly (lactic acid)–multi-wall carbon nanotube conductive biopolymer nanocomposite vapour sensors, Sensors and Actuators B: Chemical 161(1) (2012) 621-628.

[56] T. Villmow, S. Pegel, A. John, R. Rentenberger, P. Pötschke, Liquid sensing: smart polymer/CNT composites, Materials Today 14(7) (2011) 340-345.

[57] M. Stoppa, A. Chiolerio, Wearable electronics and smart textiles: a critical review, Sensors 14(7) (2014) 11957-11992.

[58] R. Rentenberger, A. Cayla, T. Villmow, D. Jehnichen, C. Campagne, M. Rochery, E. Devaux, P. Pötschke, Multifilament fibres of poly (ε-caprolactone)/poly (lactic acid) blends with multiwalled carbon nanotubes as sensor materials for ethyl acetate and acetone, Sensors and Actuators B: Chemical 160(1) (2011) 22-31.

[59] C.M. Hansen, Hansen solubility parameters: a user's handbook, CRC press2007.

[60] L.F. Francis, J.C. Grunlan, J. Sun, W. Gerberich, Conductive coatings and composites from latex-based dispersions, Colloids and Surfaces A: Physicochemical and Engineering Aspects 311(1-3) (2007) 48-54.

[61] D. Cai, M. Song, Latex technology as a simple route to improve the thermal conductivity of a carbon nanotube/polymer composite, Carbon 46(15) (2008) 2107-2112.

[62] J. Yu, K. Lu, E. Sourty, N. Grossiord, C.E. Koning, J. Loos, Characterization of conductive multiwall carbon nanotube/polystyrene composites prepared by latex technology, Carbon 45(15) (2007) 2897-2903.

[63] T.-M. Wu, E.-C. Chen, Preparation and characterization of conductive carbon nanotube–polystyrene nanocomposites using latex technology, Composites Science and Technology 68(10-11) (2008) 2254-2259.

[64] N.D. Luong, U. Hippi, J.T. Korhonen, A.J. Soininen, J. Ruokolainen, L.-S. Johansson, J.-D. Nam, J. Seppälä, Enhanced mechanical and electrical properties of polyimide film by graphene sheets via in situ polymerization, Polymer 52(23) (2011) 5237-5242.

[65] H. Deng, L. Lin, M. Ji, S. Zhang, M. Yang, Q. Fu, Progress on the morphological control of conductive network in conductive polymer composites and the use as electroactive multifunctional materials, Progress in Polymer Science 39(4) (2014) 627-655.

[66] L. Ma, G. Wang, J. Dai, Preparation of a functional reduced graphene oxide and carbon nanotube hybrid and its reinforcement effects on the properties of polyimide composites, Journal of Applied Polymer Science 134(11) (2017).

[67] F. Faraguna, P. Pötschke, J. Pionteck, Preparation of polystyrene nanocomposites with functionalized carbon nanotubes by melt and solution mixing: investigation of dispersion, melt rheology, electrical and thermal properties, Polymer 132 (2017) 325-341.

[68] Y. Li, H. Liu, K. Dai, G. Zheng, C. Liu, J. Chen, C. Shen, Tuning of vapor sensing behaviors of eco-friendly conductive polymer composites utilizing ramie fiber, Sensors and Actuators B: Chemical 221 (2015) 1279-1289.

[69] K. Ke, P. Pötschke, N. Wiegand, B. Krause, B. Voit, Tuning the network structure in poly (vinylidene fluoride)/carbon nanotube nanocomposites using carbon black: toward

improvements of conductivity and piezoresistive sensitivity, ACS applied materials & interfaces 8(22) (2016) 14190-14199.

[70] T. Villmow, P. Pötschke, S. Pegel, L. Häussler, B. Kretzschmar, Influence of twin-screw extrusion conditions on the dispersion of multi-walled carbon nanotubes in a poly (lactic acid) matrix, Polymer 49(16) (2008) 3500-3509.

[71] S. Kumar, T. Rath, R. Mahaling, C. Das, Processing and characterization of carbon nanofiber/syndiotactic polystyrene composites in the absence and presence of liquid crystalline polymer, Composites Part A: Applied Science and Manufacturing 38(5) (2007) 1304-1317.

[72] G.R. Kasaliwal, S. Pegel, A. Göldel, P. Pötschke, G. Heinrich, Analysis of agglomerate dispersion mechanisms of multiwalled carbon nanotubes during melt mixing in polycarbonate, Polymer 51(12) (2010) 2708-2720.

[73] T. Villmow, B. Kretzschmar, P. Pötschke, Influence of screw configuration, residence time, and specific mechanical energy in twin-screw extrusion of polycaprolactone/multi-walled carbon nanotube composites, Composites Science and Technology 70(14) (2010) 2045-2055.

[74] R. Socher, B. Krause, M.T. Müller, R. Boldt, P. Pötschke, The influence of matrix viscosity on MWCNT dispersion and electrical properties in different thermoplastic nanocomposites, Polymer 53(2) (2012) 495-504.

[75] P. Pötschke, B. Krause, S.T. Buschhorn, U. Köpke, M.T. Müller, T. Villmow, K. Schulte, Improvement of carbon nanotube dispersion in thermoplastic composites using a three roll mill at elevated temperatures, Composites Science and Technology 74 (2013) 78-84.

[76] R. Socher, B. Krause, R. Boldt, S. Hermasch, R. Wursche, P. Pötschke, Melt mixed nano composites of PA12 with MWNTs: Influence of MWNT and matrix properties on macrodispersion and electrical properties, Composites Science and Technology 71(3) (2011) 306-314.

[77] H. Meng, G. Sui, P. Fang, R. Yang, Effects of acid-and diamine-modified MWNTs on the mechanical properties and crystallization behavior of polyamide 6, Polymer 49(2) (2008) 610-620.

[78] S. Ban, K. Malek, C. Huang, Z. Liu, A molecular model for carbon black primary particles with internal nanoporosity, Carbon 49(10) (2011) 3362-3370.

[79] M. Qu, F. Deng, S.M. Kalkhoran, A. Gouldstone, A. Robisson, K.J. Van Vliet, Nanoscale visualization and multiscale mechanical implications of bound rubber interphases in rubber–carbon black nanocomposites, Soft Matter 7(3) (2011) 1066-1077.

[80] N. Rattanasom, T. Saowapark, C. Deeprasertkul, Reinforcement of natural rubber with silica/carbon black hybrid filler, Polymer Testing 26(3) (2007) 369-377.

[81] P. Wang, T. Ding, Conductivity and piezoresistivity of conductive carbon black filled polymer composite, Journal of Applied Polymer Science 116(4) (2010) 2035-2039.

[82] Z. Yang, M.R. Berber, N. Nakashima, A polymer-coated carbon black-based fuel cell electrocatalyst with high CO-tolerance and durability in direct methanol oxidation, Journal of Materials Chemistry A 2(44) (2014) 18875-18880.

[83] J. Byrne, H. Marsh, Porosity in carbons: Characterization and Applications, Edward Arnold, London (1995) 2-7.

[84] T.A. Vilgis, G. Heinrich, M. Klüppel, Reinforcement of polymer nano-composites: theory, experiments and applications, Cambridge University Press 2009.

[85] I. Chodak, I. Krupa, "Percolation effect" and mechanical behavior of carbon black filled polyethylene, Journal of Materials Science Letters 18(18) (1999) 1457-1459.

[86] S. Iijima, Helical microtubules of graphitic carbon, Nature 354(6348) (1991) 56-58.

[87] J. Robertson, Realistic applications of CNTs, Materials Today 7(10) (2004) 46-52.

[88] C. Li, T.-W. Chou, Elastic moduli of multi-walled carbon nanotubes and the effect of van der Waals forces, Composites Science and Technology 63(11) (2003) 1517-1524.

[89] Nanotubes. <https://worldofnanoscience.weebly.com/nanotube--carbon-fiber-overview.html>).

[90] B. Krause, R. Boldt, L. Häußler, P. Pötschke, Ultralow percolation threshold in polyamide 6.6/MWCNT composites, Composites Science and Technology 114 (2015) 119-125.

[91] B. Krause, P. Pötschke, E. Ilin, M. Predtechenskiy, Melt mixed SWCNT-polypropylene composites with very low electrical percolation, Polymer 98 (2016) 45-50.

[92] <https://de.wikipedia.org/wiki/Graphit>).

[93] A.K. Geim, K.S. Novoselov, The rise of graphene, Nanoscience and Technology: A Collection of Reviews from Nature Journals, World Scientific2010, pp. 11-19.

[94] A. Bianco, H.-M. Cheng, T. Enoki, Y. Gogotsi, R.H. Hurt, N. Koratkar, T. Kyotani, M. Monthioux, C.R. Park, J.M. Tascon, All in the graphene family–a recommended nomenclature for two-dimensional carbon materials, Elsevier, 65 (2013) 1-6.

[95] M. Terrones, A.R. Botello-Méndez, J. Campos-Delgado, F. López-Urías, Y.I. Vega-Cantú, F.J. Rodríguez-Macías, A.L. Elías, E. Munoz-Sandoval, A.G. Cano-Márquez, J.-C. Charlier, Graphene and graphite nanoribbons: Morphology, properties, synthesis, defects and applications, Nano today 5(4) (2010) 351-372.

[96] Z.-S. Wu, W. Ren, L. Xu, F. Li, H.-M. Cheng, Doped graphene sheets as anode materials with superhigh rate and large capacity for lithium ion batteries, ACS Nano 5(7) (2011) 5463-5471.

[97] C. Liu, Z. Yu, D. Neff, A. Zhamu, B.Z. Jang, Graphene-based supercapacitor with an ultrahigh energy density, Nano Letters 10(12) (2010) 4863-4868.

[98] W. Yuan, G. Shi, Graphene-based gas sensors, Journal of Materials Chemistry A 1(35) (2013) 10078-10091.

[99] S.S. Varghese, S. Lonkar, K. Singh, S. Swaminathan, A. Abdala, Recent advances in graphene based gas sensors, Sensors and Actuators B: Chemical 218 (2015) 160-183.

[100] L. Bai, S. He, J.W. Fruehwirth, A. Stein, C.W. Macosko, X. Cheng, Localizing graphene at the interface of cocontinuous polymer blends: Morphology, rheology, and conductivity of cocontinuous conductive polymer composites, Journal of Rheology 61(4) (2017) 575-587.

[101] H. Münstedt, Z. Starý, Is electrical percolation in carbon-filled polymers reflected by rheological properties?, Polymer 98 (2016) 51-60.

[102] S. Kirkpatrick, Percolation and conduction, Reviews of Modern Physics 45(4) (1973) 574.

[103] R. Zallen, The physics of amorphous compacts, John Wiley & Sons2008.

[104] R. Zhang, M. Baxendale, T. Peijs, Universal resistivity–strain dependence of carbon nanotube/polymer composites, Physical Review B 76(19) (2007) 195433.

[105] L. Duan, S. Fu, H. Deng, Q. Zhang, K. Wang, F. Chen, Q. Fu, The resistivity–strain behavior of conductive polymer composites: stability and sensitivity, Journal of Materials Chemistry A 2(40) (2014) 17085-17098.

[106] L. Wang, Z.-M. Dang, Carbon nanotube composites with high dielectric constant at low percolation threshold, Applied Physics Letters 87(4) (2005) 042903.

[107] J. Li, P.C. Ma, W.S. Chow, C.K. To, B.Z. Tang, J.K. Kim, Correlations between percolation threshold, dispersion state, and aspect ratio of carbon nanotubes, Advanced Functional Materials 17(16) (2007) 3207-3215.

[108] J. Chen, X. Cui, Y. Zhu, W. Jiang, K. Sui, Design of superior conductive polymer composite with precisely controlling carbon nanotubes at the interface of a co-continuous polymer blend via a balance of π-π interactions and dipole-dipole interactions, Carbon 114 (2017) 441-448.

[109] J. Chen, H.-y. Lu, J.-h. Yang, Y. Wang, X.-t. Zheng, C.-l. Zhang, G.-p. Yuan, Effect of organoclay on morphology and electrical conductivity of PC/PVDF/CNT blend composites, Composites Science and Technology 94 (2014) 30-38.

[110] D. Wu, Q. Lv, S. Feng, J. Chen, Y. Chen, Y. Qiu, X. Yao, Polylactide composite foams containing carbon nanotubes and carbon black: Synergistic effect of filler on electrical conductivity, Carbon 95 (2015) 380-387.

[111] H. Pang, Y. Bao, L. Xu, D.-X. Yan, W.-Q. Zhang, J.-H. Wang, Z.-M. Li, Double-segregated carbon nanotube–polymer conductive composites as candidates for liquid sensing materials, Journal of Materials Chemistry A 1(13) (2013) 4177-4181.

[112] J.Y. Oh, G.H. Jun, S. Jin, H.J. Ryu, S.H. Hong, Enhanced electrical networks of stretchable conductors with small fraction of carbon nanotube/graphene hybrid fillers, ACS Applied Materials & Interfaces 8(5) (2016) 3319-3325.

[113] a. Sumita, K. Sakata, Y. Hayakawa, S. Asai, K. Miyasaka, M. Tanemura, Double percolation effect on the electrical conductivity of conductive particles filled polymer blends, Colloid and Polymer Science 270(2) (1992) 134-139.

[114] F. Gubbels, R. Jérôme, E. Vanlathem, R. Deltour, S. Blacher, F. Brouers, Kinetic and thermodynamic control of the selective localization of carbon black at the interface of immiscible polymer blends, Chemistry of Materials 10(5) (1998) 1227-1235.

[115] F. Gubbels, R. Jérôme, P. Teyssie, E. Vanlathem, R. Deltour, A. Calderone, V. Parente, J.-L. Brédas, Selective localization of carbon black in immiscible polymer blends: a useful tool to design electrical conductive composites, Macromolecules 27(7) (1994) 1972-1974.

[116] J. Huang, C. Mao, Y. Zhu, W. Jiang, X. Yang, Control of carbon nanotubes at the interface of a co-continuous immiscible polymer blend to fabricate conductive composites with ultralow percolation thresholds, Carbon 73 (2014) 267-274.

[117] C. Mao, Y. Zhu, W. Jiang, Design of electrical conductive composites: tuning the morphology to improve the electrical properties of graphene filled immiscible polymer blends, ACS Applied Materials & Interfaces 4(10) (2012) 5281-5286.

[118] D. Yan, X. Li, H.-L. Ma, X.-Z. Tang, Z. Zhang, Z.-Z. Yu, Effect of compounding sequence on localization of carbon nanotubes and electrical properties of ternary nanocomposites, Composites Part A: Applied Science and Manufacturing 49 (2013) 35-41.

[119] J. Chen, Y.-y. Shi, J.-h. Yang, N. Zhang, T. Huang, C. Chen, Y. Wang, Z.-w. Zhou, A simple strategy to achieve very low percolation threshold via the selective distribution of carbon nanotubes at the interface of polymer blends, Journal of Materials Chemistry 22(42) (2012) 22398-22404.

[120] Y.-y. Shi, J.-h. Yang, T. Huang, N. Zhang, C. Chen, Y. Wang, Selective localization of carbon nanotubes at the interface of poly (L-lactide)/ethylene-co-vinyl acetate resulting in lowered electrical resistivity, Composites Part B: Engineering 55 (2013) 463-469.

[121] A.H.A. Hoseini, M. Arjmand, U. Sundararaj, M. Trifkovic, Tunable electrical conductivity of polystyrene/polyamide-6/carbon nanotube blend nanocomposites via control of morphology and nanofiller localization, European Polymer Journal 95 (2017) 418-429.

[122] N. George, J. Chandra, A. Mathiazhagan, R. Joseph, High performance natural rubber composites with conductive segregated network of multiwalled carbon nanotubes, Composites Science and Technology 116 (2015) 33-40.

[123] N. George, P. Bipinbal, B. Bhadran, A. Mathiazhagan, R. Joseph, Segregated network formation of multiwalled carbon nanotubes in natural rubber through surfactant assisted latex compounding: a novel technique for multifunctional properties, Polymer 112 (2017) 264-277.

[124] H. Hu, G. Zhang, L. Xiao, H. Wang, Q. Zhang, Z. Zhao, Preparation and electrical conductivity of graphene/ultrahigh molecular weight polyethylene composites with a segregated structure, Carbon 50(12) (2012) 4596-4599.

[125] J.C. Grunlan, W.W. Gerberich, L.F. Francis, Electrical and mechanical behavior of carbon black–filled poly (vinyl acetate) latex–based composites, Polymer Engineering & Science 41(11) (2001) 1947-1962.

[126] H. Deng, E. Bilotti, R. Zhang, J. Loos, T. Peijs, Effect of thermal annealing on the electrical conductivity of high-strength bicomponent polymer tapes containing carbon nanofillers, Synthetic Metals 160(5-6) (2010) 337-344.

[127] I. Alig, T. Skipa, D. Lellinger, P. Pötschke, Destruction and formation of a carbon nanotube network in polymer melts: rheology and conductivity spectroscopy, Polymer 49(16) (2008) 3524-3532.

[128] B.H. Cipriano, A.K. Kota, A.L. Gershon, C.J. Laskowski, T. Kashiwagi, H.A. Bruck, S.R. Raghavan, Conductivity enhancement of carbon nanotube and nanofiber-based polymer nanocomposites by melt annealing, Polymer 49(22) (2008) 4846-4851.

[129] T. Skipa, D. Lellinger, W. Böhm, M. Saphiannikova, I. Alig, Influence of shear deformation on carbon nanotube networks in polycarbonate melts: Interplay between build-up and destruction of agglomerates, Polymer 51(1) (2010) 201-210.

[130] W. Li, Y. Zhang, J. Yang, J. Zhang, Y. Niu, Z. Wang, Thermal annealing induced enhancements of electrical conductivities and mechanism for multiwalled carbon nanotubes filled poly (ethylene-co-hexene) composites, ACS Applied Materials & Interfaces 4(12) (2012) 6468-6478.

[131] M. Narkis, S. Srivastava, R. Tchoudakov, O. Breuer, Sensors for liquids based on conductive immiscible polymer blends, Synthetic Metals 113(1-2) (2000) 29-34.

[132] A. Romanenko, O. Anikeeva, V. Kuznetsov, T. Buryakov, E. Tkachev, A. Usoltseva, Influence of helium, hydrogen, oxygen, air and methane on conductivity of multiwalled carbon nanotubes, Sensors and Actuators A: Physical 138(2) (2007) 350-354.

[133] X. Wang, Y. Li, J. Pionteck, Z. Zhou, W. Weng, X. Luo, Z. Qin, B. Voit, M. Zhu, Flexible poly (styrene-butadiene-styrene)/carbon nanotube fiber based vapor sensors with high sensitivity, wide detection range, and fast response, Sensors and Actuators B: Chemical 256 (2018) 896-904.

[134] S. Shang, W. Zeng, X.-m. Tao, Investigation on the electrical response behaviors of multiwalled carbon nanotube/polyurethane composite in organic solvent vapors, Sensors and Actuators B: Chemical 166 (2012) 330-337.

[135] N.R. Tanguy, L.K. Fiddes, N. Yan, Enhanced radio frequency biosensor for food quality detection using functionalized carbon nanofillers, ACS Applied Materials & Interfaces 7(22) (2015) 11939-11947.

[136] S. Nag, M. Castro, V. Choudhary, J.-F. Feller, Sulfonated poly (ether ether ketone)[SPEEK] nanocomposites based on hybrid nanocarbons for the detection and discrimination of some lung cancer VOC biomarkers, Journal of Materials Chemistry B 5(2) (2017) 348-359.

[137] S.G. Chen, J.W. Hu, M.Q. Zhang, M.W. Li, M.Z. Rong, Gas sensitivity of carbon black/waterborne polyurethane composites, Carbon 42(3) (2004) 645-651.

[138] P.J. Flory, Thermodynamics of high polymer solutions, The Journal of chemical physics 10(1) (1942) 51-61.

[139] M.L. Huggins, Solutions of long chain compounds, The Journal of chemical physics 9(5) (1941) 440-440.

[140] K. Li, K. Dai, X. Xu, G. Zheng, C. Liu, J. Chen, C. Shen, Organic vapor sensing behaviors of carbon black/poly (lactic acid) conductive biopolymer composite, Colloid and Polymer Science 291(12) (2013) 2871-2878.

[141] H. Liu, W. Huang, X. Yang, K. Dai, G. Zheng, C. Liu, C. Shen, X. Yan, J. Guo, Z. Guo, Organic vapor sensing behaviors of conductive thermoplastic polyurethane–graphene nanocomposites, Journal of Materials Chemistry C 4(20) (2016) 4459-4469.

[142] K. Kobashi, T. Villmow, T. Andres, L. Häußler, P. Pötschke, Investigation of liquid sensing mechanism of poly (lactic acid)/multi-walled carbon nanotube composite films, Smart Materials and Structures 18(3) (2009) 035008.

[143] E. Segal, R. Tchoudakov, I. Mironi-Harpaz, M. Narkis, A. Siegmann, Chemical sensing materials based on electrically-conductive immiscible polymer blends, Polymer International 54(7) (2005) 1065-1075.

[144] E. Segal, R. Tchoudakov, M. Narkis, A. Siegmann, Sensing of liquids by electrically conductive immiscible polypropylene/thermoplastic polyurethane blends containing carbon black, Journal of Polymer Science Part B: Polymer Physics 41(12) (2003) 1428-1440.

[145] S. Srivastava, R. Tchoudakov, M. Narkis, A preliminary investigation of conductive immiscible polymer blends as sensor materials, Polymer Engineering & Science 40(7) (2000) 1522-1528.

[146] K. Dai, S. Zhao, W. Zhai, G. Zheng, C. Liu, J. Chen, C. Shen, Tuning of liquid sensing performance of conductive carbon black (CB)/polypropylene (PP) composite utilizing a segregated structure, Composites Part A: Applied Science and Manufacturing 55 (2013) 11-18.

[147] S. Zhao, W. Zhai, N. Li, K. Dai, G. Zheng, C. Liu, J. Chen, C. Shen, Liquid sensing properties of carbon black/polypropylene composite with a segregated conductive network, Sensors and Actuators A: Physical 217 (2014) 13-20.

[148] N. Wang, Z. Xu, Y. Qu, G. Zheng, K. Dai, C. Liu, C. Shen, Liquid-sensing behaviors of carbon black/polyamide 6/high-density polyethylene composite containing ultrafine conductive electrospun fibrous network, Colloid and Polymer Science 294(8) (2016) 1343-1350.

[149] H. Qi, B.r. Schulz, T. Vad, J. Liu, E. Mäder, G. Seide, T. Gries, Novel carbon nanotube/cellulose composite fibers as multifunctional materials, ACS Applied Materials & Interfaces 7(40) (2015) 22404-22412.

[150] H. Qi, E. Mäder, J. Liu, Unique water sensors based on carbon nanotube–cellulose composites, Sensors and Actuators B: Chemical 185 (2013) 225-230.

[151] H. Qi, J. Liu, Y. Deng, S. Gao, E. Mäder, Cellulose fibres with carbon nanotube networks for water sensing, Journal of Materials Chemistry A 2(15) (2014) 5541-5547.

[152] A. Dichiara, A. Song, S. Goodman, D. He, J. Bai, Smart papers comprising carbon nanotubes and cellulose microfibers for multifunctional sensing applications, Journal of Materials Chemistry A 5(38) (2017) 20161-20169.

[153] N. Barsan, U. Weimar, Conduction model of metal oxide gas sensors, Journal of Electroceramics 7(3) (2001) 143-167.

[154] S. Mao, G. Lu, J. Chen, Nanocarbon-based gas sensors: progress and challenges, Journal of Materials Chemistry A 2(16) (2014) 5573-5579.

[155] S.J. Tans, A.R. Verschueren, C. Dekker, Room-temperature transistor based on a single carbon nanotube, Nature 393(6680) (1998) 49.

[156] D.R. Kauffman, A. Star, Carbon nanotube gas and vapor sensors, Angewandte Chemie International Edition 47(35) (2008) 6550-6570.

[157] T.R. Pavase, H. Lin, H. Sameer, Z. Li, I. Ahmed, L. Lv, L. Sun, S.B.H. Shah, M.T. Kalhoro, Recent advances of conjugated polymer (CP) nanocomposite-based chemical

sensors and their applications in food spoilage detection: A comprehensive review, Sensors and Actuators B: Chemical (2018).

[158] Q. Fan, Z. Qin, T. Villmow, J. Pionteck, P. Pötschke, Y. Wu, B. Voit, M. Zhu, Vapor sensing properties of thermoplastic polyurethane multifilament covered with carbon nanotube networks, Sensors and Actuators B: Chemical 156(1) (2011) 63-70.

[159] S.G. Chen, J.W. Hu, M.Q. Zhang, M.Z. Rong, Effects of temperature and vapor pressure on the gas sensing behavior of carbon black filled polyurethane composites, Sensors and Actuators B: Chemical 105(2) (2005) 187-193.

[160] J.R. Li, J.R. Xu, M.Q. Zhang, M.Z. Rong, Carbon black/polystyrene composites as candidates for gas sensing materials, Carbon 41(12) (2003) 2353-2360.

[161] B. Zhang, R.W. Fu, M.Q. Zhang, X.M. Dong, P.L. Lan, J.S. Qiu, Preparation and characterization of gas-sensitive composites from multi-walled carbon nanotubes/polystyrene, Sensors and Actuators B: Chemical 109(2) (2005) 323-328.

[162] B. Zhang, X. Dong, R. Fu, B. Zhao, M. Zhang, The sensibility of the composites fabricated from polystyrene filling multi-walled carbon nanotubes for mixed vapors, Composites Science and Technology 68(6) (2008) 1357-1362.

[163] J. Gao, H. Wang, X. Huang, M. Hu, H. Xue, R.K. Li, A super-hydrophobic and electrically conductive nanofibrous membrane for a chemical vapor sensor, Journal of Materials Chemistry A 6(21) (2018) 10036-10047.

[164] I. Marriam, X. Wang, M. Tebyetekerwa, G. Chen, F. Zabihi, J. Pionteck, S. Peng, S. Ramakrishna, S. Yang, M. Zhu, Bottom-Up Approach to Design Wearable and Stretchable Smart Fibers with Organic Vapor Sensing Behaviors and Energy Storage Properties, Journal of Materials Chemistry A 6(28) (2018) 13633-13643.

[165] W. Li, F. Xu, L. Sun, W. Liu, Y. Qiu, A novel flexible humidity switch material based on multi-walled carbon nanotube/polyvinyl alcohol composite yarn, Sensors and Actuators B: Chemical 230 (2016) 528-535.

[166] P.G. Ramos, N.J. Morales, S. Goyanes, R.J. Candal, J. Rodríguez, Moisture-sensitive properties of multi-walled carbon nanotubes/polyvinyl alcohol nanofibers prepared by electrospinning electrostatically modified method, Materials Letters 185 (2016) 278-281.

[167] S. Wu, F. Li, Y. Zhu, J. Shen, The switch-type humidity sensing properties of polyacrylic acid and its copolymers, Journal of Materials Science 35(8) (2000) 2005-2008.

[168] A. Bouvree, J.-F. Feller, M. Castro, Y. Grohens, M. Rinaudo, Conductive Polymer nano-bioComposites (CPC): Chitosan-carbon nanoparticle a good candidate to design polar vapour sensors, Sensors and Actuators B: Chemical 138(1) (2009) 138-147.

[169] A.H. Nissan, H-bond dissociation in hydrogen bond dominated compacts, Macromolecules 9(5) (1976) 840-850.

[170] R. Arrigo, N.T. Dintcheva, E. Morici, F.P. La Mantia, Performances and morphology of polyamide/carbonaceous structures based fibers, AIP Conference Proceedings, AIP, 2014, pp. 330-333.

[171] M.T. Müller, B. Krause, P. Pötschke, A successful approach to disperse MWCNTs in polyethylene by melt mixing using polyethylene glycol as additive, Polymer 53(15) (2012) 3079-3083.

[172] J.A. Galloway, K.J. Koester, B.J. Paasch, C.W. Macosko, Effect of sample size on solvent extraction for detecting cocontinuity in polymer blends, Polymer 45(2) (2004) 423-428.

[173] Y. Sun, H.-D. Bao, Z.-X. Guo, J. Yu, Modeling of the electrical percolation of mixed carbon fillers in polymer-based composites, Macromolecules 42(1) (2008) 459-463.

[174] Z.-Y. Xiong, B.-Y. Zhang, L. Wang, J. Yu, Z.-X. Guo, Modeling the electrical percolation of mixed carbon fillers in polymer blends, Carbon 70 (2014) 233-240.

[175] J.C. Grunlan, A.R. Mehrabi, M.V. Bannon, J.L. Bahr, Water-Based Single-Walled-Nanotube-Filled Polymer Composite with an Exceptionally Low Percolation Threshold, Advanced Materials 16(2) (2004) 150-153.

[176] J.-F. Feller, J. Lu, K. Zhang, B. Kumar, M. Castro, N. Gatt, H. Choi, Novel architecture of carbon nanotube decorated poly (methyl methacrylate) microbead vapour sensors assembled by spray layer by layer, Journal of Materials Chemistry 21(12) (2011) 4142-4149.

[177] C. Reichardt, T. Welton, Solvents and solvent effects in organic chemistry, John Wiley & Sons2011.

[178] S. Nuriel, L. Liu, A. Barber, H. Wagner, Direct measurement of multiwall nanotube surface tension, Chemical Physics Letters 404(4) (2005) 263-266.

[179] A.H. Barber, S.R. Cohen, H.D. Wagner, Static and dynamic wetting measurements of single carbon nanotubes, Physical Review Letters 92(18) (2004) 186103.

[180] S. Wu, Polymer interfaces and adhesion Marcel Dekker, New York (1982).

[181] http://www.surface-tension.de/compact-surface-energy.htm, (2019).

[182] L. Zonder, A. Ophir, S. Kenig, S. McCarthy, The effect of carbon nanotubes on the rheology and electrical resistivity of polyamide 12/high density polyethylene blends, Polymer 52(22) (2011) 5085-5091.

[183] P. Pötschke, D.R. Paul, Detection of co-continuous structures in SAN/PA6 blends by different methods, Macromolecular Symposia, Wiley Online Library, 2003, pp. 69-82.

[184] M. Liebscher, J. Domurath, B. Krause, M. Saphiannikova, G. Heinrich, P. Pötschke, Electrical and melt rheological characterization of PC and co-continuous PC/SAN blends filled with CNTs: Relationship between melt-mixing parameters, filler dispersion, and filler aspect ratio, Journal of Polymer Science Part B: Polymer Physics 56(1) (2018) 79-88.

[185] P. Pötschke, M. Abdel-Goad, I. Alig, S. Dudkin, D. Lellinger, Rheological and dielectrical characterization of melt mixed polycarbonate-multiwalled carbon nanotube composites, Polymer 45(26) (2004) 8863-8870.

[186] X.-Q. Liu, R.-H. Li, R.-Y. Bao, W.-R. Jiang, W. Yang, B.-H. Xie, M.-B. Yang, Suppression of phase coarsening in immiscible, co-continuous polymer blends under high temperature quiescent annealing, Soft Matter 10(20) (2014) 3587-3596.

[187] Y. Pan, X. Liu, X. Hao, Z. Starý, D.W. Schubert, Enhancing the electrical conductivity of carbon black-filled immiscible polymer blends by tuning the morphology, European Polymer Journal 78 (2016) 106-115.

[188] Y. Chen, Q. Yang, Y. Huang, X. Liao, Y. Niu, Influence of phase coarsening and filler agglomeration on electrical and rheological properties of MWNTs-filled PP/PMMA composites under annealing, Polymer 79 (2015) 159-170.

[189] Y. Gao, O.T. Picot, H. Zhang, E. Bilotti, T. Peijs, Synergistic effects of filler size on thermal annealing-induced percolation in polylactic acid (PLA)/graphite nanoplatelet (GNP) nanocomposites, Nanocomposites 3 (2017) 1-9.

[190] A.K. Mohanty, M. Misra, L.T. Drzal, Natural fibers, biopolymers, and biocomposites, CRC press2005.

[191] M. Liebscher, M.-O. Blais, P. Pötschke, G. Heinrich, A morphological study on the dispersion and selective localization behavior of graphene nanoplatelets in immiscible polymer blends of PC and SAN, Polymer 54(21) (2013) 5875-5882.

[192] J. Huang, Y. Zhu, L. Xu, J. Chen, W. Jiang, X. Nie, Massive enhancement in the thermal conductivity of polymer composites by trapping graphene at the interface of a polymer blend, Composites Science and Technology 129 (2016) 160-165.

[193] A. Pyun, J.R. Bell, K.H. Won, B.M. Weon, S.K. Seol, J.H. Je, C.W. Macosko, Synchrotron X-ray microtomography for 3D imaging of polymer blends, Macromolecules 40(6) (2007) 2029-2035.

[194] C.R. Lopez-Barron, C.W. Macosko, Characterizing interface shape evolution in immiscible polymer blends via 3D image analysis, Langmuir 25(16) (2009) 9392-9404.

[195] A.T. Hedegaard, L. Gu, C.W. Macosko, Effect of extensional viscosity on cocontinuity of immiscible polymer blends, Journal of Rheology 59(6) (2015) 1397-1417.

[196] D. Battegazzore, S. Bocchini, A. Frache, Crystallization kinetics of poly (lactic acid)-talc composites, Express Polymer Letters 5(10) (2011) 849-858.

[197] H. Xu, C.Y. Liu, C. Chen, B.S. Hsiao, G.J. Zhong, Z.M. Li, Easy alignment and effective nucleation activity of ramie fibers in injection-molded poly (lactic acid) biocomposites, Biopolymers 97(10) (2012) 825-839.

[198] M. Yasuniwa, K. Sakamo, Y. Ono, W. Kawahara, Melting behavior of poly (l-lactic acid): X-ray and DSC analyses of the melting process, Polymer 49(7) (2008) 1943-1951.

[199] K. Fukushima, C. Abbate, D. Tabuani, M. Gennari, G. Camino, Biodegradation of poly (lactic acid) and its nanocomposites, Polymer Degradation and Stability 94(10) (2009) 1646-1655.

[200] T. Alizadeh, L.H. Soltani, Graphene/poly (methyl methacrylate) chemiresistor sensor for formaldehyde odor sensing, Journal of Hazardous Materials 248 (2013) 401-406.

[201] J. Lu, B. Kumar, M. Castro, J.-F. Feller, Vapour sensing with conductive polymer nanocomposites (CPC): Polycarbonate-carbon nanotubes transducers with hierarchical structure processed by spray layer by layer, Sensors and Actuators B: Chemical 140(2) (2009) 451-460.

[202] G.R. Kasaliwal, A. Göldel, P. Pötschke, G. Heinrich, Influences of polymer matrix melt viscosity and molecular weight on MWCNT agglomerate dispersion, Polymer 52(4) (2011) 1027-1036.

[203] B. Lin, U. Sundararaj, P. Pötschke, Melt Mixing of Polycarbonate with Multi-Walled Carbon Nanotubes in Miniature Mixers, Macromolecular Materials and Engineering 291(3) (2006) 227-238.

[204] F. Du, R.C. Scogna, W. Zhou, S. Brand, J.E. Fischer, K.I. Winey, Nanotube networks in polymer nanocomposites: rheology and electrical conductivity, Macromolecules 37(24) (2004) 9048-9055.

[205] J. Feller, Y. Grohens, Evolution of electrical properties of some conductive polymer composite textiles with organic solvent vapours diffusion, Sensors and Actuators B: Chemical 97(2) (2004) 231-242.

[206] J. Zuo, T.-S. Chung, G.S. O'Brien, W. Kosar, Hydrophobic/hydrophilic PVDF/Ultem® dual-layer hollow fiber membranes with enhanced mechanical properties for vacuum membrane distillation, Journal of Membrane Science 523 (2017) 103-110.

[207] Z.C. Kennedy, J.F. Christ, K.A. Evans, B.W. Arey, L.E. Sweet, M.G. Warner, R.L. Erikson, C.A. Barrett, 3D-printed poly (vinylidene fluoride)/carbon nanotube composites as a tunable, low-cost chemical vapour sensing platform, Nanoscale 9(17) (2017) 5458-5466.

[208] R. Tang, Y. Shi, Z. Hou, L. Wei, Carbon nanotube-based chemiresistive sensors, Sensors 17(4) (2017) 882.

[209] J.F. Fennell, S.F. Liu, J.M. Azzarelli, J.G. Weis, S. Rochat, K.A. Mirica, J.B. Ravnsbæk, T.M. Swager, Nanowire chemical/biological sensors: Status and a roadmap for the future, Angewandte Chemie International Edition 55(4) (2016) 1266-1281.

## *Publications and conference contributions*

**1. Y. Li**, P. Pötschke, J. Pionteck, B. Voit. Electrical and vapor sensing behavior of polycarbonate composites containing hybrid carbon fillers. 2018, European Polymer Journal, 108, 461-471.

**2. Y. Li**, J. Pionteck, P. Pötschke, B. Voit. Organic vapor sensing behavior of polycarbonate/polystyrene/multi-walled carbon nanotube blend composites with different microstructures. 2019, Materials & Design, 179, 107897.

**3. Y. Li**, Y. Zheng, P. Zhan, K. Dai, C. Liu, C. Shen. Vapor sensing performance as a diagnosis probe to estimate the distribution of multi-walled carbon nanotubes in poly (lactic acid)/polypropylene conductive composites. 2018, Sensors and Actuators B: Chemical, 255, 2809-2819.

**4.** X. Wang, **Y. Li**, J. Pionteck, Z. Zhou, W. Weng, X. Luo, Z. Qin, B. Voit, M. Zhu. Flexible poly (styrene-butadiene-styrene)/carbon nanotube fiber based vapor sensors with high sensitivity, wide detection range, and fast response. 2018, Sensors and Actuators B: Chemical, 256, 896-904.

**5.** X. Wang, S. Meng, M. Tebyetekerwa, **Y. Li**, J. Pionteck, B. Sun, Z. Qin, M. Zhu. Highly sensitive and stretchable piezoresistive strain sensor based on conductive poly (styrene-butadiene-styrene)/few layer graphene composite fiber. 2018, Composites Part A: Applied Science and Manufacturing, 105, 291-299.

**6.** Y. Zheng, **Y. Li**, K. Dai, Y. Wang, G. Zheng, C. Liu, C. Shen. A highly stretchable and stable strain sensor based on hybrid carbon nanofillers/polydimethylsiloxane conductive composites for large human motions monitoring. 2018, Composites Science and Technology, 156, 276-286.

**7.** Y. Zheng, **Y. Li**, K. Dai, M. Liu, K. Zhou, G. Zheng, C. Liu, C. Shen. Conductive thermoplastic polyurethane composites with tunable piezoresistivity by modulating the filler dimensionality for flexible strain sensors. 2017, Composites Part A: Applied Science and Manufacturing, 101, 41-49.

**8.** Y. Zheng, **Y. Li**, Z. Li, Y. Wang, K. Dai, G. Zheng, C. Liu, C. Shen. The effect of filler dimensionality on the electromechanical performance of polydimethylsiloxane based conductive nanocomposites for flexible strain sensors, 2017, Composites Science and Technology, 139, 64-73.

**9. Y. Li**, P. Pötschke, J. Pionteck. The relationship between microstructure and the vapor sensing behavior of multi-walled carbon nanotube filled polycarbonate/polystyrene blends. Oral presentation, PPS European Africa Conference, Dresden, Germany, 2017.

**10. Y. Li**, P. Pötschke, J. Pionteck. Compact and porous vapor sensors based on multi-walled carbon nanotube filled blends of poly(vinylidene fluoride) and polycarbonates with different melt viscosities. Oral presentation, PPS Americas Regional Conference, Boston, USA, 2018.

**11. Y. Li**, J. Pionteck, P. Pötschke. Immiscible poly(lactic acid)/polystyrene blend composites filled with multi-walled carbon nanotubes as chemiresistors for volatile organic compounds. Poster presentation, CNPComp2019, London, UK, 2019.

## Versicherung

Hiermit versichere ich, dass ich die vorliegende Arbeit ohne unzulässige Hilfe Dritter und ohne Benutzung anderer als der angegebenen Hilfsmittel angefertigt habe; die aus fremden Quellen direkt oder indirekt übernommen Gedanken sind als solche kenntlich gemacht. Die Arbeit wurde bisher weder im Inland noch im Ausland in gleicher oder ähnlicher Form einer anderen Prüfungsbehörde vorgelegt.

Datum                                            Unterschrift

## Erklärung

Frühere Promotionsverfahren haben nicht stattgefunden.

Die vorliegende Arbeit wurde in der Zeit von November 2015 bis May 2019 am Leibniz Institut für Polymerforschung Dresden e.V. im Rahmen des Projektes zum Thema: "Vapor sensing behavior of sensor materials based on conductive polymer nanocomposites" unter wissenschaftlicher Betreuung von Frau Dr.-Ing. Petra Pötschke und Frau Prof. Brigitte Voit durchgeführt.

Ich erkenne die Promotionsordnung dem Bereich für Chemie und Lebensmittelchemie der Technischen Universität Dresden vom 23.02.2011 in vollem Umfang an.

Datum                                            Unterschrift